On the direct hydrogenation of CO2 towards formic acid

Citation for published version (APA):
de Leeuw den Bouter, A. W. N. (2025). *On the direct hydrogenation of CO2 towards formic acid*. [Phd Thesis 1 (Research TU/e / Graduation TU/e), Chemical Engineering and Chemistry]. Eindhoven University of Technology.

Document status and date:
Published: 26/02/2025

Document Version:
Publisher's PDF, also known as Version of Record (includes final page, issue and volume numbers)

Please check the document version of this publication:

- A submitted manuscript is the version of the article upon submission and before peer-review. There can be important differences between the submitted version and the official published version of record. People interested in the research are advised to contact the author for the final version of the publication, or visit the DOI to the publisher's website.
- The final author version and the galley proof are versions of the publication after peer review.
- The final published version features the final layout of the paper including the volume, issue and page numbers.

Link to publication

General rights
Copyright and moral rights for the publications made accessible in the public portal are retained by the authors and/or other copyright owners and it is a condition of accessing publications that users recognise and abide by the legal requirements associated with these rights.

- Users may download and print one copy of any publication from the public portal for the purpose of private study or research.
- You may not further distribute the material or use it for any profit-making activity or commercial gain
- You may freely distribute the URL identifying the publication in the public portal.

If the publication is distributed under the terms of Article 25fa of the Dutch Copyright Act, indicated by the "Taverne" license above, please follow below link for the End User Agreement:

www.tue.nl/taverne

Take down policy
If you believe that this document breaches copyright please contact us at:

openaccess@tue.nl

providing details and we will investigate your claim.

Download date: 09. May. 2025

On the direct hydrogenation of CO_2 towards formic acid

Anouk W.N. de Leeuw den Bouter

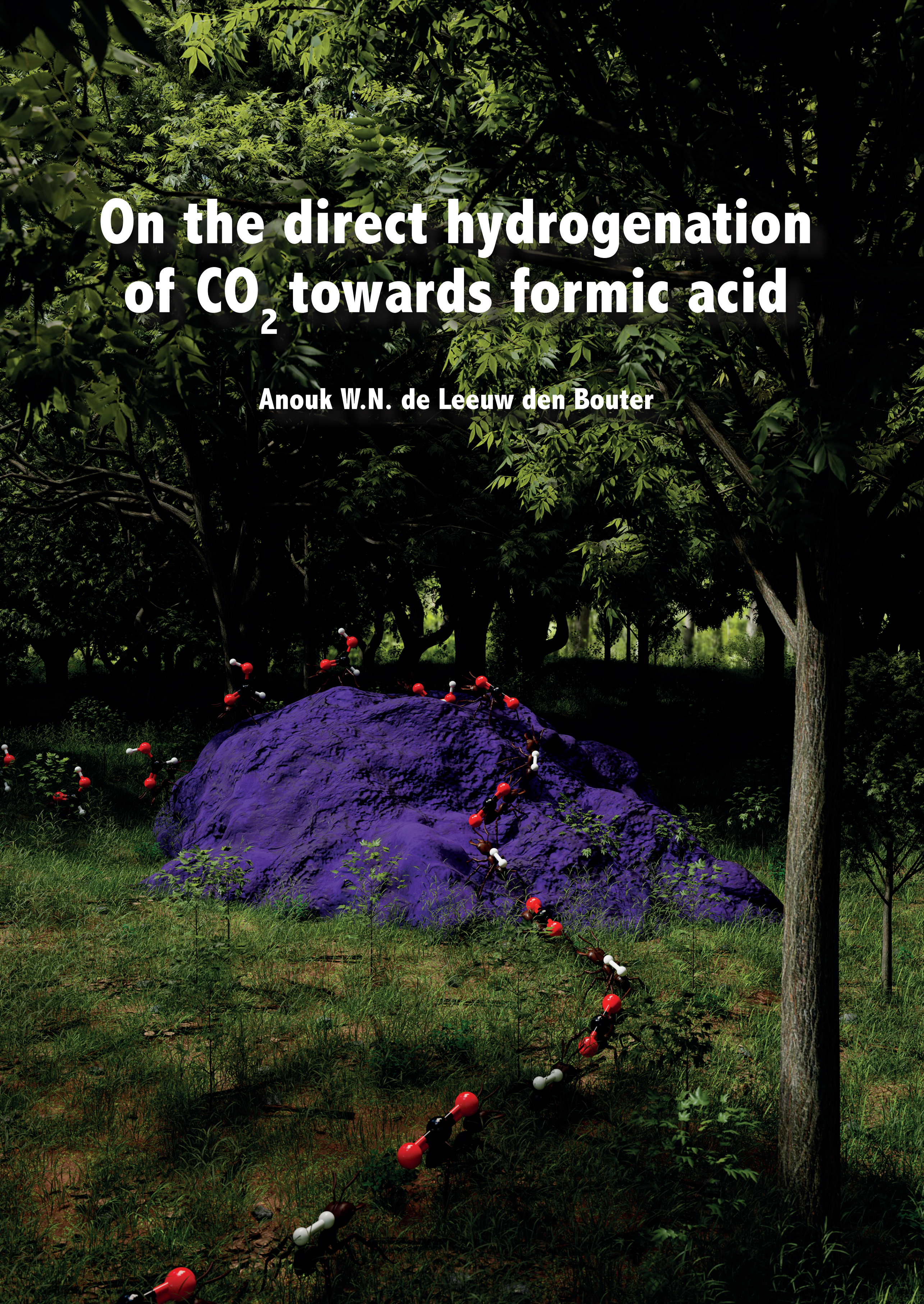

On the direct hydrogenation of CO_2 towards formic acid

PROEFSCHRIFT

ter verkrijging van de graad van doctor aan de Technische Universiteit Eindhoven,
op gezag van de rector magnificus prof.dr. S.K. Lenaerts,
voor een commissie aangewezen door het College voor Promoties,
in het openbaar te verdedigen op woensdag 26 februari 2025 om 13:30 uur

door

Anouk Wilhelmina Neeltje de Leeuw den Bouter
Geboren te Breda

Dit proefschrift is goedgekeurd door de promotoren en de samenstelling van de promotiecommissie is als volgt:

Voorzitter:	prof.dr.ir. D.C. Nijmeijer
1e promotor:	prof.dr.ir. J. van der Schaaf
2e promotor:	prof.dr.eng. F. Gallucci
Leden:	prof.dr.ir. W. de Jong (Technische Universiteit Delft)
	prof.dr.ir. D.W.F. Brilman (Universiteit Twente)
	prof.dr.ir. M. van Sint Annaland
	prof.dr.ir. E.J.M. Hensen
Adviseur	dr. L. Brito Sousa (ENGIE Lab CRIGEN)

Het onderzoek of ontwerp dat in dit proefschrift wordt beschreven is uitgevoerd in overeenstemming met de TU/e Gedragscode Wetenschapsbeoefening.

If I have seen further, it is by standing on the shoulders of giants

Isaac Newton

The research described in this thesis has been caried out in the framework of the European project *C2Fuel.* This project has received funding from the European Union’s Horizon 2020 research and innovation program under grant agreement No 838014.

A catalogue record is available from the Eindhoven University of Technology Library.
ISBN: 978-90-386-6264-0

Cover design by Anouk de Leeuw den Bouter
Printed by ProefSchriftMaken

Contents

Summary

Nowadays, the global energy demands have skyrocketed caused by mass industrialization and globalization. In order to prevent further human induced climate change, future emissions need to be drastically reduced and the urge for more renewable fuels is omnipresent. Over the last decades, the production and storage of molecular hydrogen has been identified as a key solution to the current global warming crisis, even though the energy cycle with hydrogen is highly inefficient. Additionally, hydrogen has a low boiling point and low volumetric energy density under standard conditions, resulting in the necessity of compression or liquefaction to allow for economical and safe transport and storage.

An alternative has been found in formic acid, which gained considerable traction as a possible liquid organic hydrogen carrier (LOHC) due to the possibility straightforward hydrogen release at room temperature. One of the possible production methods is the direct hydrogenation of CO_2. However, the equilibrium reaction is highly unfavorable from a thermodynamic point of view, and can be made slightly favorable by lowering the formic acid activity in solution through in-situ reduction using tertiary amines and using high, supercritical pressures of CO_2. The combination of formic acid and tertiary amines form a so-called adduct, which drive the reaction towards the product side. However, currently the competitiveness of the process is severely hindered by the challenging and energy intensive formic acid purification due to the formation of azeotropes between formic acid and the employed low boiling tertiary amines.

Given the above considerations, this thesis investigates the potential of the direct hydrogenation of CO_2 towards formic acid, addressing various aspects from the exploration of the influence of the aliphatic chain length of the tertiary amine on formic acid binding capacity, the influence of the reactive amine on key aspects such as activity and selectivity, the development of catalytic materials and lastly a demonstration of the technology at reactor and process scale.

A general introduction to the topic given is in **Chapter 1**, which, after highlighting the urgency of drastically reducing CO_2 emissions to circumvent further human induced climate change, provides an overview of possible solutions to be implemented in the chemical and energy sectors. The concept of Liquid Organic Hydrogen Carriers is introduced, highlighting the benefits of formic acid. The Chapter concludes with an overview of the conventional and several sustainable production methods.

The primary objective of **Chapter 2** was to gain a deeper understanding into the nature of the chemical bonds formed and the degree of proton transfer between formic acid and tertiary amines of different aliphatic chain lengths. Here, IR spectroscopy revealed the existence of a complex mixture of hydrogen bonding and ionic interactions. The red-shift observed for the asymmetrical COO^- band gave an indication for a decrease in proton transfer as a function of chain length, which was further quantified using ^{1}H-NMR. Interestingly, it was observed that while the degree of proton transfer decreases as a function of alkyl chain length, the hydrogen bonding characteristic increases, resulting in a constant acid-to-amine ratio. Additionally, phase separation occurred until a molar ratio of ~1.5:1 formic acid: amine was reached for all tertiary amines.

To circumvent the biphasic nature observed in **Chapter 2**, often polar solvents are utilized. With the goal of process intensification, it was attempted to increase formic acid productivity through removal of the additional alcohol based solvent and performing the reaction in pure tertiary amines as this theoretically results in a kinetic rate increase. These experiments did not result in any observable formic acid production, as shown in **Chapter 3**. Analysis on the spent catalyst revealed significant formic acid build-up within the catalyst pores. A fundamental, continuum model based on Cahn-Hilliard spinodal decomposition was developed and validated to study the influence of the biphasic nature of formic acid – trialkylamine structures during reaction at pore level. A thin shell of adduct is observed to form around the active site, with the local conditions reaching the equilibrium conversion. However, due to the strong immiscibility of the adduct and neat amine phases shown in **Chapter 2**, the produced formic acid is not transported to the bulk liquid, resulting in a net reaction rate of virtually zero.

Next, the influence of the tertiary amine on CO_2 conversion and product selectivity was studied in **Chapter 4**. Steric hindrance and the pKa of the tertiary amine were identified as key parameters influencing both the observed kinetic rates as well as the CO_2 conversion. The usage of solventless polar amines such as diethylethanolamine allowed for FA productivity up to 5x that of the benchmark triethylamine system. Catalyst deactivation of the Au/TiO_2 catalyst was observed for all amines studied. Here, a phase of high initial activities was observed at an initial gold crystallite size of 2.6 nm. In case of e.g. diethylethanolamine, an initial production of 40 mM at a residence time of 15 minutes was reduced to 7 mM after 3 hours' time-on-stream due to sintering with a final particle size of 13 nm. Within this time period, the productivity remained constant for up to 13 hours' time-on-stream.

As severe and rapid catalyst deactivation was observed in **Chapter 4** independent of the tertiary amine used within the reaction, it was attempted to develop a catalyst of increased stability. Here, a range of mono-metallic (Au/Al_2O_3, Pd/Al_2O_3 and Ru/Al_2O_3) and bimetallic catalysts (Au-Pd, Au-Ni, and Au-Cu/Al_2O_3) was studied. The synthesized catalysts were characterized through XPS, XRD, TEM, ICP and CO pulse chemisorption. As demonstrated in **Chapter 5**, their performance in terms of productivity and selectivity was tested in both the formic acid decomposition as well as formic acid formation at elevated pressures. The TOF increased up to 5.3x compared to Au/TiO_2 were obtained for Au-Pd/Al_2O_3 catalysts, while Au-Cu/Al_2O_3 resulted in large amounts of CO being produced. The activity of the Au-Ni/Al_2O_3 catalysts was observed to be similar to the activity of monometallic gold based catalysts. Testing under constant triethylamine:1-decanol ratio revealed comparable initial FA productivity for the Au, Pd and Au-Pd catalysts supported on alumina, while the Ru/Al_2O_3 catalyst has low selectivity towards FA. Furthermore, all alumina supported catalysts result in the unwanted production of CO, with the Ru-based catalyst yielding CO as the major product.

In **Chapter 6** a techno-economic evaluation is conducted using Aspen Plus, comparing the state-of-the-art process to the process developed within this thesis, based on gold catalysts. Within the state-of-the-art process, the reaction is performed using triethylamine which is exchanged to trihexylamine through reactive distillation. Based on simulations, it was concluded that the major cost contributors were the significant amounts of gold-based catalyst and the large amount of steam required to facilitate the amine exchange reaction. To circumvent the formation of the unfavorable azeotrope and thus necessity of the amine exchange reaction, n-butylimidazole was selected as a reactive amine. To obtain fuel cell grade formic acid, a pressure-swing distillation train was designed. Here, the major cost contributor was found to be the amount of catalyst required, due to low catalyst activity after the deactivation phase observed within **Chapters 4 and 5**.

Finally, the main findings of this thesis and the research outlook are summarized in **Chapter 7.**

Samenvatting

Heden ten dage is de wereldwijde energie consumptie significant gestegen ten opzichte van de pre-industriële tijd door grootschalige industrialisatie en globalisatie. Om verdere door mensen geïnduceerde veranderingen aan het klimaat te voorkomen dient de toekomstige uitstoot van broeikasgassen drastisch gereduceerd te worden, alsmede dient de overgang naar hernieuwbare brandstoffen dringend gemaakt te worden. In de afgelopen decennia is de productie en opslag van waterstof geïdentificeerd als een mogelijke oplossing voor het huidige opwarmen van de aarde, echter is de gehele waterstof cyclus inefficiënt gebleken. Deze inefficiëntie komt met name voort uit het feit dat waterstof zowel een laag kookpunt als een lage volumetrische energie dichtheid heeft onder standaard condities, waardoor compressie of liquefactie nodig is om tot economisch en veilig transport en opslag te komen.

Alternatief, zou deze opslag kunnen plaats vinden met behulp van mierenzuur, een veel onderzocht molecuul voor waterstof opslag, ook wel vloeibaar organische waterstof drager genoemd. Een mogelijke manier om dit molecuul te produceren is de directe hydrogenatie van CO_2. Echter, de ligging van het reactie evenwicht is ongunstig vanuit een thermodynamisch oogpunt, en kan verschoven worden door middel van tertiaire amines en hoge, superkritische CO_2 druk. Het gebruik van tertiaire amines resulteert in de formatie van zogenoemde adducten, waardoor de activiteit van mierenzuur in de oplossing gereduceerd wordt en zo het evenwicht verschoven naar de product kant. Niettemin is deze oplossing op dit moment niet economisch haalbaar door het gebruik van amines met een laag kookpunt. Dit lage kookpunt alsmede de formatie van azeotropen tussen de amine en het mierenzuur resulteren in een energie intensive mierenzuur purificatie.

Om deze reden ligt de focus van dit proefschrift op het demonstreren van de haalbaarheid van mierenzuur als waterstof drager, waarbij de productie plaats vindt door de directe, hydrogenatie van CO_2. Hiertoe zijn verschillende aspecten bestudeerd, zoals de invloed van de tertiaire amine koolstofketen lengte op het vermogen van de amine om mierenzuur te binden, de invloed van de amine keuze op aspecten als activiteit en selectiviteit, het ontwikkelen van nieuwe katalytisch actieve materialen en tot slot het demonstreren van de technologie op reactie en productie schaal.

Een algemene introductie op het onderwerp wordt gegeven in **Hoofdstuk 1**. Hier wordt eerst de nadruk gelegd op de urgentie van het verminderen van de broeikasgas uitstoot, gevolgd door een overzicht van mogelijke oplossingen voor de chemische en energie sector. Hierna wordt het concept van Vloeibaar Organische Waterstof Dragers geïntroduceerd met een focus op de implementatie van mierenzuur. Uiteindelijk wordt een overzicht gegeven van conventionele op fossiele brandstoffen gebaseerde productie methoden, alsmede nieuwe productie methoden op basis van het gebruik van CO_2 als bron van koolstof.

Het doel van **Hoofdstuk 2** was om te begrijpen welk type chemische bindingen gevormd worden in adduct complexen bestaande uit tertiaire amines van verschillende koolstof keten lengtes en mierenzuur. Uit IR spectroscopie kon worden geconcludeerd dat zulke adducten bestaan uit een complex mengsel van waterstof bruggen en ionische interacties. Hier gaf een roodverschuiving van de asymmetrische COO^- band een indicatie voor het afnemen van de proton transfer van mierenzuur naar de amine met toenemende koolstofketen lengte, hetgeen verder gekwantificeerd is met behulp van ^{1}H-NMR spectroscopie. Ondanks een afnemende mate van proton transfer, werd een constante zuur-base ratio geobserveerd, wat uitgelegd kan worden aan de hand van een toenemende hoeveelheid waterstof bruggen. Bovendien vond fasescheiding tot een bifasisch mengsel plaats tot een mol ratio van ~1.5 mierenzuur:amine voor alle bestudeerde amines.

Om de hiervoor in **Hoofdstuk 2** genoemde fasescheiding van mierzuur – tertiaire amine mengsels te voorkomen worden vaak polaire oplosmiddelen gebruikt. Om het proces te intensiveren is het getracht de mierenzuur productiviteit te verhogen door pure, niet verdunde amines te gebruiken. Deze experimenten resulteerden echter niet in kwantificeerbare productie van mierenzuur, zoals beschreven in **Hoofdstuk**

3. Uit analyse van de gebruikte katalysator bleek dat er een aanzienlijke hoeveelheid mierenzuur zich in de poriën van de katalysator had opgehoopt. Om dit op porie niveau te kunnen bestuderen is een fundamenteel, continue model gecreëerd en gevalideerd gebruikt makende van de beroemde Cahn-Hilliard vergelijkingen voor spinodale ontbinding. In deze simulaties werd waargenomen dat een dunne laag adduct vormt rond de katalytische actieve goud nano deeltje, waarbij een lokaal evenwicht ontstaat binnen deze laag. Echter, de sterke onmengbaarheid tussen adduct en amine geobserveerd in **Hoofdstuk 2** maakt dat het geproduceerde mierenzuur niet naar de bulk vloeistof kan diffunderen. Hierdoor ontstaat een lokaal evenwicht en wordt de reactie snelheid gereduceerd tot vrijwel nul.

Nadat het gebruik van pure alkyl tertiaire amines werd uitgesloten als middel van proces intensivering, werd de focus gelegd op de invloed van de selectie van de tertiaire amine op CO_2 conversie en product selectiviteit in **Hoofdstuk 4**. Hier bleek dat sterische hinder en de pKa van de tertiaire amine de voornaamste parameters zijn die de mierenzuur productie snelheid bepalen. Ook werd ontdekt dat het gebruik van pure, niet verdunde amines mogelijk is door de introductie van polaire groepen in de koolstof staarten van de amine. Het gebruik van een polaire amine zonder oplosmiddel, namelijk diethylethanolamine, resulteerde in een 5x hogere mierenzuur productiviteit dan de voorheen gebruikte triethylamine onder gelijke condities. Deactivatie van de Au/TiO_2 katalysator werd geobserveerd voor alle bestudeerde amines, waarbij een periode van hoge mierenzuur productiviteit werd waargenomen voor een goud deeltjes grootte van 2.6 nm. De hoge initiële productiviteit bij het gebruik van bijvoorbeeld diethylethanolamine van 40 mM reduceerde naar 7 mM na slechts 3 uur reactie tijd. Uit TEM en CO puls chemisorptie bleek dat de goud deeltjes een grootte van 13 nm hadden. Langere experimenten tot 13 uur reactie tijd lieten zien dat de productiviteit constant blijft na de initiële, snelle deactivatie.

Doordat de Au/TiO_2 katalysator snel en significant productiviteit verloor in **Hoofdstuk 4** voor alle bestudeerde amines, werd getracht een stabiele katalysator te ontwerpen in **Hoofdstuk 5**. Hiertoe zijn verschillende mono-metallische (Au/Al_2O_3, Pd/Al_2O_3 en Ru/Al_2O_3) alsmede bi-metallische materialen (Au-Pd, Au-Ni, en $Au\text{-}Cu/Al_2O_3$) getest. De gesynthetiseerde katalysatoren zijn gekarakteriseerd door middel van XPS, XRD, TEM, ICP en CO puls chemisorptie. De productiviteit en selectiviteit van alle materialen is bestudeerd zowel voor de omzetting van mierenzuur naar CO_2 en H_2 als de formatie van mierenzuur uit deze gassen. Het gebruik van Au-Pd/Al_2O_3 als mierenzuur decompositie katalysator resulteerde in een verhoging van de TOFs van tot 5.3x ten opzichte van Au/TiO_2, terwijl de introductie van koper in de vorm van Au-Cu/Al_2O_3 de selectiviteit verschoof van CO_2 naar CO. De activiteit van de Au-Ni/Al_2O_3 katalysatoren was vergelijkbaar met de mono-metallische goud gebaseerde katalysatoren. De Au, Pd en Au-Pd gebaseerde katalysatoren vertoonde gelijke initiële mierenzuur productiviteit tijdens CO_2 hydrogenatie experimenten onder een constant triethylamine:1-decanol ratio, terwijl de Ru/Al_2O_3 een verwaarloosbare selectiviteit en productiviteit (<1 mM) naar mierenzuur vertoonde. Bovendien produceerden alle op aluminium oxide gebaseerde katalysatoren het ongewenste CO, waarbij de Ru-gebaseerde katalysator CO als voornaamste product had.

In **Hoofdstuk 6** wordt een techno-economische evaluatie uitgevoerd met Aspen Plus, waarbij het state-of-the-art proces wordt vergeleken met het proces dat in dit proefschrift is ontwikkeld, op basis van goud katalysatoren. Binnen het state-of-the-art proces wordt de reactie uitgevoerd met triethylamine, dat vervolgens wordt uitgewisseld naar trihexylamine door middel van reactieve destillatie. Op basis van simulaties werd geconcludeerd dat de belangrijkste kostenposten de aanzienlijke hoeveelheden goud gebaseerde katalysator en de grote hoeveelheid stoom waren die nodig was om de amine-uitwisselingsreactie te bewerkstelligen. Om de vorming van de ongunstige azeotroop en dus de noodzaak van de amine-uitwisselingsreactie te omzeilen, werd n-butylimidazool geselecteerd als een reactief amine. Om mierenzuur van brandstofcelkwaliteit te verkrijgen, werd een druk-swing-destillatietrein ontworpen. Hier bleek de belangrijkste kostenpost de hoeveelheid benodigde katalysator te zijn, vanwege de lage katalysatoractiviteit na de deactiveringsfase die werd waargenomen in **Hoofdstukken 4 en 5**.

Tot slot worden de belangrijkste bevindingen van dit proefschrift samengevat in **Hoofdstuk 7**.

1

Introduction

1.1 CO_2 emissions and mitigation

High energy density fuels such as kerosene and gasoline derived from fossil fuels (coal, oil and natural gas) enabled the industrial revolution and following global economy. These developments, combined with the exponential growth of the world population and increased living standards [1], caused the global energy demand to skyrocket since the start of the industrial revolution in the mid-1700s. As depicted in Figure 1.1, this has resulted in significant energy consumption rates, with the global yearly energy demand in 2021 being 576 EJ [2], and is expected increase to 672 EJ in 2050 [3].

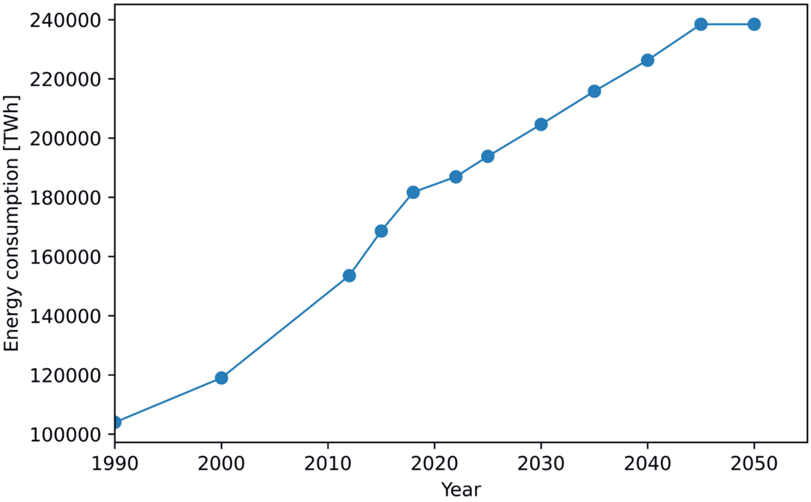

Figure 1.1: Projected worldwide energy consumption from 1990 to 2022, with furcating up to 2050. Data retrieved from reference [3].

The major energy sources nowadays are fossil fuels such as oil, coal and natural gas, with renewables only making up 4.3% of the total energy consumption in 2021 [4].

The combustion of fossil fuels for energy generation results in the emission of greenhouse gasses such as CO_2 and NO_x [5]. The combustion of such fuels for energy generation combined with CO_2 emissions from industrial processes lead to CO_2 being the most emitted greenhouse gas in 2022 at 89% of total energy-related greenhouse gas emissions, with a striking 36.8 Gt being emitted. The excessive usage of fossil-derived fuels has readily resulted in a significant increases in the atmospheric CO_2 concentrations up to 412 ppm corresponding to a 47% increase since the start of the Industrial Revolution [6].

These anthropogenic carbon emissions have been linked to negative environmental impact [7], such as global temperature increases, the disappearance of the glaciers and the acidification of the oceans [7][8][9]. In order to prevent further human induced climate change, future emissions need to be drastically reduced and the urge for more renewable energy is omnipresent [7]-[10]. The urgency also becomes apparent from the introduction of stringent regulations, large capital investments into renewable energy sources and the introduction of CO_2 emission taxes along the entire chemical value chain [11]. These investments and regulations are meant to restrict the global warming to 2 ºC compared to pre-industrial times as well to attain net zero emissions by 2050, as agreed by 196 countries in the Paris Agreement [12].

With the world population and global energy demand projected to keep growing in exponential fashion, the drastic decarbonization of the energy sector becomes essential [13]. Here, it readily becomes apparent that the development and implementation of renewable energy sources for power production will play a vital and fundamental role in a new sustainable and fossil-free era. However, renewable energy sources, such as wind and solar energy, are inherently intermittent in nature, therefore necessitating the development of reliable storage methods to ensure a continuous supply of energy [14][15].

A prime example of such a renewable energy source is hydrogen, which for example can be produced without carbon emissions from water electrolysis, combined with electricity from renewable sources such as solar or wind farms [14][15]. Currently, the widespread implementation of a so-called ‘hydrogen economy' is hindered by the challenges associated with the low volumetric energy density (0.09 g/L) of molecular hydrogen [16][17]. Conventional approaches to increase the energy density include compression and liquefaction [18][19]. Compression for mobility applications such as fuel cell driven vehicles requires pressures up to 70 MPa, while liquefaction involves cryogenic temperatures. Such low temperature applications can cost up to

30% of the energy stored within the energy carrier [20]. Due to the harsh conditions necessary to achieve an increase in energy density, these techniques have been shown to suffer from relativity high costs and to be highly energy intensive [20].

Alternatively, hydrogen could be directly transformed into dense energy carriers such as liquid fuels [21], enabling the transport of hydrogen based on the existing fuel infrastructure [11]. This concept is known as Liquid Organic Hydrogen Carriers (LOHC) and involves the reversible hydrogenation and dehydrogenation of a carrier molecule such as N_2 or CO_2, as illustrated in Figure 1.2. [22][23].

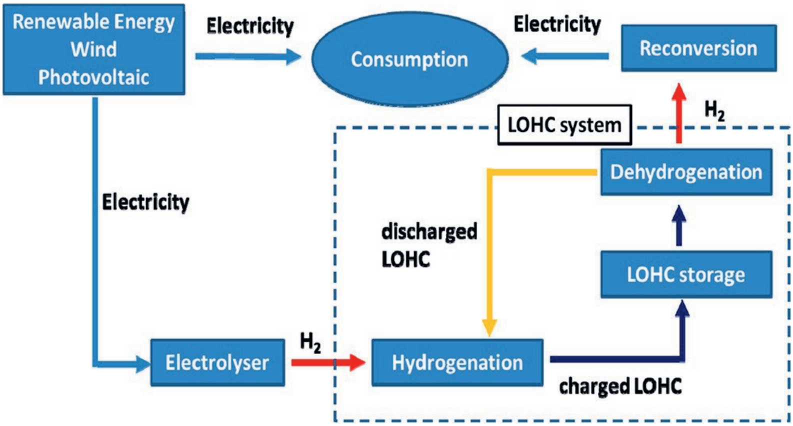

Figure 1.2: Schematic overview of the Liquid Organic Hydrogen Carrier (LOHC) concept. Figure adapted from reference [100].

Examples of LOHC include ammonia, methanol, dimethyl ether and formic acid [20]. Their respective energy densities on a volume and weight basis are compared to current fuels such as gasoline and hydrogen in Figure 1.3.

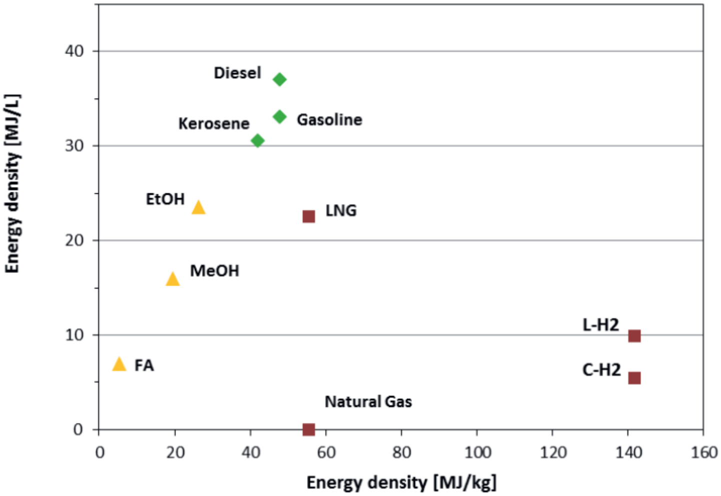

Figure 1.3: Comparison of the energy density of a several types of fuels on a volume (MJ/L) and weight (MJ/kg) basis. C-H2 represents compressed hydrogen (700 bar), L-H2 liquefied hydrogen (-253 ºC), LNG liquefied natural gas, MeOH methanol, EtOH ethanol and FA formic acid. Figures adapted from reference [101].

While the employment of renewable energy sources such as wind and solar for power generation will enable the significant mitigation of CO_2 emissions, not all CO_2 emissions arise from energy generation, as some large scale industrial processes such as waste incineration, cement and steel production also generate CO_2 emissions in vital process steps [24][102]. Thus, the currently inevitable usage of fossil fuels in combustion driven energy generation combined with hard-to-abate processes result in the necessity to remove carbonaceous components from industrial sources and the atmosphere in order to close the carbon cycle, therefore limiting and/or mitigating further anthropogenic environmental damage [25].

In this context, the principle of Carbon Capture Utilization and Storage (CCUS) has been proposed as a pivotal technology for decarbonization [24][25]. Recently, CCUS is the topic of significant research efforts [25], resulting in the development of several carbon capture technologies such as liquid absorption, adsorption onto solid carriers, cryogenic distillation and membrane separation [26]. The captured CO_2 can subsequently be sequestrated in e.g. geological reservoirs or be used as a C_1 carbon source for the production of added-value chemicals and fuels [11][14].

While the concept of Carbon Capture and Storage (CCS) has been identified as an effective short-term solution to decrease CO_2 emissions, the long-term effects of storing CO_2 on geological formation remain unknown [27]. Besides uncertainty regarding the safety of such storage methods, recent studies also revealed the CCS concept to be expensive and energy inefficient [28][29]. Alternatively, in Carbon Capture and Utilization (CCU), the carbon is utilized for the production of value-added chemicals [29]. Several versatile chemicals like methanol, dimethyl ether (DME), urea, formic acid, hydrocarbons such as ethylene and carbonates have previously been synthesized [30][31]. While no general consensus has been reached within the scientific community on the potential of the CCU concept, studies have shown that the potential for CO_2 utilization ranges from 200 to 500 million metric tons per year [32][33], allowing for the recycling of up to 10% of the current anthropogenic emissions [32][34]. The catalytic hydrogenation of CO_2 is widely recognized as one of the most effective methods to utilize the CO_2 obtained from carbon capture [30][32][33].

Therefore, combining the storage of surplus renewable energy in the form of green hydrogen through electrolysis with the inexpensive carbon obtained from CCU could pose a crucial strategy in the decarbonization of the chemical and energy industries. The purpose of such methodology is twofold: the production of high gravimetric energy density H_2 carriers in the form of hydrocarbons, and the direct production of green chemicals (i.e. methanol and dimethyl ether) that can be utilized as direct energy sources through combustion or utilization in fuel cells.

1.2 Formic acid as hydrogen carrier

A large variety of products based on direct CO_2 hydrogenation have previously been reported in literature, such as methanol, ethanol, dimethyl ether (DME), urea, formic acid, hydrocarbons such as ethylene and carbonates [30][31].

Although formic acid has a lower hydrogen density at 4.4 wt% than the aforementioned molecules in Figure 1.3, its relatively low toxicity, non-flammability, biodegradability and liquid state at ambient conditions result in FA being a competitive alternative [23][37]. Formic acid has a volumetric energy content of 2.1 kWh/L, corresponding to 53 g H_2/L [38]. Besides favourable physical and chemical properties, previous works have shown that CO_2 based FA production has a large potential for mitigating CO_2 emissions compared to the conventional methyl formate hydrolysis process [39][40].

A fundamental property of a competitive LOHC is its reversibility to enable the release of hydrogen when energy is required. A key advantage of FA as an LOHC is in readily reversible nature, as the liberation of hydrogen from formic acid is an established process which can be performed at nearly 100% selectivity at temperatures as low as room temperature [22][23], thus allowing for an ideal carbon-neutral cycle for hydrogen storage [41]. Besides applications as a hydrogen storage medium, formic acid can also be decomposed within direct formic acid fuel cells to generate electricity [42].

Besides prospected energy applications, formic acid is a valuable commodity chemical with a global annual production of approximately 300000 tonnes [43], valued at $620 million in 2019 [44]. The formic acid market demand has been estimated to increase by 5.6% on a yearly basis [45].

Formic acid has applications in textiles, agriculture, pharmaceuticals [19][46]. It is a frequently used reductant within various synthesis routes (such as Eschweiler-Clark methylation and transfer hydrogenolysis [43]) and as a green solvent [44]. Several formic acid derivatives also have a considerable market size, such as sodium formate (a de-icing salt), methyl formate, dimethyl formamide (solvent) and ethyl formate (flavouring) [43].

1.2.1. Conventional production routes

The name formic acid has been derived from the Latin word formica, meaning ants. Formic acid naturally occurs in some species of ants and bees, as well as within the atmosphere originating from forest emissions [44], and was first isolated by in 1754 by Markgraf through the distillation of red ants [43]. An overview of current fossil-based and non-fossil based FA production methods is given in Figure 1.4.

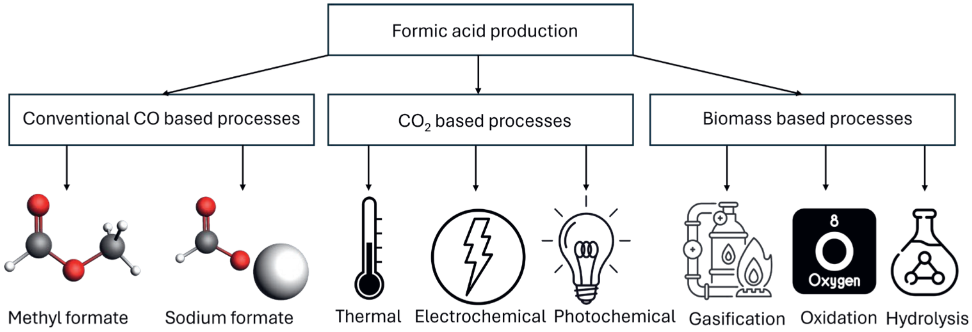

Figure 1.4: Overview of FA production methods.

Current FA production methods are based on fossil resources and include the acidolysis of alkali formates and the hydrolysis of methyl formates. The latter is the most used on industrial scale at approximately 80% of total production [47], and involves a two-step process: the reaction between CO and methanol to produce methyl formate at high pressure (> 4 MPa), followed by the subsequent hydrolysis resulting in FA and methanol [20][23]. The reaction scheme can be summarized by [20][23]:

$$CH_3OH + CO \rightarrow HCOOCH_3 \tag{1.1}$$

$$HCOOCH_3 + H_2O \rightarrow HCOOH + CH_3OH \tag{1.2}$$

A multitude of intermediates have been shown to form during the process, resulting in a complex, multistep and highly energy intensive product separation. Commonly, CO is produced through the gasification of coal or natural gas at high temperatures (> 900 K) [45], resulting in significant CO_2 emissions.

1.2.2. Novel production routes

Formic acid can be produced without the utilization of fossil sources using CO_2 as carbon source based on a variety of methods such as photochemical, electrochemical and thermal chemical methods [48][26].

1.2.2.1. Photochemical CO_2 reduction towards FA

Inspired by natural photosynthesis, which uses solar light as its main energy source, the scientific community has aimed to develop methods to allow for the direct sunlight for chemical transformations [51]. Within recent years, this resulted in a surge in publications demonstrating the visible light-mediated reduction of CO_2 towards valuable liquid products such as methanol, formic acid and gaseous products such as CO and methane [52]–[55]. Based on this approach, the most abundant renewable energy source, namely solar energy, could be directly used to aid in the synthesis of renewable fuels [56].

Photocatalytic reduction of CO_2 often involves the usage of a photosensitizer combined with a homogeneous or heterogeneous catalyst [51][56]. Here, the photons are absorbed by a sensitizer, which through the absorption of light equal or greater than the band gap initiates the excitation of valence band electrons. These excited electrons are then injected into the conduction band of the catalyst [57], resulting in the reduction of CO_2 towards formic acid in a two electron process [51].

Typical catalyst materials include solid semiconductors such as ZnS, CdS, ZnO and TiO_2 [51] or homogeneous catalysts based on Ru or Co complexes [56]. Despite extensive efforts, the productivity of the process remains low, with typical formic acid productivities in the range of $1.5 \cdot 10^{-5}$ g_{FA}/g_{cat}/hr. Such low productivities result in low overall formic acid concentrations, and thus high purification costs. Besides low productivity, the photochemical pathway also suffers from instability of the used catalytic materials under photochemical conditions leading to the loss of catalyst activity [56]. Therefore, this methodology is far from industrial application.

1.2.2.2. Electrochemical CO_2 reduction towards FA

CO_2 can be directly reduced to valuable products such as CO, methane, ethylene, formic acid, methanol and ethanol in aqueous environment within electrochemical cells at room conditions [58]. Electrochemical reduction (ECR) has emerged as a potential formic acid production method due to its controllable reaction parameters (such as temperature, pressure and applied potential), scale-up potential, and possibility for integration with renewable energy sources [59][60].

However, the standard potentials for CO_2 reduction and the Hydrogen Evolution Reaction (HER) are close to each other, resulting in the formation of undesired by-products such as hydrogen. Such competition between CO_2 and water reduction can result in low production selectivity, which combined with high activation barriers for CO_2 reduction leads to the necessity of electrocatalysts [61]. Commonly investigated materials are Sn, In and Bi [62][63].

Previous studies on electrochemical methods for FA production have highlighted the potential for a significant decrease in global warming impact (GWI) due to low steam consumption, the integration of renewable electricity and the relativity simple process layout [48]. A techno-economic evaluation performed by Kim *et al*. revealed the economic performance of the electrochemical FA production method to be competitive with liquefied H_2 distribution [40]. However, the technology has not yet been proven on a large scale continuous system, while such pilot plant studies have readily been performed for formic acid production using the direct CO_2 hydrogenation process [48].

1.2.2.3. Thermochemical CO_2 reduction towards FA

The thermochemical FA production is an exothermic hydrogenation reaction, albeit the reaction is known to be strongly endergonic due to the phase change involved in the transformation of the gaseous reactants into a liquid product. The addition of aqueous solvents results in an exergonic reaction [7][64][65], as summarized below:

$$H_{2(g)} + CO_{2(g)} \rightleftharpoons HCOOH_{(l)} \qquad \Delta G^\circ = +32.9\,\frac{\mathrm{kJ}}{\mathrm{mol}},\ \Delta H^\circ = -31.2\,\frac{\mathrm{kJ}}{\mathrm{mol}},\ \Delta S^\circ = -215\,\frac{\mathrm{J}}{\mathrm{K\,mol}} \qquad 1.3$$

$$H_{2(aq)} + CO_{2(aq)} \rightleftharpoons HCOOH_{(aq)}\ \Delta G^\circ = -4\ \mathrm{kJ/mol} \qquad 1.4$$

Due to the highly unfavourable nature of the reaction, pressures above 10 MPa and temperatures above 150 ºC are required for the reaction to proceed towards formic acid, without the addition of catalysts [27][28]. Alternatively, two strategies are commonly exploited to mitigate the thermodynamic limitations of the direct hydrogenation reaction, namely the selection of appropriate solvents such as water, alcohols and ionic liquids and the introduction of secondary reactions / molecular interactions [45][65][68].

The solvation effect reduces the entropy effect of the phase change occurring within the reaction [65], however, the most commonly exploited strategy is the addition of bases such as amines, hydroxides and (bi)carbonates [7]. Here, adducts are formed through exothermic protonation of the base by the produced formic acid, therefore shifting the equilibrium towards the product side [7][64]. Additionally, the exothermic protonation delivers sufficient energy to result in an exergonic reaction if the protonation enthalpy is > 50 kJ/mol [69], therefore driving the reaction towards formic acid:

$$H_{2(g)} + CO_{2(g)} + NH_{3(aq)} \rightleftharpoons HCO^{-}_{2(aq)} + NH^{+}_{4(aq)} \quad \Delta G^\circ = +9.5\,\frac{\mathrm{kJ}}{\mathrm{mol}},$$
$$\Delta H^\circ = -84.3\,\frac{\mathrm{kJ}}{\mathrm{mol}}, \Delta S^\circ = -250\,\frac{\mathrm{J}}{\mathrm{K\,mol}} \qquad 1.5$$

Often low boiling tertiary trialkylamines amines such as triethylamine are used [30][31], as primary and secondary amines can result in the formation of covalent bonds with formic acid to form formamides. To illustrate the importance of amine selection, when high boiling point tertiary amines are used in neat condition, such as trihexylamine, no formation of formic acid was observed by previous works due to too little reaction enthalpy being delivered by amine protonation [69][65]. The reaction enthalpy between formic acid and trihexylamine was observed to be only -28.1 kJ/mol [65]. The overall reaction is given by [65]:

$$1.5\,H_2 + 1.5\,CO_2 + NHex_3 \rightleftharpoons [HNHex_3][HCOO \cdot 0.5\,HCOOH] \qquad \Delta H^\circ = -59.3\ \text{kJ/mol} \tag{1.6}$$

However, when combined with polar solvents such as alcohols and diols, the reaction becomes exergonic, presumably through interaction with the formate anion by the alcohol functional group of the solvent. Using 2-methyl-1,3-propanediol as solvent results in [65]:

$$H_2 + CO_2 + NHex_3 \rightleftharpoons [HNHex_3][HCOO] \qquad \Delta H^\circ = -77\ \text{kJ/mol} \tag{1.7}$$

Besides adduct formation, evidence also suggests that the base aids in the desorption of formate from the catalyst surface [70], therefore suggesting the participation of the amine in the catalytic cycle [71].

The utilization of low boiling amines, required to deliver sufficient protonation enthalpy, results in the formation of stable azeotropes, rendering thermal formic acid purification challenging [72]. Commonly, formic acid purification of such formic acid – triethylamine adducts is performed according to a process developed by British Petroleum (BP) [73]. This methodology is based on a so-called amine exchange process, in which the low boiling tertiary amine is replaced by a high-boiling tertiary amine in a reactive distillation process [31][32]. This technique allows for the separation of the adduct through vacuum distillation under mild conditions and has been demonstrated on lab scale [68].

While systems utilizing low boiling point amines have shown high catalytic activity, formic acid purification is energy intensive due to the necessity of acidification or amine – exchange reactions under harsh conditions [39][40]. Previous works have shown the amine-exchange reaction to be highly energy intensive due to significant steam input required within distillation to provide sufficient energy to break the formic acid – tertiary amine bond [39][40].

Several strategies have been investigated to perform the reaction under base-free, neutral circumstances [45][74]–[77]. Common strategies include the usage of ionic liquids as solvents/buffers [75][34] and the immobilization of amines or ionic liquids onto solid carriers [74][76][77], often combined with active hydrogenation metals [78][79]. Typically, such systems operate under high H_2 and CO_2 partial pressures resulting in supercritical conditions [80] and the total system activity obtained is significantly lower compared to basic conditions [74].

While the economic competitiveness of the direct hydrogenation reaction performed under basic condition is currently hampered by the challenging and energy-intensive separation [39], the TOFs obtained are significantly higher compared to base free systems [76]. For example, TOFs up to 300 $g_{FA}/g_{cat}/h$ were reported by Weilhard *et al*. using multifunctional ionic liquids [76], while TOFs over 2000 $g_{FA}/g_{cat}/h$ were reported when using a heterogeneous Ru-based catalyst with triethylamine as base [64] under comparable reactive conditions.

Of the aforementioned methods of the previous sections, the direct reduction of CO_2 using hydrogen has been shown to be the most promising route in terms of economic viability and process maturity [16][17]. However, the high thermal stability of CO_2 towards reduction requires highly active catalysts to activate the CO_2 [9][10]. Furthermore, the production of formic acid is in competition with the reverse water gas shift reaction, resulting in the production of carbon monoxide [7][64].

A broad range of catalysts has been previously studied based on both homogeneous and heterogeneous formulations [9][10][18][8]. While homogeneous metal complexes based on Ru and Ir have shown excellent activity and selectivity [83][20], the final formic acid concentrations remain far from industrially relevant conditions when expressing the productivity per unit time and unit reactor volume, due to the low catalyst concentrations [64]. Combined with the inherent drawbacks of homogeneous catalysts such as difficult product separation and catalyst recycling have prompted research towards heterogeneous catalysts [20][21].

The heterogeneous compositions explored by previous authors focus on a wide range of noble metals including Au [86][70], Pt [24][25], Pd [26][27] and Ru [19][28][91] deposited on a wide range of supports [9][10].

While Pd-based catalysts are often hailed as promising alternatives to the homogeneous complexes due to their superior kinetic performance compared to other metals at moderate temperatures, significant limitations still have to be overcome in terms of selectivity and stability [31][32]. Pd and Pt based mono-metallic catalysts are rapidly poisoned by reaction intermediates and products such as formates and CO, resulting in limited stability [94][95]. Extraordinary selectivity and stability has been previously demonstrated for gold supported catalysts, especially colloidal gold nanoparticles, in formic acid formation and decomposition [68][70][96].

Gold colloidal nanoparticles have had applications since the fourth century AD, where they were used for the creation of dichroic filters in the well-known Lycurgus cup to create a wide range of colors depending on the incoming light direction [97]. Despite the centuries long usage in the fields of glass and metallurgy throughout modern history, the catalytic application of gold was only discovered in the late 1980' after being considered catalytically inert due to its resistance to corrosion and oxidation [98]. The most common application of gold-based catalysts is in the low temperature oxidation of CO [99], highlighting the remarkable fact that gold is not susceptible to CO poisoning, unlike other commonly used hydrogenation metals such as Pd and Pt [43]. These extraordinary properties have resulted in a surge in publications on the application of gold catalysis in a wide variety of reactions, such as propylene oxidation, hydrogenation of unsaturated hydrocarbons and the water gas shift reaction [98]. These works clearly demonstrate the potential for gold catalysis within the concept of hydrogenation reactions due to their excellent stability and selectivity, however, the catalytic activity of gold is often significantly lower than that of conventional hydrogenation metals such as Ru, Pt and Pd. This has been attributed to the less effective nature of Au to dissociate hydrogen [52].

Previous works [70][96] demonstrated the application of gold-based catalysts for the decomposition of formic acid, highlighting the exclusive production of CO_2 and H_2 with high catalyst activity. Therein, the potential in the application of gold catalysts from the production and decomposition of formic acid becomes evident.

1.3 Thesis outline

In this thesis, the potential of the production of formic acid based on the direct hydrogenation of CO_2 is thoroughly studied, addressing various aspects from the exploration of the influence of the aliphatic chain length of the tertiary amine on formic acid binding capacity, the influence of the reactive amine on key aspects such as activity and selectivity, the development of catalytic materials and lastly a demonstration of the technology at reactor and process scale, based on a combination of numerical and experimental tools.

The primary objective of **Chapter 2** is to gain a deeper understanding into the nature of different formic acid – aliphatic tertiary amine adducts. Here, a combination of ^{1}H-NMR and IR spectroscopy is used to shed light into the type of chemical bonds occurring within the formic acid – trialkylamine adducts and the degree of proton transfer between formic acid and several trialkylamines. Based on this study, several promising tertiary amines were proposed and further studied in **Chapter 3 and 4.**

Specifically, **Chapter 3** focusses on an attempt to intensify the reaction through removal of the additional alcohol based solvents in a batch reactor. First, reactions are performed with and without solvents based on triethylamine and an Au/TiO_2 catalyst. Then, a fundamental, continuum based model describing Cahn-Hilliard spinodal decomposition was developed and validated to study the influence of the biphasic nature of formic acid – trialkylamine structures during reaction at pore level, showing the formation of a thin shell of adduct formatting around the gold active sites. Within this thin shell, local concentrations correspond to the equilibrium condition. However, due to the strong immiscibility of the adduct and neat amine phases shown in **Chapter 2**, the produced formic acid is not transported to the bulk liquid, resulting in a net reaction rate of virtually zero.

In **Chapter 4**, the influence of the tertiary amine on CO_2 conversion and product selectivity is experimentally studied in batch and packed bed reactors using an Au/TiO_2 catalyst. A wide range of tertiary amines was selected, based on their boiling point, kinetic diameter, pKa and solubility with alcohol-based solvents and formic acid. Following these criteria, 15 amines were selected having a wide range of pKa values and molecule sizes. To allow for an initial screening of kinetic rates, formic acid decomposition reactions were performed in batch reactors using an Au/TiO_2 catalyst. Following the selection of the most promising amines in terms of CO_2 conversion rates, high pressure fixed bed experiments were executed.

Chapter 5 concerns the development of mono-metallic (Au/Al_2O_3, Pd/Al_2O_3 and Ru/Al_2O_3) and bimetallic catalysts (Au-Pd, Au-Ni, and Au-Cu/Al_2O_3). The synthesized catalysts were characterized through XPS, XRD, TEM, ICP and CO pulse chemisorption to identify possible deactivation mechanisms. Their performance in terms of productivity and selectivity was tested in both the formic acid decomposition as well as formic acid formation at elevated pressures. The objective of this study is to identify the best performing catalyst in terms of activity, selectivity and stability, which could be used for further scale up of the proposed technology.

Chapter 6 proposes a comparison on techno-economic level of two routes for the direct hydrogenation of CO_2 towards formic acid: 1) the conventional route based on the patents of BP and BASF, in which triethylamine is used as a reactive amine and exchanged with trihexylamine in a reactive distillation process; 2) a direct route based on the utilization of a high-boiling amine such as n-butylimidazole, allowing for direct separation through pressure swing distillation without the necessity of reactive distillation. The objective of this study is to identify, if any, the plant operating conditions that would make the high boiling reactive amine case more economically competitive compared to the conventional amine-exchange process, analysing both the technical and economic performance of both processes.

Finally, the main findings of this thesis and the research outlook are summarized in **Chapter 7.**

References

[1] J. W. Erisman, M. A. Sutton, J. Galloway, Z. Klimont, and W. Winiwarter, “How a century of ammonia synthesis changed the world,” *Nat. Geosci.*, vol. 1, no. 10, pp. 636–639, 2008, doi: 10.1038/ngeo325.

[2] H. Ritchie and P. Rosado, “Energy Mix,” *Our World Data*, 2020.

[3] Statista, “Energy consumption worldwide from 1990 to 2022, with a forecast until 2050.” https://www.statista.com/statistics/263981/worldwide-energy-consumption-forecast-between-1980-and-2030/ (accessed Aug. 10, 2024).

[4] H. Ritchie, P. Rosado, and M. Roser, “Energy Production and Consumption,” *Our World Data*, 2020.

[5] D. Welsby, J. Price, S. Pye, and P. Ekins, “Unextractable fossil fuels in a 1 . 5 ° C world,” vol. 597, no. July, 2021, doi: 10.1038/s41586-021-03821-8.

[6] A. Buis, “The Atmosphere: Getting a Handle on Carbon Dioxide.” https://science.nasa.gov/earth/climate-change/greenhouse-gases/the-atmosphere-getting-a-handle-on-carbon-dioxide/ (accessed Jun. 18, 2024).

[7] R. Sun *et al.*, “Heterogeneous catalysts for CO2hydrogenation to formic acid/formate: From nanoscale to single atom,” *Energy Environ. Sci.*, vol. 14, no. 3, pp. 1247–1285, 2021, doi: 10.1039/d0ee03575k.

[8] S. Kushwaha, J. Parthiban, and S. K. Singh, “Recent Developments in Reversible CO2 Hydrogenation and Formic Acid Dehydrogenation over Molecular Catalysts,” *ACS Omega*, vol. 8, no. 42, pp. 38773–38793, 2023, doi: 10.1021/acsomega.3c05286.

[9] J. Vansant, *Carbon Dioxide Emission and Merchant Market in the European Union*. 2003.

[10] IPCC, *1.5°C Global Warming CH4: Strengthening and Implementing the Global Response*. 2022..

[11] P. M. Modisha, C. N. M. Ouma, R. Garidzirai, P. Wasserscheid, and D. Bessarabov, “The Prospect of Hydrogen Storage Using Liquid Organic Hydrogen Carriers,” *Energy and Fuels*, vol. 33, no. 4, pp. 2778–2796, 2019, doi: 10.1021/acs.energyfuels.9b00296.

[12] M. Schneider, “The cement industry on the way to a low-carbon future,” *Cem. Concr. Res.*, vol. 124, no. December 2015, p. 105792, 2019, doi: 10.1016/j.cemconres.2019.105792.

[13] H. Ritchie, “Fossil fuels.” https://ourworldindata.org/fossil-fuels (accessed Aug. 10, 2024).

[14] A. Y. Faid and S. Sunde, “Anion Exchange Membrane Water Electrolysis from Catalyst Design to the Membrane Electrode Assembly,” vol. 2200506, 2022, doi: 10.1002/ente.202200506.

[15] N. Du, C. Roy, R. Peach, M. Turnbull, S. Thiele, and C. Bock, “Anion-Exchange Membrane Water Electrolyzers,” 2022, doi: 10.1021/acs.chemrev.1c00854.

[16] N. Frischauf *et al.*, “The hydrogen value chain: Applying the automotive role model of the hydrogen economy in the aerospace sector to increase performance and reduce costs,” *Acta Astronaut.*, vol. 88, pp. 8–24, 2013, doi: 10.1016/j.actaastro.2013.01.002.

[17] E. Tzimas, C. Filiou, S. D. Peteves, and J. Veyret, *Hydrogen Storage : State-of-the-Art and Future Perspective*. 2003.

[18] D. Pashchenko, “Green hydrogen as a power plant fuel: What is energy efficiency from production to utilization?,” *Renew. Energy*, vol. 223, no. June 2023, p. 120033, 2024, doi: 10.1016/j.renene.2024.120033.

[19] M. Felderhoff, C. Weidenthaler, R. Von Helmolt, and U. Eberle, “Hydrogen storage: The remaining scientific and technological challenges,” *Phys. Chem. Chem. Phys.*, vol. 9, no. 21, pp. 2643–2653, 2007, doi: 10.1039/b701563c.

[20] T. H. Ulucan *et al.*, “Hydrogen storage in liquid hydrogen carriers: recent activities and new trends,” *Prog. Energy*, vol. 5, no. 1, 2023, doi: 10.1088/2516-1083/acac5c.

[21] M. Jang *et al.*, “A High-Capacity, Reversible Liquid Organic Hydrogen Carrier: H 2 -Release Properties and an Application to a Fuel Cell,” *ACS Sustain. Chem. Eng.*, vol. 7, no. 1, pp. 1185–1194, 2019, doi: 10.1021/acssuschemeng.8b04835.

[22] P. Preuster, C. Papp, and P. Wasserscheid, “Liquid organic hydrogen carriers (LOHCs): Toward a hydrogen-free hydrogen economy,” *Acc. Chem. Res.*, vol. 50, no. 1, pp. 74–85, 2017, doi: 10.1021/acs.accounts.6b00474.

[23] H. Herzog, C. Schmidt, and E. Drake, *CO2 sequestration*. Dijon: Springer Berlin Heidelberg, 1999.

[24] R. Djettene, L. Dubois, M. E. Duprez, G. De Weireld, and D. Thomas, “Integrated CO2 capture and conversion into methanol units: Assessing techno-economic and environmental aspects compared to CO2 into SNG alternative,” *J. CO2 Util.*, vol. 85, no. May, p. 102879, 2024, doi: 10.1016/j.jcou.2024.102879.

[25] Faculty of Sciences Engineering and Medicine, *Negative Emissions Technologies and Reliable Sequestration: A Research Agenda*. Washington,

DC: The National Academies Press, 2019.

[26] J. C. M. Pires, F. G. Martins, M. C. M. Alvim-Ferraz, and M. Simões, “Recent developments on carbon capture and storage: An overview,” *Chem. Eng. Res. Des.*, vol. 89, no. 9, pp. 1446–1460, 2011, doi: 10.1016/j.cherd.2011.01.028.

[27] I. Havercroft and R. Purdy, “Carbon capture and storage - A Legal Perspective,” *Carbon Capture and Storage*, pp. 1–392, 2009.

[28] N. A. Rashidi, S. Yusup, and A. Borhan, “Isotherm and Thermodynamic Analysis of Carbon Dioxide on Activated Carbon,” *Procedia Eng.*, vol. 148, pp. 630–637, 2016, doi: 10.1016/j.proeng.2016.06.527.

[29] S. Selosse and O. Ricci, “Carbon capture and storage: Lessons from a storage potential and localization analysis,” *Appl. Energy*, vol. 188, pp. 32–44, 2017, doi: 10.1016/j.apenergy.2016.11.117.

[30] S. Saeidi *et al.*, “Recent advances in CO2 hydrogenation to value-added products — Current challenges and future directions,” *Prog. Energy Combust. Sci.*, vol. 85, p. 100905, 2021, doi: 10.1016/j.pecs.2021.100905.

[31] R. P. Ye *et al.*, “CO2 hydrogenation to high-value products via heterogeneous catalysis,” *Nat. Commun.*, vol. 10, no. 1, 2019, doi: 10.1038/s41467-019-13638-9.

[32] M. Aresta, A. Dibenedetto, and A. Angelini, “The changing paradigm in CO2 utilization,” *J. CO2 Util.*, vol. 3–4, pp. 65–73, 2013, doi: 10.1016/j.jcou.2013.08.001.

[33] R. Chauvy, N. Meunier, D. Thomas, and G. De Weireld, “Selecting emerging CO2 utilization products for short- to mid-term deployment,” *Appl. Energy*, vol. 236, no. April 2018, pp. 662–680, 2019, doi: 10.1016/j.apenergy.2018.11.096.

[34] X. Wang and C. Song, *Capture of CO2 from Concentrated Sources and the Atmosphere*. 2019.

[35] S. Poto, T. Vink, P. Oliver, F. Gallucci, and M. F. Neira D’angelo, “Techno-economic assessment of the one-step CO2conversion to dimethyl ether in a membrane-assisted process,” *J. CO2 Util.*, vol. 69, no. February, p. 102419, 2023, doi: 10.1016/j.jcou.2023.102419.

[36] X. Ye *et al.*, “Highly selective hydrogenation of CO2to ethanol via designed bifunctional Ir1-In2O3Single-atom catalyst,” *J. Am. Chem. Soc.*, vol. 142, no. 45, pp. 19001–19005, 2020, doi: 10.1021/jacs.0c08607.

[37] J. Eppinger and K. W. Huang, “Formic Acid as a Hydrogen Energy Carrier,”

ACS Energy Lett., vol. 2, no. 1, pp. 188–195, 2017, doi: 10.1021/acsenergylett.6b00574.

[38] B. Thijs, J. Rongé, and J. A. Martens, “Matching emerging formic acid synthesis processes with application requirements†,” *Green Chem.*, vol. 24, no. 6, pp. 2287–2295, 2022, doi: 10.1039/d1gc04791d.

[39] M. Pérez-Fortes, J. C. Schöneberger, A. Boulamanti, G. Harrison, and E. Tzimas, “Formic acid synthesis using CO2 as raw material: Techno-economic and environmental evaluation and market potential,” *Int. J. Hydrogen Energy*, vol. 41, no. 37, pp. 16444–16462, 2016, doi: 10.1016/j.ijhydene.2016.05.199.

[40] C. Kim, Y. Lee, K. Kim, and U. Lee, “Implementation of Formic Acid as a Liquid Organic Hydrogen Carrier (LOHC): Techno-Economic Analysis and Life Cycle Assessment of Formic Acid Produced via CO2 Utilization,” *Catalysts*, vol. 12, no. 10, 2022, doi: 10.3390/catal12101113.

[41] P. Riquelme-Garcia, “Hydrogen Storage System Attained by HCOOH-CO 2 Couple : Recent Developments in Pd-Based Carbon-Supported Heterogeneous catalysts,” *Energies*, vol. 17, no. 260, 2024, doi: https://doi.org/10.3390/en17010260.

[42] A. Banu, N. Mir, D. Ewis, M. H. El-Naas, A. I. Amhamed, and Y. Bicer, “Formic acid production through electrochemical reduction of CO2: A life cycle assessment,” *Energy Convers. Manag. X*, vol. 20, no. June, p. 100441, 2023, doi: 10.1016/j.ecmx.2023.100441.

[43] W. Leitner, “Carbon Dioxide as a Raw Material: The Synthesis of Formic Acid and Its Derivatives from CO2,” *Angew. Chemie Int. Ed. English*, vol. 34, no. 20, pp. 2207–2221, 1995, doi: 10.1002/anie.199522071.

[44] X. Chen, Y. Liu, and J. Wu, “Sustainable production of formic acid from biomass and carbon dioxide,” *Mol. Catal.*, vol. 483, no. November 2019, p. 110716, 2020, doi: 10.1016/j.mcat.2019.110716

.

[45] D. A. Bulushev and J. R. H. Ross, “Towards Sustainable Production of Formic Acid,” pp. 821–836, 2018, doi: 10.1002/cssc.201702075.

[46] K. Mazloomi and C. Gomes, “Hydrogen as an energy carrier: Prospects and challenges,” *Renew. Sustain. Energy Rev.*, vol. 16, no. 5, pp. 3024–3033, 2012, doi: 10.1016/j.rser.2012.02.028.

[47] J. Hietala, A. Vuori, P. Johnsson, P. Ilkka, W. Reutemann, and H. Kieczka, “Formic acid,” *Ullmann’s Encycl. Ind. Chem.*, vol. A12, no. 29, pp. 1–12, 2016, doi: 10.1002/14356007.a12.

[48] C. Kim *et al.*, “Accelerating the net-zero economy with CO2-hydrogenated

formic acid production: Process development and pilot plant demonstration," *Joule*, vol. 8, no. 3, pp. 693–713, 2024, doi: 10.1016/j.joule.2024.01.003.

[49] K. Fernández-Caso, G. Díaz-Sainz, M. Alvarez-Guerra, and A. Irabien, "Electroreduction of CO2: Advances in the Continuous Production of Formic Acid and Formate," *ACS Energy Lett.*, vol. 8, no. 4, pp. 1992–2024, 2023, doi: 10.1021/acsenergylett.3c00489.

[50] T. M. Suzuki, T. Takayama, S. Sato, A. Iwase, A. Kudo, and T. Morikawa, "Enhancement of CO2 reduction activity under visible light irradiation over Zn-based metal sulfides by combination with Ru-complex catalysts," *Appl. Catal. B Environ.*, vol. 224, no. November 2017, pp. 572–578, 2018, doi: 10.1016/j.apcatb.2017.10.053.

[51] H. Pan and M. D. Heagy, "Photons to formate—A review on photocatalytic reduction of CO2 to formic acid," *Nanomaterials*, vol. 10, no. 12, pp. 1–24, 2020, doi: 10.3390/nano10122422.

[52] J. Hong, W. Zhang, J. Ren, and R. Xu, "Photocatalytic reduction of CO2: A brief review on product analysis and systematic methods," *Anal. Methods*, vol. 5, no. 5, pp. 1086–1097, 2013, doi: 10.1039/c2ay26270c.

[53] S. Xie, Q. Zhang, G. Liu, and Y. Wang, "Photocatalytic and photoelectrocatalytic reduction of CO2 using heterogeneous catalysts with controlled nanostructures," *Chem. Commun.*, vol. 52, no. 1, pp. 35–59, 2016, doi: 10.1039/c5cc07613g.

[54] C. Janáky *et al.*, "Electro- and Photoreduction of Carbon Dioxide: The Twain Shall Meet at Copper Oxide/Copper Interfaces," *ACS Energy Lett.*, vol. 1, no. 2, pp. 332–338, 2016, doi: 10.1021/acsenergylett.6b00078.

[55] R. Pang, K. Teramura, H. Asakura, S. Hosokawa, and T. Tanaka, "Role of Bicarbonate Ions in Aqueous Solution as a Carbon Source for Photocatalytic Conversion of CO2 into CO," *ACS Appl. Energy Mater.*, vol. 2, no. 8, pp. 5397–5405, 2019, doi: 10.1021/acsaem.9b00093.

[56] R. Cauwenbergh and S. Das, "Photochemical reduction of carbon dioxide to formic acid," *Green Chem.*, vol. 23, no. 7, pp. 2553–2574, 2021, doi: 10.1039/d0gc04040a.

[57] A. L. Linsebigler, G. Lu, and J. T. Yates, "Photocatalysis on Ti02 Surfaces: Principles, Mechanisms, andSelected Results," pp. 735–758, 1995.

[58] K. Sayama, *Solar hydrogen production on photocatalysis-electrolysis hybrid system using redox mediator and porous oxide photoelectrodes*, vol. 32. 2016.

[59] D. Ewis *et al.*, "Electrochemical reduction of CO2 into formate/formic acid: A

review of cell design and operation," *Sep. Purif. Technol.*, vol. 316, no. April, p. 123811, 2023, doi: 10.1016/j.seppur.2023.123811.

[60] P. Duarah, D. Haldar, V. S. K. Yadav, and M. K. Purkait, "Progress in the electrochemical reduction of CO2 to formic acid: A review on current trends and future prospects," *J. Environ. Chem. Eng.*, vol. 9, no. 6, p. 106394, 2021, doi: 10.1016/j.jece.2021.106394.

[61] M. North, *What is CO2? Thermodynamics, Basic Reactions and Physical Chemistry*. Elsevier B.V., 2015.

[62] N. Han, P. Ding, L. He, Y. Li, and Y. Li, "Promises of Main Group Metal–Based Nanostructured Materials for Electrochemical CO2 Reduction to Formate," *Adv. Energy Mater.*, vol. 10, no. 11, pp. 1–19, 2020, doi: 10.1002/aenm.201902338.

[63] Y. Zhang, F. Li, J. Dong, K. Jia, T. Sun, and L. Xu, "Recent advances in designing efficient electrocatalysts for electrochemical carbon dioxide reduction to formic acid/formate," *J. Electroanal. Chem.*, vol. 928, no. August 2022, p. 117018, 2023, doi: 10.1016/j.jelechem.2022.117018.

[64] A. Álvarez *et al.*, "Challenges in the Greener Production of Formates/Formic Acid, Methanol, and DME by Heterogeneously Catalyzed CO2 Hydrogenation Processes," *Chem. Rev.*, vol. 117, no. 14, pp. 9804–9838, 2017, doi: 10.1021/acs.chemrev.6b00816.

[65] T. Schaub and R. A. Paciello, "A process for the synthesis of formic acid by CO2 hydrogenation: Thermodynamic aspects and the role of CO," *Angew. Chemie - Int. Ed.*, vol. 50, no. 32, pp. 7278–7282, 2011, doi: 10.1002/anie.201101292.

[66] I. Schmidt, K. Müller, and W. Arlt, "Evaluation of formic-acid-based hydrogen storage technologies," *Energy and Fuels*, vol. 28, no. 10, pp. 6540–6544, 2014, doi: 10.1021/ef501802r.

[67] K. Müller, K. Brooks, and T. Autrey, "Hydrogen Storage in Formic Acid: A Comparison of Process Options," *Energy and Fuels*, vol. 31, no. 11, pp. 12603–12611, 2017, doi: 10.1021/acs.energyfuels.7b02997.

[68] D. Preti, C. Resta, S. Squarcialupi, and G. Fachinetti, "Carbon dioxide hydrogenation to formic acid by using a heterogeneous gold catalyst," *Angew. Chemie - Int. Ed.*, vol. 50, no. 52, pp. 12551–12554, 2011, doi: 10.1002/anie.201105481.

[69] P. G. Jessop, T. Ikariya, and R. Noyori, "Homogeneous Hydrogenation of Carbon Dioxide," *Chem. Rev.*, vol. 95, no. 2, pp. 259–272, 1995, doi: 10.1021/cr00034a001.

[70] G. A. Filonenko, W. L. Vrijburg, E. J. M. Hensen, and E. A. Pidko, “On the activity of supported Au catalysts in the liquid phase hydrogenation of CO2 to formates,” *J. Catal.*, vol. 343, pp. 97–105, 2016, doi: 10.1016/j.jcat.2015.10.002.

[71] K. Park *et al.*, “CO2 hydrogenation to formic acid over heterogenized ruthenium catalysts using a fixed bed reactor with separation units,” *Green Chem.*, vol. 22, no. 5, pp. 1639–1649, 2020, doi: 10.1039/c9gc03685g.

[72] M. Sekiya, “ギ酸による還元反応．,” *有機合成化学協会誌（Journal Synth. Org. Chem. Japan）*, vol. 34, no. 2, pp. 67–81, 1976.

[73] G. Fachinetti and D. Preti, “PROCESS FOR PREPARING FORMIC ACID,” WO 2012/168396 Al, 2012.

[74] S. Jiang *et al.*, “Additive-free CO2 hydrogenation to pure formic acid solution via amine-modified Pd catalyst at room temperature,” pp. 6025–6031, 2023, doi: 10.1039/d3gc01307c.

[75] J. Hu, “iScience ll Reaction and separation system for CO 2 hydrogenation to formic acid catalyzed by iridium immobilized on solid phosphines under base-free condition,” *ISCIENCE*, vol. 26, no. 5, p. 106672, 2023, doi: 10.1016/j.isci.2023.106672.

[76] A. Weilhard, M. I. Qadir, V. Sans, and J. Dupont, “Selective CO 2 Hydrogenation to Formic Acid with Multifunc- tional Ionic Liquids.”

[77] A. Weilhard, S. P. Argent, and V. Sans, “acid with buffering ionic liquids,” *Nat. Commun.*, no. 2021, pp. 1–7, doi: 10.1038/s41467-020-20291-0.

[78] X. Wang *et al.*, “Heterogeneous Catalytic Transfer Partial-Hydrogenation with Formic Acid as Hydrogen Source Over the Schiff-Base Modified Gold Nano-Catalyst,” *Catal. Letters*, vol. 147, no. 2, pp. 517–524, 2017, doi: 10.1007/s10562-016-1929-9.

[79] Q. Liu *et al.*, “Direct catalytic hydrogenation of CO2 to formate over a Schiff-base-mediated gold nanocatalyst,” *Nat. Commun.*, vol. 8, no. 1, 2017, doi: 10.1038/s41467-017-01673-3.

[80] M. Grasemann and G. Laurenczy, “Formic acid as a hydrogen source - Recent developments and future trends,” *Energy Environ. Sci.*, vol. 5, no. 8, pp. 8171–8181, 2012, doi: 10.1039/c2ee21928j.

[81] G. H. Gunasekar, J. Shin, K. D. Jung, K. Park, and S. Yoon, “Design Strategy toward Recyclable and Highly Efficient Heterogeneous Catalysts for the Hydrogenation of CO2 to Formate,” *ACS Catal.*, vol. 8, no. 5, pp. 4346–4353, 2018, doi: 10.1021/acscatal.8b00392.

[82] A. Álvarez *et al.*, “Challenges in the Greener Production of Formates/Formic Acid, Methanol, and DME by Heterogeneously Catalyzed CO2 Hydrogenation Processes,” *Chem. Rev.*, vol. 117, no. 14, pp. 9804–9838, 2017, doi: 10.1021/acs.chemrev.6b00816.

[83] K. Sordakis *et al.*, “Homogeneous Catalysis for Sustainable Hydrogen Storage in Formic Acid and Alcohols,” *Chem. Rev.*, vol. 118, no. 2, pp. 372–433, 2018, doi: 10.1021/acs.chemrev.7b00182.

[84] M. S. Maru, S. Ram, R. S. Shukla, and N. ul H. Khan, “Ruthenium-hydrotalcite (Ru-HT) as an effective heterogeneous catalyst for the selective hydrogenation of CO2 to formic acid,” *Mol. Catal.*, vol. 446, pp. 23–30, 2018, doi: 10.1016/j.mcat.2017.12.005.

[85] M. S. Maru, S. Ram, J. H. Adwani, and R. S. Shukla, “Selective and Direct Hydrogenation of CO2 for the Synthesis of Formic Acid over a Rhodium Hydrotalcite (Rh-HT) Catalyst,” *ChemistrySelect*, vol. 2, no. 13, pp. 3823–3830, 2017, doi: 10.1002/slct.201700130.

[86] D. Preti, C. Resta, S. Squarcialupi, and G. Fachinetti, “Carbon dioxide hydrogenation to formic acid by using a heterogeneous gold catalyst,” *Angew. Chemie - Int. Ed.*, vol. 50, no. 52, pp. 12551–12554, 2011, doi: 10.1002/anie.201105481.

[87] G. Yan, Z. Gao, M. Zhao, W. Yang, and X. Ding, “CO2 hydrogenation to formic acid over platinum cluster doped defective graphene: A DFT study,” *Appl. Surf. Sci.*, vol. 517, no. December 2019, p. 146200, 2020, doi: 10.1016/j.apsusc.2020.146200.

[88] Z. Y. Hu, L. H. Luo, C. Shang, and Z. P. Liu, “Free Energy Pathway Exploration of Catalytic Formic Acid Decomposition on Pt-Group Metals in Aqueous Surroundings,” *ACS Catal.* , pp. 7684–7695, 2024, doi: 10.1021/acscatal.4c00959.

[89] H. Song, N. Zhang, C. Zhong, Z. Liu, M. Xiao, and H. Gai, “Hydrogenation of CO2 into formic acid using a palladium catalyst on chitin,” *New J. Chem.*, vol. 41, no. 17, pp. 9170–9177, 2017, doi: 10.1039/c7nj00460e.

[90] Q. Li *et al.*, “Highly Efficient Hydrogenation of CO2 to Formic Acid over Palladium Supported on Dication Poly(ionic liquid)s,” *Mol. Catal.*, vol. 509, no. May, p. 111644, 2021, doi: 10.1016/j.mcat.2021.111644.

[91] B. D. Bankar, D. R. Naikwadi, R. J. Tayade, and A. V Biradar, “Direct hydrogenation of CO 2 to formic acid using Ru supported Co 3 O 4 oxide as an efficient heterogeneous catalyst,” *Mol. Catal.*, vol. 535, no. July 2022, p. 112875, 2023, doi: 10.1016/j.mcat.2022.112875.

[92] G. Liu *et al.*, “CO2 Hydrogenation to Formate and Formic Acid by Bimetallic

Palladium-Copper Hydride Clusters," *J. Am. Chem. Soc.*, vol. 142, no. 17, pp. 7930–7936, 2020, doi: 10.1021/jacs.0c01855.

[93] Y. Wang, M. Dong, S. Li, B. Chen, H. Liu, and B. Han, "The superiority of Pd2+ in CO2 hydrogenation to formic acid," *Chem. Sci.*, vol. 15, no. 15, pp. 5525–5530, 2024, doi: 10.1039/d3sc06925g.

[94] J. L. Santos, C. León, G. Monnier, S. Ivanova, M. Á. Centeno, and J. A. Odriozola, "Bimetallic PdAu catalysts for formic acid dehydrogenation," *Int. J. Hydrogen Energy*, vol. 45, no. 43, pp. 23056–23068, 2020, doi: 10.1016/j.ijhydene.2020.06.076.

[95] S. P. Hill and J. M. Winterbottom, "The conversion of polysaccharides to hydrogen gas. Part I: The palladium catalysed decomposition of formic acid/sodium formate solutions," *J. Chem. Technol. Biotechnol.*, vol. 41, no. 2, pp. 121–133, 1988, doi: 10.1002/jctb.280410205.

[96] M. Ojeda and E. Iglesia, "Formic acid dehydrogenation on au-based catalysts at near-ambient temperatures," *Angew. Chemie - Int. Ed.*, vol. 48, no. 26, pp. 4800–4803, 2009, doi: 10.1002/anie.200805723.

[97] Q. Bi, J. Lin, Y. Liu, and F. Huang, "ScienceDirect Promoted hydrogen generation from formic acid with amines using Au / ZrO 2 catalyst," *Int. J. Hydrogen Energy*, vol. 41, no. 46, pp. 21193–21202, 2016, doi: 10.1016/j.ijhydene.2016.09.150.

[98] J. W. M. Crawley *et al.*, "Heterogeneous Trimetallic Nanoparticles as Catalysts," *Chem. Rev.*, vol. 122, no. 6, pp. 6795–6849, 2022, doi: 10.1021/acs.chemrev.1c00493.

[99] M. Haruta, "Gold as a novel catalyst in the 21st century: Preparation, working mechanism and applications," *Gold Bull.*, vol. 37, no. 1–2, pp. 27–36, 2004, doi: 10.1007/BF03215514.

[100] P. M. Modisha, C. N. M. Ouma, R. Garidzirai, P. Wasserscheid, and D. Bessarabov, "The Prospect of Hydrogen Storage Using Liquid Organic Hydrogen Carriers," *Energy and Fuels*, vol. 33, no. 4, pp. 2778–2796, 2019, doi: 10.1021/acs.energyfuels.9b00296.

[101] Fust Energy BV, "Formic Acid as Energy Carrier." https://projecten.topsectorenergie.nl/storage/app/uploads/public/5b1/551/e4f/5b1551e4f1a85026449477.pdf (accessed Oct. 04, 2024).

[102] H. Lee, S. M. Yi, T. M. Holsen, Y. S. Seo, and E. Choi, "Estimation of CO2 emissions from waste incinerators: Comparison of three methods," *Waste Manag.*, vol. 73, pp. 247–255, 2018, doi: 10.1016/j.wasman.2017.11.05

2

Chemical and phase equilibrium of formic acid – trialkylamine complexes

This chapter is based on the following publication:

A.W.N. de Leeuw den Bouter, E.J.M. Vogels, L.Brito , A. Miquelot, P.Olivier, J. van der Schaaf, “Chemical and phase equilibrium of formic acid – trialkylamine complexes,” under review in ACS Omega.

Abstract

A significant amount of research has been devoted to the topic of Protic Ionic Liquids (PILs), as they represent a new class of solvents with unusual properties such as increased thermal stability, high ionic conductivity and nonvolatility [5]. PILs are often synthesized through a proton transfer reaction of a Brønsted acid and Brønsted base [1]–[3]. A prime example of a system showing such behavior is found in mixtures of carboxylic acids with amines, which form OH ···N hydrogen bonds [1][2][17].

While the acetic acid – triethylamine mixture is widely studied, a clear gap exists within the literature for longer trialkylamines, as well as shorter chain length carboxylic acids such as formic acid.

FTIR and ^{1}H-NMR were used to establish the influence of the alkyl chain length of the nitrogenous cation on the ionicity of the resulting PIL within formic acid-tertiary alkylamine systems. The phase equilibrium was established to be independent of the alkyl chain length with the critical point determined to be at a molar ratio of 1.5 acid to amine. Remarkably, it is observed that the decrease in ionicity is exactly compensated by the increase in hydrogen bonding, resulting in a constant acid to amine ratio irrespective of the nature of the amine.

2.1 Introduction

A significant amount of research has been devoted to the topic of Protic Ionic Liquids (PILs), as they represent a new class of solvents with unusual properties such as increased thermal stability, high ionic conductivity and nonvolatility [5]. PILs are often synthesized through a proton transfer reaction of a Brønsted acid and Brønsted base [1]–[3]. A significant difference in pKa (>6) between the acid and base is required to result in complete ionization [4]. However, previous works [2][5][6] have shown that the proton transfer is often not complete due to the pKa difference being <4 [7], leading to the co-existence of molecular and ionic species within the PIL.

The degree of proton transfer, also known as the ionicity [8]–[10], is often determining for the physicochemical properties of the PIL such as viscosity, conductivity and density [5][6][11]. A variety of methods, both qualitative and quantitative, have been employed to study the ionicity of PILs [12][13]. Examples of qualitative methods include using the difference between the pKa of the acid and the base (ΔpKa) as an indicator [13] as well as the usage of Walden plots [2][14]. Quantitative methods are based on titrations (potentiometric, calorimetric) [15], or spectroscopic methods such attenuated total reflection IR (ATR-IR), nuclear magnetic resonance [2][5], Raman [4] or UV [16].

Besides the ionicity, the presence of hydrogen bonds in PILs has been shown to have a significant effect on key physical properties, as it can cause ions and neutral species to act as a single species [1][9], and can even result in the solutions becoming biphasic [17].

A prime example of a system showing such behavior is found in mixtures of carboxylic acids with amines, which form OH ···N hydrogen bonds [1][2][17]. While 1:1 and 2:1 aggregates have been found to be present in mixtures including solvents or ternary components [18], 3:1 aggregates have been observed within binary mixtures [18]–[21]. The overbinding of the carboxylic acid is often attributed to the presence of hydrogen bonded networks of the aforementioned integer ratios of carboxylic acid and trialkylamines [1][3][17][22]. Such hydrogen bonding networks have been suggested to result in nanoscale phase separation of hydrophobic and hygroscopic nature [3]. Warr *et al*. have demonstrated this nanoscale phase separation even occurs for small alkylammonium nitrates such as ethylammonium and propylammonium nitrates [23].

A widely studied PIL belonging to the class mentioned above is triethylamine – acetic acid [1][2][19], as this finds practical applications as a solvent and a catalyst [2]. While the molecular interactions within this PIL have been explored in detail [1][2][19], the phase and chemical equilibria were disregarded until the study of Zhang *et al*. [2]. Chen *et al*. [5] developed a quantitative methodology based on H-NMR and FTIR to allow for the quantification of chemical and phase equilibria of biphasic PILs.

Previous works have shown that the nature and chain length of the nitrogenous cation is of key importance for the degree of proton transfer and thus physicochemical properties of the PILs [5][24][25]. Besides the influence of the cation, also the chain length of the anion is of key importance to the properties of the PIL, as previously shown by Li et al. [12]. While the acetic acid – triethylamine mixture is widely studied, a clear gap exists within the literature for longer trialkylamines, as well as shorter chain length carboxylic acids such as formic acid.

Within this Chapter, a systematic investigation is performed into the effect of the length of the alkyl chain within the nitrogenous cation on key properties such as the chemical and phase equilibria of the formed PILs. Phase equilibria and ionicity were determined using ^{1}H-NMR, while chemical interactions were studied using ATR-FTIR.

2.2 Materials and methods

2.2.1. Materials

Triethylamine (> 99.5%), tributylamine (> 98.5%), trioctylamine (> 99%) formic acid (>99%), acetic acid (>99%), sodium hydroxide (>97%) and sodium acetate (>99%)

were obtained from Sigma-Aldrich. Dibromomethane (>99.9%, stabilized with butylhydroxytoluene), 1,3,5-trimethoxybenzene (>98.0%), trihexylamine (>95%), N,N-dimethylbutylamine(>98.0%) and N,N-dimethyloctylamine (>95.0) and trioctylamine (>95%) were obtained from TCI chemicals. Propionic acid (>99%) was received from Thermo Scientific. Acetonitrile-d_3 (D99.8%) and toluene-d_8 (D 99.0) were purchased from Deutero, while trioctylammonium (95.0%) was bought from Enamine.

All materials were used as received, without any additional purification. The water content was determined after receiving the materials using Karl Fischer titration (899 Coulometer, Metrohm) and found to be below 750 ppm for all chemicals.

2.2.2. Synthesis

For homogeneous and biphasic PILs, the appropriate amount of amine was weighed into an Erlenmeyer flask placed in an ice bath, after which the correct amount of carboxylic acid was transferred dropwise using a syringe. A stirring period of 24 hours was used. In the case of biphasic PILS, an additional settling period of 12 hours was used, following the work of [2].

Sodium formate was synthesized to aid peak assignment in FTIR analysis by adding equimolar amounts of sodium hydroxide to neat formic acid. The sodium hydroxide was added to the anhydrous acid while vigorously stirring with the flask placed in an ice bath. The mixture was allowed to stir for 5 hours, after which filtration was performed using a vacuum pump. The remaining water was removed using a RotaVap system at 75 mbar and 40 ºC, after which the resulting powder was dried under vacuum at 70 ºC for 24 hrs.

2.3 Analytical techniques

^{1}H-NMR (Bruker, 400 MHz) was used to determine the chemical compositions of all samples obtained from the monophasic and biphasic PILs. Here, 0.5 ml of deuterated solvent (Acetonitrile-d_3 or toluene-d_8) containing either dibromomethane or 1,3,5-trimethoxybenzene as internal standard was mixed with 0.1 ml of sample. The concentration of internal standard was 1 mol/liter. Molar ratios were determined using dibromomethane or 1,3,5-trimethoxybenzene as internal standards. In case of biphasic PILs, a syringe was used to sample both layers.

ATR-FTIR spectroscopy was performed using a Thermo Scientific NICOLET iS10 spectrometer with CaF_2 single crystal. Spectra were obtained at room temperature in the range of 400-4000 cm^{-1} with a scanning resolution 2 cm^{-1} and accumulated over 64 scans.

UV-VIS measurements (Shimadzu UV-2501PC) were executed to monitor the color change of formic acid – trioctylamine mixtures over time. Spectra were recorded between 300-800 nm.

Dynamic Light Scattering (DLS) measurements were performed using a Nanotrac Ultra manufactured by Microtrac, having a measuring range from 0.1 – 10000 nm. All samples were diluted in toluene and filtered using a 0.45 µm PTFE syringe filter prior to measurement. The employed reflective index was experimentally determined to be 1.437 (formic acid: 1.371, trioctylamine: 1.449).

2.4 Results and discussion

Within this study, the same anion (formic acid) was used for all PILs, while different nitrogenous trialkyl cations were used having several hydrocarbon chain lengths. Here, symmetrical tertiary amines are used having chain lengths between 2 and 8, as well as asymmetrical trialkyl amines having 2 methyl groups and a chain of 4 or 8 carbon atoms. An overview of the molecular structures of the tertiary trialkylamines and abbreviations is given in Figure 2.1.

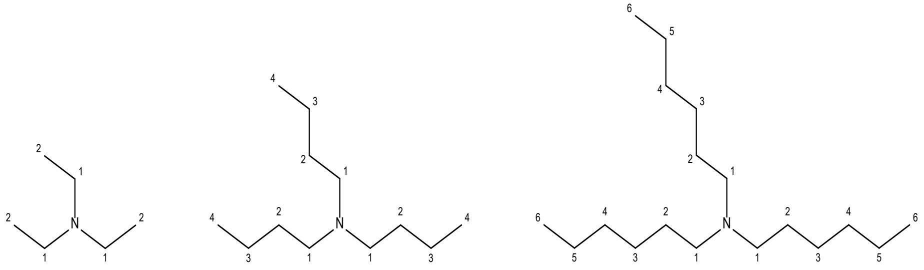

Triethylamine (TEA) Tributylamine (TBA) Trihexylamine (THA)

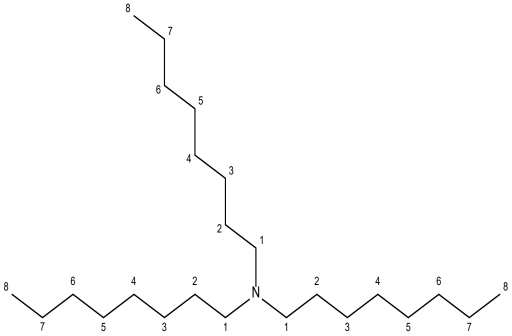

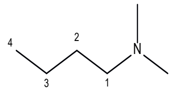

Dimethylbutylamine (DMBA)

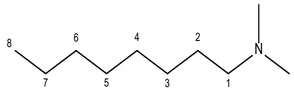

Trioctylamine (TOA) Dimethyloctylamine (DMOA)

Figure 2.1: Overview of structures and abbreviations of the nitrogenous trialkyl cations

2.4.1. Phase equilibrium

To gain a deeper understanding into biphasic PILs in terms of their phase equilibria as a function of cation chain length, PILs were synthesized over a wide range of initial anion:cation molar ratios for all nitrogenous cations depicted in 2.1.

For all tertiary alkylamine – formic acid systems the critical molar fraction of acid (x_{acid}) was established for which phase separation occurs, with the system becoming biphasic. In order to determine the chemical composition of each phase ^{1}H-NMR was used, an example NMR spectrum can be found in Appendix A (Figure A.19). The acid-base ratio was calculated from the integral area ratio of two signals, attributed to the methyl groups in the hydrocarbon tail and the carboxylic acid hydrogen of formic acid. Phase separation occurred until a molar ratio of ~1.5:1 formic acid: amine was reached for all tertiary amines, as shown in Table 2.1.

The top layer was found to be rich in amine with a low amount (up to 0.02 mol/liter) of formic acid present, while the chemical composition of the bottom layer was found to have a constant molar ratio of approximately 1.5:1 acid:amine, independent of the hydrocarbon tail length. After the critical point of ~1.5:1 acid:amine a single phase was obtained for all tertiary amines.

Tertiary amine	Critical point [mol FA / mol amine]
TEA	1.49 ± 0.02
TBA	1.52 ± 0.03
THA	1.51 ± 0.02
TOA	1.47 ± 0.04
DMBA	1.53 ± 0.03
DMOA	1.55 ± 0.06

Table 2.1: Determination of the phase equilibrium of all tertiary amines. All values are averaged over 5 measurements and determined using ^{1}H-NMR

2.4.2 Chemical equilibrium

Previous works have commonly employed NMR measurements (^{1}H HMR, ^{13}C NMR and ^{15}N-NMR) to gain a deeper understanding of the chemical interactions between the cation and anion [11][26]. However, for ammonium based ionic liquids, a single average peak is obtained between the protonated amine and molecular formic acid [1][2][27] due to the fast exchange of the proton between these compounds [27]. Nuthakki *et al*. [28] have previously shown the life-time of such ion pairs to be in the range of $20x10^{-14}$ s, while common NMR based methods have resolutions of 10^{-9} – 10^{-11} s [28]. For this reason, ATR-FTIR was deemed the most suitable method to qualitatively probe the chemical interactions present within the PILs.

Infrared spectra were recorded of all nitrogenous cations at several molar ratios below and above the critical point for phase separation. Due to contrasting identification of the key bands within literature, it was opted to synthesize sodium formate and to purchase the ammonium salt of trioctylamine. The IR spectra are depicted in Figure A1 and A2 (Appendix A). Spectra of the pure amines and formic acid were also included within Appendix A (Figures A3-A6). For all mixtures measured, the acid-base ratio was calculated based on ^{1}H-NMR spectroscopy, utilizing the integral area ratio of two signals, attributed to the methyl groups in the hydrocarbon tail and the carboxylic acid hydrogen of formic acid

The IR spectrum of the triethylamine – FA at the critical point is depicted as an example in Figure 2.2, with all others made available within the Appendix A. Here, the peaks are assigned as follows (and depicted in Figure A18): 1350-1600 cm^{-1} corresponds to the N$^+$-H deformation and the COO$^-$ band [1][17][27], the C=O stretching mode is present at 1690-1710 cm^{-1} [29], COO$^-$ at 1550-1585 [30] and the C-O asymmetric stretching band at 1190 cm^{-1} [29] . The positions of the C=O stretching mode and C-O band are often attributed to a mixture of ionic and molecular formic acid [29][31]. Previous works have attributed the presence of N-H and O-H-N hydrogen bonds to 2570-2700 cm^{-1} and 2700-3300 cm^{-1} respectively [2][3][30] and the O-H stretch of formic acid results in broad stretching from 2700-3200 cm^{-1} [2][3][30]. Due to significant overlap between the latter bands, quantitative determination of the hydrogen bridges is not possible. Besides bands belonging to ionic and molecular interactions between the anion and cation, clear bands belonging to the cation alkyl chains are also visible. C-H bending vibrations are observed around 1500 cm^{-1} and C-H stretching is observed between 2800-3000 cm^{-1} [32].

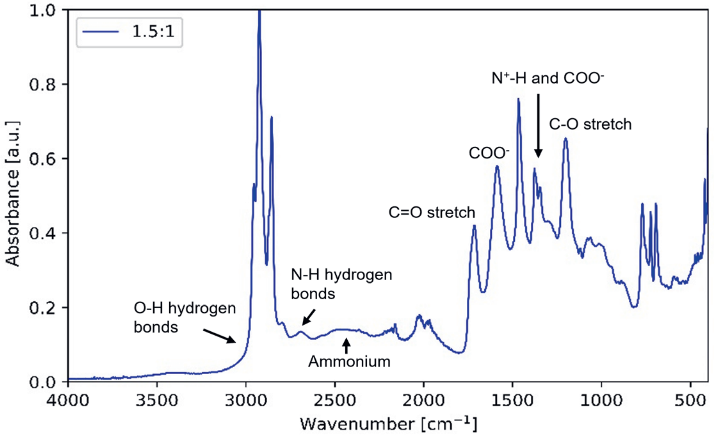

Figure 2.2: IR spectrum of a formic acid -triethylamine PIL at the critical point (1.5:1 mol/mol)

Within the previous section, a structure of the IR spectrum of the tertiary amine – formic acid systems at phase equilibrium was established. For all tertiary amines, PILs were synthesized having several molar ratios above and below the critical point and analyzed using ATR-FTIR. In order to determine the possible presence of ionic species in each of the phases, a PIL consisting of formic acid – triethylamine below the critical point having an initial molar ratio of 0.8:1 formic acid - triethylamine was synthesized. The two phases were separated by separation funnel and analyzed using ATR-FTIR with the results shown in Figure 2.3.

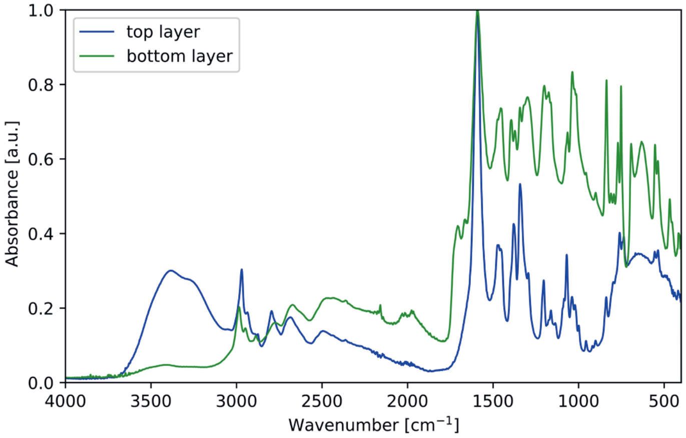

Figure 2.3: IR spectra of a formic acid – triethylamine PIL below the critical point for phase separation (initial molar ratio 0.8:1 mol/mol). ^{1}H-NMR revealed the bottom layer to have a composition of 1.5:1 mol/mol and the top layer 0.02:1 mol/mol.

Here, it emerges from the presence of the COO^- band at 1550-1585 cm^{-1} that ionic species are present in both phases, which is consistent with previous works on acetic acid – triethylamine systems [1][2]. Figure 2.4 shows the IR spectra for bottom phase of the formic acid – tributylamine mixtures below the critical point, while Figure 2.5 represents the mixtures above the critical point. Similar spectra for triethylamine, trihexylamine and trioctylamine are included in Appendix A (Figures A7-A12).

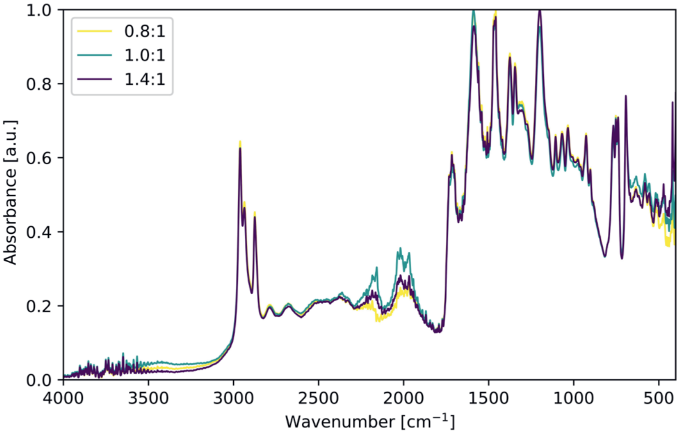

Figure 2.4: IR spectra of different formic acid-tributylamine initial molar ratios below the critical point. The spectra represent the PIL (bottom layer).

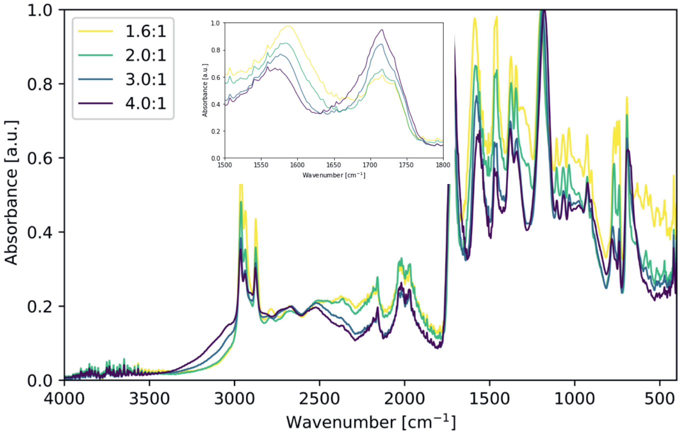

Figure 2.5: IR spectra of different formic acid-tributylamine mixtures above the critical point.

From Figure 2.4 it becomes apparent that the molecular interactions within the bottom layer are independent of the initial molar ratio due to the biphasic nature of the studied complexes. The same PIL having a molar ratio of 1.5:1 FA:amine is formed of constant chemical equilibrium, and from Figures A7-A12 it is also found that this is the case independent of the trialkyl chain length of the amine. At initial molar ratios above the critical point (Figure 2.5), a clear red shift is observed for the COO^- band at 1550-1580 cm^{-1} and C=O bands at 1720 cm^{-1} towards the band position of pure formic acid.

For all initial acid to amine ratios both the COO^- and COOH bands were observed, indicating the proton transfer to be incomplete independent of the alkyl chain length and formic acid to amine ratio. A possible explanation for the incomplete proton transfer is found in the nature of tertiary amines, as such molecules are only able to act as hydrogen bond acceptors due to the absence of a labile proton, and thus cannot form hydrogen bonds with the C=O (carboxylate group) of formic acid [9][33]. Previous works have shown the formation of hydrogen bonds between the proton of the amine and the carboxylate group to favor proton transfer from the acid to the amine. Therefore, as tertiary amine are not able to form such hydrogen bonds, non-ionic molecules could be stabilized through hydrogen bridges resulting in carboxylic acid – carboxylic acid pairs, which in turn stabilize non-ionic molecules, thus decreasing the amount of proton transfer [9][33].

To gain a deeper understanding of the influence of the alkyl chain length on molecular and ionic interactions present within the PILs, the IR spectra of all studied tertiary amine adducts at the critical point were recorded and presented in Figure 2.6.

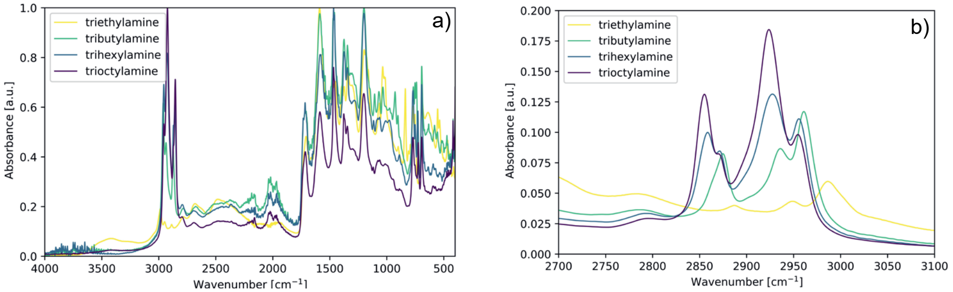

Figure 2.6: a) IR spectra of the studied cations at the critical points. b) C-H stretching frequency

Figure 2.6a reveals a significant shift towards lower wave numbers as a function of increasing alkyl chain length for the C-H stretch spectral region. Besides the shift to shorter wavelengths, the intensity of the signals is increased. The shift towards lower wave numbers is typical for long chain alkyl chains due to chain proximity [34] and was also observed within previous works studying similar compounds [24] [32]. The chain proximity is caused by the aggregation of the $-CH_2$ groups present within the alkyl chain and is typically driven by van der Waals forces [34].

Within Figure 2.6a a red-shift of the COO^- asymmetrical stretching mode (~1590 cm^{-1} to 1580 cm^{-1}) also becomes apparent. Previous works [35]–[37] have shown the COO^- stretch band to be highly sensitive to the chemical environment. Mareka *et al*. [35] have shown that COO^- engaged in hydrogen bonding occurs at lower wave numbers than free COO^- (for the asymmetrical mode). Studies on acetic acid – triethylamine PILs [1] [18]–[20] have shown an overbinding effect resulting in multiple molecules of acid binding to a single molecule of amine. Here the proposed structure would consist of a cloud of hydrogen bonding acid molecules to a single negatively charged carboxylic acid molecule. As previously noted, the existence of these carboxylic acid – carboxylic acid hydrogen bonds results in a decrease in proton transfer [9][33]. Thus, the shifting of the COO^- stretch band to lower wave numbers could be an indication of increased hydrogen bonding and thus decreased proton transfer interactions as a function of chain length. The most pronounced effect is observed for the C_2 to C_4, while almost no shift is present going from C_6 to C_8.

Due to significant overlap between the characteristic bands of COO^- and NH^+ combined with a significant red shift of the symmetrical COO^- stretch frequency, it was not possible to determine the ionicity of the PILs using FTIR. Thus, to allow for quantitative analysis of the degree of proton transfer, NMR spectroscopy was employed using the methodology developed by Li *et al.* [5][6][12]. The employed methodology has been developed and elaborated in previous works [2][5][6][12], herein, a brief introduction is given with more details described in [2][5][6][12].

Mixtures of formic acid – trioctylamine were prepared at different molar ratios. ^1H-NMR was performed on all mixtures, using toluene-d_8 as solvent and dibromomethane as internal standard. Tamada *et al*. [38][39] have previously shown that the choice of NMR solvent is vital, as commonly used solvents such as chloroform, dichloromethane, tetrahydrofuran and acetone disturb the hydrogen bonds within the adducts, thus altering the molecular interactions. For this reason, toluene-d_8 was identified as a NMR solvent [38][39].

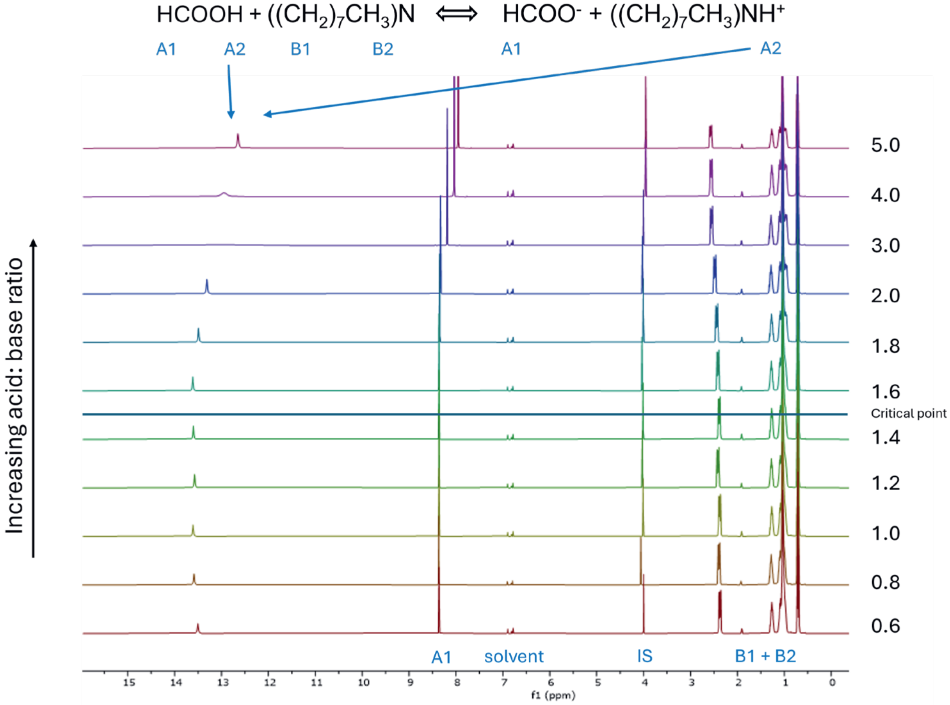

Figure 2.7: ^1H-NMR spectra of several formic acid – trioctylamine (TOA) molar ratios. Molar ratio (mol/mol) indicated on the right-hand side. Spectra are referenced to toluene-d_8

The ^{1}H-NMR spectra of various initial formic acid – trioctylamine mixtures is depicted in Figure 2.7 (the other studied amines are included within Appendix A, Figures A13-A17), here a significant upshift of the formic acid protons becomes apparent.

When the initial concentrations of formic acid and amine are below the critical point, the carboxylic acid hydrogen peak (A1) has a constant chemical shift at 8.4 ± 0.02 ppm within the obtained ^{1}H-NMR spectra, while the OH proton (A2) has a constant chemical shift of 13.5 ± 0.1 ppm. The constant chemical shifts are in line with expectation, as it was shown within the previous section that such mixtures have a constant FA:amine composition. Above the critical molar ratio of 1.5:1 in Figure 2.7, a linear relation between the obtained chemical shift and the amount of unbound formic acid in the system is present.

While a single average peak originating from the proton of the protonated amine and molecular formic acid is obtained for the exchangeable proton (A2) in ^{1}H-NMR, the effect of ionicity is reflected within the chemical shift observed [28]. This effect is commonly present in the form of an upshift of the average signal obtained from the exchange proton, caused by a rise in shielding due to increased interactions with the lone pair present on the nitrogen moiety [11]. Within the NMR-methodology developed by Li *et al*. [5][6], the peak shift is described by assuming the observed shift (δ_{obs}) to be a linear combination of the molar fractions and chemical shifts of protonated amine and molecular carboxylic acid [2][5][6]:

$$\delta_{obs} = \delta_{[TOA-H^+]} \frac{x_{[TOA-H^+]}}{x^0_{[FA]}} + \delta_{[FA]} \frac{x^0_{[FA]} - x_{[TOA-H^+]}}{x^0_{[FA]}} \qquad 2.1$$

Here, $\delta_{[TOA-H^+]}$ and $\delta_{[FA]}$ represent the chemical shifts of the protonated TOA and molecular formic acid respectively, while $x_{[TOA-H^+]}$ is the true molar fraction of the protonated amine at equilibrium conditions and $x_{[FA]}$ the initial molar fraction of FA. With the acid-base equilibrium constant (eq 2.2.) and rewriting equation 2.1, an expression is obtained for the observed chemical shift of the proton A2 (equation 2.3).

$$K = \frac{x_{[HCOO^-]} x_{[TOA-H^+]}}{x_{[HCOOH]}\, x_{[TOA]}} = \frac{x^2_{[TOA-H^+]}}{\left(x^0_{[TOA]} - x_{[TOA-H^+]}\right)\left(x^0_{[FA]} - x_{[HCOO^-]}\right)} \qquad 2.2$$

$$\delta_{obs} = \delta_{[TOA-H^+]} \frac{\left[\frac{K}{R_{AB}}(1+R_{AB}) - \sqrt{\left(\frac{K}{R_{AB}}\right)^2 (1+R_{AB})^2 - \frac{4K}{R_{AB}}(K-1)}\right]}{2(K-1)} + \delta_{[FA]} \left(1 - \frac{\left[\frac{K}{R_{AB}}(1+R_{AB}) - \sqrt{\left(\frac{K}{R_{AB}}\right)^2 (1+R_{AB})^2 - \frac{4K}{R_{AB}}(K-1)}\right]}{2(K-1)}\right) \qquad 2.3$$

with R_{AB} the acid-base molar ratio. The unknown parameters (K, $\delta_{[TOA-H^+]}$ and $\delta_{[FA])}$) were fitted using a least-squares method: the *lsqnonlin* procedure implemented in MATLAB® R2022b, according to the Levenberg- Marquardt algorithm [40]. Within the implementation of this algorithm, initial guesses are required for the all fitted parameters, as well as upper and lower bounds. To circumvent significant dependency on the initial guesses, the *Multistart* algorithm [41] was used as implemented in MATLAB® R2022b. After fitting the required parameters, the ionicity can be determined by [2]:

$$ionicity = \frac{2x_{[TOA-H^+]}}{x^0_{[TOA]} + x^0_{[FA]}} \qquad 2.4$$

Within the previous section, the mixtures were shown to have a strong biphasic character. To avoid incorrect sampling of the biphasic system, it was opted to use homogeneous formic acid – trioctylamine mixtures to determine the ionicity of the PIL, thus above the critical point. At initial formic acid – trioctylamine ratios above 10, the relation between the observed peak position and acid: base ratio is no longer linear, as shown in Figure A18. For this reason, acid:base ratio between 1.7 and 2 were used to ensure fitting within the linear range. A similar strategy was followed by Zhang *et al*. [2]. The results of the least squares fitting procedure are shown in Figure 2.8. Here the carboxylate (A2) ^{1}H-NMR signals are compared to the least squares fit.

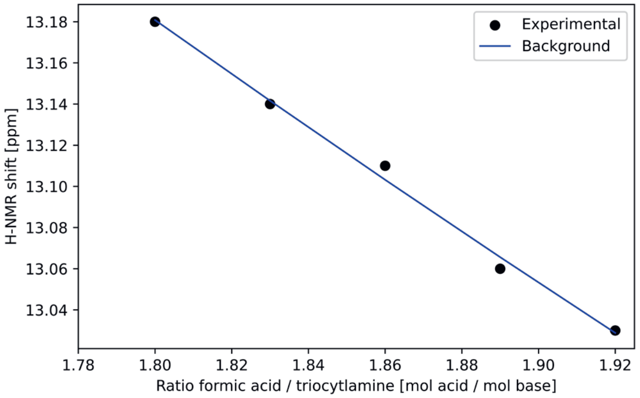

Figure 2.8: Comparison of experimental and fitted NMR data for formic acid – trioctylamine mixtures as a function of molar ratio. The signal at ~13 corresponds to the exchange proton of the amine-acid complex. K_{eq} was determined to 1.66 and the ionicity 56.3%. $\delta_{[TOA-H^+]}$ = 18.76 and $\delta_{[FA]}$ = 9.3.

The procedure was repeated for all tertiary amines, with an overview of resulting ionicity given in . The ionic percentage found for formic acid – triethylamine systems is comparable to the value reported by Zhang *et al*. [2] for acetic acid – triethylamine systems, which was found to be 64 ± 1 mol%.

Tertiary amine	K_{eq}	Ionic fraction
TEA	2.70 ± 0.1	0.622 ± 0.01
TBA	2.21 ± 0.2	0.598 ± 0.012
THA	1.73 ± 0.1	0.568 ± 0.01
TOA	1.66 ± 0.1	0.563 ± 0.01
DMBA	2.56 ± 0.2	0.615 ± 0.012
DMOA	2.30 ± 0.1	0.602 ± 0.01

Table 2.2: Equilibrium constants and ionic molar fraction for all studied amines based on the NMR-method

The IR analysis revealed a decrease in proton transfer as a function of alkyl chain length, with the largest red-shift visible going from triethylamine to tributylamine, while going from trihexylamine to trioctylamine did not lead to a significant red-shift. However, no quantitative correlation between the red shift and mole fraction was identified. The behavior observed within the IR study qualitatively aligns with the behavior observed within the ^{1}H-NMR study, with the degree of proton transfer decreasing as a function of alkyl chain length. The asymmetrical amines, DMBA and DMOA, both reveal a high degree of proton transfer comparable to triethylamine. Although there is a decrease in ionicity, the observed molar acid to amine ratio remains constant irrespective of the nature of the amine. Consequently, the decrease in ionicity must be compensated by the formation of hydrogen bridges.

2.4.3 Coloring of formic acid – trioctylamine complexes

A remarkable color change from colorless to magenta/pink was observed for formic acid -trioctylamine complexes above the critical point, while all other tertiary amines resulted in colorless mixtures in all molar ratios (Figure 2.). Previous works have reported a yellow color for acetic acid – triethylamine adducts [1][2]. As can be seen from Figure 2.9, acetic acid – triethylamine mixtures (> 1.5 molar ratio) indeed were observed to be yellow/orange, depending on the amount of acetic acid. Propionic acid-trioctylamine mixtures above a molar ratio of 1.5 acid:amine were found to have a deep red color.

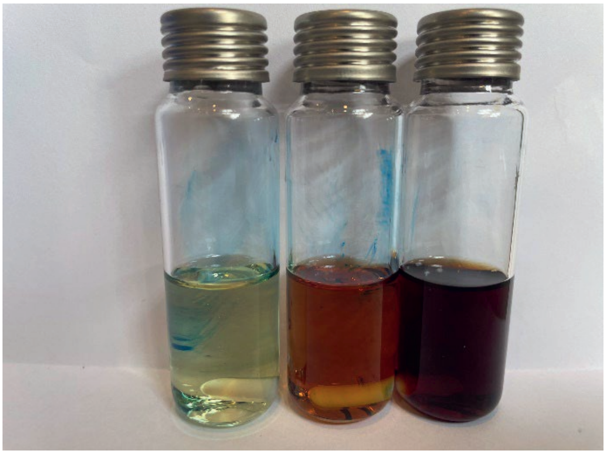

Figure 2.9: left to right: acetic acid – triethylamine (1.5:1 molar ratio), acetic acid – triethylamine (3:1 molar ratio) and propionic acid – trioctylamine (1.5:1 molar ratio), after 1 week.

The intensity of the magenta color was found to be determined by the age of the solution and the formic acid – trioctylamine molar ratio. The initial PILs were observed to be nearly colorless, and form a significant magenta color over a time span of several days. Upon storage of the solutions for several months, a bright blue color was observed. The influence of N-oxidation of the amine was excluded through inert synthesis under N_2 atmosphere, and no evidence of oxidation was observed through ^{1}H-NMR, as depicted in Figure A19. Upon heating of the solutions to a temperature of 100 degrees Celsius, the mixtures became colorless, therefore providing an additional indication that the color was not a result of chemical transformations. The color returned upon cooling of the solutions.

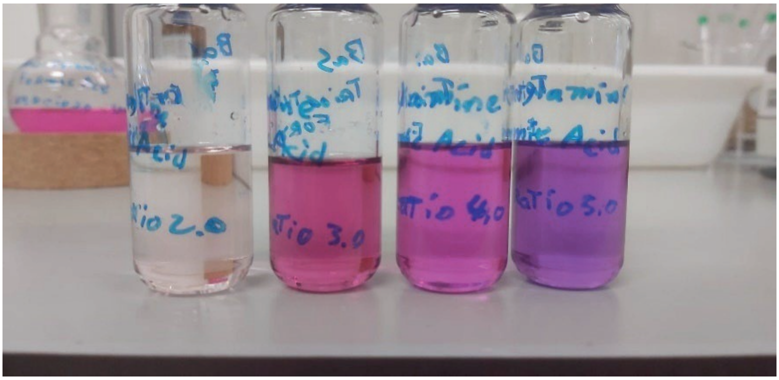

Figure 2.10: Several molar ratios formic acid – trioctylamine mixtures after 1 week.

UV-VIS spectroscopy was used to monitor the color change over time over the course of 13 weeks, as shown in Figure 2.10. Over the course of 1 week the absorbance at 533 nm increases in intensity, resulting in the observable magenta color. At a solution age of 2 weeks, a secondary absorption band is formed at 592 nm which decreases in intensity over the course of several months.

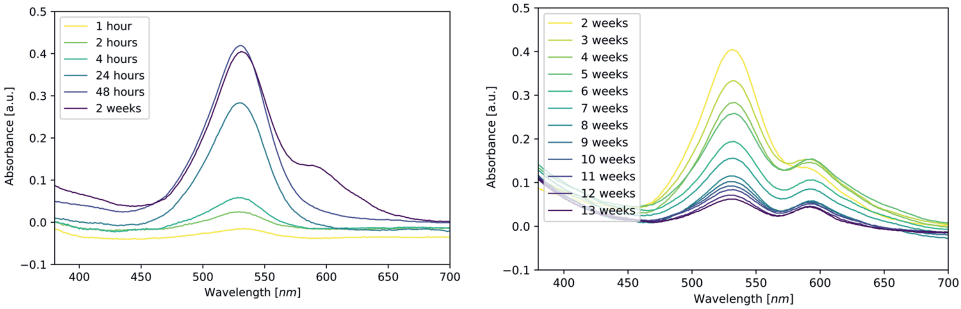

Figure 2.11: UV-VIS spectra of a 3:1 molar ratio formic acid – TOA solution over a time span of 13 weeks

Due to the lack of π-system present within the studied compounds [42] and the confirmed absence of permanent chemical transformations, it was hypothesized that the magenta color originated from light scattering due to the formation of structures of uniform size that have a scattering effect. Within previous works, nanoscale segregation was observed using SAXS/WAXS for similar systems [3][28][43][44], with the length scale of the structure depending on the aliphatic tail length of the components [3]. Here, it was observed that nanoscale structures are formed driven by the formation of hydrogen bonded networks resulting in domains of hydrophobic and hydrophilic nature [3][28][43][44]. Kobrak *et al*. [3] concluded from SAXS measurements that the domains are highly disordered and display a high polydispersity in terms of both shape and size, with a length scale in the order of 15 Å. Within Figure 2.10, wide peaks were observed in the UV-VIS measurements, which are also an indication of a high degree of disorder.

In order to probe the light scattering hypothesis, DLS was employed with a detection limit of 0.1 to 10000 nm. Here, aggregates having an approximate size of 1.78 ± 0.40 nm were observed upon assumption of spherical aggregates, independent of the acid:base ratio (Table 2.3, Figure A20) and solution age. The observed length scales are in line with previous works on acetic acid – triethylamine mixtures [3].

Acid:base ratio [mol/mol]	Diameter (nm)
1:1	1,78 ± 0,40
2:1	1,67 ± 0,31
3:1	1,78 ± 0,39
4:1	1,86 ± 0,38
5:1	1,77 ± 0,23

Table 2.3: DLS results as a function of initial acid:base ratio. All adducts were diluted in toluene, solution age was 1 day.

Unfortunately, the DLS results do not provide an explanation for the visible color differences between the different acid:base molar ratios.

2.5 Conclusions

FTIR and ^{1}H-NMR were used to establish the influence of the alkyl chain length of the nitrogenous cation on the ionicity of the resulting PIL within formic acid- tertiary alkylamine systems. The phase equilibrium was established to be independent of the alkyl chain length with the critical point determined to be at a molar ratio of 1.5 acid to amine.

IR spectroscopy was employed to probe the chemical interactions present within these systems and revealed the existence of a complex mixture of hydrogen bonding and ionic interactions. The red-shift observed for the asymmetrical COO^- band gave an indication for a decrease in proton transfer as a function of chain length. For smaller alkyl chains (up to C_4) this effect was found to be pronounced, while longer chains (C_6 and C_8) resulted in less pronounced shifts. These effects were further quantified using ^{1}H-NMR spectroscopy.

For trioctylamine-based adducts a significant color change from colorless to magenta to blue was observed over a time span of several months. UV-VIS revealed the highly dynamic nature of these complexes, while DLS revealed an average aggregate size of 1.78 nm independent of the acid:base ratio. No satisfactory explanation for the color of these solutions was found.

Appendix A

A.1 Additional FTIR spectra

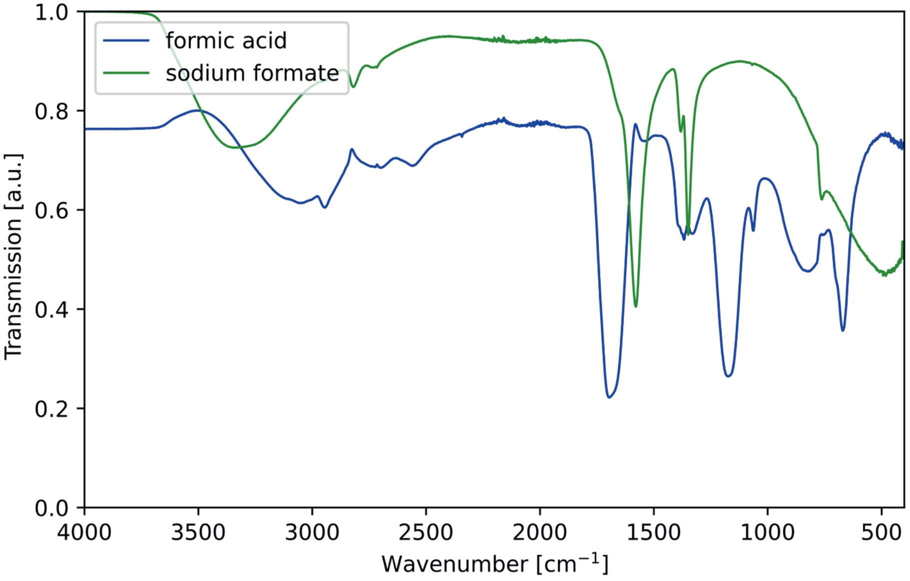

Figure A1: IR spectra of formic acid and sodium formate

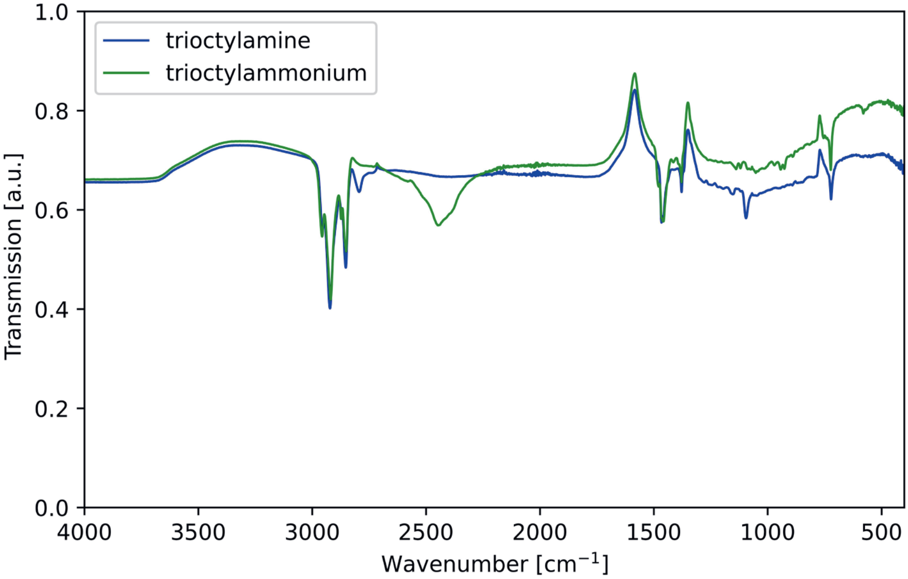

Figure A2: IR spectra of trioctylamine and trioctylammonium

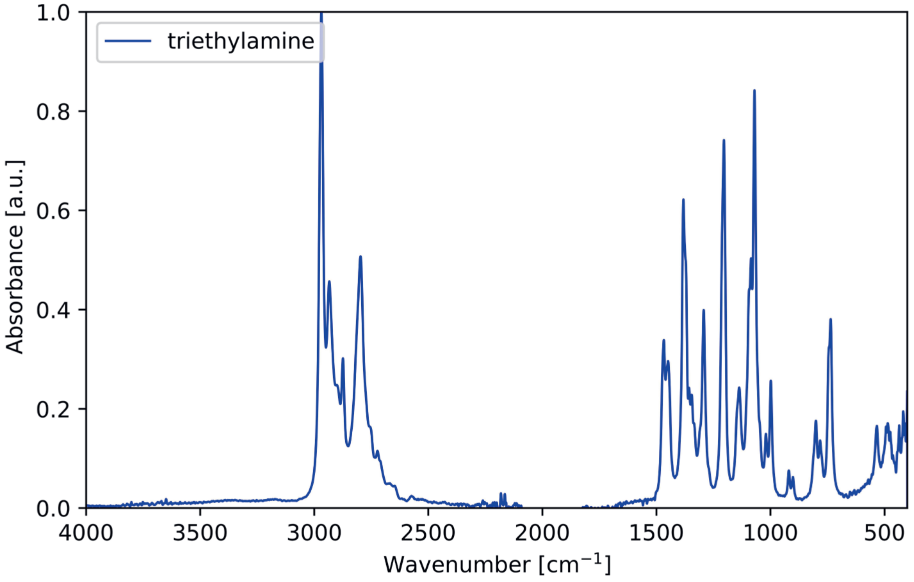

Figure A3: IR spectrum of triethylamine

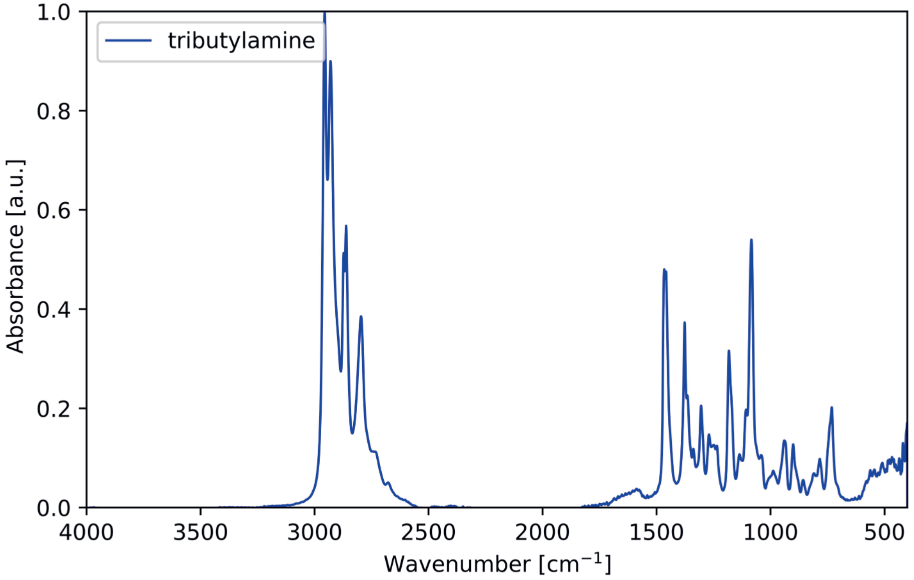

Figure A4: IR spectrum of tributylamine

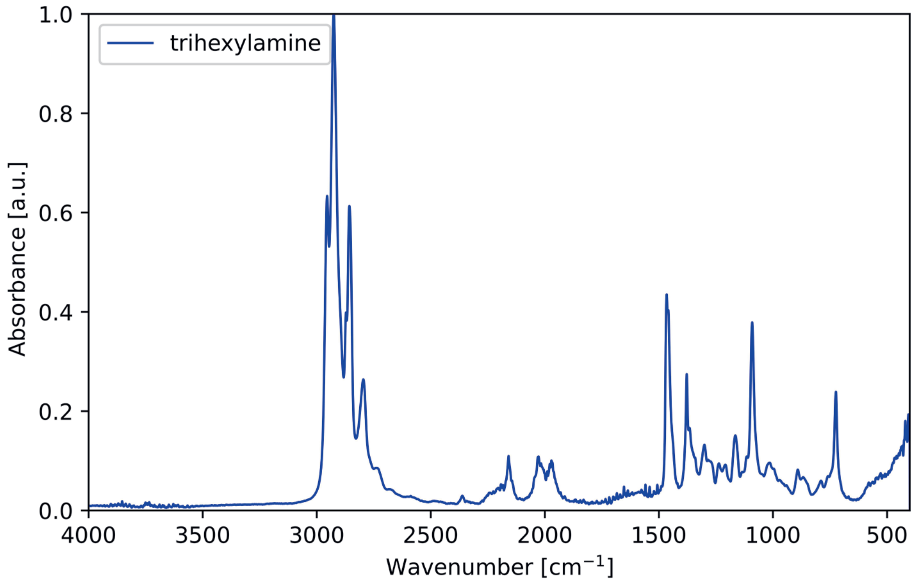

Figure A5: IR spectrum of trihexylamine

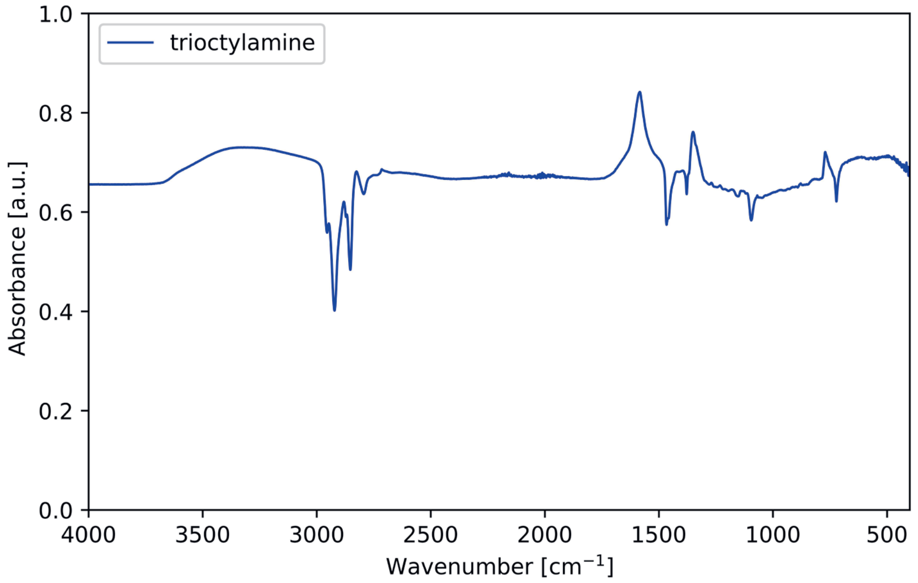

Figure A6: IR spectrum of trioctylamine

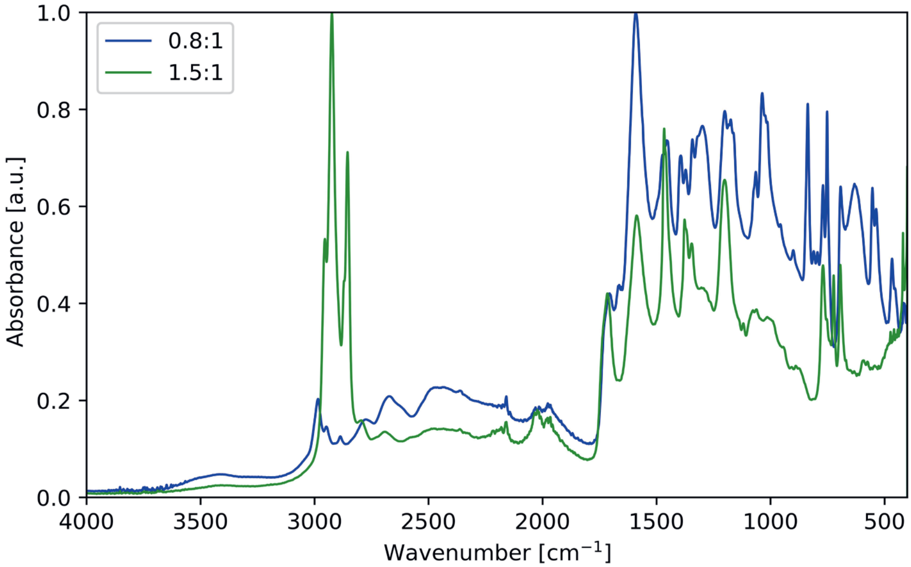

Figure A7: IR spectra of several initial formic acid: triethylamine molar ratios below the critical point for phase separation.

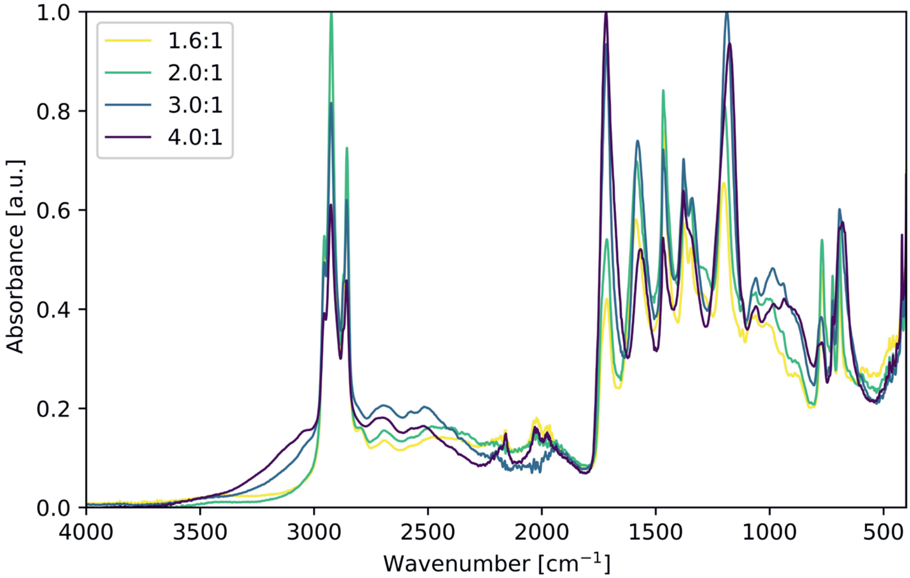

Figure A8: IR spectra of several initial formic acid: triethylamine molar ratios above the critical point for phase separation.

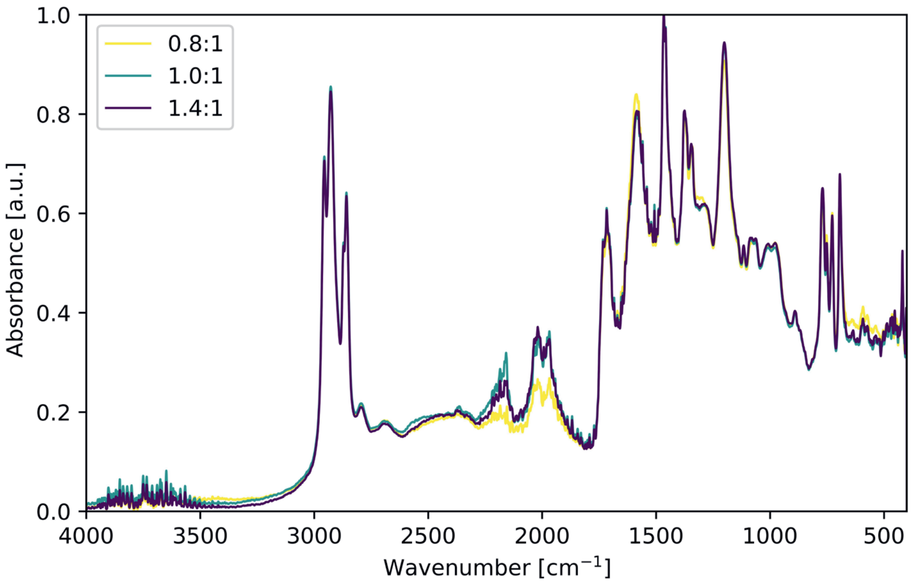

Figure A9: IR spectra of several initial formic acid: trihexylamine molar ratios below the critical point for phase separation.

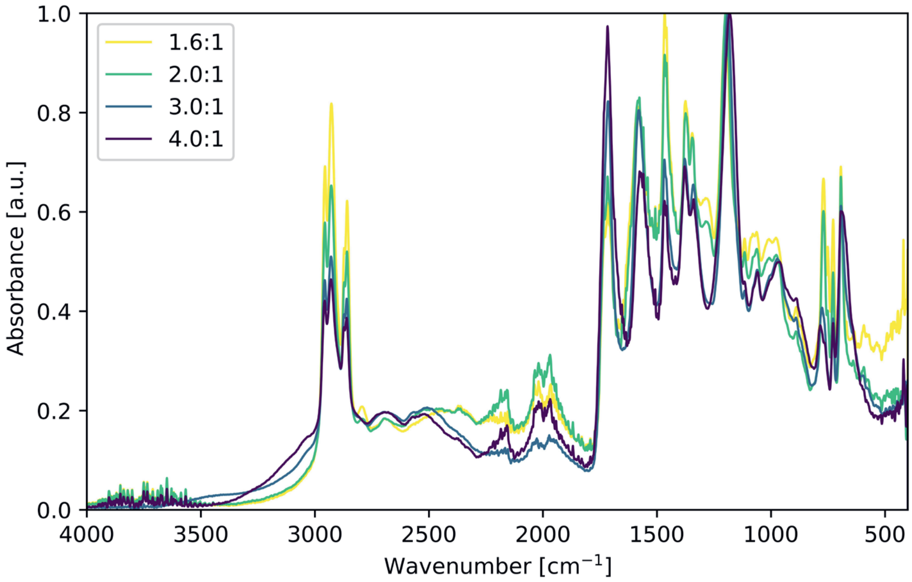

Figure A10: IR spectra of several initial formic acid: trihexylamine molar ratios above the critical point for phase separation.

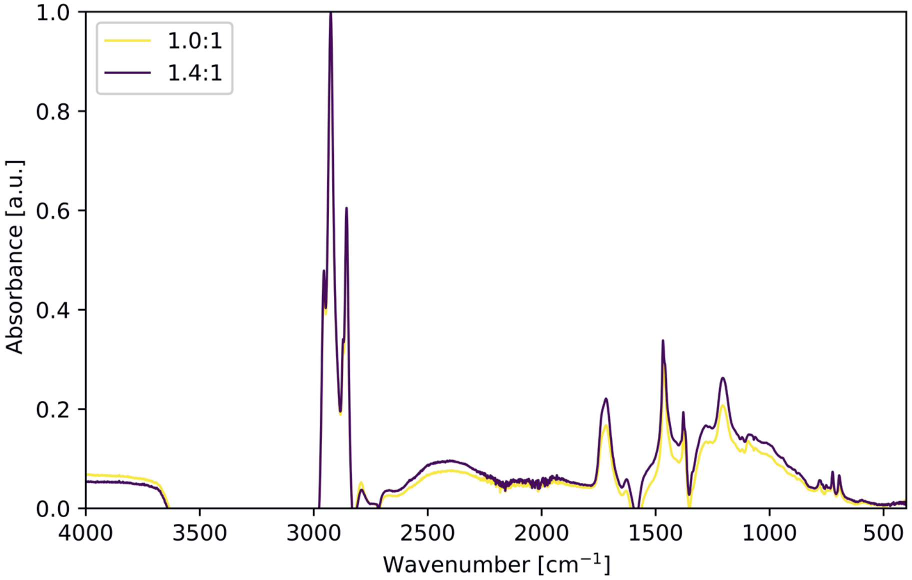

Figure A11: IR spectra of several initial formic acid: trioctylamine molar ratios below the critical point for phase separation.

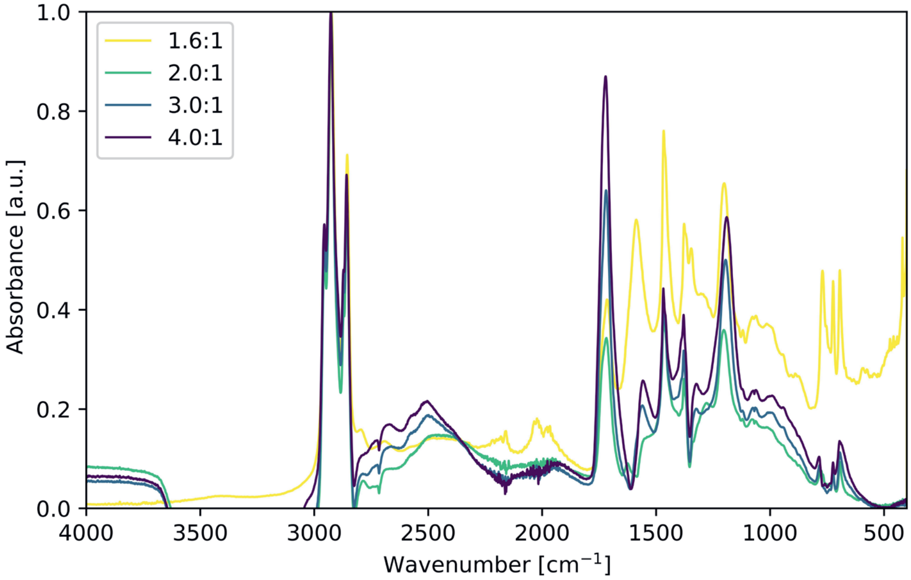

Figure A12: IR spectra of several initial formic acid: trioctylamine molar ratios above the critical point for phase separation.

A.2 C-H peak position in H-NMR as a function of formic acid:amine ratio

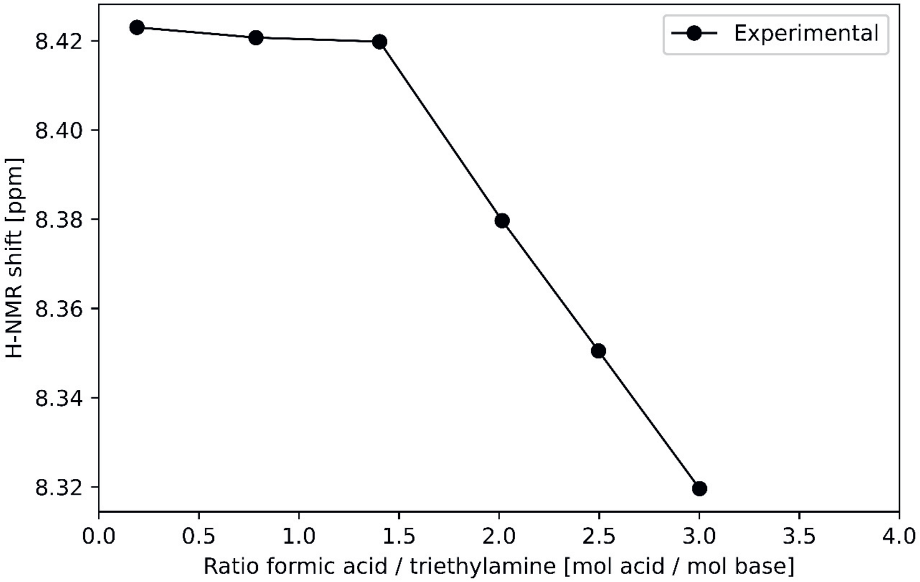

Figure A13: ^{1}H-NMR C-H peak position of several formic acid – triethylamine (TEA) molar ratios

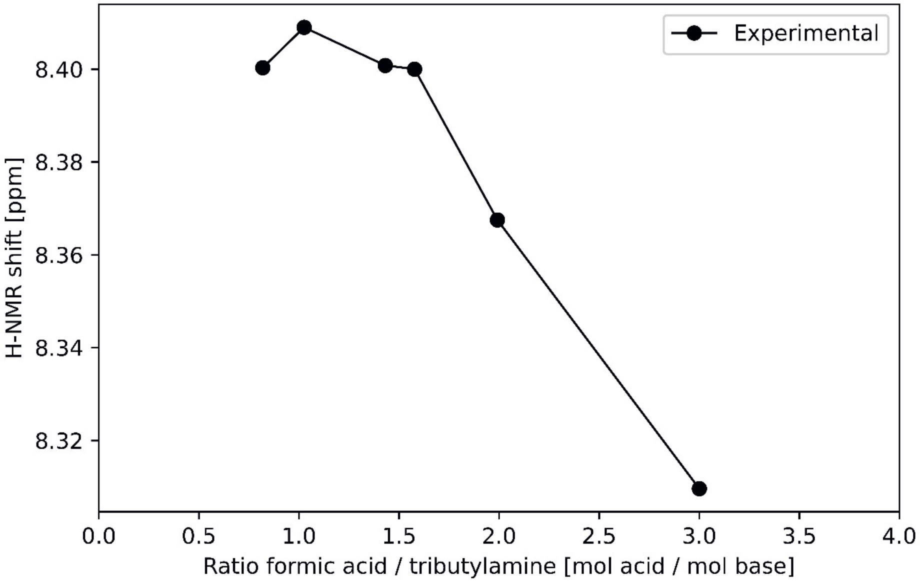

Figure A14: ^{1}H-NMR C-H peak position of several formic acid – tributylamine (TBA) molar ratios

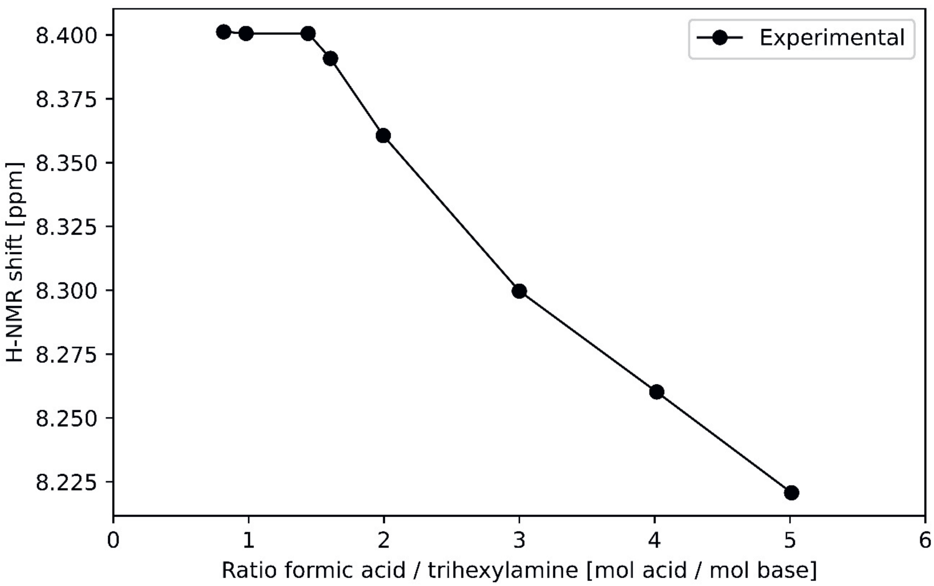

Figure A15: ^{1}H-NMR C-H peak position of several formic acid – trihexylamine (THA) molar ratios

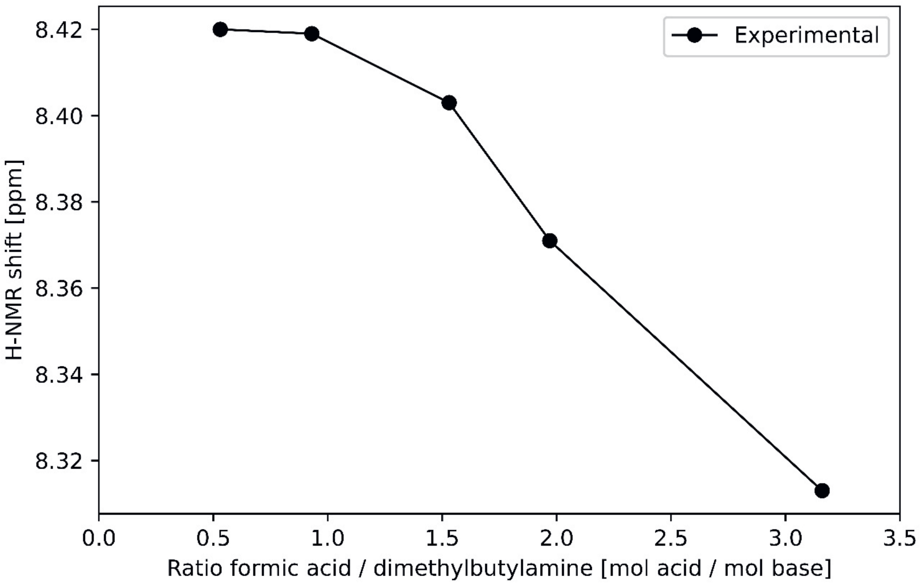

Figure A16: ^{1}H-NMR C-H peak position of several formic acid –dimethylbutylamine (DMBA) molar ratios

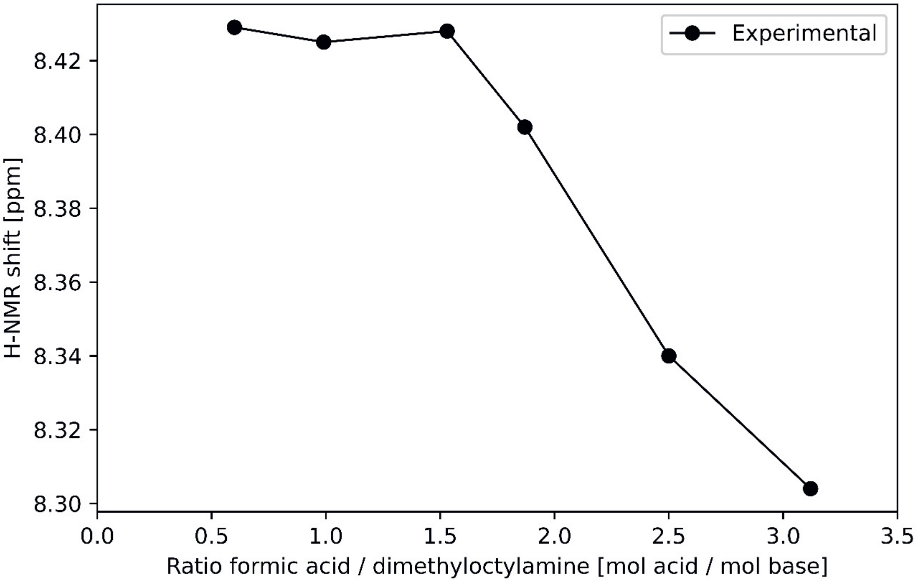

Figure A17: ^{1}H-NMR C-H peak position of several formic acid –dimethyloctylamine (DMOA) molar ratios

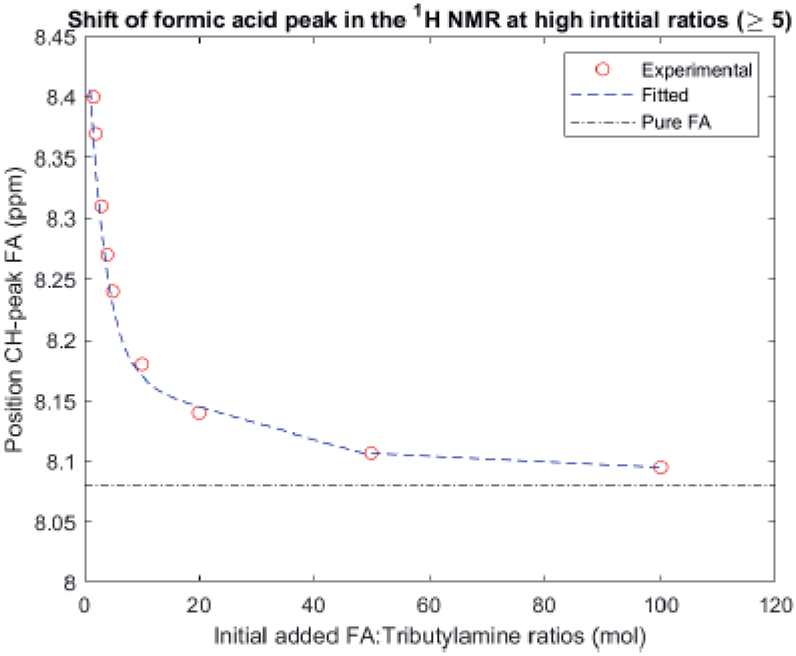

Figure A18: ^{1}H-NMR C-H peak position of several formic acid –tributylamine (TBA) molar ratios

A.3 NMR spectrum inert adduct synthesis

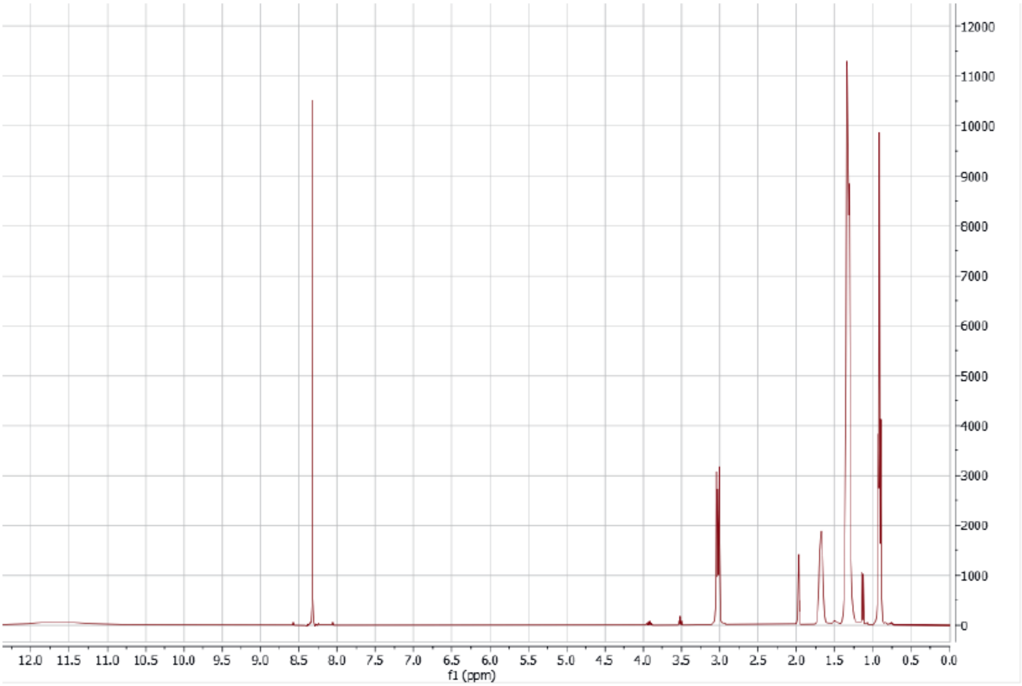

Figure A19: ^{1}H-NMR of a formic acid – trioctylamine mixture synthesized under N_2 atmosphere

A.4 DLS formic acid – trioctylamine

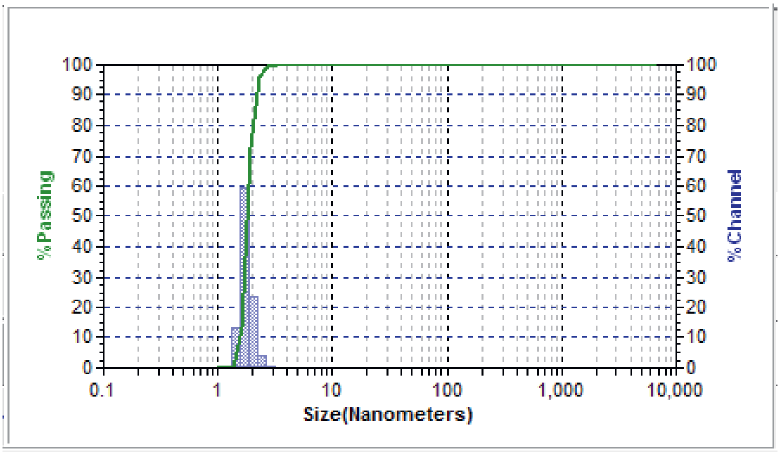

Figure A20: DLS results of a 1:1 molar solution of formic acid – trioctylamine

References

[1] P. Berton, S. P. Kelley, H. Wang, and R. D. Rogers, “Elucidating the triethylammonium acetate system: Is it molecular or is it ionic?,” *J. Mol. Liq.*, vol. 269, pp. 126–131, Nov. 2018, doi: 10.1016/j.molliq.2018.08.006.

[2] J. Zhang, J. Yao, and H. Li, “Phase and Chemical Equilibria of Biphasic Protic Ionic Liquid: Triethylamine-Acetic Acid,” *Ind. Eng. Chem. Res.*, vol. 60, no. 37, pp. 13719–13726, Sep. 2021, doi: 10.1021/acs.iecr.1c02077.

[3] M. N. Kobrak and K. G. Yager, “X-Ray scattering and physicochemical studies of trialkylamine/carboxylic acid mixtures: nanoscale structure in pseudoprotic ionic liquids and related solutions,” *Phys. Chem. Chem. Phys.*, vol. 20, no. 27, pp. 18639–18646, 2018, doi: 10.1039/c8cp02854k.

[4] H. Doi, X. Song, B. Minofar, R. Kanzaki, T. Takamuku, and Y. Umebayashi, “A new proton conductive liquid with no ions: Pseudo-protic ionic liquids,” *Chem. - A Eur. J.*, vol. 19, no. 35, pp. 11522–11526, 2013, doi: 10.1002/chem.201302228.

[5] K. Chen, Y. Wang, J. Yao, and H. Li, “Equilibrium in Protic Ionic Liquids: The Degree of Proton Transfer and Thermodynamic Properties,” *J. Phys. Chem. B*, vol. 122, no. 1, pp. 309–315, Jan. 2018, doi: 10.1021/acs.jpcb.7b10671.

[6] M. Shen, Y. Zhang, K. Chen, S. Che, J. Yao, and H. Li, “Ionicity of Protic Ionic Liquid: Quantitative Measurement by Spectroscopic Methods,” *J. Phys. Chem. B*, vol. 121, no. 6, pp. 1372–1376, Feb. 2017, doi: 10.1021/acs.jpcb.6b11624.

[7] J. Stoimenovski, E. I. Izgorodina, and D. R. MacFarlane, “Ionicity and proton transfer in protic ionic liquids,” *Phys. Chem. Chem. Phys.*, vol. 12, no. 35, pp. 10341–10347, 2010, doi: 10.1039/c0cp00239a.

[8] M. Kar, N. V. Plechkova, K. R. Seddon, J. M. Pringle, and D. R. MacFarlane, “Ionic Liquids-Further Progress on the Fundamental Issues,” *Aust. J. Chem.*, vol. 72, no. 2, pp. 3–10, 2019, doi: 10.1071/CH18541.

[9] K. M. Johansson, E. I. Izgorodina, M. Forsyth, D. R. MacFarlane, and K. R. Seddon, “Protic ionic liquids based on the dimeric and oligomeric anions: [(AcO)xHx-1]-,” *Phys. Chem. Chem. Phys.*, vol. 10, no. 20, pp. 2972–2978, 2008, doi: 10.1039/b801405a.

[10] K. R. Seddon, “Review Ionic Liquids for Clean Technolog y *,” vol. 50, no. Iii, pp. 1–6, 1997, doi: 10.1002/(SICI)1097-4660(199704)68.

[11] S. K. Davidowski *et al.*, “NMR Characterization of Ionicity and Transport Properties for a Series of Diethylmethylamine Based Protic Ionic Liquids,” *J. Phys. Chem. B*, vol. 120, no. 18, pp. 4279–4285, May 2016, doi: 10.1021/acs.jpcb.6b01203.

[12] Y. Deng, J. Yao, and H. Li, “Effects of ionicity and chain structure on the physicochemical properties of protic ionic liquids,” *AIChE J.*, vol. 66, no. 10, Oct. 2020, doi: 10.1002/aic.16982.

[13] J. P. Belieres and C. A. Angell, “Protic ionic liquids: Preparation, characterization, and proton free energy level representation,” *J. Phys. Chem. B*, vol. 111, no. 18, pp. 4926–4937, 2007, doi: 10.1021/jp067589u.

[14] W. Xu, E. I. Cooper, and C. A. Angell, “Ionic liquids: Ion mobilities, glass temperatures, and fragilities,” *J. Phys. Chem. B*, vol. 107, no. 25, pp. 6170–6178, 2003, doi: 10.1021/jp0275894.

[15] R. Kanzaki, K. Uchida, S. Hara, Y. Umebayashi, S. I. Ishiguro, and S. Nomura, “Acid-base property of ethylammonium nitrate ionic liquid directly obtained using ion-selective field effect transistor electrode,” *Chem. Lett.*, vol.

36, no. 5, pp. 684–685, 2007, doi: 10.1246/cl.2007.684.

[16] C. Adam, M. V. Bravo, and P. M. E. Mancini, “Molecular solvent effect on the acidity constant of protic ionic liquids,” *Tetrahedron Lett.*, vol. 55, no. 1, pp. 148–150, 2014, doi: 10.1016/j.tetlet.2013.10.137.

[17] E. Bodo, “Structural features of triethylammonium acetate through molecular dynamics,” *Molecules*, vol. 25, no. 6, 2020, doi: 10.3390/molecules25061432.

[18] L. M. J. Sprakel and B. Schuur, “Solvent developments for liquid-liquid extraction of carboxylic acids in perspective,” *Separation and Purification Technology*, vol. 211. Elsevier B.V., pp. 935–957, Mar. 18, 2019, doi: 10.1016/j.seppur.2018.10.023.

[19] F. Kohler *et al.*, “Molecular Interactions In Mixtures of Carboxylic Acids with Amines. 1. Melting Curves and Viscosities,” 1981. [Online]. Available: https://pubs.acs.org/sharingguidelines.

[20] F. Kohler, E. Liebermann, G. Miksch, C. Kainz, F. Kohler, and C. Kainz, “On the Thermodynamics of the Acetic Acid-Triethylamine System1.”

[21] E. Kohler, F., Gopal, R., Liebermann, “Molecular Interactions in Mixtures of Carboxylic Acids with Amines. 2. Volumetric, Conductlmetrlc, and NMR Properties,” *J. Phys. Chem*, vol. 85, pp. 2524–2529, 1981, doi: 0022-3654/81 /2085-2524$01.25/0

[22] K. Orzechowski, M. Pajdowska, K. Fuchs, and U. Kaatze, “Complex formation in binary propionic acid-triethylamine mixtures: A dielectric relaxation and titration study,” *J. Chem. Phys.*, vol. 119, no. 16, pp. 8558–8566, Oct. 2003, doi: 10.1063/1.1613635.

[23] R. Atkin and G. G. Warr, “The smallest amphiphiles: Nanostructure in protic room-temperature ionic liquids with short alkyl groups,” *J. Phys. Chem. B*, vol. 112, no. 14, pp. 4164–4166, Apr. 2008, doi: 10.1021/jp801190u.

[24] I. Abdurrokhman, K. Elamin, O. Danyliv, M. Hasani, J. Swenson, and A. Martinelli, “Protic Ionic Liquids Based on the Alkyl-Imidazolium Cation: Effect of the Alkyl Chain Length on Structure and Dynamics,” *J. Phys. Chem. B*, vol. 123, no. 18, pp. 4044–4054, May 2019, doi: 10.1021/acs.jpcb.9b01274.

[25] M. Campetella, M. Macchiagodena, L. Gontrani, and B. Kirchner, “Effect of alkyl chain length in protic ionic liquids: an AIMD perspective,” *Mol. Phys.*, vol. 115, no. 13, pp. 1582–1589, Jul. 2017, doi: 10.1080/00268976.2017.1308027.

[26] G. Yu and S. Zhang, “Insight into the cation-anion interaction in 1,1,3,3-tetramethylguanidinium lactate ionic liquid,” *Fluid Phase Equilib.*, vol. 255, no. 1, pp. 86–92, Jul. 2007, doi: 10.1016/j.fluid.2007.03.033.

[27] Y. Q. Lv, Y. Guo, X. Y. Luo, and H. R. Li, “Infrared spectroscopic study on chemical and phase equilibrium in triethylammonium acetate,” *Sci. China Chem.*, vol. 55, no. 8, pp. 1688–1694, Aug. 2012, doi: 10.1007/s11426-012-4634-6.

[28] B. Nuthakki *et al.*, “Protic ionic liquids and ionicity,” *Aust. J. Chem.*, vol. 60, no. 1, pp. 21–28, 2007, doi: 10.1071/CH06363.

[29] E. Cristina Stanca-Kaposta *et al.*, “Carbohydrate molecular recognition: A spectroscopic investigation of carbohydrate-aromatic interactions,” *Phys. Chem. Chem. Phys.*, vol. 9, no. 32, pp. 4444–4451, 2007, doi: 10.1039/b704792d.

[30] Y. K. Hong and W. H. Hong, “Influence of chain length of tertiary amines on

extractability and chemical interactions in reactive extraction of succinic acid," *Korean J. Chem. Eng.*, vol. 21, no. 2, pp. 488–493, 2004, doi: 10.1007/BF02705439.

[31] J. P Aiv Arinta, S. Karlsson, A. Poso, and M. Hotokka, "Calculated molecular properties for different alkanoic acid± alkylamine complexes: A comparison with measured FTIR and Raman spectra." [Online]. Available: www.elsevier.nl/locate/chemphys.

[32] R. Markiewicz *et al.*, "Influence of alkyl chain length on thermal properties, structure, and self-diffusion coefficients of alkyltriethylammonium-based ionic liquids," *Int. J. Mol. Sci.*, vol. 22, no. 11, Jun. 2021, doi: 10.3390/ijms22115935.

[33] R. I. Aravena and J. P. Hallett, "Protic ionic liquids based on fatty acids: A mixture of ionic and non-ionic molecules," *J. Mol. Liq.*, vol. 373, Mar. 2023, doi: 10.1016/j.molliq.2023.121241.

[34] M. N. Garaga, M. Nayeri, and A. Martinelli, "Effect of the alkyl chain length in 1-alkyl-3-methylimidazolium ionic liquids on inter-molecular interactions and rotational dynamics: A combined vibrational and NMR spectroscopic study," *J. Mol. Liq.*, vol. 210, pp. 169–177, Oct. 2015, doi: 10.1016/j.molliq.2015.06.055.

[35] B. A. Marekha *et al.*, "Intermolecular interactions in mixtures of 1-n-butyl-3-methylimidazolium acetate and water: Insights from IR, Raman, NMR spectroscopy and quantum chemistry calculations," *J. Mol. Liq.*, vol. 210, pp. 227–237, Oct. 2015, doi: 10.1016/j.molliq.2015.05.015.

[36] M. Kakihana, M. Kotaka, and M. Okamoto, "Vibrational Analysis of Acetate Ion Molecules and Estimation of Equilibrium Constants for Their Hydrogen Isotopic Exchange Reactions," 1983. [Online]. Available:

https://pubs.acs.org/sharingguidelines.

[37] J. Oomens and J. D. Steill, “Free carboxylate stretching modes,” *J. Phys. Chem. A*, vol. 112, no. 15, pp. 3281–3283, Apr. 2008, doi: 10.1021/jp801806e.

[38] J. A. Tamada, A. S. Kertes, and C. J. King, “Extraction of Carboxylic Acids with Amine Extractants. 1. Equilibria and Law of Mass Action Modeling,” 1990. [Online]. Available: https://pubs.acs.org/sharingguidelines.

[39] J. A. Tamadat and C. J. King, “Extraction of Carboxylic Acids with Amine Extractants. 2. Chemical Interactions and Interpretation of Data,” 1990. [Online]. Available: https://pubs.acs.org/sharingguidelines.

[40] P. E. Gill and W. Murray, “Algorithms for the Solution of the Nonlinear Least-Squares Problem,” 1978.

[41] Z. Ugray, L. Lasdon, J. Plummer, F. Glover, J. Kelly, and R. Marti, “Scatter search and local NLP solvers: A multistart framework for global optimization,” *INFORMS J. Comput.*, vol. 19, no. 3, pp. 328–340, 2007, doi: 10.1287/ijoc.1060.0175.

[42] A. L. Sklar, “Theory of color of organic compounds,” *J. Chem. Phys.*, vol. 5, no. 9, pp. 669–681, 1937, doi: 10.1063/1.1750099.

[43] R. Hayes, S. Imberti, G. G. Warr, and R. Atkin, “How water dissolves in protic ionic liquids,” *Angew. Chemie - Int. Ed.*, vol. 51, no. 30, pp. 7468–7471, 2012, doi: 10.1002/anie.201201973.

[44] L. I. N. Tomé *et al.*, “On the interactions between amino acids and ionic liquids in aqueous media,” *J. Phys. Chem. B*, vol. 113, no. 42, pp. 13971–13979, 2009, doi: 10.1021/jp906481m.

3

Modelling of formic acid production using solventless trialkylamine reduction strategies

This chapter is based on the following publication:

A.W.N. de Leeuw den Bouter, L.Brito, A. Miquelot, P.Olivier,J. van der Schaaf, “Modelling of formic acid production using solventless trialkylamine reduction strategies,” under review in Chem.Eng.Sci.

Abstract

Solventless fed-batch experiments at elevated pressures were performed to gain insights into the performance of using triethylamine as an extraction base during the direct hydrogenation of CO_2 to formic acid. No formic acid was observed in the bulk liquid after several hours of reaction. Analysis on the spent catalyst revealed significant formic acid build-up within the catalyst pores. A fundamental, continuum model based on Cahn-Hilliard spinodal decomposition was developed and validated to study the influence of the biphasic nature of formic acid – trialkylamine structures during reaction at pore level. The biphasic nature of the tertiary alkylamine – formic acid system was found to have significant implications for the reaction performance of the proposed system.

3.1 Introduction

The direct hydrogenation of carbon dioxide within the gaseous phase is thermodynamically unfavorable (ΔG^0 = 32.8 kJ/mol) [18][19]. Performing this reaction within the liquid phase through the usage of solvents results in a more favorable, exergonic reaction[18][19][20]. Additionally, the equilibrium of the reaction can be shifted towards the product side through the addition of bases, with particular interest in amines [20]. Commonly, nitrogen-containing bases such as trialkylamines are employed, resulting in the formation of adducts that strongly bind to the produced formic acid [19][20]. Previous works [21] have shown that the formic acid production rates scale directly with the amount of amine present, thus solventless systems are desirable. Besides an increase in kinetic rates, the equilibrium is also further shifted towards formic acid at higher amine concentrations, therefore performing the reaction in pure trialkylamine systems without additional solvents would be highly attractive.

However, within the previous chapter it was shown that such formic acid – trialkylamine adducts are nearly immiscible in non-binding trialkylamines until a critical molar ratio is achieved, thus resulting in a possible biphasic system within the catalyst particles during formic acid production.

The objective of this study is to gain a deeper understanding into the implications of the biphasic nature of the amine – adduct system during the direct hydrogenation of CO_2 to formic acid. To this end, experiments were executed in batch reactors with and without the addition of additional solvents besides triethylamine. A 2D catalyst pore was modelled at mesoscale to allow for the study of intra-particle concentration profiles at a continuum level. The spinodal decomposition of the fluid mixture was modelled using phase field models following the Cahn-Hilliard equations coupled to the law of mass action with the diffuse interface approach.

3.2 Experimental materials and methods

3.2.1. Materials

Triethylamine (> 99.5%) was obtained from Sigma-Aldrich. Dibromomethane (>99.9%, stabilized with butylhydroxytoluene) and 1,3,5-trimethoxybenzene (>98.0%), were obtained from TCI chemicals. Acetonitrile-d_3 (D99.8%) and D_2O (D 99.0) were purchased from Deutero. 1-Decanol (>98%) was purchased from Thermo Scientific Chemicals. All materials were used as received, handled in air and used without any additional purification. Commercial AUROlite Au/TiO_2 (1wt% Au, verified with ICP-OES) was purchased from Strem. In order to prevent deactivation, the catalyst was stored under Ar in a cold and dark environment.

3.2.2. Analytical methods

^{1}H-NMR (Bruker, 400 MHz) was used to determine the chemical compositions of all samples from reactive experiments. Here, 0.5 ml of deuterated solvent (Acetonitrile-d_3 or D_2O) containing either dibromomethane or 1,3,5-trimethoxybenzene as internal standard was mixed with 0.1 ml of sample. The concentration of internal standard was 1 mol/liter.

Viscosity was measured using a Brookfield Devek DV2T Viscometer (61 spindle and 200 rpm). Densities were measured using a graduated cylinder 10 mL (± 0.1 mL) and a Sartorius BP 211D scale.

3.2.3. Reactive testing

Reactive testing was conducted using a 270 mL fed – batch autoclave with integrated heating jacket at a constant working pressure of 15 bar. In a typical experiment, 20 grams of AURO*lite* Au/TiO_2 was loaded into the reactor in air. The catalyst was received in the form of extrudates, and thus subsequently crushed and sieved to a particle size of 150-250 μm. Triethylamine (110 ml) was fed into the reactor, followed by flushing of the reactor with CO_2. H_2 and CO_2 are fed using Bronkhorst mass flow controllers. A Bronkhorst back-pressure controller was used to ensure a constant pressure. Aliquots of the reaction mixture were obtained at every 10 hours. A 2 μm filter was present in the sample line to ensure no catalyst left the reactor. The reaction mixture was continuously stirred at 500 rpm.

3.3 Numerical methods

3.3.1. Phase field modelling

Phase field models enable the description of spontaneous phase separation of immiscible fluids [23]. Such models have previously been used to describe and simulate the grain growth of metal crystallites [24], electromigration [25], biological applications [26] and a simultaneous reversible chemical reaction with spinodal decomposition [23][27].

Diffuse-interface phase field models are a versatile tool for microstructure simulations at mesoscale level [28][29]. Within this approach, the structures are described by a continuous set of phase-field variables, which are also continuous over the interface [27]. This way, the necessity of explicit front tracking is prevented, leading to decreased computational load [28][29].

A commonly used example of such models is the Cahn-Hilliard equation. The Cahn-Hilliard equation describes the temporal evolution of spinodal decomposition through describing the Helmholtz free energy as a function of composition and the spatial derivative of the composition at the grid point [30]–[33]. Clavijo *et al.* [23] have previously presented a method to transform the Cahn-Hilliard equation into a thermodynamically consistent multicomponent reactive Cahn-Hilliard set of equations through the usage of *n* force balances and *n* mass balances to account for the chemical reactions. Here, *n* phase fields are considered in a set of coupled Cahn-Hilliard equations to represent the concentrations of all species (*n*), resulting in a system consisting of *n* non-linear fourth order partial differential equations in space as a result of non-constant diffusion constants.

3.3.2 Governing equations and boundary conditions

An overview of the governing equations is given, further details on the derivation can be found elsewhere [23][34].

Considering a *n*-species system where x_a, the mole fraction of component a, the sum of all mole fractions is given by

$$\sum_{a=1}^{n} x_a \equiv 1 \qquad 3.1$$

and the gradient

$$\sum_{a=1}^{n} \nabla x_a \equiv 0 \qquad 3.2$$

From here it readily becomes apparent that the set is not linearly independent, thus we consider *n* -1 independent species, while the *n*th species is used as a reference to ensure mass conservation. The general balance consists out of a diffusive flux ($\boldsymbol{J}^{\boldsymbol{a}}$) and a reactive term ($R^a$)

$$\frac{\partial x_a}{\partial t} = -\nabla \cdot \boldsymbol{J}^{\boldsymbol{a}} + R^a \qquad 3.3$$

The diffusive flux is given by

$$\boldsymbol{J}^{\boldsymbol{a}} = -\sum_{b=1}^{n-1} \boldsymbol{L}^{ab} \nabla\mu^b \qquad 3.4$$

with L_{ab} being the binary concentration-dependent diffusion coefficient and μ^b the chemical potential of component b.

$$L_{ab} = M_{ab}\varphi_a(\delta_{ab} - x_b) \qquad 3.5$$

Wherein M_{ab} are the binary diffusion coefficients, and δ_{ab} represents the Kronecker delta. The binary diffusion coefficients were determined by the Einstein-Stokes equation combined with the Stokes equation for low Reynold number flows [35]:

$$D_{ab} = \frac{k_B T}{6\pi\eta r_a} \qquad 3.6$$

With T, η and r_a the temperature, the viscosity and molecular radius of component a respectively.

Per definition, the chemical potential of the system is equal to the variational derivative of free energy in respect to the species concentration and contains both the contribution of the *n*-well and interface contribution:

$$\mu_a = \left.\frac{\partial F}{\partial x_a}\right|_{P,V} \qquad 3.7$$

As was previously suggested by previous works [23][30]–[33], the phase separation is assumed to be governed by the Ginzburg-Landau free energy ($\hat{\psi}$), expressed by

$$\hat{\psi}(x) = N_v k_B \vartheta \left(\sum_{a=1}^{n} x_a \ln x_a \right) + N_v \sum_{a=1}^{n} \sum_{b=1}^{n} \Omega^{ab} x_a x_b + \frac{1}{2} \sum_{a=1}^{n} \sum_{\mathrm{b}=1}^{n} \Gamma^{ab} \nabla x_a \cdot \nabla x_b \qquad 3.8$$

where N_v, k_B and ϑ are the number of molecules of component a per unit volume, the Boltzmann constant and the temperature respectively. Ω^{ab} is the interaction energy between the mass fractions of components. Following previous works, [23][34], Ω^{ab} is defined by

$$\Omega^{ab} = 0 \quad \text{when } a = b \qquad 3.9$$

$$\Omega^{ab} = 2 k_B \vartheta_c^{ab} \quad \text{when } a \neq b \qquad 3.10$$

Here, ϑ_c^{ab} is the critical temperature between component a and b. Additionally, Γ^{ab} is the magnitude of the interfacial energy between components, with the unit of force [30]–[33]:

$$\Gamma^{ab} = \sigma^{ab}\, l^{ab} = N_v \Omega^{ab} (l^{ab})^2 \qquad 3.11$$

With σ^{ab} the interfacial tension and l^{ab} the interfacial thickness, as calculated by a 12-6 Lennard-Jones potential. The 12-6 potential was selected due to close agreement with experimental results for small molecules in solution [33]

$$l^{ab} = \left(\frac{11}{7}\right)^{\frac{1}{2}} \left(\frac{6}{\pi N_v}\right)^{\frac{1}{3}} \tag{3.12}$$

The expression for the chemical potential is given by

$$\mu_\sigma^a = N_v k_B T \ln\left(\frac{x_a}{x_\sigma}\right) + 2N_v \sum_{b=1}^{n} (\Omega^{ab} - \Omega^{\sigma b}) x_b - \sum_{b=1}^{n} (\Gamma^{ab} - \Gamma^{\sigma b}) \nabla \cdot (\nabla x_b) \tag{3.13}$$

Here, σ represents the σth conserved species and is used as a reference, following the work of Clavijo *et al*. [34].

Lastly, the reactive term (R^a) is based on the power law kinetics determined by Hensen *et al.* [21] for an Au/Al_2O_3 catalyst.

$$R_{volumetric} = k^+ exp^{\frac{-E_a^+}{RT}} x_{CO_2} x_{H_2} \varphi_{TEA} - k^- exp^{\frac{-E_a^-}{RT}} x_{adduct} \tag{3.14}$$

On the pore wall, distinctive active sites were placed, at which point the reactive term is added to the equations through a Dirichlet boundary condition. The volumetric kinetic expression presented in [21] was rewritten to an intrinsic reaction rate per active site

$$R_{intrinsic} = R_{volumetric} \cdot \frac{\rho_{site}\, V_{site}}{\rho_{solid}\, \varepsilon_{bed} L_{cat}} \tag{3.15}$$

where ρ_{site} and ρ_{solid} are the gravimetric density of the active site and catalyst particle respectively. V_{site} is the volume of a single active site, ε_{bed} is the solid hold up within the reactor and L_{cat} is the active metal loading.

The dimensionless forms are introduced through a scaling based on a reference free energy ($\Psi_0 = 2\,N_v k_B \vartheta$) as previously suggested by [34][36][37]. The scaling is performed in order to improve numerical accuracy. This reference free energy is used to relate the free energy density to the species mobility

$$\boldsymbol{D_{ab}} = \Psi_0 M_{ab} x_a (\delta_{ab} - x_b) \qquad 3.16$$

Furthermore, the critical temperature and the length and time scales are scaled through [21,22]

$$\bar{y} = L_0^{-1}\, y \qquad 3.17$$

$$\bar{t} = T_0^{-1}\, t \quad with\ T_0 = \frac{D_0 l_0^2}{L_0^4} \qquad 3.18$$

$$\overline{\vartheta_c^{ab}} = T^{-1} \vartheta_c^{ab} \qquad 3.19$$

here, D_0 and l_0 are set according to a reference species. The reference species was taken to be the adduct. L_0 is set equal to the pore length. The resulting equations in dimensionless form are

$$\frac{\partial\, x_a}{\partial \bar{t}} = -\bar{\nabla} \cdot \bar{J_a} + \overline{R_a} \qquad 3.20$$

$$\bar{J_a} = -\sum_{b=1}^{n} \overline{\boldsymbol{D_{ab}}}\ \nabla \bar{\mu}^b \qquad 3.21$$

$$\bar{\mu}_\sigma^b = \frac{1}{2} \ln \frac{x_b}{x_\sigma} + 2 \sum_{a=1}^{n} (\bar{\vartheta}_c^{ba} - \bar{\vartheta}_c^{\sigma a}) x_a - \sum_{a=1}^{n} \left(\bar{\sigma}^{ba} \bar{\ell}^{ba} - \bar{\sigma}^{\sigma a} \bar{\ell}^{\sigma a} \right) \nabla \cdot (\nabla x_a) \qquad 3.22$$

A zero flux (Neumann) boundary condition is enforced on the pore walls, except for the active metal sites. Here, the reaction term is implemented. The catalyst pore is assumed to be in contact with an external fluid reservoir, thus the continuity of fluxes between the solid and fluid phases in the form of a Dirichlet boundary condition is assumed. Initial concentrations are equal to saturation for all reagents.

3.3.3 Discretization

The mesoscale binodal decomposition simulations were performed in C++ using CVODE provided by SUNDIALS as a solver [38][39]. Spatial discretization was performed using the Finite Volume Method and the Method of Lines, while time discretization was performed by the CVODE solver. The time integration of Cahn-Hilliard equations is non-trivial due to the non-linear fourth order dependency in space as a result of non-constant, composition-dependent diffusion constants [29][40]. Thus, the adaptive-time step strategy was used. The maximum order of the BDF solver was set to 5, with a relative tolerance of 1e-8. Boundary conditions were discretized through second order Lagrange interpolation.

3.3.4 Physical properties

Adduct density and viscosity were experimentally determined as a function of temperature, and are depicted in Appendix B Figure B1 and Figure B2 respectively. The Einstein-Stokes relation was used to calculate diffusivities, this relation requires the usage of molecular radii. An overview of the molecular radius of all components can be found in Appendix B (Table B.1). The radius of the adduct was estimated based on the structure as proposed by Sprakel *et al.* [41]. An overview of the resulting of resulting binary diffusion coefficients can be found in Appendix B (Table B.2). The solubility of the gaseous reactants CO_2 and H_2 under the studied conditions was calculated using Henry's law. The Henry coefficients were determined at 50 degrees Celsius using the SRK property method in Aspen Plus V11, and are summarized in Table 3.1. The physical properties of the catalyst are given in Table 3.1.

Parameter	Physical representation	Value	Unit	Source
$\rho_{Al_2O_3}$	Support density	$4.01 \cdot 10^3$	$\frac{kg_{Al_2O_3}}{m^3_{Al_2O_3}}$	[42]
ε_{bed}	Reactor solid hold-up	0.6	$\frac{m^3_{solid}}{m^3_{reactor}}$	-
L_{cat}	Catalyst loading	0.01	$\frac{kg_{Au}}{kg_{solid}}$	[21]
d_{site}	Active site diameter	$1.9 \cdot 10^{-9}$	m	[21]
H_{CO_2}	Henry coefficient CO_2	40	$\frac{mol}{m^3\ bar}$	
H_{H_2}	Henry coefficient H_2	1.54	$\frac{mol}{m^3\ bar}$	

Table 3.1: Overview of catalyst physical properties and Henry coefficients. Henry coefficients [mol m^{-3} bar^{-1}] for H2 and CO2 in triethylamine at 50 degrees Celsius. Coefficients were determined using the SRK property method in Aspen Plus V11.

Lastly, the studied process conditions are summarized in Table 3.2. In order to experimentally determine the critical temperature of the triethylamine adduct mixtures, a 1:1 molar ratio mixture was prepared and heated within a Rotavap. It was established that the mixture remains biphasic until all triethylamine has evaporated. For this reason, it was opted to set the critical temperature to the boiling point of triethylamine.

Parameter	Value	Unit
Temperature	323	K
Critical temperature	420	K
Pressure	15	bar
Relative tolerance	$1 \cdot 10^{-8}$	-
Number of reactive sites	8	-
H_2: CO_2 volumetric ratio	0.5	-

Table 3.2: Overview of simulation parameters

Within this study, solventless batch experiments at elevated pressures were performed to gain insights into the performance of using triethylamine as an extraction base during the direct hydrogenation of CO_2 to formic acid. Afterwards, a 2D pore model describing spinodal decomposition was created in an attempt to further clarify the experimental results. Verification and validation of the model can be found in the Appendix B.

3.4.1 Fed-batch experiments

First, the catalytic performance of a 1 wt% Au/TiO_2 catalyst in the direct hydrogenation of CO_2 at 15 bars of equimolar CO_2/H_2 mixture was tested using triethylamine as a base. In order to verify the activity of the received catalyst, an experiment was performed using a polar solvent to ensure solubility of all components. Here, a 1:3 vol/vol (0.45 mol/mol) mixture of triethylamine and 1-decanol was used, with the reaction a steady state formic acid concentration after 4 days, as shown in Figure 3.1.

Next, with fresh catalyst an experiment was performed using pure neat triethylamine, without the addition of polar solvents. After 7 hours reaction time at otherwise identical conditions, the amount of FA observed in liquid samples was negligible. While exact determination of the concentrations was deemed inaccurate due to the very low concentrations, the estimated FA concentration is within the ppm range, whereas the experiment with solvent reached the thermodynamic equilibrium FA concentration expected based on the work of Hensen *et al*. [21] .

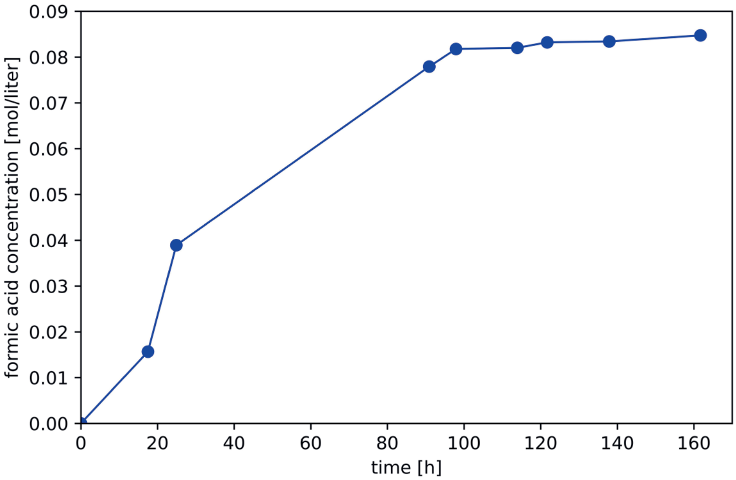

Figure 3.1: Concentration of FA in time. The reaction was run in a batch reactor, total pressure 15 bar, temperature 50 ºC, 1:3 vol/vol triethylamine:1-decanol.

Within Chapter 2, it was shown that such formic acid – triethylamine adducts are almost completely immiscible in neat triethylamine [22]. As FA is highly soluble in water, the spent catalyst was subsequently placed in 10 mL of demi water for 1 hr after reaction. ^{1}H-NMR spectroscopy revealed a significant FA concentration, with the total molar amount of formic acid in the pores being approximately 3 orders of magnitude larger than those in the bulk fluid.

The verified catalyst activity and release of formic acid from the spent catalyst in the neat amine case, provide an initial indication that while formic acid is being produced, it cannot leave the pores. Even if the formation of formic acid in the form of formic acid – triethylamine adducts would result in phase separation with the reagents, the reaction would progress if the product can diffuse away from the active site in order to retain low local concentrations. However, within the experiments, virtually no formic acid is observed to be present within the bulk fluid, providing an indication that the produced formic acid cannot diffuse away from the active site to reach the bulk liquid. This would result in high local concentrations of adduct within the pores of the catalyst resulting in a local equilibrium being reached around the active gold crystallites, therefore stopping the production of formic acid. To investigate this at pore level, a modelling approach is used.

3.4.2 Numerical modelling of catalyst pores

Numerical simulations were performed at meso-scale of a two-dimensional multicomponent system including spinodal decomposition representing the direct hydrogenation of CO_2 towards formic acid within a catalyst pore. Conditions were selected such to resemble the experimental protocol as closely as possible, with conditions summarized in Table 3.3.

The numerical simulations summarized in Table 3.2 were performed on a 40x40 cell grid, representing a physical size of 80 nm with the pore mouth exposed to a bulk liquid of constant concentration. The temporal evolution of the adduct front diffusing through the catalyst pore according to the process conditions summarized in Table 3.2 is shown in Figure 3.2, while the temporal evolution of all species is shown in Figure B7.

Here, one distinctive active site was placed on the wall of the catalyst pore. It should be noted that the active sites are placed flat against the simulation boundaries, and thus do not occupy any volume. All simulations were started with the catalyst pore filled with neat triethylamine, saturated with CO_2 and H_2. The initial adduct concentration was set to 1e-6 mol/m^3.

Within Figure 3.2, the formic acid concentration directly above the active site in the y-direction is visualized over time. Here, high concentrations of formic acid – triethylamine adducts of up to 48.6 mol/m^3 are observed directly above the active site after approximately 10 seconds, while no formic acid is present within the bulk of the pore fluid. Then, the formic acid diffuses through the catalyst pore, forming a thin shell of adduct around the active site over a distance of several grid cells, thus showing the slight miscibility of the adduct and neat triethylamine, in line with previous experimental observations reported in Chapter 2.

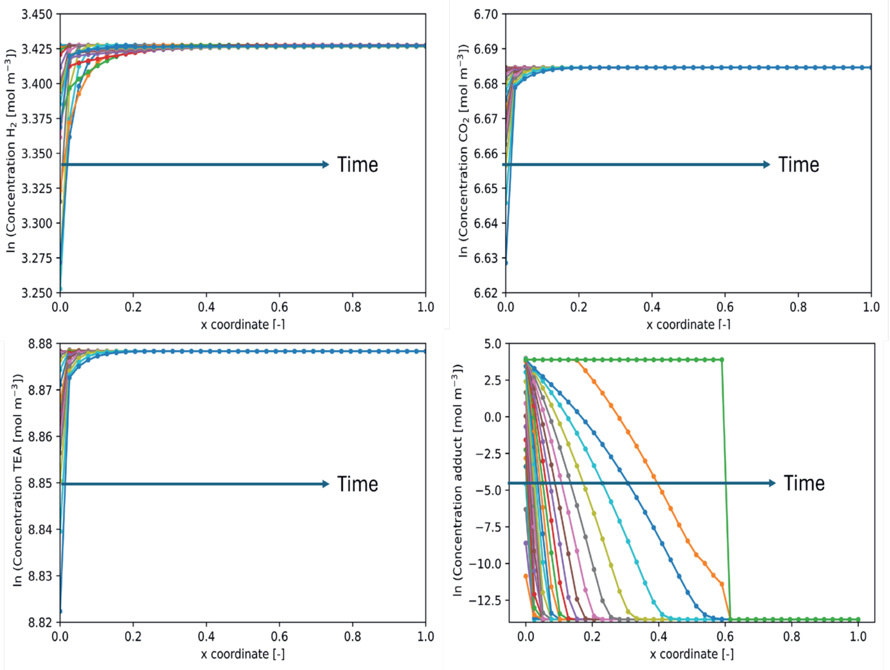

Figure 3.2: Temporal evolution of FA formation over multiple active sites using a 40x40 cell grid, representing 200x200 nm. Simulation conditions can be found in Table 3.3 (temperature of 50 degrees Celsius, 15 bar total pressure).

Figure 3.3 depicts the average adduct reaction rate and the thickness of the adduct layer formed around a single gold crystallite. The thickness of the layer was determined directly on top of the active gold site, in the y-direction, with a grid cell being part of the adduct layer if the formic acid concentration is > 0.1 mol/m^3. Here, initially a high formic acid formation rate of 0.067 mol/s is observed, followed by a rapid decline until the production rate of formic acid is decreased to nearly zero (0.0002 mol/s). While the observed reaction rate is close to zero, Figure 3.2 reveals that the reagents (CO_2, H_2 and triethylamine) are not depleted but present at the active site close to saturation concentrations.

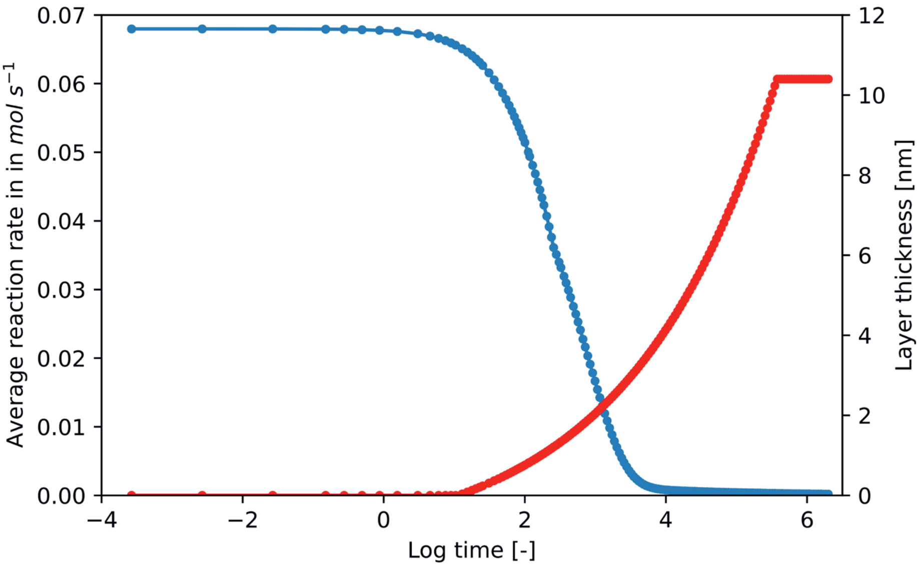

Figure 3.3: Average adduct reaction rate and adduct layer thickness over a single active site.

Therefore, the net zero production rate is not caused by diffusion limitations or unavailability of the reagents at the active site, but by local equilibrium conditions being achieved around the active site, as evident from the equal forward and backward reaction rates, which are equal to ~0.008 mol/s.

As evident from Figure 3.3, the thickness of the adduct layer follows an opposite trend to the adduct production rate, with the adduct concentration within the bulk fluid remaining equal to zero during the initial highly reactive period. After approximately 10 seconds, the decrease in formic acid production rates corresponds with the moment the formed adduct starts to diffuse away from the active site to form a layer around the active site, with the layer thickness growing up to 10.6 nm. The slow diffusion rate of the product away from the active site is also evident from the diffusivity of the adduct within the neat amine phase, which is found to be equal to 6.63e-12, compared to ~8.49e-9 for the gaseous reagents within the neat amine phase. Thus, the inability of the product to diffuse away from the active sites results in a local equilibrium condition forming around the active site, thereby reducing the average reaction rate to zero.

Simulations were also performed for larger catalyst pores. The temporal evolution of a larger catalyst pore is shown in Figure B8. Upon expending the pore size to 200 nm and placing 4 evenly spaced active sites on each side of the catalyst pore, the trends observed for the single active site are also observed for the larger pore. Here, despite a larger adduct productivity capacity due to the presence of multiple active sites, only a thin layer of adduct is formed around the active sites before reducing the average reaction rate to nearly zero due to the inability of the product to diffuse towards the bulk phase and therefore locally reaching the equilibrium condition. These numerical observations show comparable behavior to the experimental observations, in which formic acid was observed to be present within the catalyst pores, but not in the bulk reaction fluid.

3.5 Conclusion

Solventless batch experiments at elevated pressures were performed to gain insights into the performance of using triethylamine as an extraction base during the direct hydrogenation of CO_2 to formic acid.

After several hours of reaction, no formic acid was observed within the bulk liquid of the batch experiments. Due to the biphasic nature of formic acid – triethylamine systems, the formic acid concentration within the catalyst pores after reaction was evaluated by placing the spent catalyst in water. Here, the total molar amount of formic acid in the pores being orders of magnitude larger than those in the reactor fluid.

In order to investigate this at pore level, a 2D model describing spinodal decomposition was created and verified in C++. Here, the Cahn – Hilliard equation was used to describe the temporal evolution of spinodal decomposition through describing the Helmholtz free energy as a function of composition and the spatial derivative of the composition at the grid point.

The biphasic nature of the tertiary alkylamine – formic acid system was found to have significant implications for the reaction performance of the proposed system. The inability of the adduct to dissolve in the available non-binding amine results in the catalyst pores readily reaching the equilibrium condition, therefore reducing the average reaction rate by two orders of magnitude, from 0.067 to 0.0002 mol/s.

Appendix B

B.1 Density and viscosity measurements

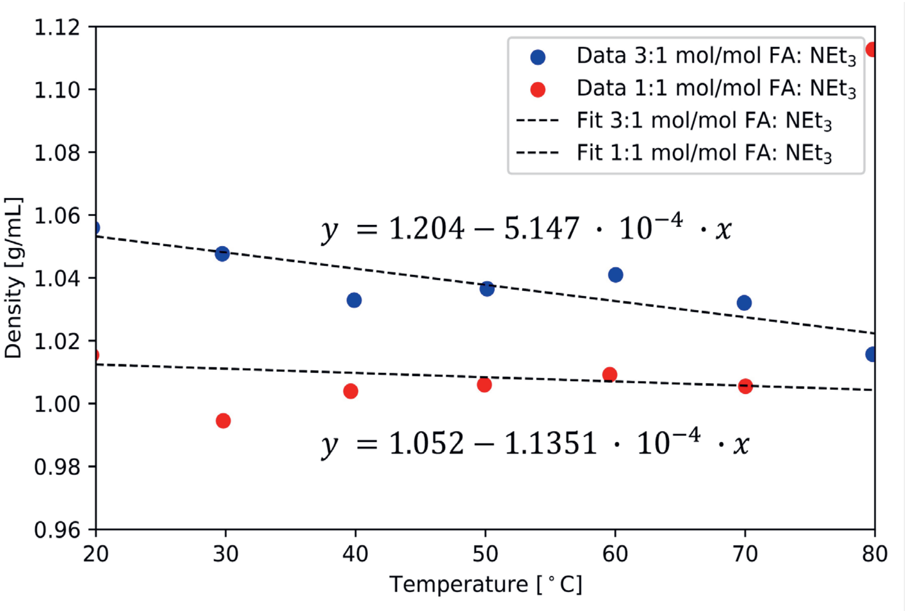

Figure B1: Density measurements as a function of temperature for a 1:1 FA:NEt$_3$ molar adduct and 3:1 FA:NEt$_3$ molar adduct.

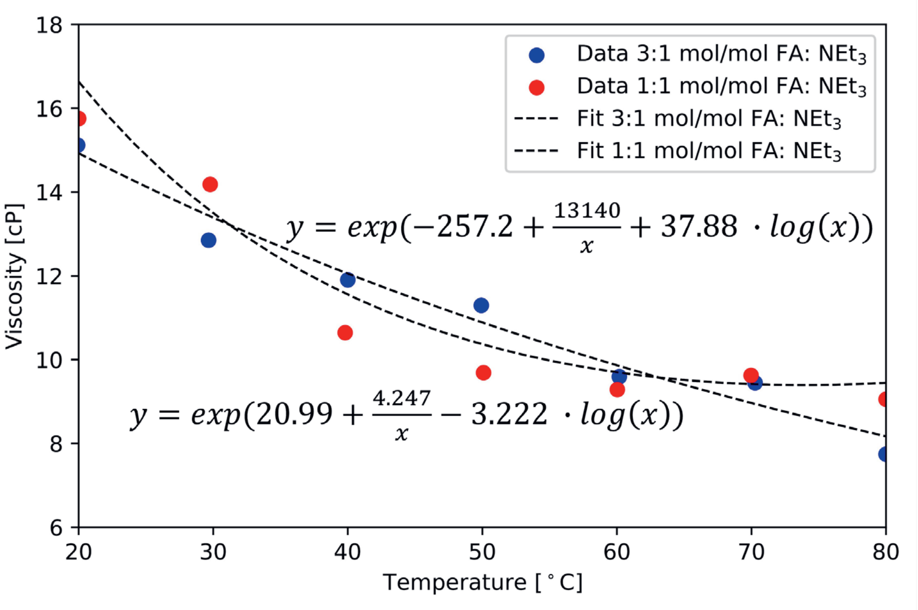

Figure B2: Viscosity measurements as a function of temperature for a 1:1 FA:NEt$_3$ molar adduct and 3:1 FA:NEt$_3$ molar adduct

B.2 Molecular properties

	M [g/mol]	V [Å^3/molecule]	r [Å^3/molecule]	Source
H_2	2.016	10.495	1.358	[1]
CO_2	44.01	32.713	1.984	[1]
HCO_2H	46.03	37.762	2.082	[1]
NEt_3	101.19	123.36	3.089	[2]
Adduct	170.235	287.32	4.094	This work

Table B1: Overview of molar weights, volumes and radii of reactants

Component	H_2	CO_2	NEt_3	NEt_3
H_2	$6.38 \cdot 10^{-9}$	$6.38 \cdot 10^{-9}$	$6.38 \cdot 10^{-9}$	$1.68 \cdot 10^{-11}$
CO_2	$6.38 \cdot 10^{-9}$	$4.37 \cdot 10^{-9}$	$4.37 \cdot 10^{-9}$	$1.15 \cdot 10^{-11}$
NEt_3	$6.38 \cdot 10^{-9}$	$4.37 \cdot 10^{-9}$	$2.80 \cdot 10^{-9}$	$7.38 \cdot 10^{-12}$
NEt_3	$1.68 \cdot 10^{-11}$	$1.15 \cdot 10^{-11}$	$7.38 \cdot 10^{-12}$	$5.57 \cdot 10^{-12}$

Table B2: Matrix of binary diffusion coefficients in m^2/s. Diffusion coefficients were calculated using equation 3.15 and the data given in Table B1.

B.3 Model verification and validation

The validation of the models is performed by validating each key ingredient. First, the implementation of the temporal and spatial discretization schemes is verified through the analytical solution for unsteady Fickian diffusion in 1D. Secondly, proof-of-concept simulations were performed in 1D and 2D to validate the Cahn-Hilliard equation implementation. Here, the interaction parameter and solvency parameter were chosen such to represent a system undergoing spinodal decomposition.

To verify the implementation of the numerical discretization schemes, let us consider an infinitely long flat plate of thickness 2L with a homogeneous initial concentration as an elementary verification case. At outer ends of the plate (-L and L), a constant concentration is applied (Dirichlet boundary condition), while a Neumann boundary condition is enforced at the center of the plate. The unsteady analytical solution to this problem was previously derived by [3]. A comparison between the analytical solution and the solution obtained numerically is shown in Figure B3. Here, an absolute error of maximum 1e^{-3} mol/m^3 is found when using 100 grid cells.

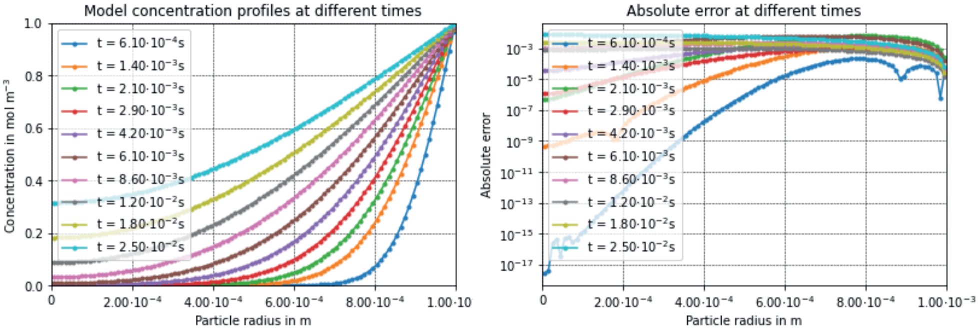

Figure B3: left) Model solution of 1D Fickian diffusion in a flat plate using a 100x1 grid. The analytical solution was taken from [7]. Right) absolute error between analytical and model solutions.

To test the qualitative implementation of the phase field model, the equations presented in Section 3.3.2 were rewritten to allow for freely chosen interaction parameters (the interface parameter and the solvency parameter). Here, a closed system is considered with no flux at the simulation boundaries. The system is initialized using 2 components with a binary diffusion coefficient of 1, no reaction and the concentrations to form a linear gradient over the grid. The solvency parameter was set to 3 to invoke spinodal decomposition, and the interface parameter was set to -0.5, with the obtained concentration profiles shown in Figure B4.

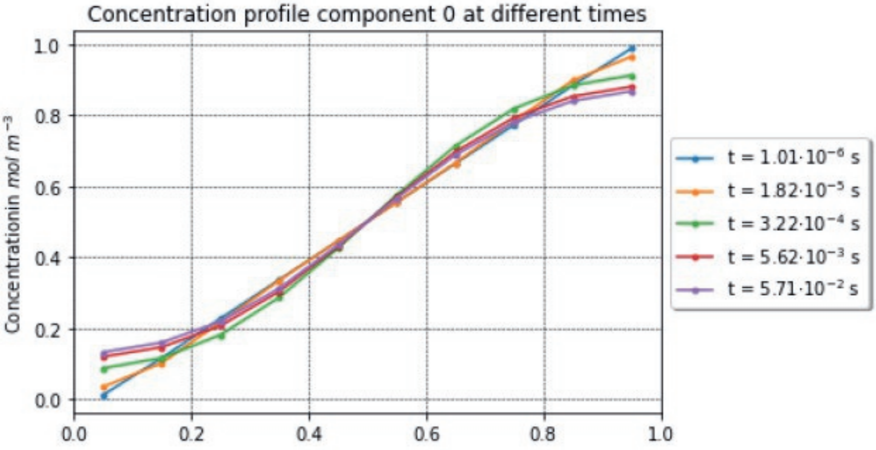

Figure B4: Temporal evolution of a 1D simulation of 2 components for a system having a solvency parameter of 3 and interface parameter of -0.5. Concentrations were initialized having a linear profile, and the grid was divided into 10 grid cells

Figure B4 reveals the expected demixing of the system, with a smooth and continuous tangent hyperbolic curve at the interface. This hyperbolic curve was previously shown in the original works of Cahn and Hilliard [3]-[5].

Next, the domain size is decreased to 0.1 and the interface parameter set to 0.5 while keeping all other parameters constant. From Figure 3, it is observed that the initialized linear profile readily mixes into a flat homogeneous profile even below the critical temperature because the domain size is smaller than the interface parameter.

Repeating these simulations at domain sizes above the interface parameter, a gradient in concentration is observed instead due to non-homogeneous mixing instead of the homogeneous profiles observed in Figure B4, as shown in Figure B5a. Lastly, a simulation is performed in which a homogeneous concentration profile is initialized subject to a stochastic noise in concentration (Figure B5b).

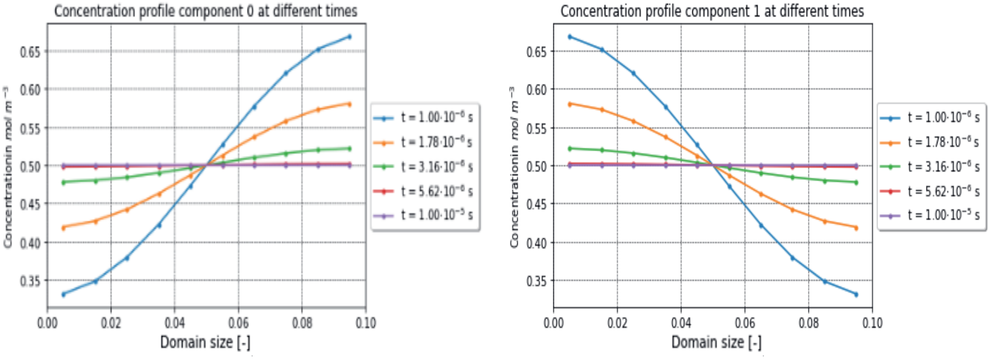

Figure B5: Temporal evolution of a 1D simulation of 2 components for a system having a solvency parameter of 3 and interface parameter of 0.5. Concentrations were initialized having a linear profile, and the grid was divided into 10 grid cells. The domain size is smaller than the interface parameter

Here spinodal decomposition is observed, resulting in the formation of domains of component 0. The formation of domains is inherent to one-dimensional systems as the formation of 2 separate phases would involve the diffusion of component 0 through component 1 rich domains. Hence, a meta-stable system is formed, as previously described by [6].

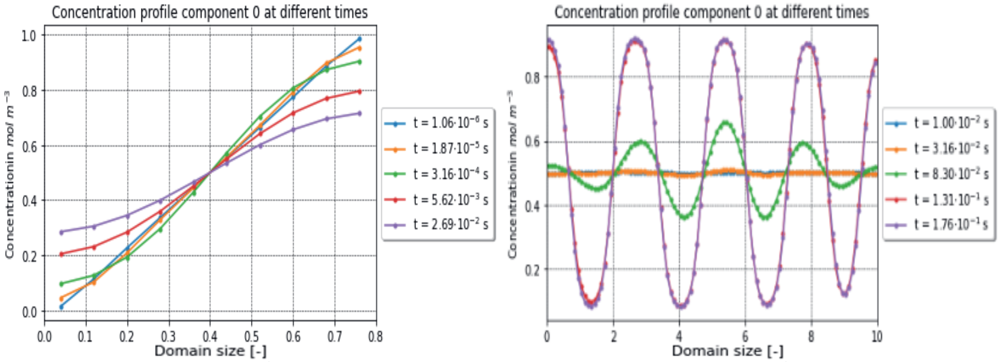

Figure B6: Temporal evolution of a 1D simulation of 2 components for a system having a solvency parameter of 3 and interface parameter of 0.5, and discretized into 10 grid cells . left) Concentrations were initialized having a linear profile. The domain size is larger than the interface parameter. Right) Concentrations were initialized having a homogeneous profile subjected to a stochastic noise of 2%.

A two-dimensional simulation was performed on a 50 x 50 grid in which random perturbations of 0.05 mol/m^3 were applied to an initial concentration of 0.5 mol/m^3 in order to supply a driving force for spinodal decomposition. The solvency parameter was set to 3, while the interface parameter was set to -0.02. The temporal evolution as shown in Figure 3.5 initially reveals the formation of droplets. Subsequently, these droplets are merging and agglomerating, resulting in the formation of larger structures. Through the agglomeration, the interfacial area is minimized and thus the surface energy. When simulated for sufficiently long times, the structures will develop into two separate phases.

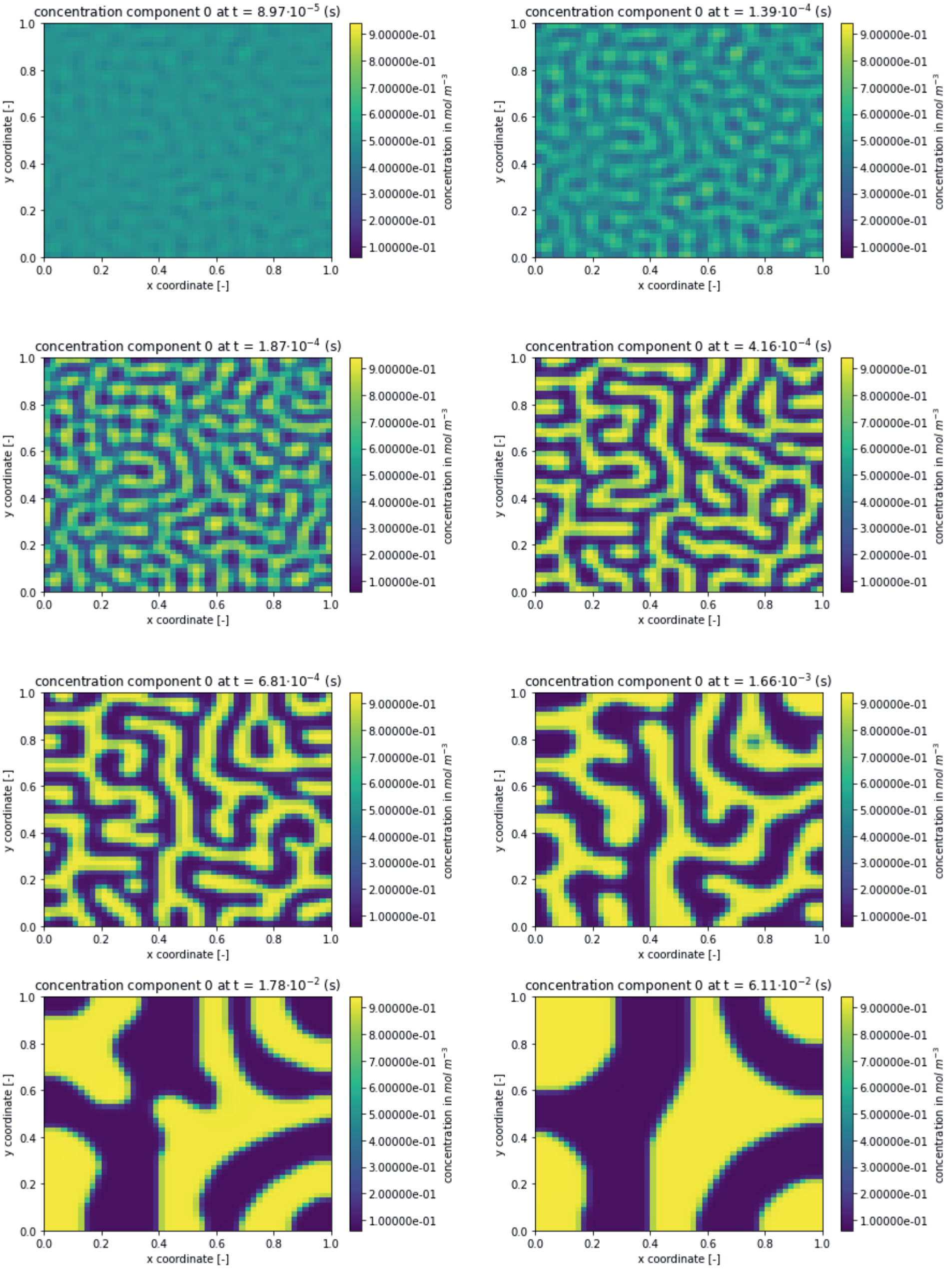

concentration component 0 at t = $8.97 \cdot 10^{-5}$ (s)

concentration component 0 at t = $1.39 \cdot 10^{-4}$ (s)

concentration component 0 at t = $1.87 \cdot 10^{-4}$ (s)

concentration component 0 at t = $4.16 \cdot 10^{-4}$ (s)

concentration component 0 at t = $6.81 \cdot 10^{-4}$ (s)

concentration component 0 at t = $1.66 \cdot 10^{-3}$ (s)

concentration component 0 at t = $1.78 \cdot 10^{-2}$ (s)

concentration component 0 at t = $6.11 \cdot 10^{-2}$ (s)

Figure B7: Temporal evolution of 2D spinodal decomposition from randomly initialized concentration profiles on a 50 x 50 grid. Solvency parameter = 3, interfacial parameter = -0.02, noise of 2%.

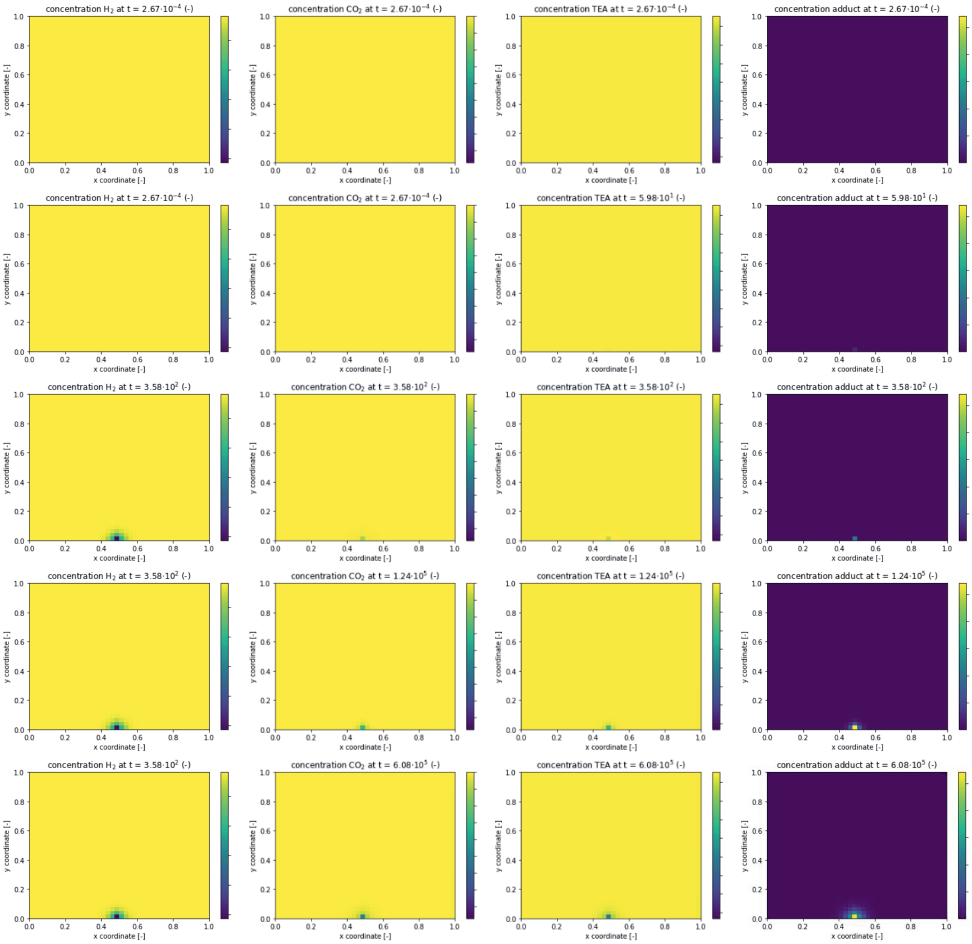

Figure B8: Temporal evolution of FA formation over a single active site using a 40x40 cell grid, representing 80x80 nm. Simulation conditions can be found in Table 3.3 (temperature of 50 degrees Celsius, 15 bar total pressure)

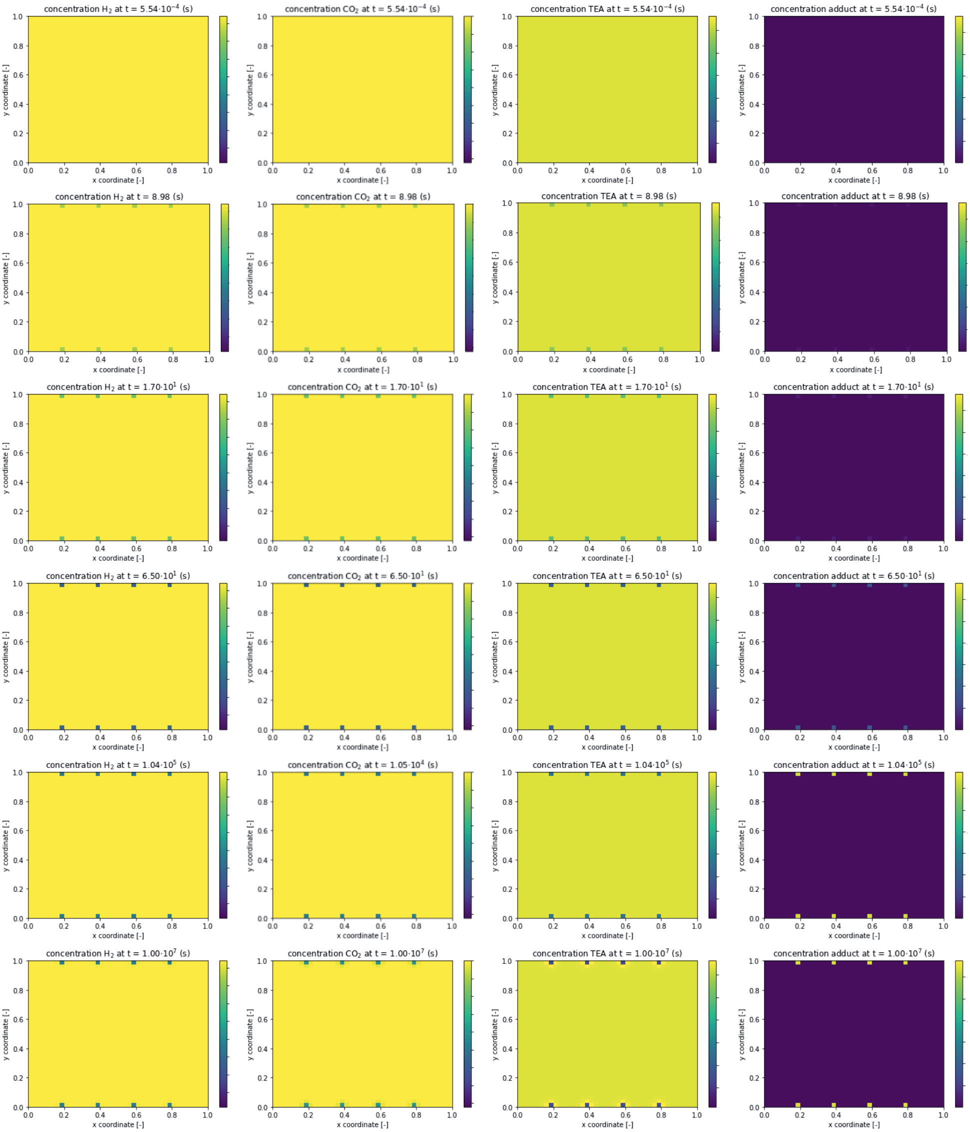

Figure B9: Temporal evolution of FA formation over multiple active sites using a 40x40 cell grid, representing 200x200 nm. Simulation conditions can be found in Table 3.3 (temperature of 50 degrees Celsius, 15 bar total pressure)

B.4 References Appendix B

[1] Brigham Young University, “Sample Database - DIPPR801.” https://dippr.aiche.org/SampleD (accessed Aug. 11, 2024).

[2] Y. H. Zhao, M. H. Abraham, and A. M. Zissimos, “Fast calculation of van der Waals volume as a sum of atomic and bond contributions and its application to drug compounds,” *J. Org. Chem.*, vol. 68, no. 19, pp. 7368–7373, 2003, doi: 10.1021/jo034808o.

[3] J. W. Cahn, “Phase separation by spinodal decomposition in isotropic systems,” *J. Chem. Phys.*, vol. 42, no. 1, pp. 93–99, 1965, doi: 10.1063/1.1695731.

[4] D. N. Bhate, A. Kumar, and A. F. Bower, “Diffuse interface model for electromigration and stress voiding,” *J. Appl. Phys.*, vol. 87, no. 4, pp. 1712–1721, 2000, doi: 10.1063/1.372082.

[5] J. W. Cahn and J. E. Hilliard, “Free energy of a nonuniform system. III. Nucleation in a two-component incompressible fluid,” *J. Chem. Phys.*, vol. 31, no. 3, pp. 688–699, 1959, doi: 10.1063/1.1730447.

[6] S. Scholtes and M. G. Westdickenberg, “Metastability of the Cahn–Hilliard equation in one space dimension,” *J. Differ. Equ.*, vol. 265, no. 4, pp. 1528–1575, 2018, doi: 10.1016/j.jde.2018.04.012.

[7] Byron Bird, Warren E. Stewart, *Transport Phenomena*, 2nd ed. 2007.

References

[1] R. Sun *et al.*, “Heterogeneous catalysts for CO2hydrogenation to formic acid/formate: From nanoscale to single atom,” *Energy Environ. Sci.*, vol. 14, no. 3, pp. 1247–1285, 2021, doi: 10.1039/d0ee03575k.

[2] M. Cokoja, C. Bruckmeier, B. Rieger, W. A. Herrmann, and F. E. Kühn, “Transformation of carbon dioxide with homogeneous transition-metal catalysts: A molecular solution to a global challenge?,” *Angew. Chemie - Int. Ed.*, vol. 50, no. 37, pp. 8510–8537, 2011, doi: 10.1002/anie.201102010.

[3] S. Kushwaha, J. Parthiban, and S. K. Singh, “Recent Developments in Reversible CO2 Hydrogenation and Formic Acid Dehydrogenation over Molecular Catalysts,” *ACS Omega*, vol. 8, no. 42, pp. 38773–38793, 2023, doi: 10.1021/acsomega.3c05286.

[4] J. Vansant, *Carbon Dioxide Emission and Merchant Market in the European Union*. 2003.

[5] IPCC, *1.5°C Global Warming CH4: Strengthening and Implementing the Global Response*. 2022.

[6] Intergovernmental Panel on Climate Change, Climate Change 2022: Mitigation of Climate Change *Technical Summary*. 2022.

[7] S. Moret, P. J. Dyson, and G. Laurenczy, “Direct synthesis of formic acid from carbon dioxide by hydrogenation in acidic media,” *Nat. Commun.*, vol. 5, pp. 1–7, 2014, doi: 10.1038/ncomms5017.

[8] M. Scott, B. Blas Molinos, C. Westhues, G. Franciò, and W. Leitner, “Aqueous Biphasic Systems for the Synthesis of Formates by Catalytic CO2 Hydrogenation: Integrated Reaction and Catalyst Separation for CO2-Scrubbing Solutions,” *ChemSusChem*, vol. 10, no. 6, pp. 1085–1093, 2017,

doi: 10.1002/cssc.201601814.

[9] A. Rosas-Hernández, C. Steinlechner, H. Junge, and M. Beller, *Chemical Transformations of Carbon Dioxide*. 2017.

[10] C. Kim *et al.*, “Accelerating the net-zero economy with CO2-hydrogenated formic acid production: Process development and pilot plant demonstration,” *Joule*, vol. 8, no. 3, pp. 693–713, 2024, doi: 10.1016/j.joule.2024.01.003.

[11] M. Pérez-Fortes, J. C. Schöneberger, A. Boulamanti, G. Harrison, and E. Tzimas, “Formic acid synthesis using CO2 as raw material: Techno-economic and environmental evaluation and market potential,” *Int. J. Hydrogen Energy*, vol. 41, no. 37, pp. 16444–16462, 2016, doi: 10.1016/j.ijhydene.2016.05.199.

[12] M. Byun, A. Lee, S. Cheon, H. Kim, and H. Lim, “Preliminary feasibility study for hydrogen storage using several promising liquid organic hydrogen carriers: Technical, economic, and environmental perspectives,” *Energy Convers. Manag.*, vol. 268, no. June, p. 116001, 2022, doi: 10.1016/j.enconman.2022.116001.

[13] D. D. Papadias, J. K. Peng, and R. K. Ahluwalia, “Hydrogen carriers: Production, transmission, decomposition, and storage,” *Int. J. Hydrogen Energy*, vol. 46, no. 47, pp. 24169–24189, 2021, doi: 10.1016/j.ijhydene.2021.05.002.

[14] J. Eppinger and K. W. Huang, “Formic Acid as a Hydrogen Energy Carrier,” *ACS Energy Lett.*, vol. 2, no. 1, pp. 188–195, 2017, doi: 10.1021/acsenergylett.6b00574.

[15] J. O. M. Bockris, “The hydrogen economy: Its history,” *Int. J. Hydrogen Energy*, vol. 38, no. 6, pp. 2579–2588, 2013, doi: 10.1016/j.ijhydene.2012.12.026.

[16] G. H. Gunasekar, K. Park, K. D. Jung, and S. Yoon, “Recent developments in the catalytic hydrogenation of CO2 to formic acid/formate using heterogeneous catalysts,” *Inorg. Chem. Front.*, vol. 3, no. 7, pp. 882–895, 2016, doi: 10.1039/c5qi00231a.

[17] A. Álvarez *et al.*, “Challenges in the Greener Production of Formates/Formic Acid, Methanol, and DME by Heterogeneously Catalyzed CO2 Hydrogenation Processes,” *Chem. Rev.*, vol. 117, no. 14, pp. 9804–9838, 2017, doi: 10.1021/acs.chemrev.6b00816.

[18] R. Tanaka, M. Yamashita, L. W. Chung, K. Morokuma, and K. Nozaki, “Mechanistic studies on the reversible hydrogenation of carbon dioxide catalyzed by an Ir-PNP complex,” *Organometallics*, vol. 30, no. 24, pp. 6742–6750, 2011, doi: 10.1021/om2010172.

[19] T. Schaub and R. A. Paciello, “A process for the synthesis of formic acid by CO2 hydrogenation: Thermodynamic aspects and the role of CO,” *Angew. Chemie - Int. Ed.*, vol. 50, no. 32, pp. 7278–7282, 2011, doi: 10.1002/anie.201101292.

[20] D. Preti, C. Resta, S. Squarcialupi, and G. Fachinetti, “Carbon dioxide hydrogenation to formic acid by using a heterogeneous gold catalyst,” *Angew. Chemie - Int. Ed.*, vol. 50, no. 52, pp. 12551–12554, 2011, doi: 10.1002/anie.201105481.

[21] G. A. Filonenko, W. L. Vrijburg, E. J. M. Hensen, and E. A. Pidko, “On the activity of supported Au catalysts in the liquid phase hydrogenation of CO2 to formates,” *J. Catal.*, vol. 343, pp. 97–105, 2016, doi: 10.1016/j.jcat.2015.10.002.

[22] A.W.N. de Leeuw den Bouter, E.J.M. Vogels, L.Brito , A. Miquelot, P.Olivier,

J.van der Schaaf “Chemical and phase equilibrium of formic acid – trialkylamine complexes,” *Unde review in ACS Omega.*

[23] S. P. Clavijo, A. F. Sarmiento, L. F. R. Espath, L. Dalcin, A. M. A. Cortes, and V. M. Calo, “Reactive [n]-species Cahn–Hilliard system: A thermodynamically-consistent model for reversible chemical reactions,” *J. Comput. Appl. Math.*, vol. 350, no. October, pp. 143–154, 2019, doi: 10.1016/j.cam.2018.10.007.

[24] M. Honjo and Y. Saito, “Numerical simulation of phase separation in Fe-Cr binary and Fe-Cr-Mo ternary alloys with use of the Cahn-Hilliard equation,” *ISIJ Int.*, vol. 40, no. 9, pp. 914–919, 2000, doi: 10.2355/isijinternational.40.914.

[25] D. N. Bhate, A. Kumar, and A. F. Bower, “Diffuse interface model for electromigration and stress voiding,” *J. Appl. Phys.*, vol. 87, no. 4, pp. 1712–1721, 2000, doi: 10.1063/1.372082.

[26] Q. Du, C. Liu, and X. Wang, “Simulating the deformation of vesicle membranes under elastic bending energy in three dimensions,” *J. Comput. Phys.*, vol. 212, no. 2, pp. 757–777, 2006, doi: 10.1016/j.jcp.2005.07.020.

[27] J. J. Christensen, K. Elder, and H. C. Fogedby, “Phase segregation dynamics of a chemically reactive binary mixture,” *Phys. Rev. E - Stat. Physics, Plasmas, Fluids, Relat. Interdiscip. Top.*, vol. 54, no. 3, pp. 2212–2215, 1996, doi: 10.1103/PhysRevE.54.R2212.

[28] N. Moelans, B. Blanpain, and P. Wollants, “An introduction to phase-field modeling of microstructure evolution,” *Calphad Comput. Coupling Phase Diagrams Thermochem.*, vol. 32, no. 2, pp. 268–294, 2008, doi: 10.1016/j.calphad.2007.11.003.

[29] H. Gómez, V. M. Calo, Y. Bazilevs, and T. J. R. Hughes, “Isogeometric analysis of the Cahn-Hilliard phase-field model,” *Comput. Methods Appl. Mech. Eng.*, vol. 197, no. 49–50, pp. 4333–4352, 2008, doi: 10.1016/j.cma.2008.05.003.

[30] J. W. Cahn, “Phase separation by spinodal decomposition in isotropic systems,” *J. Chem. Phys.*, vol. 42, no. 1, pp. 93–99, 1965, doi: 10.1063/1.1695731.

[31] J. W. Cahn and J. E. Hilliard, “Free energy of a nonuniform system. III. Nucleation in a two-component incompressible fluid,” *J. Chem. Phys.*, vol. 31, no. 3, pp. 688–699, 1959, doi: 10.1063/1.1730447.

[32] J. W. Cahn, “Free energy of a nonuniform system. II. Thermodynamic basis,” *J. Chem. Phys.*, vol. 30, no. 5, pp. 1121–1124, 1959, doi: 10.1063/1.1730145.

[33] J. W. Cahn and J. E. Hilliard, “Free energy of a nonuniform system. I. Interfacial free energy,” *J. Chem. Phys.*, vol. 28, no. 2, pp. 258–267, 1958, doi: 10.1063/1.1744102.

[34] S. P. Clavijo, L. Espath, and V. M. Calo, “Extended Larché–Cahn framework for reactive Cahn–Hilliard multicomponent systems,” *Contin. Mech. Thermodyn.*, vol. 33, no. 6, pp. 2391–2410, 2021, doi: 10.1007/s00161-021-01045-9.

[35] P.Atkins, *Physical chemistry*, 10th ed. 2017.

[36] V. Blickle, T. Speck, C. Lutz, U. Seifert, and C. Bechinger, “Einstein relation generalized to nonequilibrium,” *Phys. Rev. Lett.*, vol. 98, no. 21, pp. 1–4, 2007, doi: 10.1103/PhysRevLett.98.210601.

[37] A. Einstein, “Über die von der molekularkinetischen Theorie der Wärme

geforderte Bewegung von in ruhenden Flüssigkeiten suspendierten Teilchen," *Ann. Phys.*, vol. 322, no. 8, pp. 549–560, 1905, doi: 10.1002/andp.19053220806.

[38] A. C. Hindmarsh *et al.*, "SUNDIALS: Suite of nonlinear and differential/algebraic equation solvers," *ACM Trans. Math. Softw.*, vol. 31, no. 3, pp. 363–396, 2005, doi: 10.1145/1089014.1089020.

[39] D. J. Gardner, D. R. Reynolds, C. S. Woodward, and C. J. Balos, "Enabling New Flexibility in the SUNDIALS Suite of Nonlinear and Differential/Algebraic Equation Solvers," *ACM Trans. Math. Softw.*, vol. 48, no. 3, 2022, doi: 10.1145/3539801.

[40] J. Kim, K. Kang, and J. Lowengrub, "Conservative Multigrid Methods for Ternary Cahn-Hilliard Systems*," *Commun. Math. Sci.*, vol. 2, no. 1, pp. 53–77, 2004, doi: 10.4310/CMS.2004.v2.n1.a4.

[41] L. M. J. Sprakel and B. Schuur, "Solvent developments for liquid-liquid extraction of carboxylic acids in perspective," *Sep. Purif. Technol.*, vol. 211, no. June 2018, pp. 935–957, 2019, doi: 10.1016/j.seppur.2018.10.023.

[42] NIST center for neuron research, "Reference tables." https://www.nist.gov/ncnr/sample-environment/sample-mounting/reference-tables (accessed Apr. 05, 2024).

4

Effect of tertiary amine selection on CO_2 to formic acid hydrogenation with Au-np catalyst

This chapter is based on the following publication:

A.W.N. de Leeuw den Bouter, L.M.P. Meijer, L.Brito , A. Miquelot, P.Olivier,J. van der Schaaf, “Effect of tertiary amine selection on CO_2 to formic acid hydrogenation with Au-np catalyst”, under review in Industrial & Engineering Chemistry Research

Abstract

The influence of the tertiary amine on CO_2 conversion and product selectivity is experimentally studied in batch and packed bed reactors using a Au/TiO_2 catalyst. A wide range of tertiary amines were selected, based on their boiling point, kinetic diameter, pKa and solubility with alcohol-based solvents and formic acid. Following these criteria, 15 amines were selected having a wide range of pKa values and molecule sizes. To allow for an initial screening of kinetic rates, formic acid decomposition reactions were performed in batch reactors using an Au/TiO_2 catalyst. Following the selection of the most promising amines in terms of CO_2 conversion rates, high pressure fixed bed experiments were executed.

Steric hindrance and the pKa of the tertiary amine were identified as key parameters influencing both the observed kinetic rates as well as the CO_2 conversion. The usage of solventless polar amines such as diethylethanolamine allowed for FA productivity up to 5x that of the benchmark triethylamine system. Catalyst deactivation of the Au/TiO_2 catalyst was observed for all amines studied within this work, and the deactivation mechanism was shown to be sintering of the Au nanoparticles with no significant leaching, morphological changes or oxidation of the Au species observed.

4.1 Introduction

Several strategies have been investigated to perform the reaction under base-free, neutral circumstances [27][31]–[34]. Common strategies include the usage of ionic liquids as solvents/buffers [27][34] and the immobilization of amines or ionic liquids onto solid carries [31][32][34], often combined with active hydrogenation metals [35][36]. Typically, such systems operate under high H_2 and CO_2 partial pressures resulting in supercritical conditions [37] and the total system activity obtained is significantly lower compared to basic conditions [31].

While the economic competitiveness of the direct hydrogenation reaction performed under basic condition is currently hampered by the challenging and energy-intensive separation [28], the TOFs obtained are significantly higher compared to base free systems [32]. Previous works have shown the employed tertiary amine to be of significant influence on the observed kinetic rates [25][31][41]. Loges *et al.* have studied the influence of the tertiary amine performing the formic acid decomposition reaction on 5/2 molar ratio adducts using a homogeneously catalyzed batch process. TOFs up to 445 h^{-1} were observed after 2 hours using asymmetrical tertiary amines such as dimethyloctylamine at 40 ºC [39]. Cao *et al.* performed a similar study, revealing promising results using a heterogeneous gold supported on amphoteric zirconia catalyst showing a TOF up to 1166 h^{-1} for a FA-dimethylethanolamine system at 60 ºC [23]. Recently, Lee *et al.* studied the hydrogenation of CO_2 towards formic acid as a reactive CO_2 capture process based on the formation of bicarbonates using water as solvent under supercritical conditions. Based on a heterogeneous Ru/bpyTNCTF catalyst, formic acid production was performed in a batch reactor, showing clear correlation between the pKa of the amine, steric hindrance and CO_2 conversion rates [38].

Within Chapter 3 it was shown that the inability of formic acid – tertiary amine adduct to dissolve in free amine results in formic acid remaining confined in the catalyst pores. This rapidly leads to the formation of a local equilibrium with 100x lower productivity. Consequently, a solvent is required to overcome the adduct insolubility. Within this work, 1-decanol is used as a solvent for all trialkylamines studied.

Triethylamine was regarded as the state-of-the-art amine due to numerous works reporting promising results [15][28], and thus used as a reference. However, triethylamine has been shown to form a stable azeotrope with formic acid at 27 mol% formic acid [30], rendering direct thermal splitting intractable. While low-boiling tertiary amines such as triethylamine result in azeotrope formation, longer hydrocarbon chain length amines such as trihexylamine do not [25].

In order to overcome the limitations posed by the employment of low boiling tertiary amines, this work aims to study the influence of the nature of the tertiary amine used to shift the equilibrium to the product side on CO_2 conversion rates and product selectivity using alcohol based solvents in non-supercritical conditions.

In Chapter 2, it was revealed that the formic acid binding capacity of tertiary amines is virtually independent of the hydrocarbon chain length [42]. Therefore, allowing for the usage of a wide variety of tertiary amines. Amines were selected based on their boiling point, steric hindrance, pKa and solubility with alcohol-based solvents and formic acid. Following these criteria, 15 amines were selected having a wide range of pKa values and molecule sizes. To allow for an initial screening of kinetic rates, the much faster formic acid decomposition reactions was performed in a batch reactor using an Au/TiO_2 catalyst. Following the selection of the most promising amines in terms of FA conversion rates, high pressure fixed bed experiments were executed for the CO_2 hydrogenation.

4.2 Experimental materials and methods

4.2.1. Materials

Au/TiO_2 cylindrical catalyst pellets (AURO*lite*) were bought from Strem Chemicals, Inc. (1 wt.% Au, d_p = 2.6 nm). 1-Decanol (>98%), 2-diethylaminoethanol (99%) and 1-(n-butyl)imidazole (99%) from Thermo Scientific Chemicals. Formic acid (>99%), Triethylamine (>99.5%), Methyldiethanolamine (> 99%), N-Methylimidazole (>99%), N-methylpiperidine (>99%), N,N-dimethylbenzylamine (>99%) and Tributylamine (>98.5%) from Sigma-Aldrich. Trihexylamine(> 95.0%), N,N-Dimethylbutylamine (>98.0%), N-N-dimethyloctylamine (>95%), 2-(Dimethylamino)ethanol (> 99.0%), 4-Dimethylamino-1-butanol (> 98.0%), 6-dimethylamino-1-hexanol (>98%) and 1-(3-dimethylaminophenyl)ethanol (>98%) from TCI Chemicals. Gasses (H_2 (5.0), CO_2 (4.5) and Ar (5.0)) were supplied by Linde Gas in bottles.

The chemicals used for H-NMR and ICP analysis were: acetonitrile-d_3, obtained from Thermo Scientific Chemicals (> 99 atom% D). Chloroform-d from Sigma-Aldrich (> 99.8 atom% D). 1,3,5-Trimethoxybenzene from TCI Chemicals (> 98.0%). Gold standard for ICP from Fluka TraceCERT Ultra (1002 ppm). Hydrofluoric acid EMSURE (48%), nitric acid (65%) EMPLURA (>99.9%) and hydrochloric acid (37%) a.c.s. reagent from Merck.

All materials were used as received, handled in air and used without any additional purification. In order to prevent catalyst deactivation, the catalyst was stored under Ar in a cold and dark environment.

4.2.2 Tertiary amine testing

Due to the slow kinetic nature of this reaction and the requirement of significant amounts of catalyst, it was opted to use the formic acid decomposition reaction as a screening tool on the basis of microscopic reversibility. To allow for an initial assessment of activity, formic acid decomposition reactions were performed in batch reactors using an Au/TiO_2 catalyst. Prior to reactive testing, the catalyst was reduced off-line at 423 K in 5 vol.% H_2 / He [40] at a total flowrate of 50 mLn/min. The catalyst was received in the form of extrudates, and thus subsequently crushed and sieved to a particle size of 150-250 µm.

Formic acid decomposition experiments were conducted in glass batch reactors. Since it was not possible to sample from these reactors without disturbing the equilibrium, 7 identical vials (N18, Machery-Nagel, 20ml, N18 magnetic screw caps) were prepared for each reaction. Each vial contained 10 ± 1 mg of Au/TiO_2 catalyst and 1 ml of reaction mixture. The results were normalized per catalyst mass. The reaction mixture consisted out of a tertiary amine, formic acid and, in case of non-polar tertiary amines, 1-decanol as solvent. The formic acid and amine concentration was 1 mol/liter, ensuring no unbound formic acid is present within the solution. In case of the OH-substituted amines, no solvents are required as these amines do not show biphasic behavior. The formic acid concentration was kept constant at 1 mol/liter, with the tertiary amine used for dilution.

The vials were prepared and subsequently put in an aluminum heating block and placed on a magnetic stirring hotplate (IKA RCT basic). The temperature was controlled using a PID controller (IKA ETS-D5). The heating block was thermally insulated using thermal insulation to prevent the formation of radial temperature profiles along the radial direction of the heating block. An image of the set-up can be found in Appendix C Figure 6.

CO_2 hydrogenation experiments were performed at elevated pressure in a stainless steel packed bed reactor, with a schematic overview given in Figure 4.1. The reactor consisted of ½” Swagelok VCR connections (internal diameter 10 mm) and a stainless steel tube with a total length of 10 cm. Metal gaskets with 5 µm pore size were used on either end to prevent the catalyst from flushing out of the reactor. The reactor was placed vertically, and packed using 1 mm glass beads and quartz wool above and below the catalyst bed to ensure proper liquid-solid contact. The catalyst bed consisted out of 2.5 grams Au/TiO_2 catalyst (125-180 µm), with no further dilution. The reactor was placed inside an electrical oven, with the temperature monitored using two PT-100 thermal probes, one placed at the beginning of the catalyst bed and one at the reactor outlet. Liquid was pumped using a syringe-pump (Teledyne ISCO 260D). The gas streams are controlled by Bronkhorst MFCs (EL-FLOW Prestige, F_{max} = 50 mL_n/min). To ensure proper gas – liquid mixing, the incoming streams are mixed in a T-piece prior to entering the reactor. The pressure was controlled by a Bronkhorst back pressure controller (EL-PRESS, F_{max} = 50 mL_n/min) . A condenser is placed after the reactor to liquefy any condensables, after which the gas and liquid were separated using a gas – liquid separator. Liquid samples were taken from a valve placed behind the cold trap. The gaseous reaction products were analyzed with a compact gas chromatograph (Global Analyser Solution) equipped with a TCD detector and two packed columns (Molsieve 5A and Rt-Q-BOND). The lower detection limit for CO was established to be 2 ppm. This lower detection limit was determined using calibration bottles supplied by Linde Gas. All reaction tests were performed at a residence time of 15 minutes (Liquid flowrate 1 mL/min, CO_2 flow rate 1 mL_n/min and H_2 flow rate 1 mL_n/min). As the desired product is present in the liquid phase, the liquid residence time τ is used and is calculated by:

$$\tau = \frac{V_r \, \varepsilon_L}{F_{v,liq}} \qquad 4.1$$

Here, V_r represents the total reactor volume, ε_L the liquid hold-up and $F_{v.liq}$ the liquid flow rate.

Liquid samples were analyzed using ^{1}H-NMR (Bruker, 400 MHz) to determine the chemical composition. Here, 0.5 mL of deuterated solvent (Acetonitrile-*d₃* or chloroform-*d*) and 1,3,5-trimethoxybenzene as internal standard was mixed with 0.1 mL of sample.

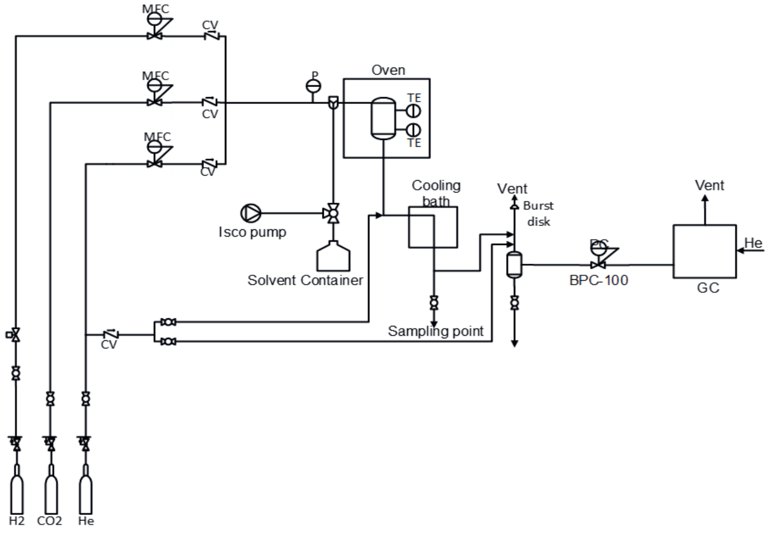

Figure 4.1 Schematic overview of the set-up used for CO_2 hydrogenation experiments. P, CV, MFC, TE and BPC indicate pressure transmitters, check valves, mass flow controller, PT-100 and back pressure controller respectively

4.2.3 Catalyst characterization

Transmission electron microscopy (TEM) images of fresh and spent catalysts were acquired using a FEI CryoTitan transmission electron microscope operating at 300 kV. HAADF-STEM was also acquired on the CryoTitan (300 kV) at room temperature. Samples were prepared by finely crushing the sample, followed by ultrasonic suspension in ethanol and dispersed over a Cu grid with holey carbon film. The particles were individually identified using the image software ImageJ and the particle size distribution of each catalyst sample was quantified accordingly.

CO pulse chemisorption was performed using a Micromeritics Autochem II 2920. First, the catalyst is dried and reduced at 300 degrees Celsius for 60 minutes under a 40 mL/min 10 vol.% H_2/Ar flow. During this time, the TCD signals are recorded to ensure full reduction. The H_2 is then purged using a He flow for 60 minutes. A temperature of -72 degrees Celsius was reached by submerging the U-shaped glass reaction in a dry ice-isopropanol slurry. For the pulse chemisorption, a 5 vol.% CO/He is utilized at a flowrate of 30 mL/min with a pulse time of 2 minutes. The pulsing is continued until a stable saturation is reached.

Inductively Coupled Plasma – Optical Emission Spectroscopy (ICP-OES; iCAP™ PRO ICP-OES; Thermo Scientific™) was used to obtain the Au concentrations of the fresh and spent catalysts. Samples were prepared by dissolution of 50 mg of catalyst in a mixture of concentrated HF (3 ml) and aqua regia (6 ml) at elevated temperatures. After digestion, the samples were filtered and diluted using double distilled water.

X-Ray Diffraction (XRD) was used for crystal phase identification in the 2θ range 10-120º with a Rigaku MiniFlex600 operating with a Ni β-filtered Cu-Kα radiant (40 kV, 30 mA). The scan rate was 0.05º/min. The diffraction peaks were identified using the JCPDS database.

X-ray photoelectron spectroscopy (XPS) samples were prepared by finely crushing the catalyst, following by drying *in vacuo* at 50 degrees Celsius. Measurements were performed using conventional ultrahigh vacuum XPS (Thermo Scientific K-Alpha, equipped with Al anode ((Al K_α=1,486.68 eV) monochromatized X-ray source). Samples were prepared by placing the finely crushed catalyst onto double sided carbon tape. Wide-range survey spectra were recorded using a 200 eV pass energy using 10 scans, while high-resolution core level spectra were measured using a 50 eV pass energy and 50 scans. The pressure inside the analysis chamber was kept below 8e^{-8} mbar at all times. Surface charging was prevented by using the flood gun (low energy Ar^+ ions). Energy referencing was performed using the adventitious carbon peak at 284.5 eV [44]-[46].

4.3 Results and discussion

The results obtained from the FA decomposition reaction are presented first, followed by a validation of using the decomposition reaction as a screening tool. The most promising amines were identified and studied for formic acid production in longer time-on-stream experiments in a high pressure fixed bed reactor. Lastly, the spent catalysts were studied using several solid state characterization techniques. The absence of internal and external mass transfer limitations was confirmed using the Mears and Weisz-Prater criteria. Example calculations are including in Appendix C.

4.3.1 Formic acid decomposition

In order to investigate the effect of the tertiary amine used as an extraction base, different formic acid decomposition experiments were carried out in glass batch reactors using Au/TiO_2 as catalyst at 50 ºC. An overview of the pKa and molar volume of all amines is given in Appendix C Table 1. Figure 2a reveals a significant effect of the aliphatic chain length with kinetic rates decreasing going from triethylamine to tributylamine to trihexylamine, with the FA conversion being almost negligible in the case of trihexylamine.

While previous works reported a significant dependency between activity and pKa [38], the difference between the pKa values of triethylamine (10.225) and trihexylamine (10.318) is negligible. Thus, this decrease in reactivity is likely caused by the bulky alkyl chains leading to kinetics effects.

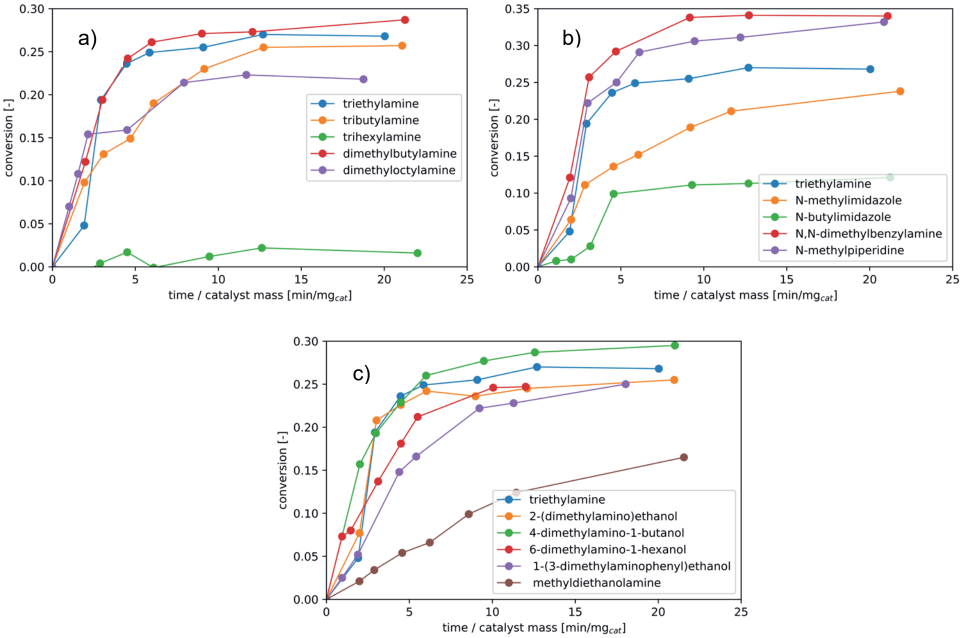

Figure 4.2: Formic acid conversion versus time for several types of amines in glass batch reactors (20 ml): straight chain trialkylamines (top left), cyclic trialkylamines (top right) and alcohol-group substituted trialkylamines (bottom). Conditions: 1:1 molar ratio FA:amine, with a total formic acid concentration of 1 mol/liter using either the alcohol amine or 1-decanol as diluent. Temperature was 50 degrees Celsius, catalyst: 10 mg Au/TiO_2. The total batch time is 4 hours.

To decrease the kinetic diameter of the tertiary amines and subsequently the kinetic effects, asymmetrical amines (Figure 4.2a) and cyclic amines (Figure 4.2b) were tested. Figure 4.2a reveals comparable performance in terms of CO_2 conversion and kinetic rates between triethylamine (pKa 10.225) and dimethylbutylamine (pKa 10.191). Extending the alkyl chain to dimethyloctylamine (pKa 10.200) results in a decrease in the observed FA conversion. Interestingly, while the reaction time required to reach the equilibrium conversion is comparable between all amines, the equilibrium conversion for the dimethyloctylamine is ~18% lower. The addition of bases to CO_2 hydrogenation reactions is known to result in an enthalpy driven process [27][41], with the equilibrium composition being a strong function of the protonation enthalpy gained by formic acid protonating the tertiary amine.

Three types of cyclic amines were tested, as shown in Figure 4.2b: piperidines (pKa

~10.1), imidazoles (pKa ~5.1) and cyclic tertiary amines (pKa ~9). Here, FA conversions and kinetics outperforming the benchmark triethylamine were observed for N-methylpiperidine and N,N-dimethylbenzylamine, imidazoles of several chain lengths result in significant decreases in performance. The pKa value of imidazoles is much lower than that of N-methylpiperidine and N,N-dimethylbenzylamine, leading to lower FA conversions. Similar to the case of the alkylamines, an increase in kinetic diameter caused by an extension of the alkyl chain of the imidazoles leads to a significant decrease in kinetic rates. These effects are visualized within Figure 4.3, where the TOF versus pKa is graphed for all alkyl- and cyclic amines. As an activation phase seems to be present for nearly all amines depicted in Figure 4.2, the TOF values were determined based on the time required to reach equilibrium.

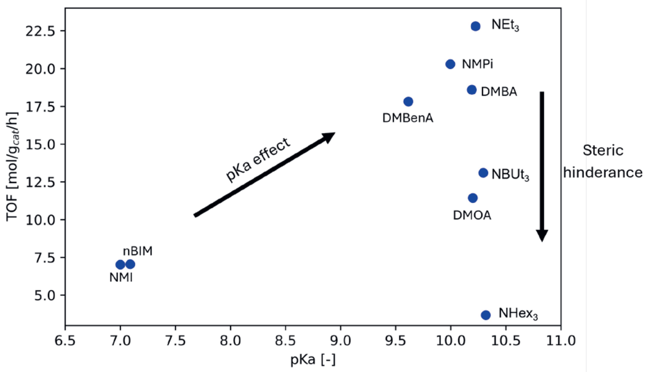

Figure 4.3: pKa versus TOF observed during FA decomposition over an Au/TiO_2 catalyst for trialkylamines and cyclic amines. NMI represents n-methylimidazole, nBIM n-butylimidazole, DMBenA dimethylbenzylamine, NMPi n-methylpiperidine, NEt_3 triethylamine, DMBA dimethylbutylamine, $NBut_3$ tributylamine, DMOA dimethyloctylamine and $NHex_3$ trihexylamine.

From Figure 4.3 two trends can be distinguished, namely an increase in TOF with an increase in pKa for amines of similar molar volume, and a significant decrease in TOF for amines of similar pKa but increasing molar volume. For symmetrical and asymmetrical amines, this trend is observed to be linear, as shown in Figure 4.4.

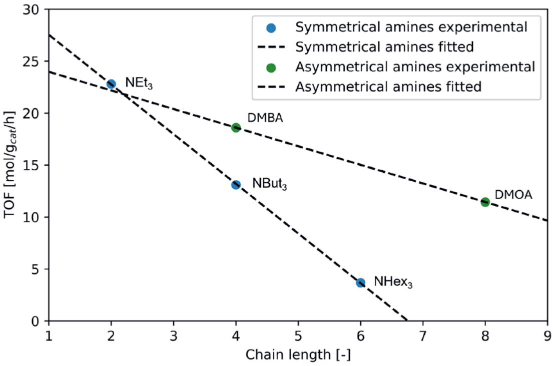

Figure 4.4: TOF versus alkyl tail length observed during FA decomposition over an Au/TiO_2 catalyst for trialkyl amines. NEt_3 represents triethylamine, $NBut_3$ tributylamine, $NHex_3$ trihexylamine, DMBA dimethylbutylamine, and DMOA dimethyloctylamine.

From Figure 4.4, it is found that the slope of the decrease in TOF with increasing hydrocarbon chain length is much less steep than is the case for symmetrical amines. This effect is most likely due to the decrease in volume of the bulky alkyl tails, thus reducing the degree of steric hindrance, of the amine, therefore allowing the formic acid – tertiary amine adducts to diffuse faster through the catalyst pores to reach the catalytic active site.

Filonenko *et al.* have previously shown the kinetic rate of CO_2 hydrogenation to formic acid to directly scale with the amine concentration in the reactor [13], while Schaub *et al.* [25] and de Leeuw den Bouter *et al.* [41] have demonstrated the necessity of polar solvents. Subsequently, it was hypothesized that the employment of polar tertiary amines could allow for the removal of additional solvents such as ethanol or 1-decanol and give rise to enhancement of the kinetic rates. Several OH-group substituted tertiary amines (2-(dimethylamino)ethanol, 6-dimethylamino-1-hexanol, methyldiethanolamine and triethanolamine) were mixed with formic acid in molar ratios ranging from 0.1 to 10. No phase separation was observed for any of the amines or at any molar ratio, thus allowing for the reaction to proceed without the addition of any additional polar solvents. However, triethanolamine yielded highly viscous, close to solid adducts, which were not suitable for batch or continuous processing.

Based on the results of the alkylamines, it was opted to focus on asymmetrical and cyclic polar amines, with results depicted in Figure 4.2c. To allow for comparison to the previous experiments, a total formic acid concentration of 1 mol/liter was maintained. From Figure 4.2c, it becomes apparent that the effect of steric hindrance is much less pronounced for asymmetrical amines with one OH-group compared to asymmetrical amines without the OH-group, with the performance in terms of kinetics and FA conversion of 2-(dimethylamino)ethanol, 4-dimethylamino-1-butanol and 6-dimethylamino-1-hexanol being very comparable to triethylamine. 1-(3-dimethylaminophenyl)ethanol yielded lower kinetic rates, most likely due to steric hindrance as the pKa value is comparable to the basicity of triethylamine. Lastly, methyldiethanolamine was tested, yielding a very significant decrease in kinetic rates, with no equilibrium achieved after 4 hours of reaction. The methyldiethanolamine – formic acid adducts were observed to be highly viscous, posing a possible explanation for the slower kinetics.

Severe catalyst deactivation was reported for a Pd/C catalyst exposed to formic acid – triethylamine adducts under similar conditions [39] to the ones used within this study. To ensure stability of the Au/TiO_2 catalyst, ICP and TEM analyses were performed on the post mortem samples of the catalyst tested through at least each type of amine. An overview of the obtained results is shown in Table 4.1. A comparison of the particle size distribution obtained based on TEM measurements for the fresh catalyst and a catalyst exposed to triethylamine – formic acid adducts is shown in Figure 4.5. All other particle size distributions and exemplary TEM images can be found in Figure C2.

Tertiary amine	Particle size (TEM) [nm]	Catalyst loading [wt%]
Triethylamine	4.69 ± 1.84	1.17 ± 0.05
Tributylamine	5.78 ± 3.26	1.14 ± 0.03
Trihexylamine	5.45 ± 2.22	1.15 ± 0.07
N,N-dimethylbenzylamine	4.50 ± 1.68	1.17 ± 0.02
2-(dimethylamino)ethanol	4.98 ± 1.74	1.09 ± 0.07
Methyldiethanolamine	4.41 ± 1.32	1.11 ± 0.05
6-dimethylamino-1-hexanol	4.32 ± 1.10	1.15 ± 0.03
1-(3-dimethylaminophenyl)ethanol	6.95 ± 1.92	1.10 ± 0.09

Table 4.1: Formic acid decomposition post-mortem particle size (obtained from TEM) and catalyst loading (obtained from ICP-OES). Reaction time was 4 hours at 50 degrees Celsius. Initial particle size was established to be 2.6 ± 0.8 nm and the loading 1.21 wt%. For TEM, at least 50 particles were analyzed for each sample. The average particle size of the fresh catalyst was confirmed using CO pulse chemisorption (2.63 nm)

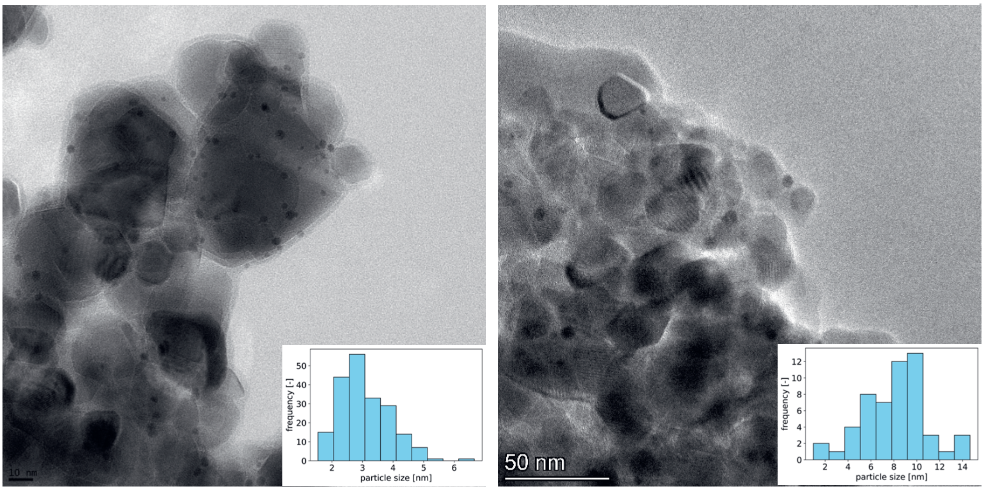

Figure 4.5: TEM images of a fresh Au/TiO$_2$ catalyst (left) and catalyst exposed to formic acid – triethylamine adducts for 4 hours at 50 ºC (right). At least 50 particles were analyzed for each sample. The average particle size of the fresh catalyst was confirmed using CO pulse chemisorption, assuming an equal Au/CO chemisorption stoichiometry and hemispherical particles, following the work of [43]

No significant leaching is observed for any of the amines, while gold nanoparticle sizes increase from 2.6 nm to 4-7 nm depending on the amine the catalyst was exposed to. While no significant conversion was observed in case of formic acid – trihexylamine adducts, a particle size increase from 2.6 to 5.5 nm is observed, leading to the hypothesis that the observed sintering is not caused by the reaction itself, but by exposure to formic acid – tertiary amine adducts.

4.3.2 Formic acid formation

To validate the usage of the formic acid decomposition reaction as a screening tool to predict the activity of the tertiary amine for formic acid production, triethylamine, tributylamine and trihexylamine were used in a high pressure continuous flow packed bed reactor. Experiments were performed under a constant solvent:amine molar ratio and residence time to allow for direct comparison of kinetic rates, and the carbon balance of all experiments was found to be >95%. Figure 4.6 reveals a trend similar to the one observed in Figure 4.2 based on the formic acid decomposition reaction with formic acid production decreasing with an increase in aliphatic chain length going from triethylamine to trihexylamine. In agreement with the previous observations, the reactive test with trihexylamine resulted in very low to no CO_2 conversion, while the usage of N,N-dimethylbenzylamine outperformed triethylamine in terms of productivity. This validates the use of the decomposition reaction for measurement of kinetic rate and equilibrium composition.

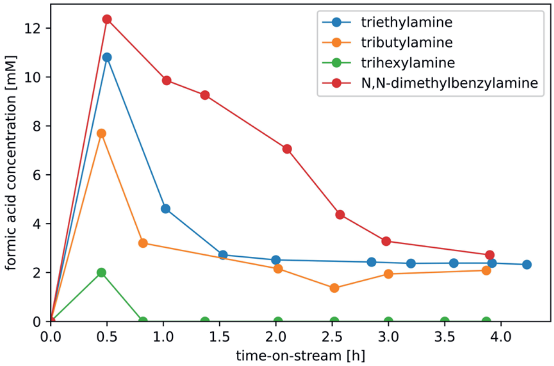

Figure 4.6: Amine screening of the commercial Au/TiO_2 catalyst using a continuous flow reactor performing in CO_2 hydrogenation mode for several amines. The catalyst was replaced for each test. Employed conditions: 2.5 g of catalyst, amine:solvent ratio of 1:3(mol/mol), 70 degrees Celsius, 40 bar total pressure and a CO_2:H_2 feed ratio of 1:1 at 1 ml/min. Liquid flowrate was 1 mL/min (resulting residence time approximately 10 minutes)

While predictions can be made for the FA productivity, Figure 4.6 reveals severe catalyst deactivation which was not expected based on the decomposition study. For the linear chain amines, the rapid deactivation phase of approximately 1.5 hours is followed by a constant productivity up to 4 hours time-on-stream in a 4 hour experiment. The rate of deactivation is much lower for N,N-dimethylbenzylamine, as it does not reach this stable phase within 4 hours time-on-stream.

As shown in Figure 4.7, a significant increase of initial formic acid production compared to the benchmark triethylamine is observed when polar amines such as diethylethanolamine and ethyldiethanolamine are used, with the FA productivity increasing up to a factor of 5. This increase of productivity is the consequence of no longer requiring the usage of additional solvents such as 1-decanol, resulting in much higher tertiary amine concentrations compared to the case where the amine is diluted within a solvent phase. However, also exposure of the Au/TiO_2 catalyst to diethylethanolamine and ethyldiethanolamine at the studied conditions results in a rapid decrease of productivity, followed by stabilization. Interestingly, the stable formic acid productivity lies in the same concentration range for both triethylamine and ethyldiethanolamine, with the exception of diethylethanolamine. No CO formation was detected during any of the experiments.

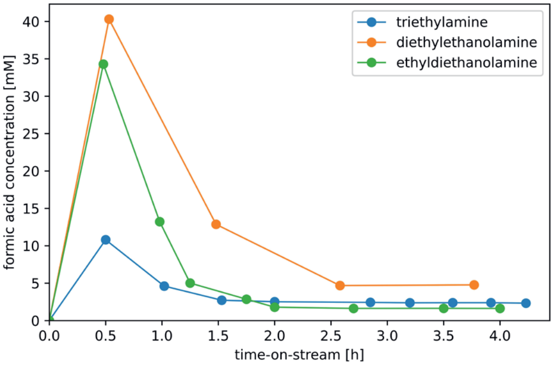

Figure 4.7: Alcohol amine screening of the commercial Au/TiO_2 catalyst using a continuous flow reactor performing in CO_2 hydrogenation mode, without the usage of additional solvents. The catalyst was replaced each test. Employed conditions: 2.5 g of catalyst, 70 degrees Celsius, 40 bar total pressure and a CO_2:H_2 feed ratio of 1:1 at 1 ml/min. Liquid flowrate was 1 ml/min (resulting residence time approximately 10 minutes)

To gain a deeper understanding into the deactivation and subsequent stabilization for longer times on stream, 2 long duration experiments (1:3 mol/mol triethylamine: 1-decanol and diethylethanolamine) were performed in which the catalyst was re-used in 4 separate experiments. Between experiments, the catalyst was kept under argon to prevent air exposure.

As shown in Figure 4.8, the stable FA production rate after the rapid deactivation remains for longer time on streams up to 12 hours. The steady-state production of the conventional triethylamine based process is the range of 2-3 mM at a residence time of 10 minutes, while diethylethanolamine results in a nearly double productivity at roughly 5 mM.

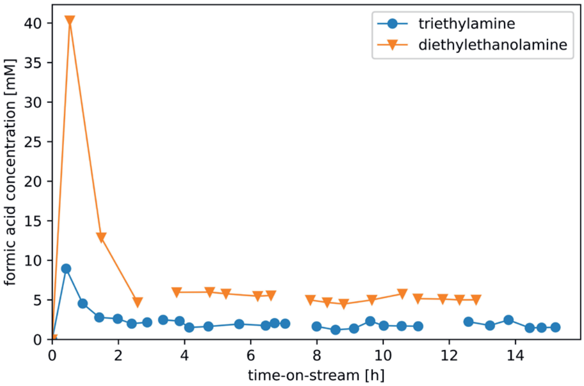

Figure 4.8: Long duration stability test of an Au/TiO_2 catalyst using a continuous flow reactor performing in CO_2 hydrogenation mode, The catalyst was re-used for 4 cycles. Employed conditions: 2.5 g of catalyst, 70 degrees Celsius, 40 bar total pressure and a CO_2:H_2 feed ratio of 1:1 at 1 mL/min. Liquid flowrate was 1 mL/min (resulting residence time approximately 10 minutes)

Consecutively, the catalysts used for formic acid production (single runs and long duration tests) were analyzed using a variety of characterization techniques (TEM, ICP-OES, CO pulse chemisorption). The TEM and ICP-OES results are summarized in Table 4.2.

Tertiary amine	Particle size (TEM) [nm]	Catalyst loading [wt%]
Triethylamine (15 minutes residence time)	12.33 ± 2.91	1.09
Tributylamine	7.06 ± 2.52	1.08
Trihexylamine	5.50 ± 3.45	1.17
N,N-dimethylbenzylamine	8.47 ± 3.68	1.13
Diethylethanolamine (15 minutes residence time)	9.14 ± 3.17	1.16
Ethyldiethanolamine	5.43 ± 2.32	1.14
Triethylamine (4 cycles)	8.76 ± 4.11	1.06
Diethylethanolamine (4 cycles)	12.99 ± 3.69	1.19
n-butylimidazole (time-on-stream 50 hr)	8.57 ± 3.17	1.17

Table 4.2: Formic acid production post-mortem particle size (obtained from TEM) and catalyst loading (obtained from ICP-OES). Reaction time was 4 hours at 70 degrees Celsius. Initial particle size was established to be 2.6 ± 0.8 nm and the loading 1.21 wt%. For TEM, at least 50 particles were analyzed for each sample. The average particle size of the fresh catalyst was confirmed using CO pulse

Similar to the catalysts exposed to formic acid – tertiary amine adducts, no significant leaching is observed for the catalysts used for formic acid production. However, the size of the gold nanoparticles increases from 2.6 nm up to 13 nm. The catalytic behavior of gold nanoparticles has been shown to be strongly affected by the particle size for several reactions, such as CO oxidation, formic acid decomposition and the water gas shift reaction [43]. Loges *et al*. have demonstrated that the TOFs of the FA decomposition reaction based on an Au/ZrO_2 catalyst decrease rapidly when increasing the Au particle size from 0.8 nm to negligible at a particle size of 10 nm [39].

Further catalyst characterization (XPS, XRD and CO pulse chemisorption) was performed on the catalysts used in the stability test. To eliminate the possibility of TEM-invisible Au species existing on the catalyst surface, low-temperature CO pulse chemisorption was employed. The average particle sizes obtained were in line with the TEM results, with the determined particle sizes being 2.63, 8.82 and 13.03 nm for the fresh catalyst, 4 cycle triethylamine catalyst and the 4 cycle diethylethanolamine catalyst, respectively.

XRD measurements were performed to study the crystallographic structure of the fresh and spent catalysts, with the XRD patterns given in Figure C5 and Figure C6. No morphological changes were observed, and no reflections pertaining to the Au nanoparticles in metal or oxide state were detected. The lack of Au reflections is caused by the small particle size (< 20 nm) of the gold nanoparticles, and is in line with previous works on titania support Au catalysts [48].

Filonenko *et al.* have previously determined the active species during the reaction to be zero valence Au species [13]. Thus, the oxidation state of Au on the surface nanoparticles was analyzed using XPS, with the resulting fitting shown in Figure C4. The spectra of fresh and spent catalysts are presented in Figure C4. The $4f_{7/2}$ and $4f_{5/2}$ Au orbitals were fitted to the obtained data using a peak area ratio of 3:4 between the 7/2 and 5/2 spin orbits [45]. Peak splitting between these peaks was constrained to be 3.7 eV. A Shirley background and a GL(90) line shape were used, along with a charge correction of adventitious carbon at 248.8 eV [44]–[46]. The fits on the spectra indicate that metallic gold was exclusively present on the surface of the catalyst of both fresh and spent catalyst, since only Au^0 without Au^{1+} and Au^{3+} could be fitted to the obtained data.

The significant decrease in FA productivity observed in this work is thus caused by the growth of the Au particles. Yang *et al.* have reported the sintering of Au nanoparticles supported on titania. During this study, the catalyst was exposed to a 1:1 CO/CO_2 gaseous mixture, with gold nanoparticles becoming mobile in the range of 300 – 410 K. It was hypothesized the movement of Au particles was caused by CO adsorbates [47]. However, within this work no CO was detected using in line GC with a lower detection limit of 2 ppm.

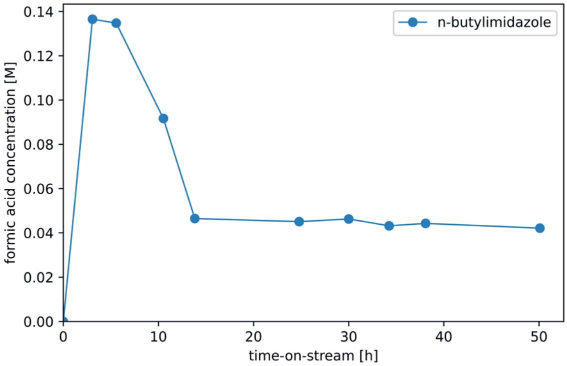

Figure 4.9: Long duration testing of n-butylimidazole in combination with the commercial Au/TiO_2 catalyst using a continuous flow reactor performing in CO_2 hydrogenation mode, without the usage of additional solvents. The catalyst was replaced each test. Employed conditions: 2.5 g of catalyst, 70 degrees Celsius, 40 bar total pressure and a CO_2:H_2 feed ratio of 1:1 at 0.73 mL/min. Liquid flowrate was 0.025 mL/min (resulting residence time approximately 2hr).

To investigate if the catalyst deactivation also occurs when using less strong bases such as n-butylimidazole, long duration experiments were performed. N-butylimidazole was found to be completely miscible with formic acid in any molar ratio, thus no additional solvents were required. Experiments with a residence time of 15 minutes resulted in formic acid productivity below the NMR detection limit. Subsequently, the residence time was increased to 100 minutes, with the FA production as a function of time-on-stream as shown in Figure 4.9. Similar behavior is observed as when employing strong bases such as triethylamine, a phase of catalyst deactivation followed by stable FA production of roughly 5mM. TEM and

ICP-OES (Table 4.2) reveal significant particle growth and no leaching.

4.4 Conclusion

The activity of the direct hydrogenation of CO_2 towards formic acid was found to strongly depend on the tertiary amine used to reduce the formic acid in the reaction mixture to reduce its activity and thus shift the equilibrium.

Due to the slow kinetic nature of the CO_2 hydrogenation to formic acid, the formic acid decomposition reaction was used to screen a wide variety of tertiary amines based on the principle of microscopic reversibility. Steric hindrance and the pKa of the tertiary amine were identified as a key parameters influencing both the observed kinetic rates as well as the formic acid conversion. Polar tertiary amines allow solventless formic acid production, with significantly higher kinetic rates due to higher amine concentrations. Here, the amount of alcohol groups showed a strong influence on the observed kinetic rates, most likely due to viscosity effects.

The assumption of microscopic reversibility was verified in a high pressure packed bed reactor. Here, the usage of solventless polar amines such as diethylethanolamine allowed for FA productivity up to 5x that of the benchmark triethylamine system. Catalyst deactivation of the Au/TiO_2 catalyst was observed for all amines studied within this work, and the deactivation mechanism was shown to be sintering of the Au nanoparticles with no significant leaching, morphological changes or oxidation of the Au species observed. The catalyst deactivation was found to be very rapid, with the catalyst allowing for stable FA production up to 50 hours after the initial gold nanoparticle growth.

Appendix C

C.1 TEM imaging

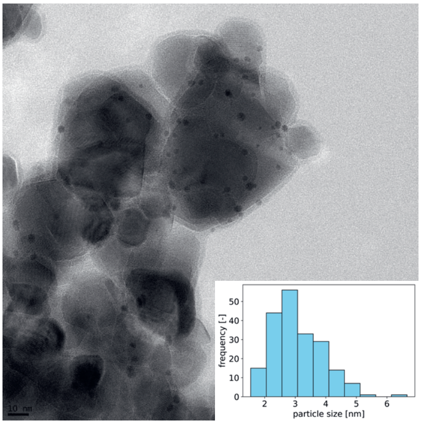

fresh Au/TiO₂

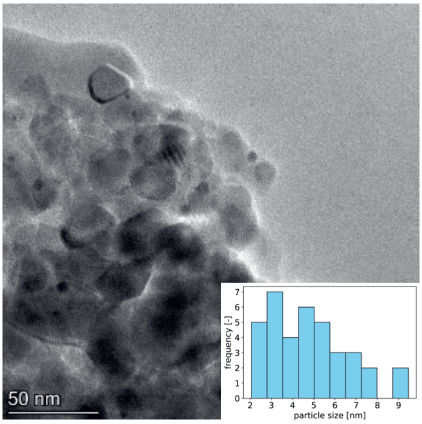

Triethylamine

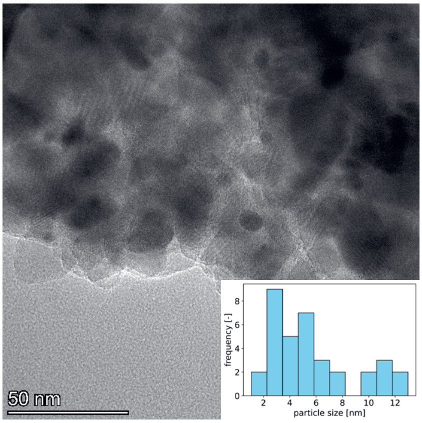

Tributylamine

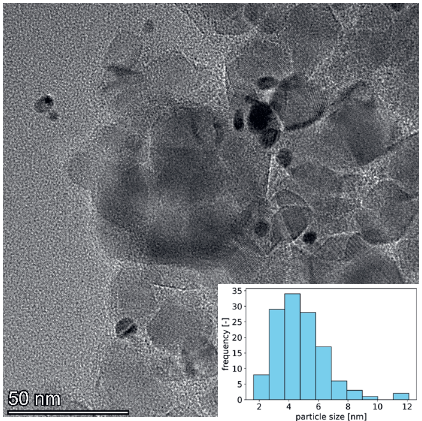

Trihexylamine

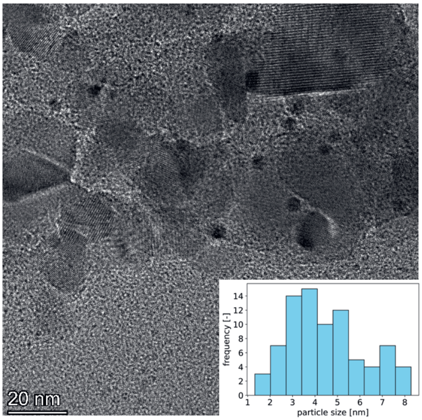

N,N-dimethylbenzylamine

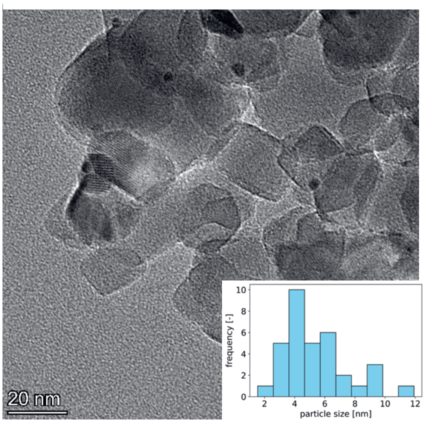

2-(dimethylamino)ethanol

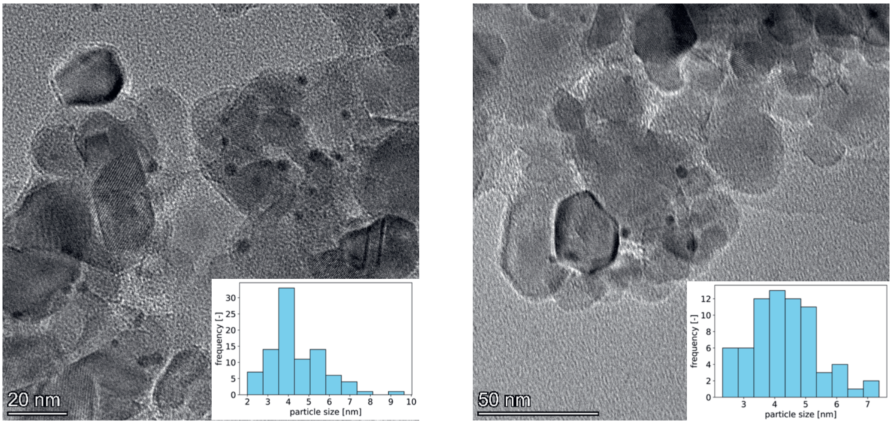

Methyldiethanolamine

6-dimethylamino-1-hexanol

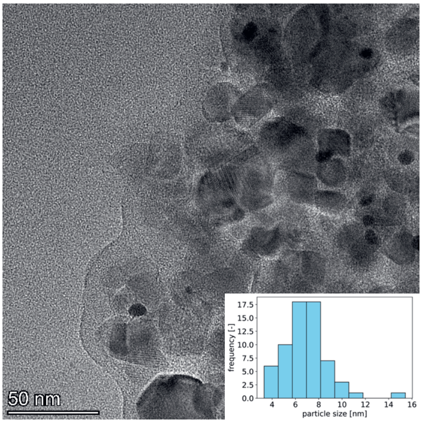

1-(3-dimethylaminophenyl)ethanol

Figure C1: TEM images and particle size distributions of Au/TiO_2 catalysts used in formic acid decomposition. Reaction time was 4 hours at 50 degrees. At least 35 particles were analyzed per sample

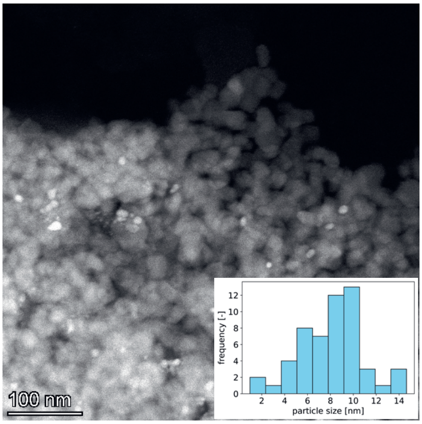

Triethylamine

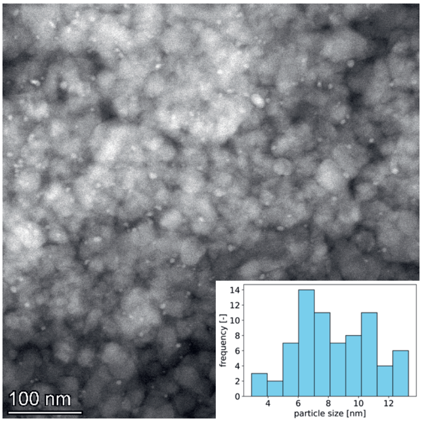

Tributylamine

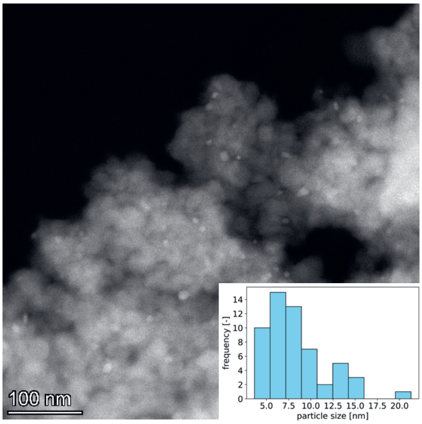

Trihexylamine

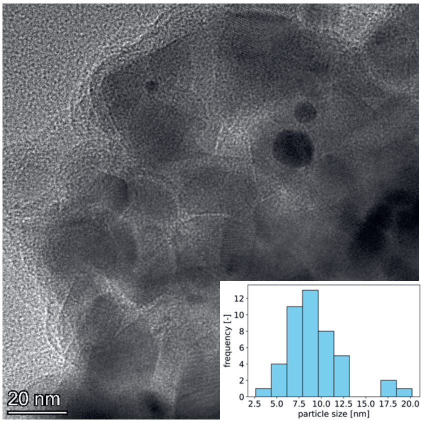

Diethylethanolamine

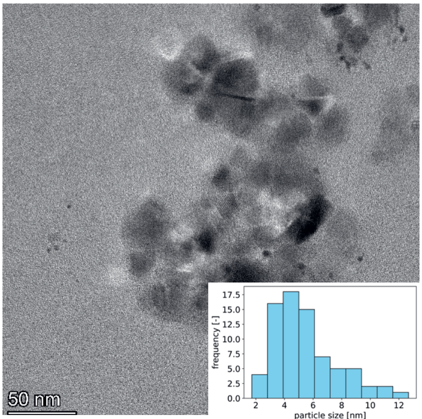

Ethyldiethanolamine

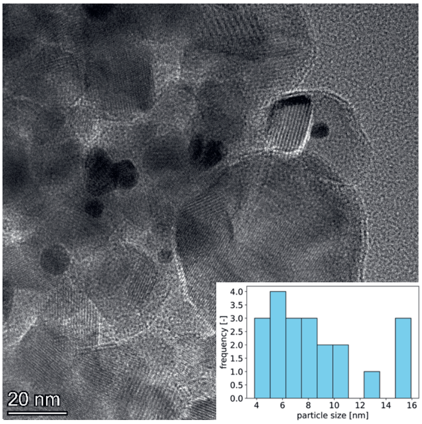

N,N-dimethylbenzylamine

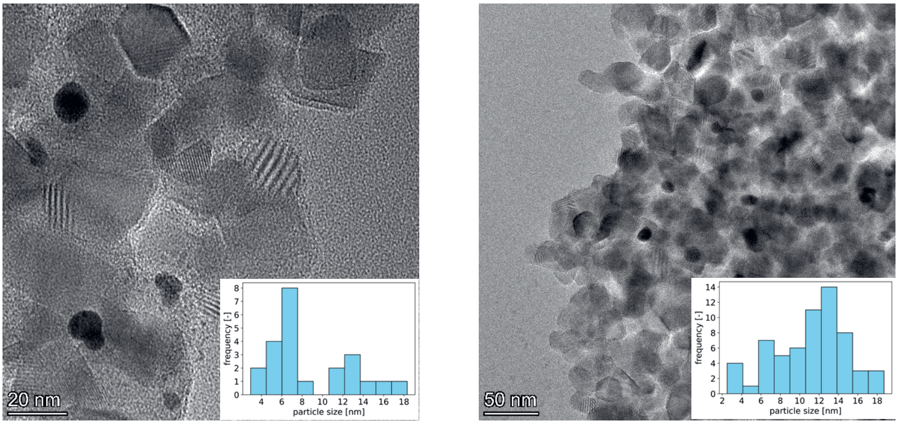

Triethylamine, 4 cylces

Diethylethanolamine, 4 cylces

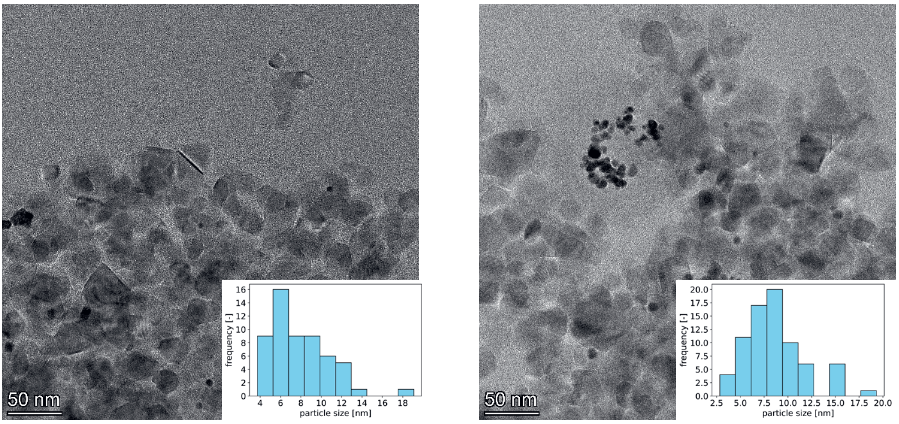

N,N-dimethylbenzylamine, 72hr reaction

N-butylimidazole, 72hr reaction

Figure C2: TEM images and particle size distributions of Au/TiO_2 catalysts using in the direct hydrogenation of CO_2 to formic acid . Reaction time was 4 hours at 70 degrees, unless otherwise indicated. At least 50 particles were analyzed per sample

C.2 XPS and XRD

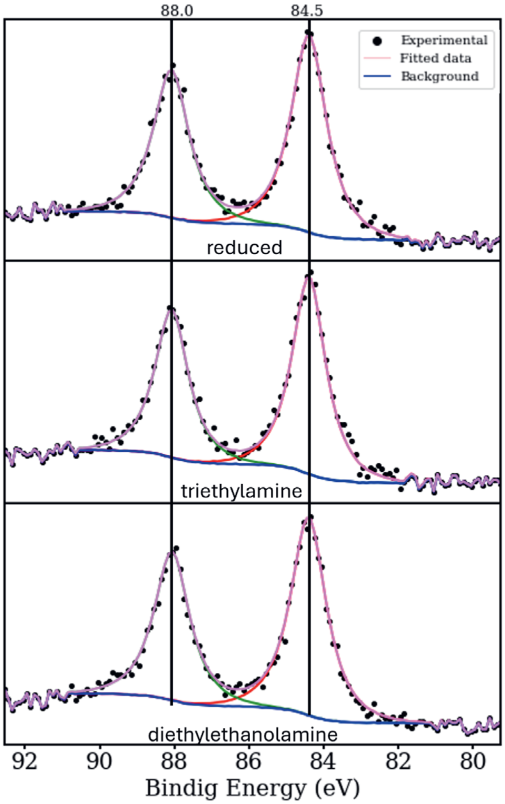

Figure C3: XPS spectra of the Au 4f orbital of fresh Au/TiO_2, spent Au/TiO_2 exposed to 1:3 mol/mol triethylamine: 1-decanol for 12 hours time-on-stream and spent Au/TiO_2 exposed to diethylethanolamine for 12 hours time-on-stream

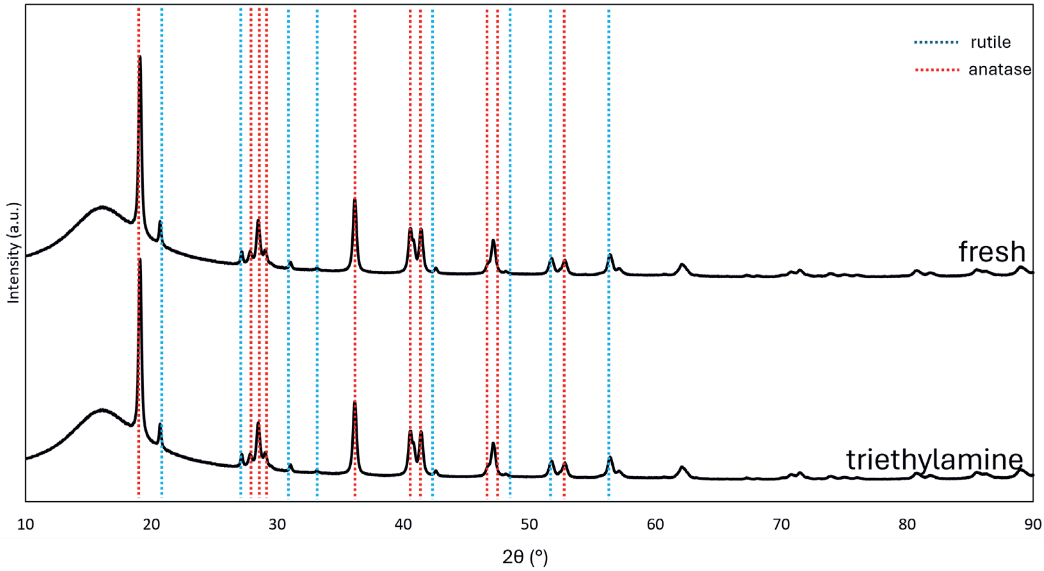

Figure C4: XRD pattern of fresh Au/TiO_2 and spent Au/TiO_2 exposed to 1:3 mol/mol triethylamine: 1-decanol for 12 hours time-on-stream

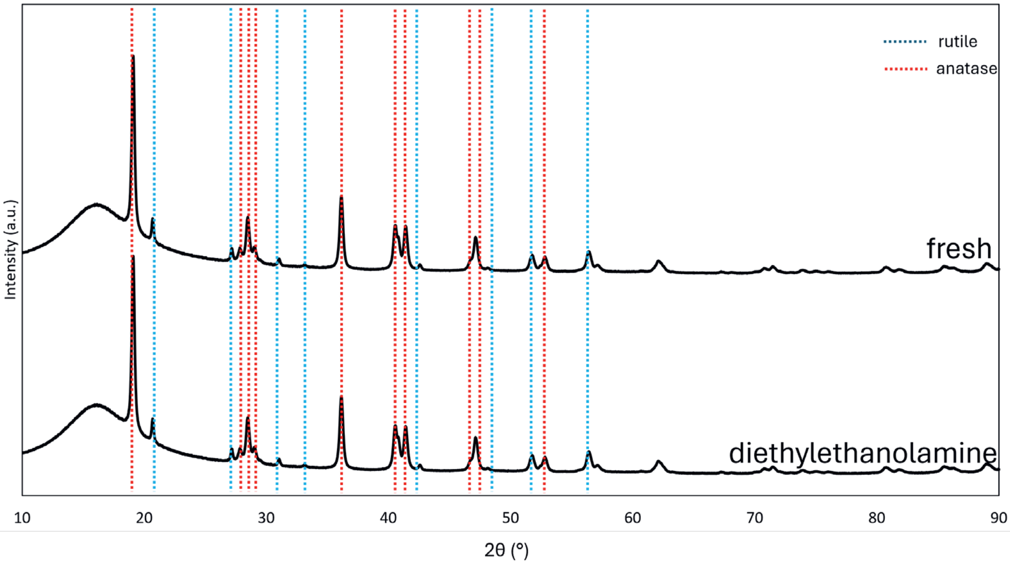

Figure C5: XRD pattern of fresh Au/TiO_2 and spent Au/TiO_2 exposed to diethylethanolamine for 12 hours time-on-stream

C.3 Formic acid decomposition set-up

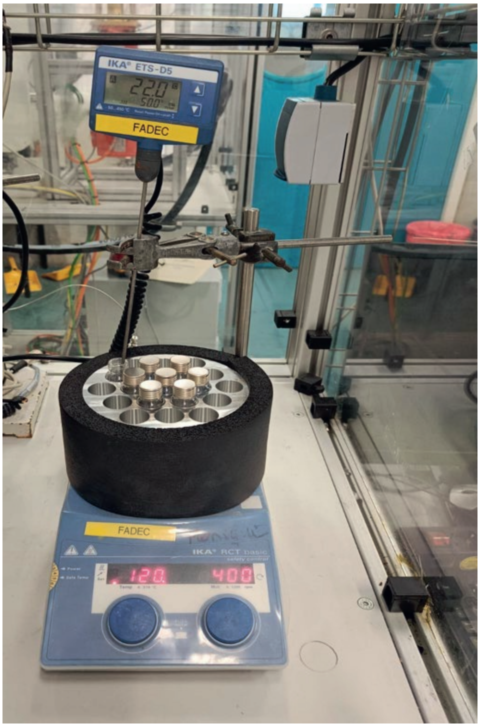

Figure C6: Set-up for batch formic acid decomposition

C.4 Absence of mass transfer limitations

External Diffusion: *Mears Criterion*

The absence of external mass transfer limitations can be evaluated using the Mears criterion [1]:

$$w = \frac{r_{obs} \cdot \rho_B \cdot R_p}{k_{ls} \cdot C_{Ab}} \leq 0.15 \qquad C.1$$

Here, r_{obs} represents the observed reaction rate per kilogram of catalyst, ρ_B the bulk density of the catalyst bed, R_p the catalyst particle size, k_{ls} the external mass transfer coefficient and C_{Ab} the bulk concentration. The bulk density of the catalyst was determined by

$$\rho_B = \frac{\rho_{TiO_2}}{1 - \varepsilon_{void}} \qquad C.2$$

The mass transfer coefficient was determined using a mass transfer coefficient correlation for small laboratory batch reactors by Pestre *et al*. [2]:

$$k_{ls}a_{ls} = 9.5 \cdot 10^{-4}\, N^{2.2} \qquad C.3$$

Here, N is the stirring speed. The Mears criteria were calculated for all reactions, however, the only the formic acid decomposition reaction with dimethylbenzylamine (highest observed reaction rate) is illustrated here.

$$w = \frac{r_{obs} \cdot \rho_B \cdot R_p}{k_{ls} \cdot C_{Ab}} = \frac{11.1 \cdot 37.5 \cdot 10^{-6}}{1000} \cdot \frac{4230}{(1-0.4)} \cdot \frac{75 \cdot 10^{-6}}{2 \cdot 10^{-6}} = 0.11 \leq 0.15 \qquad C.4$$

It can thus be concluded that the system does not suffer form external mass transfer limitations for any of the reactions.

Internal diffusion: *Weisz-Prater Criterion*

The absence of internal mass transfer limitations was evaluated using the Weisz-Prater criterion [1]. Here, internal mass transfer limitations are absent when:

$$C_{wp} = \frac{-r_{obs} \cdot R_p^2}{D_e \cdot C_{As}} \leq 3\beta \qquad C.5$$

Here, r_{obs} is the observed volumetric reaction rate, R_p the catalyst particle size, D_e the effective diffusivity and C_s the reactant concentration at the particle surface. β is described by:

$$\beta = \frac{4\,(1-\eta)}{n} \qquad C.6$$

where η and n are the effectiveness factor and reaction order respectively. The effectiveness factor was determined by the Thiele equation for spherical particles:

$$\eta = \frac{\tanh \varphi}{\varphi} \qquad C.7$$

$$\varphi = \sqrt{\frac{2k^{-} \cdot R_p^2 \cdot C_0^{n+1}}{D_e}} \qquad C.8$$

and,

$$D_e = \frac{\varepsilon_{void}}{\tau} \cdot D \qquad C.9$$

With τ the tortuosity, which was taken equal to 3. The diffusivity was taken equal to 1e-6.

$$\varphi = \sqrt{\frac{2k^{-} \cdot R_p^2 \cdot C_0^{n+1}}{D_e}}$$
$$= \sqrt{\frac{2 \cdot 6.88 \cdot 10^3 \cdot \exp\left(\frac{-31200}{8.314 \cdot 373}\right) \cdot (37.5 \cdot 10^{-6})^2 \cdot 1000^2}{\frac{0.492}{2.93} \cdot 10^{-6}}} = 2.22 \qquad C.10$$

$$\frac{-r_{obs} \cdot R_p^2}{D_e \cdot C_{As}} \leq 3\,\frac{4\,(1 - \frac{\tanh \varphi}{\varphi})}{n} \rightarrow 0.0066 \leq 6.72 \qquad C.11$$

It can thus be concluded that the system does not suffer form internal mass transfer limitations for any of the reactions.

C.5 Molecular structures and pKa

Structure	pKa	Molar volume [cm^3/mol]
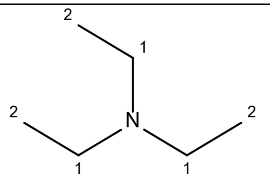 triethylamine	10.225	34.34
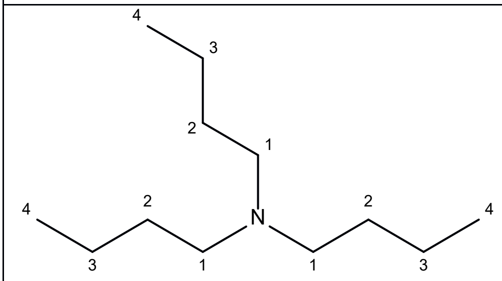 tributylamine	10.295	61.94
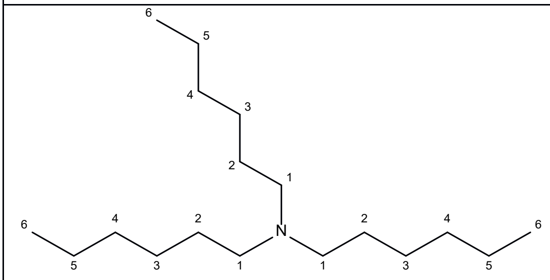 trihexylamine	10.318	89.53
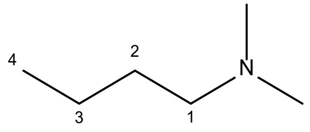 dimethylbutylamine	10.191	33.94

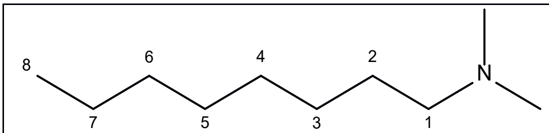 dimethyloctylamine	10.200	52.34
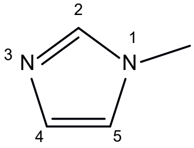 N-Methylimidazole	7.0	24.34
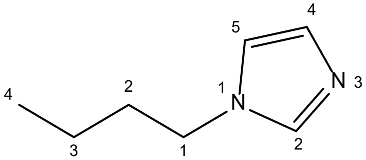 N-butylimidazole	7.09	38.34
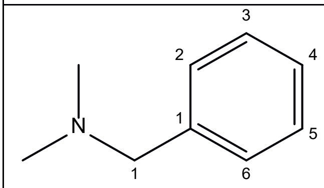 dimethylbenzylamine	9.615	44.44
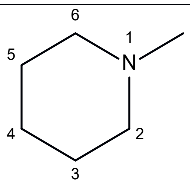 N-Methylpiperidine	9.996	31.86

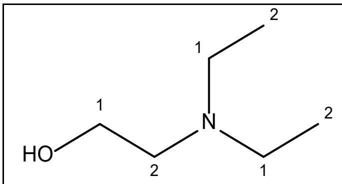 diethylethanolamine	9.389	35.71
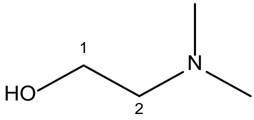 Dimethylethanolamine	9.331	26.11
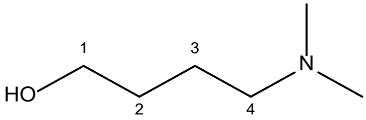 Dimethylbutanolamine	10.002	35.31
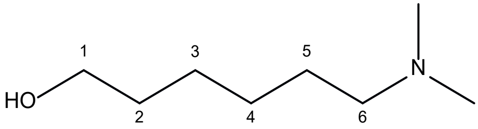 dimethylhexanolamine	10.176	44.50
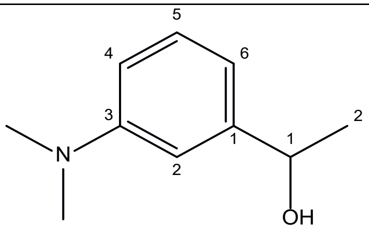 1-(3-Dimethylaminophenyl)ethanol	14.373	52.41

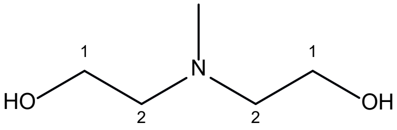 Methyl diethanolamine	8.524	32.27
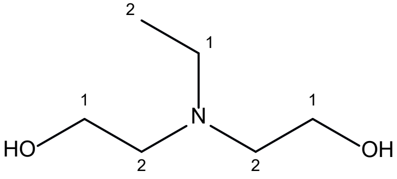 ethyldiethanolamine	8.553	35.71

Table C.1: pKa and molecular volume for all studied amines. Values were predicted using Chemdraw Professional 18.0

References Appendix C

[1] H. Scott Fogler, "Elements of chemical reaction engineering," *Chem. Eng. Sci.*, vol. 42, no. 10, p. 2493, 1987, doi: 10.1016/0009-2509(87)80130-6.

[2] N. Pestre, P. Fongarland, and C. De Bellefon, "Gas / Liquid Mass Transfer in Small Laboratory Batch Reactors :," *Ind. Eng. Chem. Res.*, vol. 43, pp. 924–927, 2004.

References

[1] H. Ritchie and P. Rosado, "Energy Mix," *Our World Data*, 2020.

[2] H. Ritchie, P. Rosado, and M. Roser, "Energy Production and Consumption," *Our World Data*, 2020.

[3] D. Welsby, J. Price, S. Pye, and P. Ekins, "Unextractable fossil fuels in a 1.5 ° C world," vol. 597, no. July, 2021, doi: 10.1038/s41586-021-03821-8.

[4] R. Sun *et al.*, "Heterogeneous catalysts for CO2 hydrogenation to formic acid/formate: From nanoscale to single atom," *Energy Environ. Sci.*, vol. 14, no. 3, pp. 1247–1285, 2021, doi: 10.1039/d0ee03575k.

[5] Intergovernmental Panel on Climate Change, Climate Change 2022: Mitigation of Climate Change *Technical Summary*. 2022.

[6] M. S. Salman, N. Rambhujun, C. Pratthana, K. Srivastava, and K. F. Aguey-Zinsou, "Catalysis in Liquid Organic Hydrogen Storage: Recent Advances, Challenges, and Perspectives," *Ind. Eng. Chem. Res.*, 2021, doi: 10.1021/acs.iecr.1c03970.

[7] L. Schlapbach and A. Züttel, "Hydrogen Stogare materials for Mobile Applications," *Nature*, vol. 414, no. November, pp. 353–358, 2001, doi: 10.1038/35104634.

[8] M. Aresta, A. Dibenedetto, and A. Angelini, "Catalysis for the valorization of exhaust carbon: From CO2 to chemicals, materials, and fuels. technological use of CO2," *Chem. Rev.*, vol. 114, no. 3, pp. 1709–1742, 2014, doi: 10.1021/cr4002758.

[9] A. Züttel, "Hydrogen storage methods," *Naturwissenschaften*, vol. 91, no. 4, pp. 157–172, 2004, doi: 10.1007/s00114-004-0516-x.

[10] E. Masika and R. Mokaya, "Exceptional gravimetric and volumetric hydrogen storage for densified zeolite templated carbons with high mechanical stability," *Energy Environ. Sci.*, vol. 7, no. 1, pp. 427–434, 2014, doi: 10.1039/c3ee42239a.

[11] H. W. Langmi, J. Ren, B. North, M. Mathe, and D. Bessarabov, "Hydrogen storage in metal-organic frameworks: A review," *Electrochim. Acta*, vol. 128, no. 2014, pp. 368–392, 2014, doi: 10.1016/j.electacta.2013.10.190.

[12] Y. Liu, Y. Yang, M. Gao, and H. Pan, "Tailoring Thermodynamics and Kinetics for Hydrogen Storage in Complex Hydrides towards Applications," *Chem. Rec.*, vol. 16, no. 1, pp. 189–204, 2016, doi: 10.1002/tcr.201500224.

[13] G. A. Filonenko, W. L. Vrijburg, E. J. M. Hensen, and E. A. Pidko, “On the activity of supported Au catalysts in the liquid phase hydrogenation of CO2 to formates,” *J. Catal.*, vol. 343, pp. 97–105, 2016, doi: 10.1016/j.jcat.2015.10.002.

[14] A. Álvarez *et al.*, “Challenges in the Greener Production of Formates/Formic Acid, Methanol, and DME by Heterogeneously Catalyzed CO2 Hydrogenation Processes,” *Chem. Rev.*, vol. 117, no. 14, pp. 9804–9838, 2017, doi: 10.1021/acs.chemrev.6b00816.

[15] S. Enthaler, “Carbon dioxide-the hydrogen-storage material of the future?,” *ChemSusChem*, vol. 1, no. 10, pp. 801–804, 2008, doi: 10.1002/cssc.200800101.

[16] F. Joó, “Breakthroughs in hydrogen storage\-formic acid as a sustainable storage material for hydrogen,” *ChemSusChem*, vol. 1, no. 10, pp. 805–808, 2008, doi: 10.1002/cssc.200800133.

[17] K. Yu, I. Curcic, J. Gabriel, and S. C. E. Tsang, “Recent advances in CO2 capture and utilization.,” *ChemSusChem*, vol. 1, no. 11, pp. 893–899, 2008, doi: 10.1002/cssc.200800169.

[18] C. Weidenthaler and M. Felderhoff, “Solid-state hydrogen storage for mobile applications: Quo Vadis?,” *Energy Environ. Sci.*, vol. 4, no. 7, pp. 2495–2502, 2011, doi: 10.1039/c0ee00771d.

[19] U. Eberle, M. Felderhoff, and F. Schüth, “Chemical and physical solutions for hydrogen storage,” *Angew. Chemie - Int. Ed.*, vol. 48, no. 36, pp. 6608–6630, 2009, doi: 10.1002/anie.200806293.

[20] P. Moriarty and D. Honnery, “Hydrogen’s role in an uncertain energy future,” *Int. J. Hydrogen Energy*, vol. 34, no. 1, pp. 31–39, 2009, doi: 10.1016/j.ijhydene.2008.10.060.

[21] A. W. C. Van Den Berg and C. O. Areán, “Materials for hydrogen storage: Current research trends and perspectives,” *Chem. Commun.*, no. 6, pp. 668–681, 2008, doi: 10.1039/b712576n.

[22] T. Leppänen, M. Karttunen, K. Kaski, R. A. Barrio, and L. Zhang, “A new dimension to Turing patterns,” *Phys. D Nonlinear Phenom.*, vol. 168–169, pp. 35–44, 2002, doi: 10.1016/S0167-2789(02)00493-1.

[23] Q. Bi, J. Lin, Y. Liu, and F. Huang, “ScienceDirect Promoted hydrogen generation from formic acid with amines using Au / ZrO 2 catalyst,” *Int. J. Hydrogen Energy*, vol. 41, no. 46, pp. 21193–21202, 2016, doi: 10.1016/j.ijhydene.2016.09.150.

[24] R. Tanaka, M. Yamashita, L. W. Chung, K. Morokuma, and K. Nozaki,

"Mechanistic studies on the reversible hydrogenation of carbon dioxide catalyzed by an Ir-PNP complex," *Organometallics*, vol. 30, no. 24, pp. 6742–6750, 2011, doi: 10.1021/om2010172.

[25] T. Schaub and R. A. Paciello, "A process for the synthesis of formic acid by CO2 hydrogenation: Thermodynamic aspects and the role of CO," *Angew. Chemie - Int. Ed.*, vol. 50, no. 32, pp. 7278–7282, 2011, doi: 10.1002/anie.201101292.

[26] D. Preti, C. Resta, S. Squarcialupi, and G. Fachinetti, "Carbon dioxide hydrogenation to formic acid by using a heterogeneous gold catalyst," *Angew. Chemie - Int. Ed.*, vol. 50, no. 52, pp. 12551–12554, 2011, doi: 10.1002/anie.201105481.

[27] J. Hu, "Reaction and separation system for CO 2 hydrogenation to formic acid catalyzed by iridium immobilized on solid phosphines under base-free condition," *ISCIENCE*, vol. 26, no. 5, p. 106672, 2023, doi: 10.1016/j.isci.2023.106672.

[28] M. Pérez-Fortes, J. C. Schöneberger, A. Boulamanti, G. Harrison, and E. Tzimas, "Formic acid synthesis using CO2 as raw material: Techno-economic and environmental evaluation and market potential," *Int. J. Hydrogen Energy*, vol. 41, no. 37, pp. 16444–16462, 2016, doi: 10.1016/j.ijhydene.2016.05.199.

[29] C. Kim, Y. Lee, K. Kim, and U. Lee, "Implementation of Formic Acid as a Liquid Organic Hydrogen Carrier (LOHC): Techno-Economic Analysis and Life Cycle Assessment of Formic Acid Produced via CO2 Utilization," *Catalysts*, vol. 12, no. 10, 2022, doi: 10.3390/catal12101113.

[30] M. Sekiya, "ギ酸による還元反応．," *有機合成化学協会誌（Journal Synth. Org. Chem. Japan）*, vol. 34, no. 2, pp. 67–81, 1976.

[31] S. Jiang *et al.*, "Additive-free CO2 hydrogenation to pure formic acid solution via amine-modified Pd catalyst at room temperature," *Green Chem.* vol. 25, pp. 6025–6031, 2023, doi: 10.1039/d3gc01307c.

[32] A. Weilhard, M. I. Qadir, V. Sans, and J. Dupont, "Selective CO2 Hydrogenation to Formic Acid with Multifunctional Ionic Liquids.", *ACS Catalysis,* vol. 8, no.3, 2018, doi:10.1021/acscatal.7b03931

[33] D. A. Bulushev and J. R. H. Ross, "Towards Sustainable Production of Formic Acid," *ChemSusChem Reviews,* pp. 821–836, 2018, doi: 10.1002/cssc.201702075.

[34] A. Weilhard, S. P. Argent, and V. Sans, "Efficient carbon dioxide hydrogenation to formic acid with buffering ionic liquids," *Nat. Commun.*, no.

2021, pp. 1–7, doi: 10.1038/s41467-020-20291-0.

[35] X. Wang *et al.*, “Heterogeneous Catalytic Transfer Partial-Hydrogenation with Formic Acid as Hydrogen Source Over the Schiff-Base Modified Gold Nano-Catalyst,” *Catal. Letters*, vol. 147, no. 2, pp. 517–524, 2017, doi: 10.1007/s10562-016-1929-9.

[36] Q. Liu *et al.*, “Direct catalytic hydrogenation of CO2 to formate over a Schiff-base-mediated gold nanocatalyst,” *Nat. Commun.*, vol. 8, no. 1, 2017, doi: 10.1038/s41467-017-01673-3.

[37] M. Grasemann and G. Laurenczy, “Formic acid as a hydrogen source - Recent developments and future trends,” *Energy Environ. Sci.*, vol. 5, no. 8, pp. 8171–8181, 2012, doi: 10.1039/c2ee21928j.

[38] C. Kim *et al.*, “Accelerating the net-zero economy with CO2-hydrogenated formic acid production: Process development and pilot plant demonstration,” *Joule*, vol. 8, no. 3, pp. 693–713, 2024, doi: 10.1016/j.joule.2024.01.003.

[39] B. Loges, A. Boddien, H. Junge, and M. Beller, “Controlled Generation of Hydrogen from Formic Acid Amine Adducts at Room Temperature and Application in H 2 / O 2 Fuel Cells **,” vol. 4, pp. 3962–3965, 2008, doi: 10.1002/anie.200705972.

[40] T. Akita, P. Lu, S. Ichikawa, K. Tanaka, and M. Haruta, “Analytical TEM study on the dispersion of Au nanoparticles in Au/TiO2 catalyst prepared under various temperatures,” *Surf. Interface Anal.*, vol. 31, no. 2, pp. 73–78, 2001, doi: 10.1002/sia.959.

[41] A.W.N. de Leeuw den Bouter, L.Brito, A. Miquelot, P.Olivier,J. van der Schaaf, “Modelling of formic acid production using solventless trialkylamine reduction strategies,” *Under review in Chemical Engineering Science*

[42] A.W.N. de Leeuw den Bouter, E.J.M. Vogels, L.Brito , A. Miquelot, P.Olivier, J. van der Schaaf, “Chemical and phase equilibrium of formic acid – trialkylamine complexes,” *Under review in ACS Omega*

[43] Q. Bi, X. Du, Y. Liu, Y. Cao, H. He, and K. Fan, “Efficient Subnanometric Gold-Catalyzed Hydrogen Generation via Formic Acid Decomposition under Ambient Conditions,” *J.Am.Chem.Soc,* vol. 134, pp. 8926-8933, 2012, doi: 10.1021/ja301696e.

[44] J. P. Sylvestre, S. Poulin, A. V. Kabashin, E. Sacher, M. Meunier, and J. H. T. Luong, “Surface chemistry of gold nanoparticles produced by laser ablation in aqueous media,” *J. Phys. Chem. B*, vol. 108, no. 43, pp. 16864–16869, 2004, doi: 10.1021/jp047134.

[45] N. Kruse and S. Chenakin, “XPS characterization of Au/TiO2 catalysts: Binding energy assessment and irradiation effects,” *Appl. Catal. A Gen.*, vol.

391, no. 1–2, pp. 367–376, 2011, doi: 10.1016/j.apcata.2010.05.039.

[46] T. Ishida, T. Murayama, A. Taketoshi, and M. Haruta, “Importance of Size and Contact Structure of Gold Nanoparticles for the Genesis of Unique Catalytic Processes,” *Chem. Rev.*, vol. 120, no. 2, pp. 464–525, 2020, doi: 10.1021/acs.chemrev.9b00551.

[47] F. Yang, M. S. Chen, and D. W. Goodman, “Sintering of Au particles supported on TiO 2(110) during CO oxidation,” *J. Phys. Chem. C*, vol. 113, no. 1, pp. 254–260, 2009, doi: 10.1021/jp807865w.

[48] B. Tahir, M. Tahir, and N. A. S. Amin, “Photocatalytic CO2 conversion over Au/TiO2 nanostructures for dynamic production of clean fuels in a monolith photoreactor,” Clean Technol. Environ. Policy, vol. 18, no. 7, pp. 2147–2160, 2016, doi: 10.1007/s10098-016-1181-4

5

Development of bimetallic catalysts for the direct hydrogenation of CO_2 to formic acid

This chapter is based on the following publication:

A.W.N. de Leeuw den Bouter, P.Naik, Z.Adnin, L.Brito , A. Miquelot, P.Olivier, J. van der Schaaf, “Development of bimetallic catalysts for the direct hydrogenation of CO_2 to formic acid”, Under review in Applied Catalysis O.

Abstract

Within this work the performance of several gold based bimetallic catalysts (Au-Cu, Au-Ni and Au-Pd supported on alumina) was evaluated and compared to mono-metallic (Au, Pd and Ru based) catalysts for the direct hydrogenation of CO_2 towards formic acid. The doping of Au-based catalysts with Ni or Cu was shown to be detrimental for selectivity towards FA and catalyst stability. Promising behavior in terms of catalyst activity and selectivity was observed for Au-Pd based catalysts with low Pd concentrations.

Severe catalyst deactivation up to ~88% of the original activity was observed for all catalysts studied within this work. The influence of the triethylamine:1-decanol ratio on the catalyst deactivation was studied, identifying different deactivation mechanisms for the Au and Pd based catalysts. Ru-based catalysts were observed to have extremely low (< 1 mM) FA productivity. Extraordinary selectivity of 100% was demonstrated using an Au/TiO_2 compared to the other studied mono- and bimetallic catalysts, with all other catalysts producing significant amounts of undesired CO.

5.1 Introduction

A broad range of catalysts has been previously studied for the hydrogenation of CO_2 to formic acid, with catalysts based on both homogeneous and heterogeneous formulations [9][10][18][19]. While homogeneous metal complexes based on Ru and Ir have shown excellent activity and selectivity [18]-[20], the inherent drawbacks of homogeneous catalysts such as difficult product separation and catalyst recycling have prompted research towards heterogeneous catalysts [20][21].

The heterogeneous compositions explored by previous authors focus on a wide range of noble metals including Au [23][24], Pt [24][25], Pd [26][27] and Ru [19][28][30] deposited on a wide range of supports [9][10].

Bredig and Carter reported the hydrogenation of gaseous CO_2 and carbonates to formates in 1914 using Pd black as a catalyst [31]. While Pd-based catalysts are often hailed as promising alternatives to the homogeneous complexes due to their superior kinetic performance compared to other metals at moderate temperatures, significant limitations still have to be overcome in terms of selectivity and stability [31][32]. Pd based mono-metallic catalysts have been shown readily poisoned by reaction intermediates such as CO and formates, resulting in limited stability [34][35].

In 2011, Preti *et al*. demonstrated the ability of Au black (gold black) [22][35][37] to catalyze the hydrogenation of supercritical CO_2 towards formic acid using triethylamine as a base. In their work, rapid deactivation of gold black due to particle sintering was observed. However, Au supported on titania showed a remarkable stability for 37 days at temperatures of 40 degrees Celsius [23]. Following the promising results obtained by Preti *et al.,* Hensen *et al.* [24] studied gold-based colloidal nanoparticles and gold supported on a wide selection of metal oxides, basic Mg-Al supports and Mg-Cr hydrotalcite supports. Here, it was concluded that besides the nature of the support, also the support itself is of vital importance, as no FA production was observed for the colloidal nanoparticles, thus proposing the reaction to occur at the metal-support interface. Upon comparison of Au/Al_2O_3 and Au/TiO_2 catalysts of similar loading and particle size at non-supercritical pressures, the

Au/Al_2O_3 catalyst showed a nearly two-fold activity with no signs of catalyst deactivation.

While no catalyst deactivation was observed by previous works for gold based catalysts at supercritical conditions and moderate temperatures (> 90 bar and 40-90 ºC) [23][38] and non-supercritical conditions at 40 ºC [24], Chapter 4 revealed significant catalyst deactivation of an Au/TiO_2 catalyst at 40 bar and 70 ºC in a packed bed reactor using a wide range of tertiary amine bases. The cause of deactivation was shown to be rapid nanoparticle sintering over a period of 2 hours, followed by stable catalyst activity up to 50 hours during a 50 hour time-on-stream experiment.

Doping the mono-metallic catalyst with a second noble metal has been shown to result in significant increases in catalyst stability, with promising results obtained for Au-Pd [33][39][40], Co-Pd [34] and Pd-Ag [42] formulations. Barlocco *et al.* reported an enhanced activity, selectivity, and stability for Au-Pd bimetallic catalysts over their mono-metallic counterparts in the dehydrogenation of formic acid at room temperature due to mitigating the sintering of Pd nanoparticles [43]. Similarly, Grad *et al*. observed significantly lower FA decomposition activation energies for an Au-Pd/carbon catalyst compared to the mono-metallic Pd counterpart [44]. Several groups also reported an enhanced CO poisoning tolerance for Au-Pd/C catalysts [44][45]. Besides the usage of precious noble metals, Cu/TiO_2 was previously demonstrated in the direct hydrogenation of CO_2, displaying a TOF of 1.8 h^{-1}. However, significant catalyst deactivation was observed [46]. Alternatively, the incorporation of Ni was illustrated to have a potentially high activity in FA decomposition based on DFT and microkinetic modelling [47].

In this work, we have evaluated a number of mono-metallic (Au/TiO_2, Au/Al_2O_3, Pd/Al_2O_3 and Ru/Al_2O_3) and bimetallic catalysts ($Au\text{-}Pd/Al_2O_3$, $Au\text{-}Ni/Al_2O_3$, and $Au\text{-}Cu/Al_2O_3$) in terms of productivity, selectivity and stability. Due to the low CO_2 hydrogenation kinetic rates observed in Chapters 3 and 4, it was opted to perform the initial screening using the of decomposition of formic acid – triethylamine adduct.

These experiments were performed in batch reactors for the bimetallic catalysts. Following the identification of the most promising catalysts in terms stability and selectivity, CO_2 hydrogenation high pressure fixed bed experiments were conducted using triethylamine and diethylethanolamine as reactive bases. Within Chapter 4, it was discovered that alcohol substituted amines allowed for a near doubling of kinetic rates compared to triethylamine, motivating the kinetic tests using diethylethanolamine as extractive base with bimetallic catalysts.

5.2 Experimental materials and methods

5.2.1. Materials

Au/TiO_2 and Au/Al_2O_3 cylindrical catalyst pellets (AURO*lite*) were purchased from Strem Chemicals, Inc. (TiO_2 supported: 1 wt.% Au, *dp* = 2.6 nm) (Al_2O_3 supported: 1 wt.% Au, *dp* = 1.9 nm), Pd/Al_2O_3 (1 wt.% Pd, d_p = 3.5 nm) and Ru/Al_2O_3 (5 wt.% Ru) from Thermo Scientific. Dibromomethane (>99.9%, stabilized with butylhydroxytoluene) was purchased from TCI chemicals.

Chloroauric acid trihydrate ($HAuCl_4 \cdot 3\ H_2O$) (99.995%), palladium(II) chloride ($PdCl_2$) (99%), nickel(II) acetylacetonate ($Ni(acac)_2$) (95%) and γ-alumina powder (99.9%) were purchased from Sigma Aldrich. Copper (II) nitrate trihydrate ($Cu(NO_3)_2 \cdot 3\ H_2O$) (99%) was supplied by Fischer Scientific. N,N-diethylethanolamine (>99%) was received from Merck, 1-decanol (>98%) from Thermo Scientific Chemicals, formic acid (>99%) and triethylamine (>99.5%) from Sigma-Aldrich.

The chemicals used for H-NMR and ICP analysis are: acetonitrile-d_3, obtained from Thermo Scientific Chemicals (> 99 atom% D). 1,3,5-Trimethoxybenzene from TCI Chemicals (> 98.0%). Gold standard for ICP from Fluka TraceCERT Ultra (1002 ppm). Hydrofluoric acid EMSURE (48%), nitric acid (65%) EMPLURA (>99.9%) and hydrochloric acid (37%) a.c.s. reagent and sulfuric acid (98%) from Merck.

All materials were used as received, handled in air and used without any additional purification. In order to prevent catalyst deactivation, the commercially obtained catalysts were stored under Ar in a cold and dark environment.

5.2.2. Catalyst preparation

Au/TiO_2, Au/Al_2O_3, Pd/Al_2O_3 and Ru/Al_2O_3 were commercially obtained. All other materials were synthesized using the deposition-precipitation technique with NaOH as precipitation agent, based on protocols described elsewhere [48]–[50]. All metal precursors were selected based on their excellent water solubilities. In a typical procedure, a 10 g/L suspension containing γ-alumina in water was prepared. The suspension temperature was raised to 70 ºC. To ensure proper metal precursor dispersion, the metal precursor was added dropwise using a burette. Once a stable suspension is obtained, the NaOH is added dropwise until the desired pH is reached. The mixture is stirred for 1 hour while shielded from light to prevent bulk precipitation of the gold. Afterwards, the mixture is quenched using an ice bath. In order to remove any residual Cl^- ions, the catalyst is washed 5 times using DI-water. The absence of Cl^- is confirmed using $Ag(NO)_3$. All catalysts were calcined in air at 250 ºC for 4 hours, followed by reduction for 3 hours in a 10 vol.% H_2 stream at a temperature of 300 ºC using a 2 ºC /min ramp rate. Commercial catalysts were reduced according to the same protocol.

5.2.3. Catalyst testing

Chapter 3 and 4 revealed the slow kinetic nature of CO_2 hydrogenation to formic acid, as well as the necessity of significant amounts of catalyst. For this reason, it was opted to perform an initial assessment of activity, selectivity and stability of the catalysts based on the decomposition of formic acid – triethylamine adducts in glass batch reactors. Details of the set-up and the validation of this approach are described in Chapter 4. CO_2 hydrogenation experiments were performed at elevated pressure in a stainless steel packed bed reactor, as described in Chapter 4.

Liquid samples were analyzed using ^{1}H-NMR (Bruker, 400 MHz) to determine their chemical composition. Here, 0.5 mL of deuterated solvent (acetonitrile-d_3) and 1,3,5-trimethoxybenzene or dibromomethane as internal standard were mixed with 0.1 ml of sample. The gaseous reaction products were analyzed with a compact gas chromatograph (Global Analyser Solution) equipped with a TCD detector and two -

packed columns (Molsieve 5A and Rt-Q-BOND). The lower detection limit for CO was established to be 2 ppm.

5.2.3. Catalyst characterization

Metal loadings of fresh and spent catalysts were determined using ICP-OES (iCAP™ PRO ICP-OES; Thermo Scientific™). TiO_2 supported catalysts were digested using a mixture of concentrated HF (3 ml) and aqua regia (6 ml) at elevated temperatures [52]. Al_2O_3 supported catalysts were digested based on a two-step protocol, based on the work of [24]: the active metals were digested in aqua regia at 60 ºC for 2 hours, followed by digestion of the γ-alumina through the addition of 1 ml of DI water and 1 ml of concentrated H_2SO_4 at 70 ºC. After digestion, the samples were filtered and diluted using double distilled water. All ICP results were averaged over 3 lines with each measurement performed 3 times.

Particle sizes were obtained based on TEM and HAADF-STEM measurements performed on a FEI CryoTitan transmission electron microscope operating at 300 kV. Samples were prepared by finely crushing the sample, followed by ultrasonic suspension in ethanol and dispersion over a Cu grid with holey carbon film. The particles were individually identified using the image software ImageJ and the particle size distribution of each catalyst sample was quantified accordingly through the measurement of at least 50 particles.

5.3 Results and discussion

5.3.1 Formic acid decomposition

First the catalytic performance of a series of bimetallic Au-based catalysts were evaluated for the decomposition of formic acid – triethylamine adducts, as depicted in Figure 5.1 and 5.2. A blank test without the presence of a catalyst revealed no thermal formic acid decomposition at the studied conditions. The usage of Al_2O_3 and TiO_2 without additional metals present did also not result in any observable FA decomposition. The molar ratio between Au and the second metal (Cu, Ni or Pd), as well as the total loading of the catalysts based on ICP-OES measurements is shown in Table D1-4. Previous works have shown the FA decomposition reaction over an

Au/TiO_2 catalyst to be 100% selective towards CO_2 and hydrogen [23][29][39] thus depicting the thermodynamic equilibrium conversion of the studied system where no CO production occurs. Reproducibility experiments performed at 70 ºC established the equilibrium conversion to be 39.7 ± 3.0 %, with individual experiments tabulated in Table D5. The formation of gaseous products resulted in a pressure increase of approximately 0.75 bar. The low standard deviation also confirms the reproducibility of the batch and ^{1}H-NMR methods.

Figure 5.1 reveals full FA conversion for all Au-Cu/Al_2O_3 catalysts, irrespective of the Au:Cu molar ratio, therefore suggesting significant CO production through the dehydration pathway. Contrarily, conversions below the thermodynamic limit are observed for all Au:Ni molar ratios in steady-state conditions. Such behaviour is a clear indication of rapid catalyst deactivation, as the observed reaction rate is reduced to zero before reaching the thermodynamic limit.

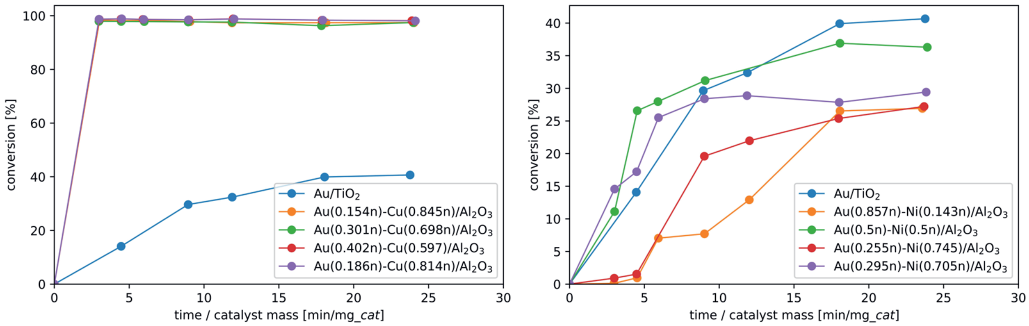

Figure 5.1: Formic acid conversion versus time for Au-Cu/Al_2O_3 (left) and Au-Ni/ Al_2O_3 (right) catalysts of several active metal molar ratios (n) in glass batch reactors (20 ml). Conditions: 1:1 molar ratio FA:amine, with a total formic acid concentration of 1 mol/liter using 1-decanol as solvent and triethylamine as base. Temperature was 70 degrees Celsius, catalyst mass 10 ± 0.2 mg. The total batch time is 4 hours.

Au-Pd/Al_2O_3 catalysts were studied at two different temperatures, namely 50 and 70 ºC. The performance of several molar ratio Au-Pd/Al_2O_3 catalysts at 50 ºC is compared to mono-metallic Au/TiO_2, Au/Al_2O_3 and Pd/Al_2O_3, with the FA conversion shown in Figure 5.2.

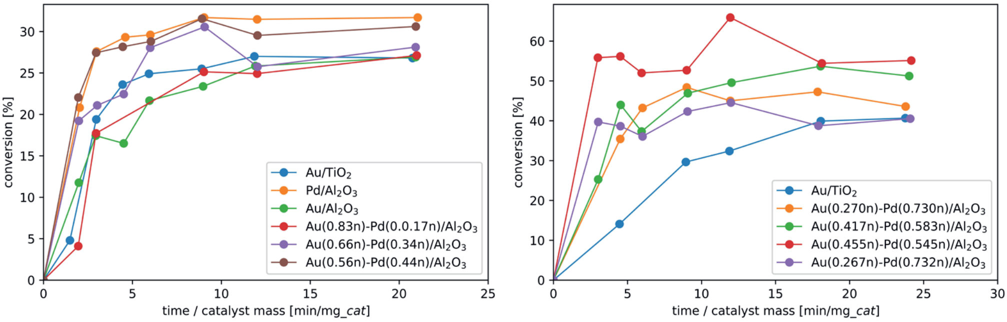

Figure 5.2: Formic acid conversion versus time for several molar ratio Au-Pd/Al_2O_3 at 50 ºC (left) and Au-Pd/ Al_2O_3 at 70 ºC (right) catalysts in glass batch reactors (20 ml). Conditions: 1:1 molar ratio FA:amine, with a total formic acid concentration of 1 mol/liter using 1-decanol as solvent and triethylamine as base. Catalyst mass 10 ± 0.4 mg. The total batch time is 4 hours.

Here, it is observed that Au supported on alumina and low Pd concentration Au-Pd bimetallic catalysts are able to perform FA decomposition with similar selectivity and conversion rates as Au/TiO_2, as evidenced by the observed steady state conversion being equal to the thermodynamic limit. An increase in catalyst activity is discerned with an increase in Pd molar ratio, with the 0.56:0.44 molar ratio Au:Pd showing similar kinetic behavior as the Pd/Al_2O_3 catalyst. Besides similar FA conversion rates, both catalysts achieve FA conversions that surpass the thermodynamic limit, indicating the production of CO as a byproduct. The formation of an apparent equilibrium in these cases is most likely the result of catalyst deactivation. Similar to the Au-Ni/Al_2O_3 catalysts, the high ratio Pd catalyst and the mono-metallic Pd catalyst seem to rapidly deactivate. Upon increasing the temperature to 70 ºC, similar trends are observed.

5.3.2 Formic acid production

In Chapter 4, CO_2 hydrogenation using Au-based monometallic catalysts in a flow reactor highlighted significant catalyst deactivation caused by sintering of the Au nanoparticles after exposure to formic acid – tertiary amine adducts with and without solvents [39]. Therefore, to gain a deeper understanding into the influence of the amount of tertiary amine present on the sintering of Au nanoparticles supported on titania, high-pressure packed bed experiments were performed using several triethylamine:1-decanol volumetric ratios as well solventless experiments using diethylethanolamine.

Figure 5.3 shows an increase in formic acid productivity with an increasing amount of triethylamine, which is in line with previous observations [24]. Inline GC measurements revealed no CO was produced above the lower detection limit, thereby confirming the 100% selectivity reported in previous works [23][29][39]. However, for all ratios of triethylamine:1-decanol as well as the solventless case using diethylethanolamine, initially a decrease in catalyst activity is observed, followed by stable formic acid productivity.

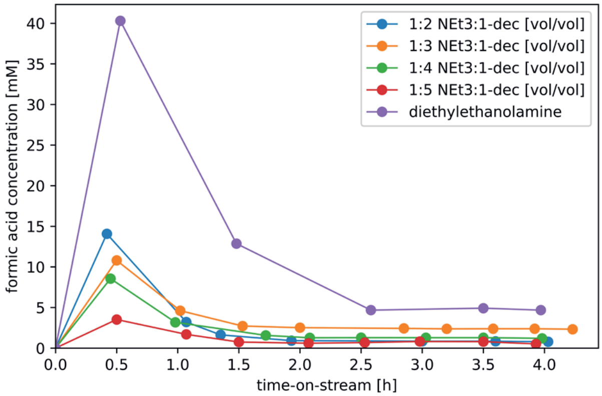

Figure 5.3: Several ratios of triethylamine (NEt_3) to 1-decanol (solvent) using a commercial Au/TiO_2 catalyst. Experiments performed in a continuous flow reactor performing in CO_2 hydrogenation mode. The catalyst was replaced each test. Employed conditions: 2.5 g of catalyst, 70 degrees Celsius, 40 bar total pressure and a CO_2:H_2 feed ratio of 1:1 at 1 mln/min. Liquid flowrate was 1 ml/min (resulting residence time approximately 10 minutes)

Deactivation of Au-based catalysts is often attributed to sintering of Au particles and the formation and subsequent accumulation of carbonate species on the catalyst surface [53]. TEM measurements confirmed agglomeration of the Au particles for all amine:solvent ratios, with particle sizes increasing from 2.6 nm up to 9.6 nm, as summarized in Table 5.1. Exemplary TEM images and particle size distributions are shown in Figure D1. No trend can be distinguished between the amine:solvent ratio and the final nanoparticle size. The leaching of Au was excluded based on ICP measurements summarized in Table 5.1.

	Particle size [nm]	Catalyst loading [wt%]
Fresh catalyst	2.6 ± 0.8	1.01 ± 0.01
1:2 vol/vol	7.4 ± 3.3	1.00 ± 0.02
1:3 vol/vol	9.6 ± 3.7	0.99 ± 0.04
1:4 vol/vol	6.1 ± 2.2	1.01 ± 0.01
1:5 vol/vol	6.9 ± 2.7	0.99 ± 0.01
Diethylethanolamine (no solvent)	9.1 ± 3.2	0.99 ± 0.03

Table 5.1: Formic acid production post-mortem particle size of a 1 wt% Au/TiO_2 catalyst (obtained from TEM) and catalyst loading (obtained from ICP-OES). Reaction time was 4 hours at 70 degrees Celsius.

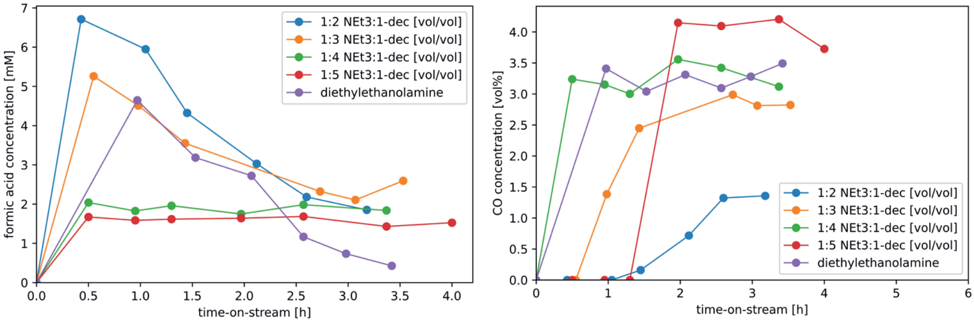

Figure 5.4: Several ratios of triethylamine (NEt_3) to 1-decanol (solvent) using a commercial Pd/Al_2O_3 catalyst. Experiments performed in a continuous flow reactor performing in CO_2 hydrogenation mode. The catalyst was replaced each test. Employed conditions: 2.5 g of catalyst, 70 degrees Celsius, 40 bar total pressure and a CO_2:H_2 feed ratio of 1:1 at 1 mln/min. Liquid flowrate was 1 ml/min (resulting residence time approximately 10 minutes). The uncorrected CO outlet curve and selectivity data (F_{CO}/F_{FA}) is given in Figure D3.

The experiments were repeated using a commercially available Pd/Al_2O_3 catalyst. In Figure 5.4, a similar trend is observed as for the Au/TiO_2 catalyst, with the initial formic acid productivity increasing with increasing ratios of triethylamine to solvent. For the solventless diethylethanolamine and the high volumetric ratios of triethylamine, a 1:2 and 1:3 volumetric ratio of triethylamine to 1-decanol, a clear decrease in catalyst activity as a function of time-on-stream is discerned. Contrary to the Au-based catalyst, no regime of constant productivity is reached, highlighting a slower and continuous catalyst deactivation mechanism.

The employment of low triethylamine:solvent (1:4 and 1:5) ratio results in constant catalyst activity. Similar continuous catalyst deactivation behaviour was reported by Lefferts *et al*. for FA decomposition in aqueous media and was shown to be induced by CO poisoning [54]. Continuous catalyst deactivation was also observed by Upadhye *et al*. during FA decomposition, and was attributed to the formation of palladium hydrides [55]. Alternatively, Hu *et al.* propose competitive adsorption and thus occupation of active sites by intermediate species to be responsible for the Pd catalyst deactivation [56]. In line with findings of previous works [33][45], the selectivity of the Pd-based mono-metallic catalysts was found to be below 100%, with CO production observed for all amine:solvent ratios. No other gaseous hydrocarbons such as methane or ethylene were detected. Due to the presence of a large volume gas-liquid separation vessel (500 ml) within the experimental set-up, the gaseous phase requires much longer experimental times to reach steady state conditions than the liquid phase, with current experimental times not allowing to reach steady state performance. In order to correct for this, the gas-liquid separator was modelled as an unsteady state CSTR to calculate the CO concentration at the reactor outlet, with final equations shown in the Appendix D. The CO concentration as measured by the GC is shown in Appendix D, Figure 3. As shown in Figure 5.4, the amount of CO produced is inversely proportional to the amine:solvent ratio, with larger amounts of triethylamine resulting in higher selectivity towards formic acid production.

Catalyst characterization, as shown in Table 5.2, revealed no significant leaching (ICP-OES) and very minor nanoparticle agglomeration (TEM) for any amine:solvent ratio, while only exposure to diethylethanolamine resulted in significant (~10%) leaching of Pd. Interestingly, the amine:decanol mixtures resulting in the highest CO productivity and lowest FA productivity show constant catalyst activity towards FA during 4 hours time-on-stream, making it unlikely that CO poisoning is the sole deactivation mechanism.

	Particle size [nm]	Catalyst loading [wt%]
Fresh catalyst	3.4 ± 1.0	0.91 ± 0.02
1:2 vol/vol	5.7 ± 2.5	0.90 ± 0.04
1:3 vol/vol	3.6 ± 0.9	0.91 ± 0.05
1:4 vol/vol	3.8 ± 1.0	0.92 ± 0.03
1:5 vol/vol	4.1 ± 1.5	0.93 ± 0.01
Diethylethanolamine (no solvent)	4.1 ± 1.8	0.79 ± 0.02

Table 5.2: Post-mortem particle size of a 0.9 wt Pd/Al_2O_3 catalyst (obtained from TEM) and catalyst loading (obtained from ICP-OES). Reaction time was 4 hours at 70 degrees Celsius.

5.3.3 CO_2 hydrogenation: comparison of catalysts

Based on the catalyst activity and stability observed during the formic acid decomposition reaction, $Au\text{-}Pd/Al_2O_3$ was selected to further test in the direct CO_2 hydrogenation. The decomposition results shown in Section 5.3.1 revealed an Au:Pd molar ratio of 3:1 to result in significant increased catalyst activities while maintaining selectivity towards H_2 and CO_2. This catalyst was compared to mono-metallic Au-based catalysts supported on titania and alumina, Pd/Al_2O_3 of similar active metal loadings and a 5 wt% Ru/Al_2O_3 catalyst, as shown in Figure 5.5. A triethylamine:1-decanol ratio of 1:2 was selected.

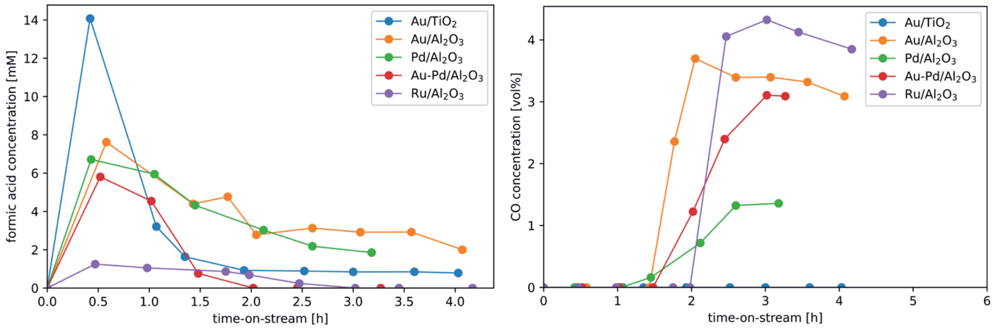

Figure 5.5: Comparison of catalysts using a 1:2 vol/vol triethylamine: 1-decanol ratio. Experiments performed in a continuous flow reactor performing in CO_2 hydrogenation mode. Employed conditions: 2.5 g of catalyst, 70 degrees Celsius, 40 bar total pressure and a CO_2:H_2 feed ratio of 1:1 at 1 mln/min. Liquid flowrate was 1 ml/min (resulting residence time approximately 10 minutes). The uncorrected CO outlet curve and selectivity data (F_{CO}/F_{FA}) is given in Figure D4.

Comparable initial FA productivity is observed for the Au, Pd and Au-Pd catalysts supported on alumina, while the Ru/Al_2O_3 catalyst has low (<1 mM) selectivity towards FA. Furthermore, all alumina supported catalysts result in the unwanted production of CO, with the Ru-based catalyst yielding CO as the major product. While the Au catalyst supported on titania is fully selective towards FA, the alumina supported catalyst results in the production of significant amounts of CO. Previous works have highlighted the fact that the presence of alumina instead of titania could enhance the decomposition of formate species. Here, it was shown that the Au nanoparticles themselves do not contribute to formate decomposition, but that the decomposition is strongly influenced by the acidity of the catalyst support with the introduction of Au on alumina resulting in the formation of CO via FA [57]. Also, it was shown by Laszlo *et al*. that Au/TiO_2 catalysts do not produce CO via the rWGS or formate decomposition at temperatures below 450 K [58].

Interestingly, while the FA productivity and rate of deactivation for Au and Pd supported on alumina are comparable, the Pd-based catalyst is found to have a higher selectivity towards FA as evident from the much lower CO production rates. Catalyst deactivation is observed for all studied catalysts with the FA productivity reducing to zero for the $Au\text{-}Pd/Al_2O_3$ and Ru/Al_2O_3 catalysts, while Au/Al_2O_3 and Pd/Al_2O_3 have much lower rates of deactivation and do not show a steady FA productivity during the 4 hour time-on-stream experiments. No steady FA productivity is observed for these catalysts, but a steady CO productivity is found for the Au-Pd and Pd/Al_2O_3 catalysts, with CO productivity decreasing for the Au and Ru/Al_2O_3 catalysts, being indicative of total catalyst deactivation.

Section 5.3.1 showed the FA productivity of Au/TiO_2 in combination with diethylethanolamine as a base to be 3.8x higher than the 1:3 vol/vol triethylamine case, whilst the Pd/Al_2O_3 catalyst deactivated continuously. While significant increases in initial FA productivity are observed for Au/TiO_2 with the FA concentration increasing from 14 mM to 40 mM with diethylethanolamine as a base, this is not observed for Pd/ Al_2O_3 with FA productivity remaining equal to the productivity using a 1:2 vol/vol triethylamine:1-decanol mixture.

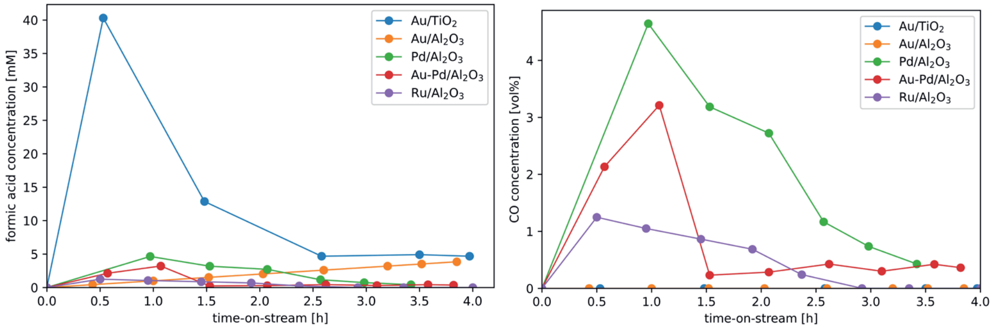

Figure 5.6: Comparison of catalysts using diethylethanolamine as a base. Experiments performed in a continuous flow reactor performing in CO_2 hydrogenation mode. Employed conditions: 2.5 g of catalyst, 70 degrees Celsius, 40 bar total pressure and a CO_2:H_2 feed ratio of 1:1 at 1 mln/min. Liquid flowrate was 1 ml/min (resulting residence time approximately 10 minutes*)*. The uncorrected CO outlet curve and selectivity data (F_{CO}/F_{FA}) is given in Figure D5.

As evident from Figure 5.6, the increase in FA productivity with diethylethanolamine as base is solely observed for Au based catalysts, while comparable or lower productivities observed for Pd and Ru based catalysts compared to the usage of triethylamine.

Besides an influence on FA productivity, the usage of diethylethanolamine instead of triethylamine also results in a significant influence on product selectivity. This becomes evident from Au-based catalyst being fully selective towards FA, with Au supported on alumina producing significant amounts of CO in combination with triethylamine. Furthermore, the initial catalyst activity of the Pd and Au-Pd catalysts remains comparable, with the Au-Pd bimetallic catalyst now being more selective towards FA than the Pd based catalyst. Full catalyst deactivation towards FA is observed for Pd/Al_2O_3, $Au-Pd/Al_2O_3$ and Ru/Al_2O_3 catalysts. While CO productivity was found to slightly decrease when using triethylamine, significant reduction in CO production was observed during the 4 hour experiments using diethylethanolamine.

5.4 Conclusion

Within this work the performance of several gold based bimetallic catalysts (Au-Cu, Au-Ni and Au-Pd supported on alumina) was evaluated for the direct hydrogenation of CO_2 towards formic acid.

Due to the slow kinetic nature of the hydrogenation reaction, it was opted to perform an initial screening of the bimetallic catalysts based on the formic acid decomposition reaction, comparing the conversion, selectivity and catalyst stability to Au/TiO_2. Here, it was found that Au-Cu based catalysts result in complete FA conversion for all Au:Cu molar ratios, therefore producing significant amounts of undesired CO. Au-Ni catalysts supported on alumina generally demonstrated poorer catalytic activity compared to mono-metallic gold on titania, with the catalysts showing significant deactivation, therefore suggesting the synergetic effects between gold and nickel or copper to be detrimental. Lastly, promising behavior in terms of catalysts activity and selectivity was observed for Au-Pd based catalysts with low Pd concentrations.

Performing CO_2 hydrogenation experiments at elevated pressures revealed significant catalyst deactivation for the mono-metallic Au/TiO_2 and Pd/Al_2O_3 catalysts. The influence of the triethylamine:1-decanol ratio on the catalyst deactivation was studied, identifying different deactivation mechanisms for the Au and Pd based catalysts. In case of Au supported on titania, the deactivation is caused by Au nanoparticle agglomeration. For Pd, the amount of CO produced was found to be inversely proportional to the amount of amine present within the reactive mixture. Stable FA productivity was observed for low amine:solvent ratios, making that the deactivation cannot solely be attributed to CO poisoning.

Testing under constant triethylamine:1-decanol ratio revealed comparable initial FA productivity for the Au, Pd and Au-Pd catalysts supported on alumina, while the Ru/Al_2O_3 catalyst has low (<1 mM) selectivity towards FA. Furthermore, all alumina supported catalysts result in the unwanted production of CO, with the Ru-based catalyst yielding CO as the major product. The replacement of triethylamine:1-decanol with diethylethanolamine was observed to result in an increase in FA productivity and selectivity for gold based catalysts, while Pd and Ru-based materials have comparable or lower FA productivity compared to when triethylamine is used.

Appendix D

D.1 Catalyst composition

Au loading [wt%]	Ni loading [wt%]	Molar Au:Ni ratio
1.98	0.11	0.85
0.93	0.16	0.69
0.46	0.52	0.26
0.81	0.67	0.30

Table D.1: Loading and active metal molar ratio for the Au-Ni/Al_2O_3 catalysts

Au loading [wt%]	Cu loading [wt%]	Molar Au:Cu ratio
0.57	0.27	0.40
0.56	0.42	0.30
0.58	0.51	0.27
0.53	0.75	0.19

Table D.2: Loading and active metal molar ratio for the Au-Cu/Al_2O_3 catalysts

Au loading [wt%]	Pd loading [wt%]	Molar Au:Pd ratio
0.58	0.11	0.46
0.65	0.15	0.42
0.44	0.30	0.27
0.81	0.52	0.26

Table D.3: Loading and active metal molar ratio for the Au-Pd/Al_2O_3 catalysts tested at 70 ºC

Au loading [wt%]	Pd loading [wt%]	Molar Au:Pd ratio
0.62	0.097	0.77
0.52	0.12	0.70
0.32	0.23	0.43

Table D.4: Loading and active metal molar ratio for the Au-Pd/Al_2O_3 catalysts tested at 50 ºC

D.2 Reproducibility formic acid decomposition

	FA conversion [-]
1	0.412
2	0.384
3	0.370
4	0.394
5	0.388
6	0.389
7	0.403
8	0.406
9	0.398

Table D.5: Reproducibility formic acid decomposition

D.3 GC calculations

Due to the presence of a large volume gas-liquid separation vessel (500 ml) within the experimental set-up, the gaseous phase requires much longer experimental times to reach steady state conditions than the liquid phase, with current experimental times not allowing to reach steady state performance. In order to correct for this, the gas-liquid separator was modelled as an unsteady state CSTR to calculate the CO concentration at the reactor outlet:

$$\frac{dN_a}{dt} = F_{a0} - F_a \qquad \mathrm{D.1}$$

with N_a the total amount of moles of species A and F_a the molar flowrate. Due to the liquid accumulating within the vessel, the gaseous volume is not constant. To correct for this, the average residence time in the sample interval is used:

$$\tau_{avg} = \frac{V_{vessel}}{F_v} = \frac{\tau_{sample} + \tau_{sample-1}}{2} \qquad \mathrm{D.2}$$

Here, V_{vessel} represents the volume of the gas liquid separator, F_v the gaseous volumetric flowrate and τ_{avg} the average residence time.

$$\int_{t=\tau_{avg}-1}^{\tau_{avg}} V_{vessel}\frac{dC_a}{dt} = \int_{C_{a(t-1)}}^{Ca} F_v C_{a0} - F_v C_a \qquad \mathrm{D.3}$$

$$C_{a0} = \frac{C_a}{\left(1- exp(\left(\frac{-t}{\tau_{avg}}\right)\right)} \tag{D.4}$$

D.4 TEM imaging

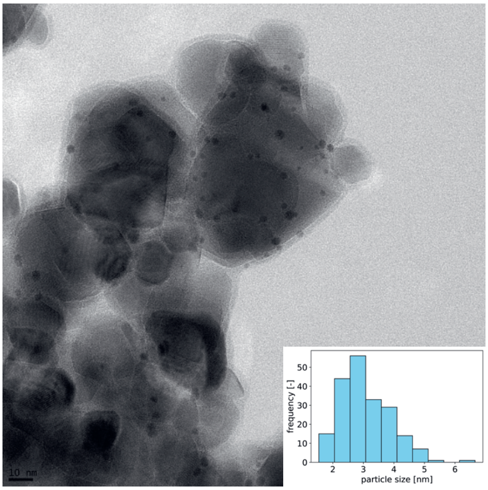

fresh Au/TiO₂

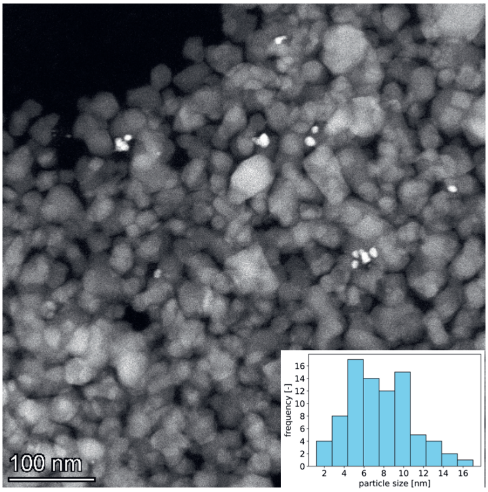

Au/TiO₂ exposed to 1:2 [vol/vol] triethylamine:1-decanol

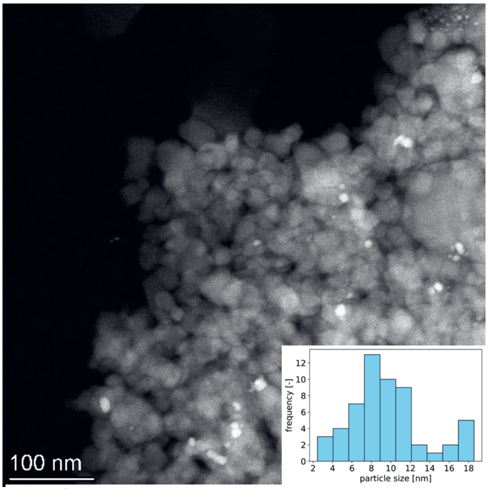

Au/TiO₂ exposed to 1:3 [vol/vol] triethylamine:1-decanol

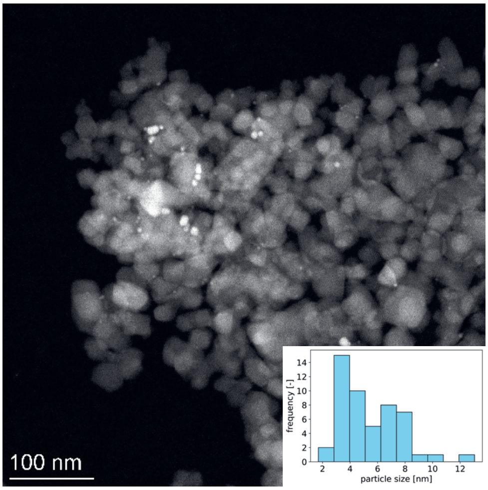

Au/TiO₂ exposed to 1:4 [vol/vol] triethylamine:1-decanol

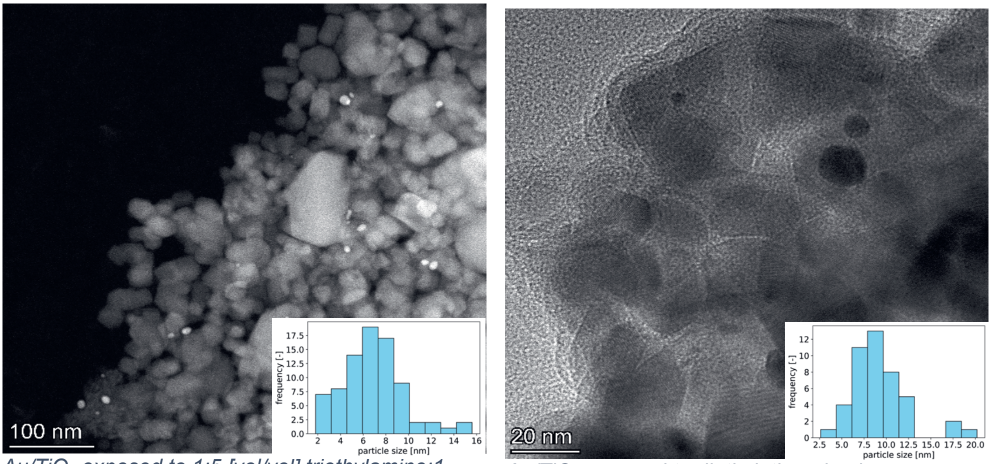

Au/TiO₂ exposed to 1:5 [vol/vol] triethylamine:1-decanol

Au/TiO₂ exposed to diethylethanolamine

Figure D1: TEM images and particle size distributions of Au/TiO_2 catalysts using in the direct hydrogenation of CO_2 to formic acid . Reaction time was 4 hours at 70 degrees

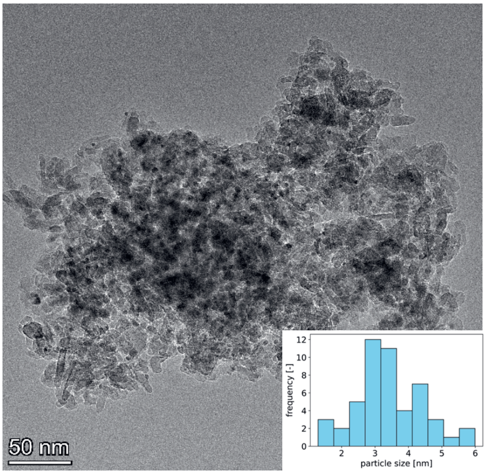

fresh Pd/Al₂O₃

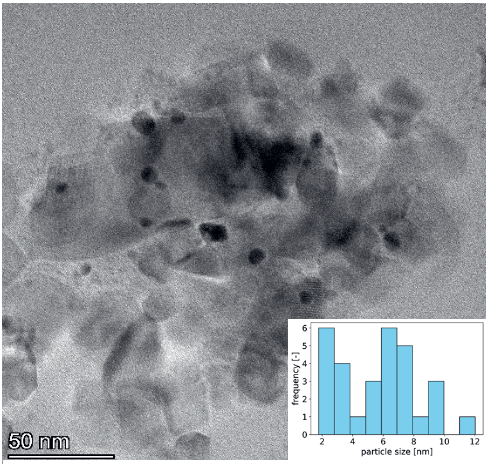

Pd/Al₂O₃ exposed to 1:2 [vol/vol] triethylamine:1-decanol

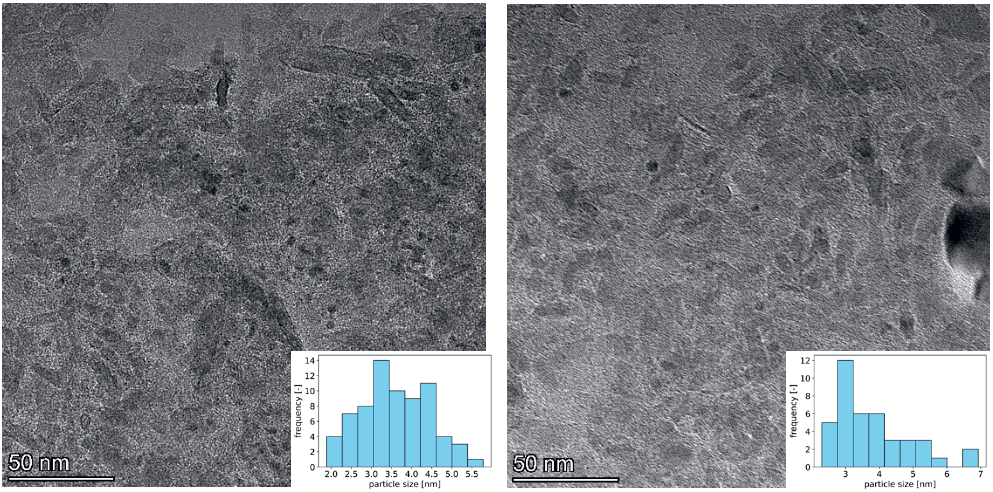

Pd/Al$_2$O$_3$ exposed to 1:3 [vol/vol] triethylamine:1-decanol

Pd/Al$_2$O$_3$ exposed to 1:4 [vol/vol] triethylamine:1-decanol

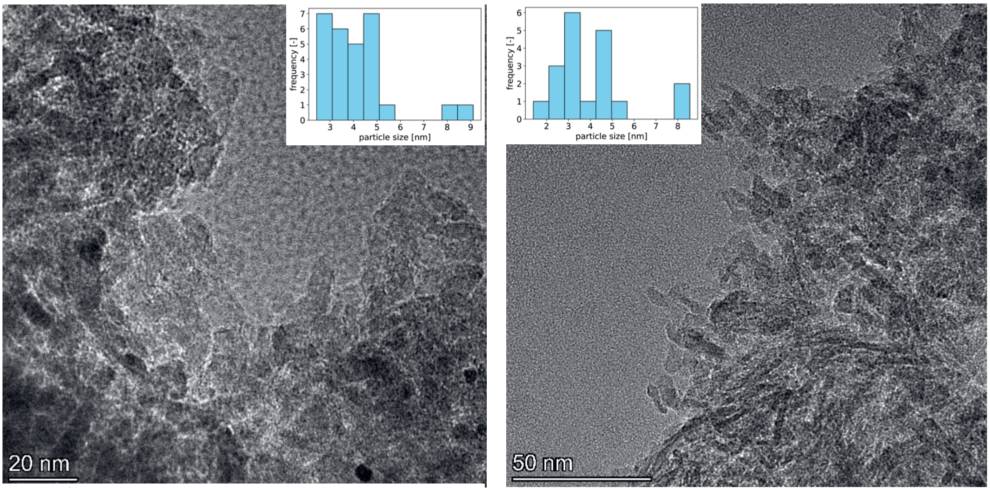

Pd/Al$_2$O$_3$ exposed to 1:5 [vol/vol] triethylamine:1-decanol

Pd/Al$_2$O$_3$ exposed to diethylethanolamine

Figure D2: TEM images and particle size distributions of Pd/Al$_2$O$_3$ catalysts using in the direct hydrogenation of CO$_2$ to formic acid. Reaction time was 4 hours at 70 degrees

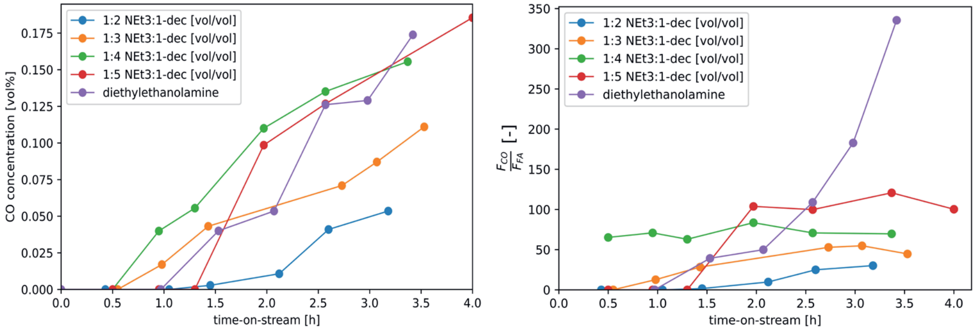

Figure D3: CO concentrations obtained from inline GC-TC before dilution correction for several ratios of triethylamine (NEt_3) to 1-decanol (solvent) using a commercial Pd/Al_2O_3 catalyst (left), and selectivity (F_{CO}/F_{FA}), with F the molar flow rate [mol/s] (right). Experiments performed in a continuous flow reactor performing in CO_2 hydrogenation mode. The catalyst was replaced each test. Employed conditions: 2.5 g of catalyst, 70 degrees Celsius, 40 bar total pressure and a CO_2:H_2 feed ratio of 1:1 at 1 mln/min. Liquid flowrate was 1 ml/min (resulting residence time approximately 10 minutes).

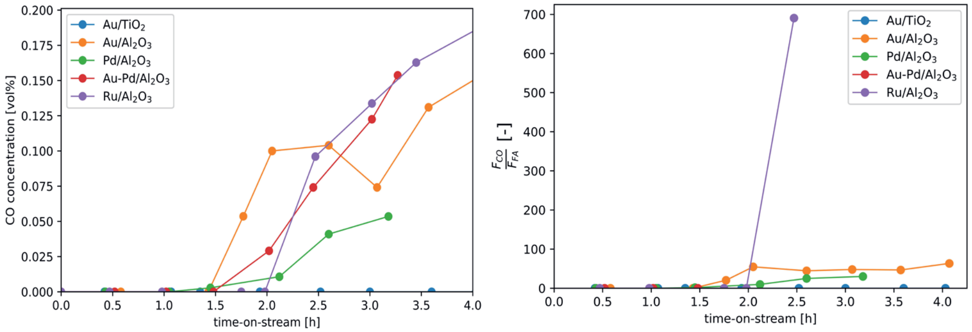

Figure D4: CO concentrations obtained from inline GC-TC before dilution correction for the comparison of catalysts using a 1:2 vol/vol triethylamine: 1-decanol ratio (left), and selectivity (F_{CO}/F_{FA}), with F the molar flow rate [mol/s] (right). Experiments performed in a continuous flow reactor performing in CO_2 hydrogenation mode. Employed conditions: 2.5 g of catalyst, 70 degrees Celsius, 40 bar total pressure and a CO_2:H_2 feed ratio of 1:1 at 1 mln/min. Liquid flowrate was 1 ml/min (resulting residence time approximately 10 minutes).

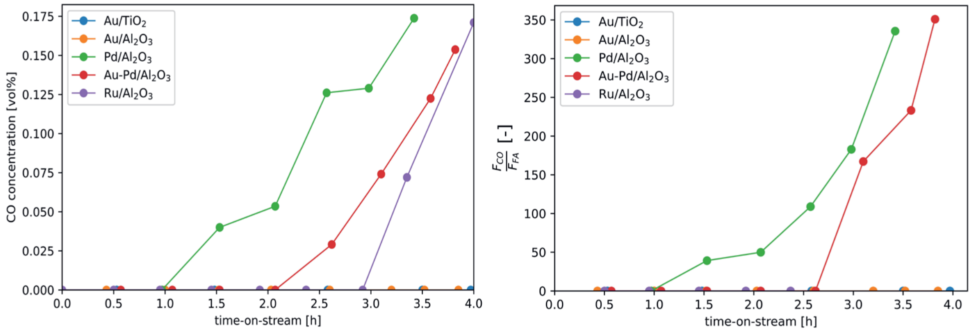

Figure D5: CO concentrations obtained from inline GC-TC before dilution correction for the comparison of catalysts using diethylethanolamine as a base (left), and selectivity (F_{CO}/F_{FA}) with F the molar flow rate [mol/s] (right). Experiments performed in a continuous flow reactor performing in CO_2 hydrogenation mode. Employed conditions: 2.5 g of catalyst, 70 degrees Celsius, 40 bar total pressure and a CO_2:H_2 feed ratio of 1:1 at 1 mln/min. Liquid flowrate was 1 ml/min (resulting residence time approximately 10 minutes). Uncorrected CO outlet curve given in Figure D5.

References

[1] A. Buis, “The Atmosphere: Getting a Handle on Carbon Dioxide.” https://science.nasa.gov/earth/climate-change/greenhouse-gases/the-atmosphere-getting-a-handle-on-carbon-dioxide/ (accessed Jun. 18, 2024).

[2] N. A. Rashidi, S. Yusup, and A. Borhan, “Isotherm and Thermodynamic Analysis of Carbon Dioxide on Activated Carbon,” *Procedia Eng.*, vol. 148, pp. 630–637, 2016, doi: 10.1016/j.proeng.2016.06.527.

[3] S. Selosse and O. Ricci, “Carbon capture and storage: Lessons from a storage potential and localization analysis,” *Appl. Energy*, vol. 188, pp. 32–44, 2017, doi: 10.1016/j.apenergy.2016.11.117.

[4] S. Saeidi *et al.*, “Recent advances in CO2 hydrogenation to value-added products — Current challenges and future directions,” *Prog. Energy Combust. Sci.*, vol. 85, p. 100905, 2021, doi: 10.1016/j.pecs.2021.100905.

[5] S. Poto, T. Vink, P. Oliver, F. Gallucci, and M. F. Neira D’angelo, “Techno-economic assessment of the one-step CO2conversion to dimethyl ether in a membrane-assisted process,” *J. CO2 Util.*, vol. 69, no. February, p. 102419, 2023, doi: 10.1016/j.jcou.2023.102419.

[6] X. Ye *et al.*, “Highly selective hydrogenation of CO2to ethanol via designed bifunctional Ir1-In2O3Single-atom catalyst,” *J. Am. Chem. Soc.*, vol. 142, no. 45, pp. 19001–19005, 2020, doi: 10.1021/jacs.0c08607.

[7] R. P. Ye *et al.*, “CO2 hydrogenation to high-value products via heterogeneous catalysis,” *Nat. Commun.*, vol. 10, no. 1, 2019, doi: 10.1038/s41467-019-13638-9.

[8] J. Hietala, A. Vuori, P. Johnsson, P. Ilkka, W. Reutemann, and H. Kieczka, “Formic acid,” *Ullmann’s Encycl. Ind. Chem.*, vol. A12, no. 29, pp. 1–12, 2016, doi: 10.1002/14356007.a12.

[9] G. H. Gunasekar, J. Shin, K. D. Jung, K. Park, and S. Yoon, “Design Strategy toward Recyclable and Highly Efficient Heterogeneous Catalysts for the Hydrogenation of CO2 to Formate,” *ACS Catal.*, vol. 8, no. 5, pp. 4346–4353, 2018, doi: 10.1021/acscatal.8b00392.

[10] A. Álvarez *et al.*, “Challenges in the Greener Production of Formates/Formic Acid, Methanol, and DME by Heterogeneously Catalyzed CO2 Hydrogenation Processes,” *Chem. Rev.*, vol. 117, no. 14, pp. 9804–9838, 2017, doi: 10.1021/acs.chemrev.6b00816.

[11] S. E. Sanni *et al.*, “Strategic examination of the classical catalysis of formic acid decomposition for intermittent hydrogen production, storage and supply: A review,” *Sustain. Energy Technol. Assessments*, vol. 45, no. December 2020, p. 101078, 2021, doi: 10.1016/j.seta.2021.101078.

[12] S. Schlussel and S. Kwon, “A review of formic acid decomposition routes on transition metals for its potential use as a liquid H2 carrier,” *Korean J. Chem. Eng.*, vol. 39, no. 11, pp. 2883–2895, 2022, doi: 10.1007/s11814-022-1276-z.

[13] P. Riquelme-Garcia, “Hydrogen Storage System Attained by HCOOH-CO 2 Couple : Recent Developments in Pd-Based Carbon-Supported Heterogeneous catalysts,” *Energies*, vol. 17, no. 260, 2024, doi: https://doi.org/10.3390/en1701026

[14] T. M. Suzuki, T. Takayama, S. Sato, A. Iwase, A. Kudo, and T. Morikawa, “Enhancement of CO2 reduction activity under visible light irradiation over Zn-based metal sulfides by combination with Ru-complex catalysts,” *Appl. Catal. B Environ.*, vol. 224, no. November 2017, pp. 572–578, 2018, doi: 10.1016/j.apcatb.2017.10.053.

[15] K. Fernández-Caso, G. Díaz-Sainz, M. Alvarez-Guerra, and A. Irabien, "Electroreduction of CO2: Advances in the Continuous Production of Formic Acid and Formate," *ACS Energy Lett.*, vol. 8, no. 4, pp. 1992–2024, 2023, doi: 10.1021/acsenergylett.3c00489.

[16] C. Kim *et al.*, "Accelerating the net-zero economy with CO2-hydrogenated formic acid production: Process development and pilot plant demonstration," *Joule*, vol. 8, no. 3, pp. 693–713, 2024, doi: 10.1016/j.joule.2024.01.003.

[17] M. Pérez-Fortes, J. C. Schöneberger, A. Boulamanti, G. Harrison, and E. Tzimas, "Formic acid synthesis using CO2 as raw material: Techno-economic and environmental evaluation and market potential," *Int. J. Hydrogen Energy*, vol. 41, no. 37, pp. 16444–16462, 2016, doi: 10.1016/j.ijhydene.2016.05.199.

[18] K. Sordakis *et al.*, "Homogeneous Catalysis for Sustainable Hydrogen Storage in Formic Acid and Alcohols," *Chem. Rev.*, vol. 118, no. 2, pp. 372–433, 2018, doi: 10.1021/acs.chemrev.7b00182.

[19] S. Kushwaha, J. Parthiban, and S. K. Singh, "Recent Developments in Reversible CO2 Hydrogenation and Formic Acid Dehydrogenation over Molecular Catalysts," *ACS Omega*, vol. 8, no. 42, pp. 38773–38793, 2023, doi: 10.1021/acsomega.3c05286.

[20] M. S. Maru, S. Ram, R. S. Shukla, and N. ul H. Khan, "Ruthenium-hydrotalcite (Ru-HT) as an effective heterogeneous catalyst for the selective hydrogenation of CO2 to formic acid," *Mol. Catal.*, vol. 446, pp. 23–30, 2018, doi: 10.1016/j.mcat.2017.12.005.

[21] M. S. Maru, S. Ram, J. H. Adwani, and R. S. Shukla, "Selective and Direct Hydrogenation of CO2 for the Synthesis of Formic Acid over a Rhodium Hydrotalcite (Rh-HT) Catalyst," *ChemistrySelect*, vol. 2, no. 13, pp. 3823–

3830, 2017, doi: 10.1002/slct.201700130.

[22] A. Álvarez *et al.*, “Challenges in the Greener Production of Formates/Formic Acid, Methanol, and DME by Heterogeneously Catalyzed CO2 Hydrogenation Processes,” *Chem. Rev.*, vol. 117, no. 14, pp. 9804–9838, 2017, doi: 10.1021/acs.chemrev.6b00816.

[23] D. Preti, C. Resta, S. Squarcialupi, and G. Fachinetti, “Carbon dioxide hydrogenation to formic acid by using a heterogeneous gold catalyst,” *Angew. Chemie - Int. Ed.*, vol. 50, no. 52, pp. 12551–12554, 2011, doi: 10.1002/anie.201105481.

[24] G. A. Filonenko, W. L. Vrijburg, E. J. M. Hensen, and E. A. Pidko, “On the activity of supported Au catalysts in the liquid phase hydrogenation of CO2 to formates,” *J. Catal.*, vol. 343, pp. 97–105, 2016, doi: 10.1016/j.jcat.2015.10.002.

[25] G. Yan, Z. Gao, M. Zhao, W. Yang, and X. Ding, “CO2 hydrogenation to formic acid over platinum cluster doped defective graphene: A DFT study,” *Appl. Surf. Sci.*, vol. 517, no. December 2019, p. 146200, 2020, doi: 10.1016/j.apsusc.2020.146200.

[26] Z. Y. Hu, L. H. Luo, C. Shang, and Z. P. Liu, “Free Energy Pathway Exploration of Catalytic Formic Acid Decomposition on Pt-Group Metals in Aqueous Surroundings,” *ACS Catal.* , pp. 7684–7695, 2024, doi: 10.1021/acscatal.4c00959.

[27] H. Song, N. Zhang, C. Zhong, Z. Liu, M. Xiao, and H. Gai, “Hydrogenation of CO2 into formic acid using a palladium catalyst on chitin,” *New J. Chem.*, vol. 41, no. 17, pp. 9170–9177, 2017, doi: 10.1039/c7nj00460e.

[28] Q. Li *et al.*, “Highly Efficient Hydrogenation of CO2 to Formic Acid over

Palladium Supported on Dication Poly(ionic liquid)s," *Mol. Catal.*, vol. 509, no. May, p. 111644, 2021, doi: 10.1016/j.mcat.2021.111644.

[29] K. Park *et al.*, "CO2 hydrogenation to formic acid over heterogenized ruthenium catalysts using a fixed bed reactor with separation units," *Green Chem.*, vol. 22, no. 5, pp. 1639–1649, 2020, doi: 10.1039/c9gc03685g.

[30] B. D. Bankar, D. R. Naikwadi, R. J. Tayade, and A. V Biradar, "Direct hydrogenation of CO 2 to formic acid using Ru supported Co 3 O 4 oxide as an efficient heterogeneous catalyst," *Mol. Catal.*, vol. 535, no. July 2022, p. 112875, 2023, doi: 10.1016/j.mcat.2022.112875.

[31] T. H. Karlsruhe, B. Alkalimetalle, D. Gegenwart, B. Energiemengen, and B. Fermentea, "541 - 81.," vol. 1212, 1914.

[32] G. Liu *et al.*, "CO2 Hydrogenation to Formate and Formic Acid by Bimetallic Palladium-Copper Hydride Clusters," *J. Am. Chem. Soc.*, vol. 142, no. 17, pp. 7930–7936, 2020, doi: 10.1021/jacs.0c01855.

[33] Y. Wang, M. Dong, S. Li, B. Chen, H. Liu, and B. Han, "The superiority of Pd2+ in CO2 hydrogenation to formic acid," *Chem. Sci.*, vol. 15, no. 15, pp. 5525–5530, 2024, doi: 10.1039/d3sc06925g.

[34] J. L. Santos, C. León, G. Monnier, S. Ivanova, M. Á. Centeno, and J. A. Odriozola, "Bimetallic PdAu catalysts for formic acid dehydrogenation," *Int. J. Hydrogen Energy*, vol. 45, no. 43, pp. 23056–23068, 2020, doi: 10.1016/j.ijhydene.2020.06.076.

[35] S. P. Hill and J. M. Winterbottom, "The conversion of polysaccharides to hydrogen gas. Part I: The palladium catalysed decomposition of formic acid/sodium formate solutions," *J. Chem. Technol. Biotechnol.*, vol. 41, no. 2, pp. 121–133, 1988, doi: 10.1002/jctb.280410205.

[36] G. Fachinetti and D. Preti, “PROCESS FOR PREPARING FORMIC ACID,” WO 2012/168396 Al, 2012.

[37] D. Preti, S. Squarcialupi, and G. Fachinetti, “Production of hcooh/net3 adducts by co2/h2 incorporation into neat NEt3,” *Angew. Chemie - Int. Ed.*, vol. 49, no. 14, pp. 2581–2584, 2010, doi: 10.1002/anie.200906054.

[38] Q. Liu *et al.*, “Direct catalytic hydrogenation of CO2 to formate over a Schiff-base-mediated gold nanocatalyst,” *Nat. Commun.*, vol. 8, no. 1, 2017, doi: 10.1038/s41467-017-01673-3.

[39] A.W.N. de Leeuw den Bouter, L.M.P. Meijer, L.Brito , A. Miquelot, P.Oliver, J. van der Schaaf “Effect of tertiary amine selection on CO2 to formic acid hydrogenation with Au-np catalyst,” *Prep.*

[40] D. Liu, Z. Y. Gao, X. C. Wang, J. Zeng, and Y. M. Li, “DFT study of hydrogen production from formic acid decomposition on Pd-Au alloy nanoclusters,” *Appl. Surf. Sci.*, vol. 426, pp. 194–205, 2017, doi: 10.1016/j.apsusc.2017.07.165.

[41] Z. Zhao, K. N. Heck, P. Limpornpipat, H. Qian, J. T. Miller, and M. S. Wong, “Hydrogen-generating behavior of Pd-decorated gold nanoparticles via formic acid decomposition,” *Catal. Today*, vol. 330, no. December 2017, pp. 24–31, 2019, doi: 10.1016/j.cattod.2018.06.044.

[42] K. Mori, T. Sano, H. Kobayashi, and H. Yamashita, “Surface Engineering of a Supported PdAg Catalyst for Hydrogenation of CO 2 to Formic Acid: Elucidating the Active Pd Atoms in Alloy Nanoparticles,” *J. Am. Chem. Soc.*, vol. 140, no. 28, pp. 8902–8909, 2018, doi: 10.1021/jacs.8b04852.

[43] I. Barlocco *et al.*, “Disclosing the Role of Gold on Palladium – Gold Alloyed

Supported Catalysts in Formic Acid Decomposition," *ChemCatChem*, vol. 13, no. 19, pp. 4210–4222, 2021, doi: 10.1002/cctc.202100886.

[44] O. Grad, M. Mihet, M. Coros, M. Dan, M. D. Lazar, and G. Blanita, "Reduced graphene oxide modified with noble metal nanoparticles for formic acid dehydrogenation," *Catal. Today*, vol. 366, no. November 2019, pp. 41–47, 2021, doi: 10.1016/j.cattod.2020.08.009.

[45] Ö. Metin, X. Sun, and S. Sun, "Monodisperse gold-palladium alloy nanoparticles and their composition-controlled catalysis in formic acid dehydrogenation under mild conditions," *Nanoscale*, vol. 5, no. 3, pp. 910–912, 2013, doi: 10.1039/c2nr33637e.

[46] P. H. Pandey and H. S. Pawar, "Cu dispersed TiO2catalyst for direct hydrogenation of carbon dioxide into formic acid," *J. CO2 Util.*, vol. 41, no. June, p. 101267, 2020, doi: 10.1016/j.jcou.2020.101267.

[47] J. S. Yoo, F. Studt, F. Abild-Pedersen, and J. K. Nørskov, "Theoretical analysis of formic acid decomposition on transition-metal catalysts," *Fuels Petrochemicals Div. 2013 - Core Program. Area 2013 AIChE Annu. Meet. Glob. Challenges Eng. a Sustain. Futur.*, pp. 299–300, 2013.

[48] H. Yazid, R. Adnan, M. A. Farrukh, and S. A. Hamid, "Synthesis of Au/Al2O3 nanocatalyst and its application in the reduction of p-Nitrophenol," *J. Chinese Chem. Soc.*, vol. 58, no. 5, pp. 593–601, 2011, doi: 10.1002/jccs.201190093.

[49] J. H. Yang *et al.*, "Understanding preparation variables in the synthesis of Au / Al 2 O 3 using EXAFS and electron microscopy," vol. 291, pp. 73–84, 2005, doi: 10.1016/j.apcata.2004.11.052.

[50] G. Zhao *et al.*, "Structure-Activity Relationships of Au/Al2O3 Catalyst for the Selective Oxidative Esterification of 1,3-Propanediol and Methanol,"

ChemistrySelect, vol. 4, no. 43, pp. 12479–12490, 2019, doi: 10.1002/slct.201903059.

[51] A.W.N. de Leeuw den Bouter, L.Brito , A. Miquelot, P.Olivier, “Modelling of formic acid production using solventless trialkylamine reduction strategies,” *Under review in Chemical Engineering Science*

[52] C. Rodr *et al.*, “Synthesis of Supported Metal Nanoparticles (Au / TiO 2) by the Suspension Impregnation Method.”

[53] B. Zhu, X. S. Li, J. L. Liu, J. B. Liu, X. Zhu, and A. M. Zhu, “In-situ regeneration of Au nanocatalysts by atmospheric-pressure air plasma: Significant contribution of water vapor,” *Appl. Catal. B Environ.*, vol. 179, pp. 69–77, 2015, doi: 10.1016/j.apcatb.2015.05.020.

[54] P. Xu, F. D. Bernal-Juan, and L. Lefferts, “Effect of oxygen on formic acid decomposition over Pd catalyst,” *J. Catal.*, vol. 394, no. xxxx, pp. 342–352, 2021, doi: 10.1016/j.jcat.2020.10.032.

[55] D. M. Ruthven and R. S. Upadhye, “The catalytic decomposition of aqueous formic acid over suspended palladium catalysts,” *J. Catal.*, vol. 21, no. 1, pp. 39–47, 1971, doi: 10.1016/0021-9517(71)90118-7.

[56] C. Hu, J. K. Pulleri, S. W. Ting, and K. Y. Chan, “Activity of Pd/C for hydrogen generation in aqueous formic acid solution,” *Int. J. Hydrogen Energy*, vol. 39, no. 1, pp. 381–390, 2014, doi: 10.1016/j.ijhydene.2013.10.067.

[57] N. Ishito, K. Hara, K. Nakajima, and A. Fukuoka, “Selective synthesis of carbon monoxide via formates in reverse water-gas shift reaction over alumina-supported gold catalyst,” *J. Energy Chem.*, vol. 25, no. 2, pp. 306–310, 2016, doi: 10.1016/j.jechem.2015.12.005.

[58] B. László *et al.*, “ Gold Size Effect in the Thermal-Induced Reaction of CO 2 and H 2 on Titania- and Titanate Nanotube-Supported Gold Catalysts ,” *J. Nanosci. Nanotechnol.*, vol. 19, no. 1, pp. 470–477, 2018, doi: 10.1166/jnn.2019.15772.

6

Techno-economic comparison of low-pressure FA production via the direct hydrogenation of CO_2 using triethylamine and n-butylimidazole

This chapter is based on the following publication:

A.W.N. de Leeuw den Bouter, A.Chila, D.Castillo Guerra, L.Brito, A.Miquelot, P.Olivier, J. van der Schaaf, "Techno-economic comparison of low-pressure FA production via the direct hydrogenation of CO_2 towards formic acid using triethylamine and n-butylimidazole", to be submitted to the Journal of CO_2 utilization.

Abstract

Within this work, this state-of-the-art process configuration was compared with the usage of high-boiling (i.e. n-butylimidazole), less reactive amines within the reactor, followed by pressure-swing distillation. The overall plant efficiency significantly increased (i.e. 2.08% to 3.47%) when n-butylimidazole was used as the reactive amine due to a decrease in heating requirement in the distillation train.

From an economic perspective, the determined minimum selling price of formic acid was found to be heavily dominated by the OPEX, caused by the amount of catalyst volume required to achieve the annual productivity of 35 kton/year. The minimum formic acid selling price was calculated to be €10821.47 and €18913.15 per ton of formic acid for the amine-exchange and pressure-swing process, respectively, based on a hydrogen price of 2945 euro/ton. Nevertheless, these FA prices are up to 12.3 and 21.4 times the current market value, making the process uneconomic.

6.1 Introduction

Formic acid can also be decomposed within direct formic acid fuel cells (DFAFC) to generate electricity [22]. Previous work has shown that the utilization of formic acid within DFAFC's would result in higher overall energy efficiencies than the hydrogenation/dehydrogenation pathway, allowing for hydrogen storage energy efficiencies comparable or larger than existing methods for hydrogen storage [20][21][23]. Therefore, this application is selected as an used case for this work.

Besides energy related applications, formic acid is a valuable commodity chemical with applications in textiles, agriculture, pharmaceuticals etc. [8][9], and a frequently used reductant within various synthesis routes, and solvents [26].

An overview of current, CO based, and novel FA production methods based on CO_2 and biomass is given in Figure 6.1.

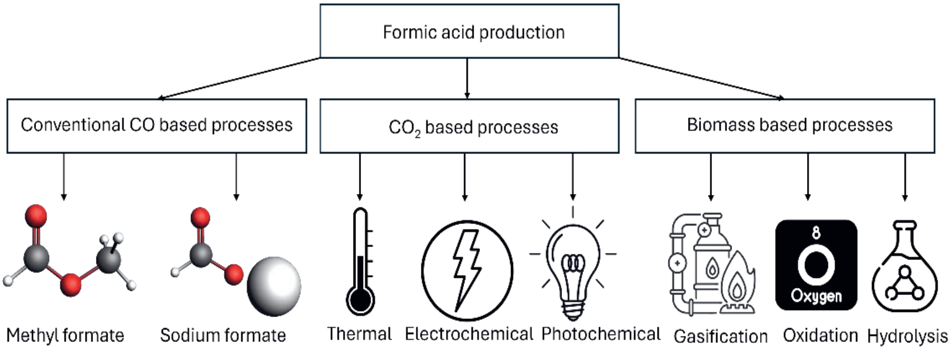

Figure 6.1: Overview of FA production methods.

Current FA production methods are based on fossil resources and include the acidolysis of alkali formates and the hydrolysis of methyl formates. The latter is the most used on industrial scale [24], and involves a two-step process: the reaction between CO and methanol to produce methyl formate, followed by the subsequent hydrolysis resulting in FA and methanol [20][23]. A multitude of intermediates have been shown to form during the process, resulting in a complex, multistep and highly energy intensive product separation. Commonly, CO is produced through the gasification of coal or natural gas at high temperatures (> 900 K) [27], resulting in significant CO_2 emissions.

Alternatively, FA can be produced from biomass through a variety of transformation methods such as acid hydrolysis, wet oxidation and catalytic oxidation. High yields of FA has already been obtained on lab scale. [26][28]. A prime example here is the acid catalyzed hydrolysis of cellulosic biomass, yielding equimolar amounts of formic acid and levulinic acid [29]. However, these processes still suffer from problems with product purification and has been shown to be energy intensive [26][29]. Alternatively, biomass can be gasified to produce syngas, allowing for the continuation of the previously discussed methyl formate pathway [30][31].

CO_2 based FA production has a large potential for mitigating CO_2 emissions compared to the conventional methyl formate hydrolysis process [14][15]. Formic acid can be sustainably produced from CO_2 based on a variety of methods such as photochemical, electrochemical and thermal chemical methods [32][25][26].

Previous studies on electrochemical methods have highlighted the potential for a significant decrease in global warming impact (GWI) due to low steam consumption, the integration of renewable electricity and the relativity simple process layout [32]. A techno-economic evaluation performed by Kim *et al*. revealed the economic performance of the electrochemical FA production method to be competitive with liquefied H_2 distribution [15]. However, the technology has not yet been proven on a large scale continuous system, while such pilot plant studies have readily been performed for the thermal chemical production method [32].

With the later method, the thermochemical FA production, the process is however highly thermodynamically unfavorable and pressures above 10 MPa are required for the reaction to proceed towards formic acid [27][28]. The addition of solvents results in an exergonic reaction, that can be shifted to the product side using bases or amines [36][37]. One solution often used is low boiling tertiary amines such as triethylamine, which are known to form stable azeotropes with formic acid [30]. Commonly, formic acid purification of such formic acid – triethylamine adducts is performed according to a process developed by British Petroleum (BP) [38]. This methodology is based on a so-called amine exchange process, in which the low boiling tertiary amine is replaced by a high-boiling tertiary amine in a reactive distillation process [31][32]. However, this process is yet to be employed at industrial scale, but is already proven at pilot scale [32]. The amine – exchange methodology is required instead of e.g. pressure-swing distillation as the azeotropes formed by formic acid – trialkylamine mixtures are virtually independent of pressure [40].

Pérez-Fortes *et al.* performed the design and techno-economic evaluation of a thermal formic acid production process with a final FA purity of 85 wt.% using a Ru-based homogeneous catalyst at 105 bar in a batch reactor [14]. The study highlighted the ability of the CO_2 hydrogenation to formic acid process to aid in mitigating CO_2 emissions compared to the conventional methyl formate hydrolysis process. The negative CO_2 emissions balance can only be achieved on the condition of using renewable electricity to generate renewable hydrogen through electrolysis and to produce high-pressure steam. However, in its current form, the process is not economically viable compared to the conventional two-step hydrolysis of methyl formate process, due to the consumption of large amounts of steam required to drive the reboilers of the distillation train and the usage of a homogeneous catalyst. Here, the large energy requirement arises from the energy required to break the formic acid – tertiary amine bond.

Park *et al*. published a techno-economic evaluation and life cycle assessment based on continuous FA production using a Ru-based heterogeneous catalyst at 120 bar, using triethylamine as reactive amine and n-butylimidazole (nBIM) as amine-exchange amine in the reactive distillation train [41]. The energy intensive amine – exchange step was found to be one of the major contributors to the overall formic acid price, and the process was concluded to require a significant reduction in high-pressure steam consumption to become economically viable. FA – nBIM adducts were observed to be readily separable using thermal splitting.

Recently, Kim *et al*. continued upon the work of Park *et al.*, optimizing the combination of the reactive amine (N-methyl-2-pyrrolidone) and the amine (nBIM) used within reactive distillation train [32]. Validating their techno-economic assessment with a 10 kg/day pilot plant, they concluded that the optimization of the amine-couple results in an economically viable process with a decrease of 37% in production cost compared to the conventional methyl formate process, as well as a 42% decrease in global warming impact. However, while the optimization of the amine pair results in an economically viable process, the energy intensive reactive distillation amine-exchange step is still observed to be the major driver of the formic acid price.

This study proposes a methodology to circumvent the necessity of the amine-exchange step in an attempt to propose a significantly simpler process design and decrease both the CAPEX and the energy requirements of the process, and thus the formic acid price. Previous works have investigated the influence of different tertiary amines on key parameters such as FA productivity and selectivity [42]. Here, the high boiling amine nBIM was identified as a promising candidate and is thus selected as an amine for this work.

While techno-economic evaluations have been performed based on high supercritical CO_2 pressures and high H_2 pressures [14] [15][16][28], a clear gap exists within literature for techno-economic evaluations below the supercritical pressure limit (<50 bar) and the circumvention of the amine-exchange step. Therefore, within this study, the extension will be made towards low pressure (< 50 bar) applications and the utilization of n-butylimidazole as sole amine. A techno-economic comparison of two routes for the direct CO_2 hydrogenation based on non-supercritical conditions is demonstrated: 1) the conventional route based on the patents of BP and BASF, in which triethylamine is used as a reactive amine and exchanged with trihexylamine in a reactive distillation process using an Au/Al_2O_3 catalyst; 2) a direct route in which no amine exchange is performed, but purification is performed directly through pressure swing distillation without the necessity of a second amine using an Au/TiO_2 catalyst. A schematic overview of the two proposed processes is given in Figure 6.2.

Amine-exchange process

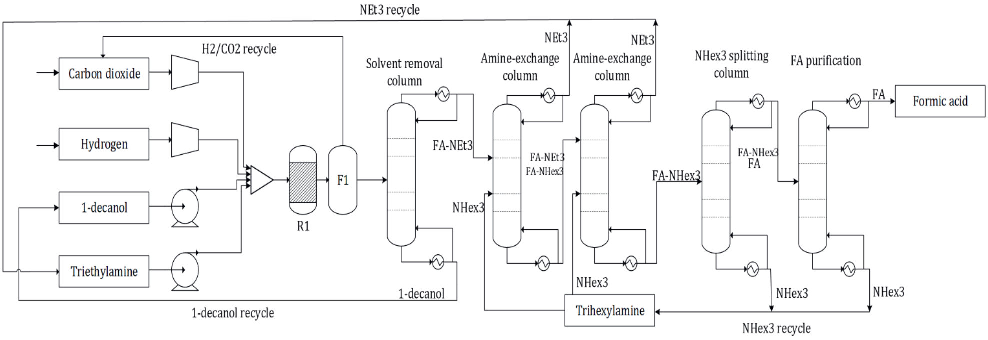

Pressure-swing process

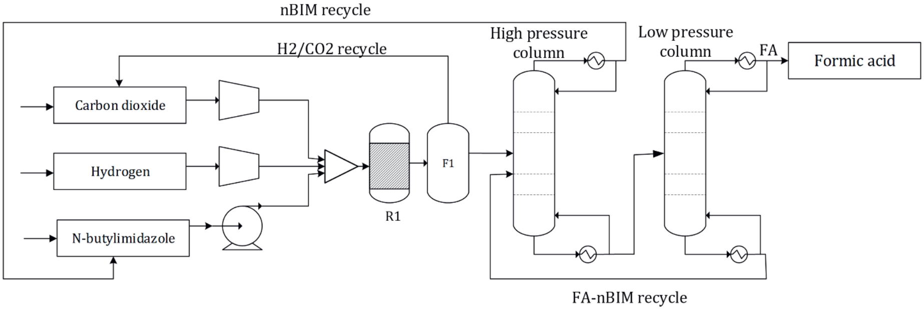

Figure 6.2: Overview of the proposed, CO_2 based, processes. The amine-exchange route corresponds to the state-of-the-art CO_2 route based on the patents of BASF and BP. The pressure-swing route (direct route) represents a significant simplification to the process and is proposed within this work.

The two processes are designed in Aspen Plus V14 at a 35 kton/year scale, which corresponds to the average yearly productivity of the 20 largest FA production plants [43]. The final FA impurity level is set to <1 ppm of tertiary amine, in line with the FA purities required for Direct Formic Acid Fuel Cell (DFAFC) applications [35]. We will show whether the exchange from a low boiling amine to a high boiling amine as a reactive amine can improve the economic performance of the direct hydrogenation to formic acid, and therefore the economic competitiveness of the process.

6.2 Methodology and assumptions

Mass and energy balances calculations were performed using process flow modelling software (Aspen Plus V14) targeting a productivity of 35 kton/year at 99.9999% purity, while reactor optimization was carried out in MATLAB 2022B.

Physical properties missing from the Aspen Plus database were obtained using either the COSMO-SAC implementation in the Amsterdam Modelling Suite (AMS) [34][35] or based on experimental literature. Energy optimalization was done using the Aspen Plus Energy Analyzer. Afterwards, the CAPEX and OPEX of both processes was evaluated based on the Lang factor approach, resulting in a minimum formic acid selling price (MFSP).

6.2.1. System boundaries

- This analysis focuses on the production and purification of formic acid, with the production, purification and transportation of hydrogen and CO_2 falling outside the scope of this work. The CO_2 is assumed to originate from sustainable sources, such as the sorption enhanced water gas shift (SEWGS) process used at iron and steel plants [46]. CO_2 enters the plant at ambient conditions (1 bar, 20 ºC). H_2 is assumed to originate from Solid Oxide Electrolyzers(SOEC), entering the plant at 30 bar and 20 ºC [47]. The gaseous streams are assumed to be of 100% purity, as purification is usually performed at the production site. The cost of purification is taken into account in the feedstock price. All tertiary amines and solvents (1-decanol, triethylamine, trihexylamine and n-butylimidazole) are assumed to enter at ambient conditions and 100 % purity.
- The formic acid production facility comprises of the following building blocks (inside battery limits (ISBL)): 1) compression section for the gaseous and liquid streams, 2) the formic acid production reactors, 3) distillation train either based on the amine exchange strategy or pressure swing distillation, 4) recycle of unconverted feedstock and 5) the heat exchanger network. The outside battery limits (OSBL) include electricity and high-pressure steam generation, a cooling tower for the cooling water and a refrigeration cycle based on Freon. All utilities are assumed to be derived from the grid.
- Both technologies target a productivity of 35 kton/year, as this is equal to the average yearly productivity of the 20 largest FA production plants globally [48]. Furthermore, a plant lifetime of 20 years is assumed with a

production time of 8000 hours a year, corresponding to a capacity factor of 91.3% [49].

- Both processes target the purity required for fuel cells applications, meaning the residual tertiary amine and CO concentrations have to be below 1 ppm [23].
- The plant is considered to be constructed and located in the Netherlands, thus the cost of labor is taken according to the Dutch regulations.

6.2.2. Reactor design and sizing approach and assumptions

- The reactor in which triethylamine is the reactive base of choice is designed based on a heterogeneous, steady state, non-isothermal one-dimensional reactor model, taking into account catalyst efficiency (i.e. internal diffusion limitations) and external mass transfer limitations. The kinetics are based on the work of Filonenko *et al*. [50]. No dispersion profiles were taken into account in the axial and radial direction, as well as no pressure drop in the axial direction. A detailed description of the governing mass and energy balances, as well as model validation, can be found in the supporting information. It was chosen to optimize the reactor in terms of productivity, due to the slow kinetic nature of the direct hydrogenation reaction. The n-butylimidazole case is designed based on previous experimental data [42]. For this reason, the reactor is modelled in Aspen Plus using a RStoic block at a total pressure of 40 bar. The gas-liquid ratio, residence time and fractional CO_2 conversion are enforced using design specs to ensure a close agreement with experimental data. In both cases, the H_2:CO_2 stoichiometric ratio of 1:1 is set. For both cases, the reaction enthalpy is taken from literature [24][30][51].
- Au/Al_2O_3 (1wt.%) is used as a catalyst in the amine-exchange scenario, while Au/TiO_2 (1wt.%) is used in case of n-butylimidazole. Moreover, the solid hold-up of the catalyst bed is set to 0.6 m^3_{solid} / $m^3_{reactor}$ and the particle void fraction to 0.5 m^3_{void} / $m^3_{catalyst}$ for both cases.
- The reactor is designed to have an external reactor shell, with heat supplied by low-pressure steam.

- The reactors are sized to meet the target productivity of the plant accounting for possible FA losses in the separation train, based on an aspect (L/D) ratio of 7.

6.2.3. Process design approach and assumptions

- n-butylimidazole (nBIM) is selected as the tertiary amine for the pressure swing distillation case. This choice was motivated by promising FA productivity observed by previous works [42], combined with facile separation of formic acid – through thermal splitting [15][24]. Previous work [42] showed no phase separation to occur between FA and nBIM over a wide range of molar ratios. This makes that pure nBIM without solvents can be fed to the reactor. FA-nBIM adducts were shown to have an azeotropic point at 25mol% at 100 torr.
- The NRTL-HOC method is selected as equation of state for the pressure swing distillation approach because of its proven ability to describe the highly non-ideal formic acid – tertiary amine system [41][52].
- The amine – exchange process was designed as reactive distillation using the RadFrac model in Aspen Plus. The formic acid – triethylamine and formic acid – trihexylamine compounds are not present within the Aspen Plus database, so their physical properties including enthalpy of reaction and entropy were predicted using the COSMO-SAC implementation of the Amsterdam Modelling Suite. The thermodynamic method in Aspen Plus was chosen to be COSMO-SAC. The equilibrium constants of each of the compounds were implemented within the RadFrac models to account for the reactive amine exchange. More details are described in Section 3.1.3. Within the RadFrac model, a Murphree efficiency of 85% and pressure drop of 7 mbar per stage are taken into account, following the work of Poto *et al.*[53]. Column height and diameter as well as column internals were designed to prevent stages drying up based on a 80% flooding approach.
- The pressure swing distillation train for formic acid n-butylimidazole separation was designed based on the graphical McCabe-Thiele method to obtain the minimum number of stages, the feed stage and the minimum

reflux ratio (R_{min}). The optimal reflux ratio was taken as 1.2 times R_{min}. The sieve tray spacing was set to 0.5 meters, with a stage efficiency of 85% [54]. Column diameters were determined using the flooding chart of Fair, as given in Perry's Chemical Engineers' Handbook. Pressure drop over the column was not taken into consideration.

- The recycle streams between the two distillation towers in the pressure swing distillation design was taken into account on the basis of molar balances. As illustrated in Figure 3, the bottom stream of the second tower (stream 30) is recycled to the feed of the first tower (stream 23). The composition (x_{F1}) and molar flowrate (F_1) entering the first tower are given by

$$x_{F1} = \frac{x_R + x_R x_{D1} C - x_{B2} x_{D1} C}{1 - x_{B2} C + x_R C} \qquad 6.1$$

$$F_1 = \frac{x_R R}{x_{F1} - x_{B2}(x_{F1} - x_{D1)}C} \qquad 6.2$$

$$A = \frac{x_{B1} - x_{D2}}{x_{B2} - x_{D2}} \qquad 6.3$$

$$C = \frac{A}{x_{B1} - x_{D1}} \qquad 6.4$$

With *x* the molar composition, A and C constants and R the molar flow rate leaving the reactor. The subscripts R, D and B indicate the reactor, distillate and bottom respectively. As indicated in Figure 6, x_R corresponds to stream 21, x_{D1} stream 24, x_{B1} steam 25, x_{D2} stream 28 and x_{B2} to stream 30.

- The heat exchanger (HEX) network was designed based on counter-current shell and tube heat exchangers and the shortcut method implemented in Aspen Plus. Energy optimalization was performed using pinch analysis in combination with a minimum temperature approach. A minimum temperature difference (ΔT_{min}) of 5 ºC is considered for HEXs in the 0 – 200 ºC range, while for operating temperatures outside this range the ΔT_{min} is set to 10 ºC.
- All turbomachines (i.e. compressors, steam turbines and pumps) are simulated within Aspen Plus V14 considering mechanical (0.95) and

isentropic (0.72) efficiencies to obtain the thermodynamic conditions of the outlet streams as well as the accompanying energy balances [53]. In case of multistage compressors, the discharge temperature and power consumption are optimized based on inter-refrigerated multistage compressors as implemented in Aspen Plus. The maximum pressure ratio was set to 3, as this is the optimum economic ratio [54]. The intermediate cooler outlet temperature was chosen based on the required cooling energy input and energy requirement of the compressor.

- The high pressure (HP) steam conditions are assumed to be 40 bar and 250 ºC.
- A cooling tower is used to enable cooling water recirculation, therefore reducing the cost of cold utilities.
- The selected material depends on the amount of formic acid present in the process stream. High concentrations of formic acid (>50mol%) have been shown to cause heavy corrosion to stainless steel [32]. Besides corrosion, the Ni and Fe species present in SS304 and SS306 can result in undesired FA decomposition [55]. For this reason, the material of choice is stainless steel 316 L (high grade) at FA concentrations < 50 mol%, and Inconel above this threshold. Inconel has previously been shown to be fully compatible with formic acid [56].
- Within the amine-exchange process, a recovery of 99% is achieved for the amines and 1-decanol. Within the pressure-swing process, the n-butylimidazole is fully recycled.

6.2.4 Economic analysis and economic indicators

The economic section is divided into two parts: the initial capital investment (i.e. CAPEX) and the operational expenditures (i.e. OPEX). The factorial method based on Lang factors is used to determine the CAPEX of both processes. Within this method, the total CAPEX is taken as a factor of the purchase equipment cost (PEC), as summarized in Table 6.1. To determine the PEC, the correlation of R.Smith [57] is used, given by:

$$C_E = C_B \left(\frac{Q}{Q_B}\right)^M f_m\, f_p\, f_T \qquad 6.5$$

where C_E is the equipment cost of an equipment with a capacity Q; C_B is the base cost with base capacity Q_B; Q and Q_B are capacity measures which depends on the equipment type. $f_m, f_p\ and\ f_T$ are correction factors for the material of construction, the operational pressure and temperature respectively. Details on the correlations used for the determination of the PEC of all equipment are reported in the supporting information.

The costs given within the work of Smith are based on pricing in 2000, to actualize these costs to the base year of this study (i.e. 2023), the Chemical Engineering Plant Cost Index (CEPCI) index is used:

$$CE_{2023} = \frac{CEPCI_{2023}}{CEPCI_{2000}}\, CE_{2000} \qquad 6.6$$

The CEPCI was taken to be 435.8 in January 2000 [57], and 797.94 in 2023 [58].

Cost component	Lang factor
Purchase Equipment Cost (PEC)	1
Purchase equipment installation	0.39
Instrumentation and controls	0.26
Piping	0.31
Electrical system	0.1
Building (including services)	0.29
Yard improvements	0.12
ISBL	**2.47 * PEC**
OSBL	**0.12 * PEC**
Engineering and supervision	0.32 * (ISBL+ OSBL)
Construction expenses	0.34 * (ISBL+ OSBL)
Legal expenses	0.04 * (ISBL+ OSBL)
Contractor’s fee	0.19 * (ISBL+ OSBL)
Indirect Costs (IC)	**0.89 * (ISBL+ OSBL)**
Project contingency	0.89 * (ISBL+ OSBL + IC)
Process contingency	0.89 * (ISBL+ OSBL + IC)

Fixed Capital Investment (FCI)	**0.89 * (ISBL+ OSBL + IC)**
Working Capital (WC)	0.15 * FCI
Start-up costs	0.15 * FCI
CAPEX	**0.15 * FCI**

Table 6.1: Lang factors used for the determination of CAPEX costs [44][48]

The OPEX is split into two contributions, namely the variable ($OPEX_{var}$) and fixed OPEX ($OPEX_{fix}$). $OPEX_{fix}$ is used to account for labor, supervison, working capital and maintenance, with the methodology summarized in Table 6.3. Correlations used for the determination of the total labor requirement can be found in Appendix E. The cost of labor is based on the average yearly operator salary within the Netherlands (i.e. 60000 euro) [59].The variable OPEX comprises the costs of feedstock (i.e. tertiary amine and solvent make-up, CO_2 and H_2), utilities (i.e. electricity, HP steam, freon cooling cycle) and the cost of the catalysts. An overview of the $OPEX_{var}$ methodology is given in Table 6.2.

To evaluate the total annual cost (TAC) comprising of the annual CAPEX (ACAPEX) and OPEX is defined as:

$$TAC = ACAPEX + OPEX \tag{6.7}$$

The methodoloy to determine ACAPEX is given within Appendix E.

	Price	Unit	Reference
H_2 (from SOEC)	6000	€/ton	[60]
CO_2 (SEWGS)	33	€/ton	[46]
Electricity	0.07	€/KWh	[32]
Cooling water	0.2	€/ton	[54]
HP Steam	25.12	€/ton H_2O	[14]
Au/TiO_2	692,61	€/kg	[61][62]
Au/Al_2O3	700,66	€/kg	[53][63]
1-decanol	43,67	€/kg	[64]
n-butylimidazole	23,56	€/kg	[32]
Triethylamine	320	€/ton	[65]

Trihexylamine	724	€/ton	[14]

Table 6.2: Assumed feedstock and utility prices used to obtain the variable OPEX

Cost component	Value
Supervision	0.25 * Labor
Direct overhead	0.25 * (Labor + Supervision)
General overhead	0.65 * (Labor + Supervision + Direct overhead)
Maintenance labor	0.65 * FCI
Maintenance materials	0.03 * ISBL
Insurance and tax	0.015 * FCI
Financing working capital	Debt interest * WC

Table 6.3: Methodology for the calculation of the fixed OPEX ($OPEX_{fix}$)

The TAC allows for the calculation of the minimum formic acid selling price (MFSP) based on the methodology of discounted cash flow (DCF) analysis, with the equations given within Appendix E. An overview of all assumptions and financial parameters such as the interest rate, debt/equity ratio and cost of equity used within the DCF are summarized in Table 6.4. Following the work of [66] the plant is assumed to be constructed in a 3 year time period, with the following division of capital investments: 20%, 50% and 30%. The prices of feedstock, products and utilities were assumed constant over the 20 year operational lifetime of the plant. No salvage value is expected for the plant equipment, however, it is assumed the precious noble metals of the gold-based catalysts are extracted after the plant lifetime. Following the work of Hachhach *et al.*, it is assumed that 96% of the gold can be reclaimed at a cost of 3.30 dollar/kg catalyst [61].

Parameter	Value
Location	Netherlands
Base year	2023
Project lifetime (year)	20
Construction period (year)	3
Plant availability (hour/year)	8000
Tax rate (%)	25
Equity/Debt rate	50/50
Debt interest rate (%)	4
Cost of equity (%)	12
WACC (%)	8

Depreciation period (year)	10
Salvage value (-)	96% gold recovery from the catalyst
Exchange rate (USD/EUR)	0.92
Catalyst lifetime (year)	20
Tertiary amine lifetime (year)	20

Table 6.4: Overview of economic assumptions and parameters

6.2.5. Key performance indicators (KPI)

The reactor designs are compared in terms of the CO_2 conversion, reaction conditions and residence time. The CO_2 conversion is given by:

$$X_{CO_2} = \frac{F_{CO_2,in} - F_{CO_{2,out}}}{F_{CO_2,in}} \tag{6.8}$$

The plant designs were evaluated in terms of several carbon and energy metrics: cold gas efficiency (CGE), the overall energy efficiency (η_{tot}) and the overall carbon footprint.

The CGE is defined as the ratio of the energy content stored in formic acid referred to the lower heating value (LHV), to the energy content of the feedstock:

$$CGE = \frac{\dot{m}_{FA}\, LHV_{FA}}{\dot{m}_{H_2}\, LHV_{H_2}} \tag{6.9}$$

The overall energy efficiency (η_{tot}) is defined based on previous works, and represents the ratio of the energy stored to the total energy used to produce formic acid [66]:

$$\eta_{tot} = \frac{W_{chem}}{W_{feed} + \frac{W_{steam,NG}}{\eta_{steam,NG}} + \frac{W_{el}}{\eta_{el}}} \tag{6.10}$$

The energy content on the product and feed based on the lower heating values is given by W_{chem} and W_{feed}, respectively. To account for the energy put into the production in the form of electricity and HP steam, the W_{steam} and W_{el} terms are added to the denominator. Two cases were considered, one in which the steam and electricity are derived from fossil fuels, and one in which all heating requirement is derived from renewable electricity. HP steam and electricity are assumed to be obtained from the grid, we assumed that the HP steam produced using natural gas at an efficiency of 77.5% [57] and electricity is produced at an efficiency of 58.4% [67].

To evaluate the ability of the process to reduce carbon emissions, the amount of CO_2 consumed through FA production ($\dot{m}_{CO2,in}$) is compared to the amount of CO_2 emitted ($\dot{m}_{CO2,emissions}$) by the plant. Within the fossil fuel derived case, the emissions account for the burning of natural gas to produce HP steam and the production of electricity. The CO_2 emissions from energy consumption are taken to be 0.47 t_{CO2}/(MWh) [68] for electricity and 0.317 t_{CO2}/(MWh) for heat in the form of HP steam [69]. In case of electrical heating based on renewables, the CO_2 emissions are taken to be 0.013 t_{CO2}/(MWh), which corresponds to shore wind production [70]. All CO_2 emissions correspond to studies conducted by the U.S. Department of Energy. Any CO_2 emissions originating from storage, transport etc. of feedstock and products is deemed to be outside the scope of this work.

6.3. Process modelling

6.3.1. Amine exchange process

6.3.1.1. FA production reactor design

The reactor is designed based on a heterogeneous, steady state, non-isothermal one-dimensional reactor model, taking into account catalyst efficiency (i.e. internal diffusion limitations) and external mass transfer limitations. The kinetics are based on the work of Filonenko *et al*. [50]. A detailed description of the governing equations and model verification is given in Appendix E. Figure 6.3 evaluates the influence of reaction temperature, pressure, liquid residence time and amine:solvent ratio on the formic acid productivity based on the reactor model.

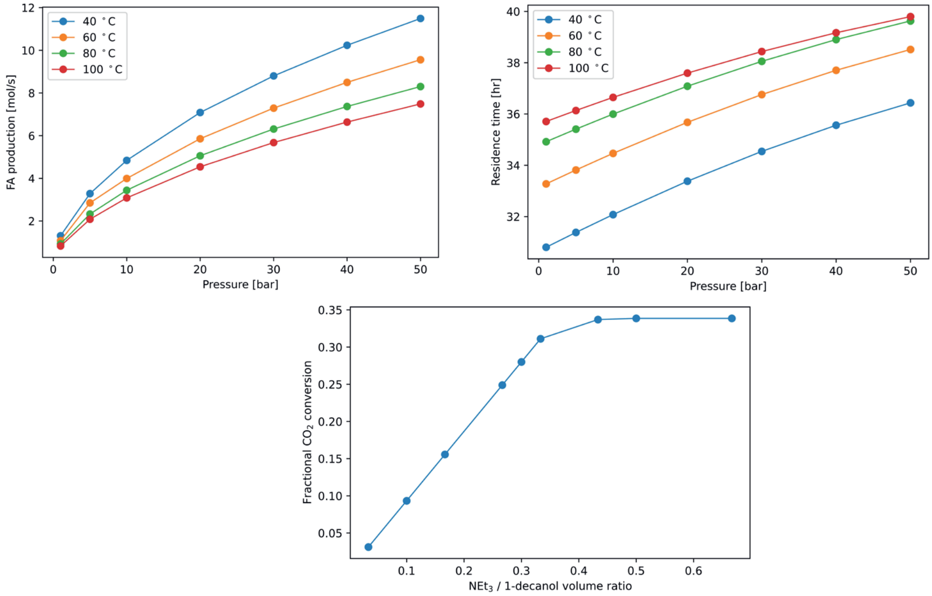

Figure 6.3: Design of reactor using triethylamine as reactive base. Left top) Influence of temperature and pressure on FA productivity for a reactor length of 50 m and 5 m wide. right top) Residence times used in the left top graph. Bottom) CO_2 conversion at a temperature of 40 ºC , pressure of 50 bar (1:1 vol/vol H_2:CO_2) and a reactor size of 50x5 m as a function of triethylamine:1-decanol ratio

Residence times are calculated by setting superficial liquid velocities such that a constant trickle flow regime and full catalyst wetting are ensured, according to the correlations presented by [71]. From Figure 6.3, it becomes apparent that higher pressures and lower temperatures result in higher FA productivities at lower residence times. The effect of higher pressure is expected due to increased CO_2 and H_2 solubility, as is the observed temperature behaviour due to the exothermicity of the reaction. Based on Figure 6.3, an operational pressure and temperature of 40 ºC and 50 bar was selected. The incorporated kinetics derived by Filonenko *et al*. [50] assume a direct relation between the FA productivity and the amount of amine present. However, previous works highlighted the evaporation of triethylamine within the purification section to be highly energy intensive [15]. Thus, the amount of triethylamine should be minimized but not limit the kinetic performance of the reactor. The influence of the triethylamine:1-decanol volumetric ratio on CO_2 conversion is shown in Figure 1 for the selected operational conditions. An increase of FA productivity is observed until a volumetric ratio of 0.43, which is taken as the optimal amine:solvent ratio.

Particle size was determined based on the Ergun equation, with the maximum pressure drop set to 0.2 bar over the reactor length. This results in cylindrical catalyst particles, with a diameter of 0.2 mm and a length of 1 mm. At these operating conditions and particle size, no internal or external mass transfer limitations occur, as evidenced by the Weisz-Prater and first Mears' criteria.

6.3.1.2. Physical properties

Physical properties such as the vapor-liquid equilibria (VLE) of the triethylamine – formic acid and trihexylamine – formic acid adducts were determined using COSMO-SAC due to unavailability of such properties within literature and imported into Aspen Plus using the calculated sigma profiles and van der Waals volume. To perform the COSMO – SAC simulations, geometric structure optimization at DFT level was performed using the B3LYP functional [72] in conjunction with a TZP Slater-type basis set in the Amsterdam Modelling Suite (AMS) software package version 21 [34][35][73]. The geometric structure of the adducts was based on that of acetic acid – triethylamine complexes [74].

The reactions between the tertiary amines and formic acid are modelled as equilibria [61][62]:

$$NEt_3 + FA \leftrightarrow FA{:}NEt_3 \tag{6.11}$$

$$NHex_3 + FA \leftrightarrow FA{:}NHex_3 \tag{6.12}$$

To obtain the equilibrium constants for each of the adducts, the Gibbs free energy (ΔG) of each of the complexes was calculated:

$$\Delta G = -RTln(K_{eq}) = \Delta H - T\Delta S \tag{6.13}$$

With, R the universal gas constant, T the temperature in Kelvin, ΔH the enthalpy of protonation taken from [30][42], and ΔS the entropy obtained from DFT simulations. The resulting equilibrium constants are depicted in Figure 6.4.

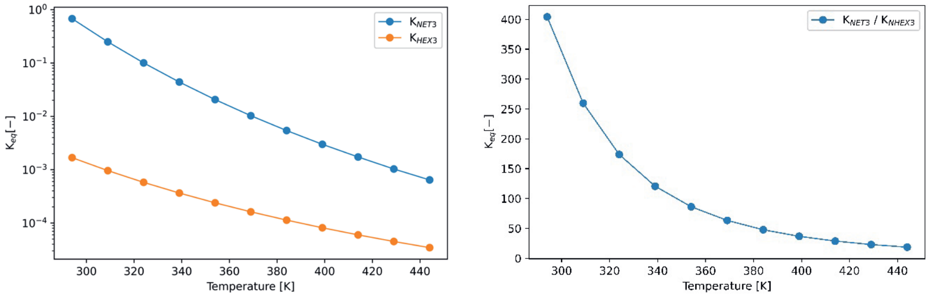

Figure 6.4: left) Equilibrium constants of the reactions between formic acid – triethylamine and formic acid – trihexylamine as a function of temperature. The equilibrium constants were determined using experimental literature and COSMO-SAC simulations. Right) Ratio between the equilibrium constants

To validate the amine-exchange distillation methodology, the amine-exchange was experimentally performed at lab scale using a RotaVap (IKA RV 10 Basic) at 120 mbar. A mixture of formic acid, triethylamine and trihexylamine was heated using an external oil bath. Experiments were performed between 110 and 170 ºC, with steps of 10 ºC. ^{1}H-NMR analysis of the distillate is summarized in Table 6.5.

T [ºC]	x_{FA}	x_{NET3}	X_{NHEX3}
110	0	1	0
120	0	1	0
130	0	1	0
140	0	1	0
150	0	0	0
160	0.92	0.06	0.02
170	0.94	0.04	0.02

Table 6.5: The molar fractions of each component in the distillate of a formic acid – triethylamine – trihexylamine mixture distilled in a single stage RotaVap at 120 mbar. Molar fractions determined using ^{1}H-NMR.

At 170 ºC, the molar formic acid fraction within the distillate is 94%, while the azeotropic point for a formic acid – triethylamine mixture at 120 mbar is 28 mol% [76]. As formic acid purities surpassing the azeotropic point are observed, the proposed methodology is considered validated.

6.3.1.3. Process description: amine-exchange method

Figure 6.5 depicts the process flow diagram of the direct hydrogenation of CO_2 to formic acid process in which triethylamine is used as a base within the packed bed reactor (Au/Al_2O_3 catalyst). Here, the concept of amine-exchange is used for FA purification. CO_2 enters the plant at ambient conditions (i.e. 1 bar and 20 ºC) as stream 1 and is compressed to 50 bar (the working pressure of the packed bed reactors, R1) via a multistage compressor unit (MCU) comprising of 4 compressors with intermediate cooling. The outlet temperature of the MCU unit is 40 ºC. H_2 (stream 2) enters the plant at 30 bar and 20 ºC, and is compressed and heated to 50 bar and 40 ºC. The 1-decanol and triethylamine recycle is pumped to reach 50 bar, heated and mixed with the gaseous feed stream before entering the fixed bed reactors. 2 parallel fixed bed reactors are used, at an operational temperature of 40 ºC and 50 bar. The reactor is heated using low pressure (LP) steam. The gaseous and liquid streams are separated using a flash column (F1) operating at 1 bar. The gaseous stream (stream 17) is repressurized and fed back to the reactor. The liquid product (stream 18) is then fed to distillation column T1 to remove the 1-decanol solvent. Distillation tower 1 operates at 1 bar and in the temperature range of 116.5 – 228.8 ºC to separate 1-decanol (stream 20) over the bottom. Next, the top stream (stream 21) is cooled down to 70 ºC, the pressure reduced to 0.11 bar and eventually fed to distillation tower 2 (T2) and 3 (T3). To break the azeotropic point, the amine-exchange strategy is followed, in which triethylamine is replaced by trihexylamine. To maximize the contact time between the $NHex_3$ and the FA – NEt_3 adducts, the $NHex_3$ is fed near the top (stage 8), while the FA – NEt_3 adducts are fed at the bottom of the tower (stage 6) in T2, and stage 5 and 4 respectively in T3. The operating temperatures of T2 are 107.9 – 202.2 ºC, while T3 operates between 40.6 and 214.1 ºC. The majority (95%) of the distillate of T3 (stream 27) is recycled to T2. The recovered triethylamine (stream 63) is cooled to 40 ºC and recycled to the reactor after pumping to 50 bar. The formic acid – trihexylamine adducts leaving the bottom of T3 (stream 30) are fed to T4, where the adducts are separated to FA over the top (stream 32) and trihexylamine over the bottom (stream 33). The trihexylamine is cooled to 60 ºC and recycled to T2 and T3 (stream 34). The stringent purity demands of the FA products requires an additional distillation tower (T5) in which formic acid (stream 35) is separated from trace amounts of trihexylamine and 1-decanol (stream

36) .The bottom steam of T5 (stream 36) comprises mostly out of $NHex_3$ and is recycled to stream 34. The formic acid is cooled to 20 and repressurized to 1 bar for storage.

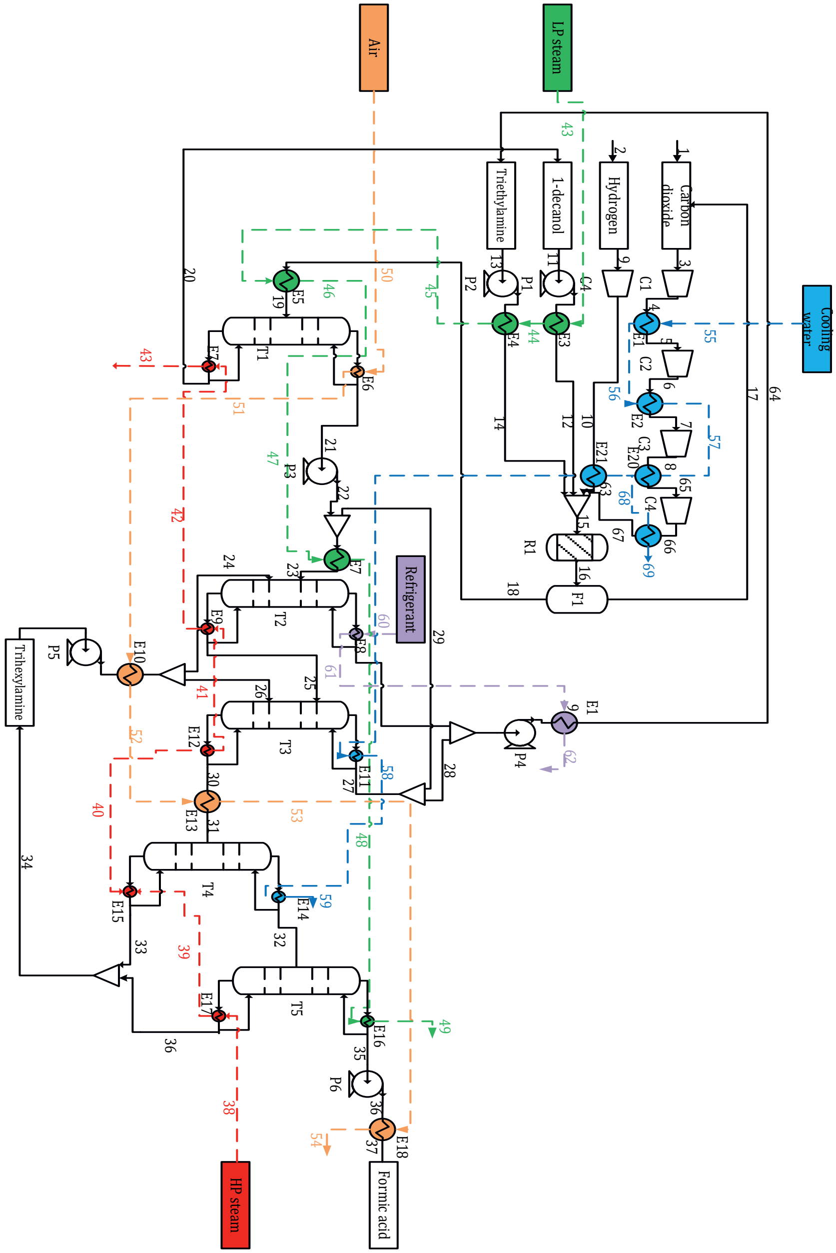

Figure 6.5: Process flow diagram for the direct hydrogenation of CO_2 to formic acid using the amine-exchange strategy for formic acid purification

6.3.2.Pressure swing distillation process

6.3.2.1. FA production reactor design

Due to a lack of kinetic descriptions for the direct CO_2 hydrogenation using n-butylimidazole as base over an Au/TiO_2 catalyst, the reactor was designed based on the experimental data presented Chapter 4. Here, the operational conditions were 40 bar (1:1 vol/vol H_2:CO_2) and 75 ºC, a gaseous flowrate of 1.46 mL_n/min, a liquid flow rate of 0.025 mL_n /min. The resulting gas/liquid ratio is 0.78 with a liquid residence time of 75 minutes, resulting in a fractional conversion of 0.136. The catalyst FA productivity ([g_{FA}/ g_{cat}/s]) was determined by:

$$FA\,productivity = \frac{[FA]_{out} M_{w,FA} \varepsilon_l V_r}{m_{tot,cat} \tau} \qquad 6.14$$

with $[FA]_{out}$ the experimental outgoing FA concentration, $M_{w,FA}$ the molecular weight of FA, ε_l the liquid hold-up, V_r the experimental reactor volume, $m_{tot,cat}$ the amount of catalyst used in the experimental reactor and τ the residence time.

The reactor volume was scaled to meet the target plant productivity. A final reactor length of 50 m and diameter of 7.5 m was chosen. The number of reactors in parallel was defined as the ratio of the total required reactor volume by the reactor volume of one reactor. The resulting required catalyst weight is 8.57 kton, which translates to 4 reactors at a solid hold-up of 0.6 m^3_{solid} / $m^3_{reactor}$. The reaction enthalpy is set to -20.15 kJ/mol [32].

6.3.2.2. Physical properties

Due to n-butylimidazole (nBIM) physical properties missing from the Aspen Plus database, all physical properties were manually imported based on literature. The parameters required for the NRTL-HOC model were obtained from Usosky *et al.* [52][77], including the Antoine equation parameters. The heat capacity coefficient under constant pressure (Cp) was obtained by interpolating literature data of imidazoles with different chain length, as shown in Appendix E. All other parameters of chemicals and mixtures were obtained from Aspen Plus V14.

VLE data of nBIM-FA complexes at a pressure of 50 mmHg is presented by Park *et al*. [41]. In order to extent the VLE data to a wider set of pressures, the raw VLE dataset was extracted and regressed in Aspen Plus V14 to obtain the first three binary parameters (a_{ij}, a_{ji}, b_{ij}, b_{ji}, c_{ij} and c_{ji}) of the NRTL equation, assuming a_{ij} is not equal to a_{ji}. The predefined algorithm options chosen were: Maximum-likelihood objective function, Britt-Luecke algorithm and Deming initialization method with a convergence tolerance of 1e-5. An overview of fitted binary interaction parameters and the resulting VLE curve are included in the Appendix E.

6.3.2.3 Process description

Figure 6.6 depicts the process flow diagram of the direct hydrogenation of CO_2 to formic acid process in which n-butylimidazole is used as a base within the packed bed reactor (Au/TiO_2 catalyst). CO_2 enters the plant at ambient conditions (i.e. 1 bar and 20 ºC) as stream 1 and is compressed to 40 bar (the working pressure of the packed bed reactors, R1) via a multistage compressor unit (MCU) comprising of 4 compressors with intermediate cooling. The outlet temperature of the MCU unit is 75 ºC. H_2 (stream 2) enters the plant at 30 bar and 20 ºC, and is compressed and heated to 40 bar and 75 ºC. The temperatures of the four intermediate coolers are set to 49, 50, 45 and 75 ºC respectively. Liquid nBIM (stream 3) enters the system at ambient conditions (20 °C and 1 bar) into pump P1 increasing its pressure to 40 bar. Due to recycle stream 31, and negligible amine losses, no additional heating is required. Both gas and liquid streams are mixed together to enter the reaction section (R1). The reactants are converting CO_2 into formic acid in R1 with a molar fractional CO_2 conversion of 0.136. The outlet flow of R1 (stream 19) is send to flash drum F1 for gas-liquid separation. The unreacted gases that leave F1 (stream 20) are repressurized and recycled with the inlet CO_2 stream. The liquid stream leaves F1 from the bottom of the drum, and its pressure is reduced to 0.16 bar (120 torr). The stream contains 2,3mol.% formic acid, thus the mixture is on the left side of the azeotropic point on the Txy diagram. The mixture is preheated in heat exchanger E5, which uses HP steam as a hot side. The outlet temperature is 176 °C, the boiling point of the feed. The stream is then fed into distillation tower T1, where pure nBIM is obtained over the top and the azeotropic mixture is separated at the bottom. The condenser is operating at 167 °C, the boiling point of nBIM, and the reboiler is operating at 201.6 °C, the boiling point of the azeotropic mixture. The top stream is cooled down with E12 to 75 °C to be recycled and mixed with the inlet nBIM. The bottom stream of T1, containing the azeotropic mixture at 120 torr, is cooled to 180 °C with E8. E8 uses pressurized and heated water as a coolant to generate LP steam. The liquid mixture is lowered in pressure to 0.133 bar (100 torr) with P3 before entering T2. With change in pressure, the azeotropic composition is reduced in terms of formic acid content. The condenser is operating at 44 °C, a temperature just below the boiling temperature of formic acid and the reboiler is operating at 181 °C, the boiling point of the azeotropic mixture. The bottom of T2 is sent to P4 to increase the pressure to 120 torr and is recycled back (stream 31) to T1. The distillate steam of T2, containing pure formic acid, is cooled to 20°C with E11 using Freon 12 as coolant and repressurized to 1 bar with P6.

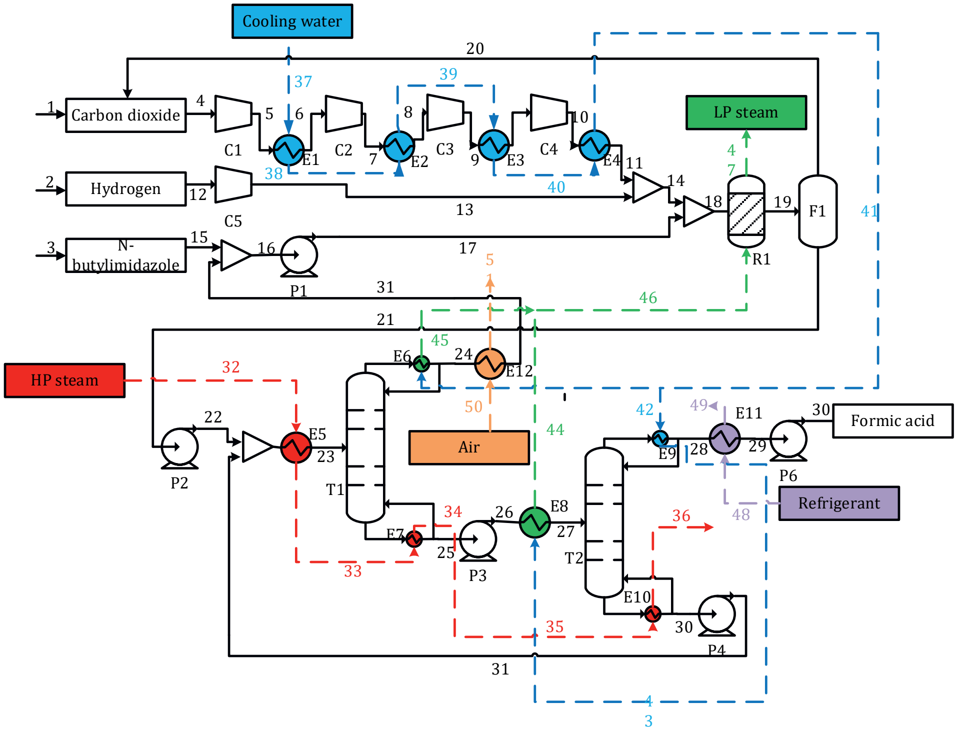

Figure 6.6: Process flow diagram for the direct hydrogenation of CO_2 to formic acid using the pressure-swing distillation strategy for formic acid purification.

6.4. Technical comparison

The technologies proposed within this work are first compared at reactor scale, followed by comparison at process level. An overview of operating conditions and KPIs is given in Table 6.6. Both processes require significant amounts of gold based catalyst to achieve an FA productivity of 35 kton/year, at a total catalyst amount of 2.8 and 8.57 kton for the amine-exchange process and the pressure-swing process, respectively. The increase of amount of catalyst for the pressure-swing process is caused by the lower residence time within the reactor, as well as the lower reactivity of n-butylimidazole compared to triethylamine. This results in very substantial reactors, having a length of 50 meters and a diameter of 7.5m, of which a single reactor is required when triethylamine is the reactive base (amine-exchange process) and 4 reactors operating in parallel are required for the utilization of n-butylimidazole as reactive base.

KPI	Unit	Amine-exchange process	Pressure-swing distillation process
Catalyst	-	Au/Al_2O_3	Au/TiO_2
Number of reactors	-	1	4
Reaction temperature	°C	40	75
Reaction pressure	bar	50	40
Mass of catalyst	kton	2.8	8.57
Residence time	h	36	1.25
CO_2 conversion	%	33	13.6
H_2 feed	kton/year	1.7	1.8
CO_2 feed	kton/year	38.1	38.2

Table 6.6: An overview of key performance indicators (KPI) at reactor scale

The hydrogen and carbon dioxide consumption of both processes is comparable due to the processes being designed for the same FA productivity and recycling of the reactor outlet stream after gas-liquid separation.

The technical performance of the amine-exchange and pressure-swing distillation processes on plant level are summarized and compared in Table 6.7, based on the technical performance indicators discussed in Section 6.2.5, evaluated from the mass and energy balances. To minimize the energy requirement of both processes, the pinch method developed by Linnhoff [78] was used. As a consequence, the heat integration within the processes was performed maximizing the internal cooling and heating based on process streams, rather than solely relying on external utilities. Most cooling capacity is supplied by cooling water, supplemented with air and refrigerant (Freon 12) when required. Instead of a continuous fresh water supply, both processes make use of cooling towers, allowing for the recycling of cooling water.

From Table 6.7, it is observed that the pressure-swing distillation process in which triethyamine is replaced by n-butylimidazole as reactive amine allows for a significant reduction in overall heating requirement in the form of HP steam from 270 MW to 186 MW, corresponding to a 31% decrease. Particularly, while the cold gas efficiencies are comparable at 90.7% versus 86.6%, explained by the comparable hydrogen consumptions, formic acid productivities and final formic acid purities (< 1 ppm amine) between the processes, a significant increase (37.4% increase) of the overall energy efficiency is observed for the pressure-swing distillation design. This increase of the overall energy efficiency in both the case of HP steam heating or electrical heating (2.08% versus 3.47%, 1.23% versus 2.11%) is mostly due to the decreased reboiler duties within the separation section of the proposed processes.

	Unit	Amine-exchange process	Pressure-swing distillation process
Feedstock			
H_2	kg/hr	190.8	199.88
CO_2	kg/hr	5500.8	4363.68
Thermal input (W_{feed})	MW	6.36	6.66
Products			
Formic acid	kg/hr	3844.8	4496.35
Thermal output (W_{chem})	MW	5.76	6.74
Cold Gas Efficiency (CGE)	%	90.7	86.6
Electricity	MW	0.81	0.87
Compressors	MW	0.60	
Pumps	MW	0.21	
Electrical energy input ($\frac{W_{el}}{\eta_{el}}$)	MW	1.38	1.49
Heating			

HP steam flow	MW	269.91	185.74
Natural gas energy input ($\frac{W_{NG}}{\eta_{NG}}$)	MW	347.88	239.98
Natural gas feedstock	kg/hr	22524.6	15538.3
Electric heating energy input ($\frac{W_{el}}{\eta_{el}}$)	MW	462.17	318.05
Overall energy efficiency ($\eta_{tot,NG}$)	%	2.08	3.47
Overall energy efficiency ($\eta_{tot,elec}$)	%	1.23	2.11

Table 6.7: Technical comparison in case of fossil-fuel derived steam production of the amine-exchange process based on triethylamine as reactive base, and the pressure-swing distillation process using n-butylimidazole as reactive base.

While the overall energy efficiency significantly increases when using n-butylimidazole instead of triethylamine, due to preventing the necessity of the energy intensive amine exchange reaction, the overall heating requirement remains very large and thus the plant efficiency low, as only ~3.5% of the input energy is stored within the chemical bonds of formic acid. The steam requirement for the proposed processes is 269.9 and 185.7 MJ/kg FA, for the amine-exchange process and the pressure-swing process, respectively. Comparing the steam requirement per kg of produced formic acid (MJ/kg FA) to the conventional carbon monoxide based process, the proposed processes are up to ~17 times more energy intensive in terms of steam consumption, as the conventional process only requires 19.25 MJ/kg FA [14].

Within the application of formic acid as hydrogen carrier, the energy efficiency will most likely be even lower due to the energy required to produce the hydrogen, obtain and purify the CO_2 feedstock and the energy required to liberate either hydrogen or electricity from the produced formic acid, which was deemed outside the scope of this work. Such low energy utilization is most likely not acceptable in future applications due to the scarcity and high prices of renewable energy [67][68].

To evaluate the carbon footprint of the proposed processes, a gate-to-gate analysis on the CO_2 emissions was performed. Here, no direct CO_2 emissions for the processes are considered, as no CO_2 is present in any of the purge or residual streams. To determine the indirect CO_2 emissions, natural gas-based electricity and natural gas-based HP steam are considered. The CO_2 emissions from energy consumption are taken to be 0.47 t_{CO2}/(MWh) [68] for electricity and 0.317 t_{CO2}/(MWh) for heat in the form of HP steam [69]. An overview of CO_2 emissions is given in Table 6.8.

	Amine-exchange process	Pressure-swing distillation process
CO_2 emissions electricity [tCO_2/year]	5188.8	5601.4
CO_2 emissions heat (NG) [tCO_2/year]	882233.5	471036.6
CO_2 emissions [tCO_2/t_{FA}]	25.4	11.9
CO_2 net emissions [tCO_2/year]	840433.5	438438.0

Table 6.8: Gate-to-gate analysis of the carbon footprint in case of fossil fuel derived heat of the proposed processes.

Due to the very significant energy consumption associated with the large HP steam consumption of the processes, the proposed processes do not result in net negative CO_2 emissions. The CO_2 emissions of the processes are found to be 25.4 tCO_2/t_{FA} (amine-exchange) and 11.9 tCO_2/t_{FA} (pressure-swing), while the current fossil fuel based process only results in the emission of 2.18 tCO_2/t_{FA} [14]. An overview of the yearly CO_2 emissions in case of renewably sourced electrical heating is given in Table 6.9.

	Amine-exchange process	Pressure-swing distillation process
CO_2 emissions electricity [tCO_2/year]	5188.8	5601.4
CO_2 emissions heat (elec)[tCO_2/year]	52487.7	36120.3
CO_2 emissions [tCO_2/t_{FA}]	1.65	1.04
CO_2 net emissions [tCO_2/year]	57638.4	41638.6

Table 6.9: Gate-to-gate analysis of the carbon footprint in case of electrical heating of the proposed processes.

When renewable electrical energy is used instead of fossil fuel derived heat, the CO_2 emissions per ton of produced formic acid are significantly decreased from 25.4 to 1.65 and 11.9 to 1.04 for the amine-exchange and pressure-swing distillation process respectively, and becomes lower than the emissions of the current methyl formate process. However, the CO_2 emissions remain larger than the CO_2

consumption, resulting in a non-negative net CO_2 emissions. Therefore, the currently proposed formic acid production processes cannot result in net negative emissions. However, the current comparison only concerns the formic acid production, and does not take into account the production of the feedstock. Indeed, within the proposed process, green H_2 and CO_2 obtained from CCU can directly be utilized, opening perspectives towards much lower CO_2 emissions compared to the current pathway which utilizes CO. Therefore, we open the door towards a negative emissions balance, as reported in the literature [14].

6.5. Economic comparison

An overview of the economic comparison between the amine-exchange and pressure-swing processes is given in Table 10 and Figure 7, for an annual productivity of 35 kton/year. The cost evaluation is based on the Lang Factor approach, as described in Section 2.4. Both proposed configurations have roughly the same purchase equipment cost (PEC) (i.e. 42.3 M€ vs 38.22 M€). While in the amine-exchange process the PEC is dominated by the heat-exchanger network (55.65%) and the distillation towers (31.7%) in line with the substantial HP steam consumption, the PEC of the pressure-swing process is mostly dominated by the reactor costs (62.38%). Previous work has shown n-butylimidazole to be less reactive than triethylamine [42], explaining the quadrupling of the reactor size and thus cost observed.

Cost component	Unit	Amine-exchange process	Pressure-swing process
Initial capital investment			
PEC	**M€**	**42.347**	**38.22**
Compressors	%	1.81	4.59
Pumps	%	1.41	0.85
Distillation towers	%	31.69	3.53
Flash columns	%	1.10	0.29
Heat exchanger	%	55.65	28.35
Reactors	%	8.31	62.38
CAPEX	**M€**	**321.414**	**290.130**
Operating costs			
Total variable	**M€ / year**	**301.779**	**741.62**

costs			
Feedstock (H_2)	%	3.03	1.29
Feedstock (CO_2)	%	0.48	0.19
Feedstock (NEt_3)	%	0.418	-
Feedstock ($NHex_3$)	%	0.06	-
Feedstock (nBIM)	%	-	0.10
Feedstock (1-decanol)	%	2.92	-
Catalyst	%	61.48	89.08
Utilities	%	31.60	9.33
Fixed OPEX	**M€ / year**	**6.73**	**6.17**
OPEX	**M€ / year**	**308.51**	**747.79**
ACAPEX	**M€ / year**	**32.74**	**29.55**
TAC	**M€ / year**	**341.25**	**777.34**
MFSP	**€ / ton FA**	**10821.47**	**18913.15**

Table 6.10: Overview of the economic analysis for both proposed processes

Previous experimental work highlighted the promising FA productivity of the high-boiling nBIM [42]. The lower reactivity of n-butylimidazole is explained by its lower enthalpy of protonation with formic acid [24][30], as the reaction is enthalpy driven [37]. While the lower protonation enthalpy of n-butylimidazole compared to triethylamine is a downside in reactive conditions, it is majorly beneficial within the separation train as less energy has to be supplied by the reboilers of the distillation towers to break the formic acid tertiary amine bond. The implication of the selection of n-butylimidazole as reactive base is also visible within the total OPEX and the cost distribution of the OPEX.

The amine-exchange process has a total OPEX of 308.51 M€/year, while the OPEX of the n-butylimidazole based pressure-swing distillation process is 747.79 M€/year, i.e. more than twice the cost. The main cost contributors to the OPEX expenses in the amine-exchange case are observed to be the annualized catalyst cost (i.e. 61.5%) and the utilities (i.e. 31.6%). Of the utilities, the majority (i.e. 97.8%) corresponds to the HP stream consumption of the reboilers. For the pressure-swing process, the main cost contributor (i.e. 89.08%) is the cost of the large amount catalyst required. It is worth noticing that even though, the combination of lower reactivity and lower protonation enthalpy of n-butylimidazole resulted in the expected decrease in total utility cost caused by a decrease in HP steam consumption (due to requiring less energy to break the FA-amine bond), it does not counteract the detrimental effect of the significant increase in required catalyst mass resulted in a the highest yearly OPEX expenditure.

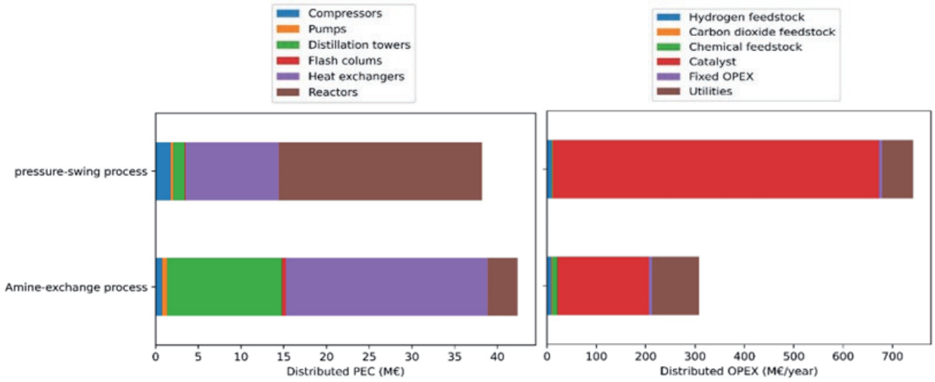

Figure 6.7: left) Distributed PEC. right) Distributed OPEX for both proposed processes

The formic acid price is heavily driven by the OPEX expenditures for both processes, with the OPEX being 90.4% and 96.2% of the total annual expenses (TAC) for the amine-exchange and pressure-swing process, respectively. Accounting for the salvage value of the gold-based catalysts after the operational life time of the plants, the minimum formic acid selling price is calculated to be €10821.47 and €18913.15 per ton of formic acid for the amine-exchange and pressure-swing process, respectively.

Currently, the formic acid price is 881.36 € per ton [43]. This analysis is based on the strong assumption that the catalyst does not deactivate within the 20 year operational lifetime. If the catalyst has to be replaced within the operational lifetime, the formic acid prices are expected to increase significantly due to the large amounts of catalyst required for the 35 kton/year FA production. If this is not taken into account, the obtained formic acid prices are up to 12.3 and 21.4 times the current market value. However, this is the market price corresponding to technical grade formic acid (85%). Within this work, the formic acid purity is much higher (<1 ppm impurities), fitting with fuel cell applications envisioned for formic acid. Therefore, prices are not directly comparable due to purity differences.

6.6 Sensitivity analysis and forecasting

The economic analysis presented in Section 6.5 revealed that the proposed direct CO_2 hydrogenation pathways for formic acid production are not yet competitive with the current benchmark process (i.e methyl formate hydrolysis), based on the current market conditions.

From Table 6.10 it readily becomes evident that the formic acid production pathways proposed are OPEX intensive processes, with the ACAPEX only accounting for 9.6% and 3.8% of the TAC for the amine-exchange and pressure-swing process, respectively. Thus, the MFSP is mainly influenced by the OPEX costs, with small contributions from the CAPEX.

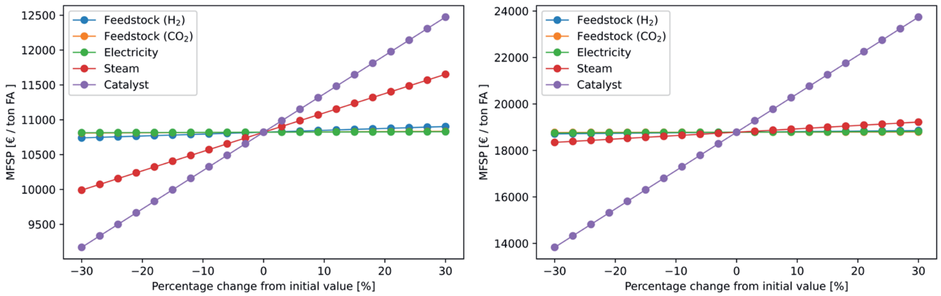

Figure 6.8: Effect of a variation of ± 30% in the price of the main OPEX cost contributions on the MFSP. Left) Amine-exchange process. Right) Pressure-swing process.

Figure 6.8 shows that the price of the catalyst is the largest contributor to the MFSP for both processes, followed by the price of steam. Furthermore, the cost of the other OPEX cost drivers such as the chemical feedstock and electricity only show minor effects on the MFSP. The results of this analysis reveal that the MFSP can be significantly reduced upon the reduction of the total catalyst price, or the utilization of a more active catalyst, as this would result in a decrease in the required catalyst volume. Thus, a forecasting analysis was carried out to estimate the required increase in catalyst activity to allow the proposed processes to become economically competitive to the current methyl formate hydrolysis process. The result of this forecasting analysis is presented in Figure 6.9.

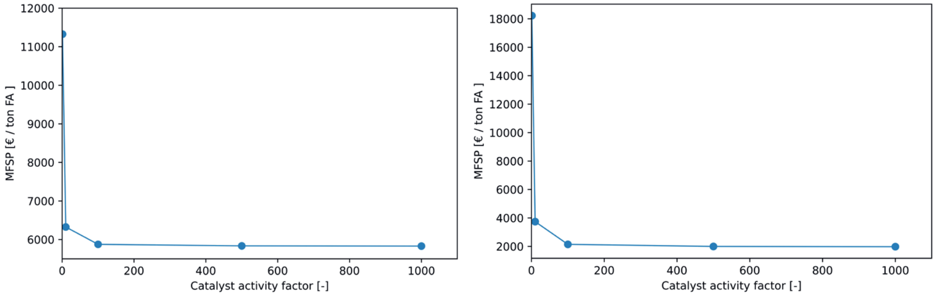

Figure 6.9: Forecasting the cost of formic acid based on an improvement in catalyst activity. Left) Amine-exchange process. Right) Pressure-swing process.

Figure 6.9 reveals a significant decrease of the MFSP as a function of catalyst activity, however, at a catalyst activity factor of 100 the catalyst price no longer has a significant impact on the MFSP and the price becomes dominated by steam consumption. However, at this catalyst activity increase, the steam consumption corresponds to 75.9% and 71.1% of the OPEX cost for the amine-exchange and pressure-swing process, respectively. For both processes, it was observed from Figure 6.9 that a catalyst activity increase of a factor 10 is sufficient to decrease the contribution of the catalyst cost from 60.1 to 13.1% and 88.06 to 42.45%, for the amine-exchange and pressure-swing process, respectively.

While significant cost reductions can be achieved for both proposed processes if more active catalyst formulations are designed and developed while maintaining the current extraordinary selectivity of supported gold nanoparticles, the proposed processes remain economically uncompetitive compared to the current methyl formate hydrolysis process due to the significant energy requirement of formic acid purification. Further optimization of the utilized amine is thus required to decrease the required energy consumption.

6.7 Conclusions

Within this work, two routes for the direct hydrogenation of CO_2 to formic acid at non-supercritical pressures were designed and compared at a techno-economic level. The formic acid productivity was set to 35 kton/year, with the formic acid produced at fuel cell purity (<1 ppm impurities).

The first route represents the conventional CO_2 hydrogenation route based on the state-of-the-art literature to perform the azeotropic separation between formic acid and the low boiling tertiary amine used to shift the equilibrium towards formic acid in the reactor. Here, the low boiling amine (triethylamine) is replaced by a higher boiling amine using reactive distillation, followed by thermal splitting. The second route presents a methodology to circumvent the amine-exchange through the usage of a higher boiling amine (n-butylimidazole) within the reactor, followed by vacuum pressure-swing distillation. The overall energy efficiency significantly increased (i.e. 2.08% to 3.47%) when n-butylimidazole was used as the reactive amine due to a decrease in heating requirement in the distillation train (i.e. 347 MW vs 240 MW).

The environmental analysis revealed no net carbon emission reduction if fossil-based or renewable sources are used for steam and electricity production. From an economic perspective, the determined minimum selling price of formic acid was found to be heavily dominated by the OPEX, i.e. 90.4 and 96.2% of the total annual expenses (TAC) for the amine-exchange and pressure-swing process, respectively. The majority of these costs arises from the large energy consumption of both processes, as well as the very significant amounts of catalysts required (i.e. 2.7 and 8.5 kton). The minimum formic acid selling price was calculated to be €10821.47 and €18913.15 per ton of formic acid for the amine-exchange and pressure-swing process, respectively. These FA prices are up to 12.3 and 21.4 times the current market value. However, the current comparison only concerns the formic acid production, and does not take into account the production of the feedstock. Indeed, within the proposed process, green H_2 and CO_2 obtained from CCU can directly be utilized, opening perspectives towards much lower CO_2 emissions compared to the current pathway which utilizes CO.

While significant cost reductions can be achieved for both proposed processes if substantially more active and stable catalyst formulations are designed and developed while maintaining the current extraordinary selectivity of supported gold nanoparticles, the proposed processes remain economically uncompetitive compared to the current methyl formate hydrolysis process due to the significant energy requirement of formic acid purification under the current market conditions.

Appendix E

E.1 Stream table amine-exchange process

Stream Name	Units	1	2	3	9	11+13
Temperature	C	21	21	40	40	152,6857123
Pressure	bar	1	30	50,00000583	50,00000076	1
Molar Enthalpy	cal/mol	-94023,73135	-27,47930102	-93853,4514	103,259522	-77438,37863
Mass Flows	kg/hr	5501,225	191,5086	5501,225	191,5086	50806,51377
DECANOL		0	0	0	0	0,750818359
NET3		0	0	0	0	0,225063227
NHEX3		0	0	0	0	0,00531158
H2		0	1	0	1	0
CO2		1	0	1	0	0
FOR-ACID		0	0	0	0	0,00481641
ADDNET3		0	0	0	0	0,013981238
ADDNHEX3		0	0	0	0	9,18693E-06
H2O		0	0	0	0	0
CO		0	0	0	0	0

Stream Name	Units	12+14	16	17	18
Temperature	C	40	40	40	38,33661693
Pressure	bar	50	50	50	1
Molar Enthalpy	cal/mol	-87655,67936	-111025,5469	-93778,34611	-112624,7908
Mass Flows	kg/hr	50806,51377	55543,43758	1320,342381	54223,0952
DECANOL		0,750818359	0,686786143	0	0,703509513
NET3		0,225063227	0,032793309	0	0,033591832
NHEX3		0,00531158	0,004852318	0	0,004970472
H2		0	8,7105E-07	3,66429E-05	0
CO2		0	0,023770477	0,999963357	0
FOR-ACID		0,00481641	0	0	0
ADDNET3		0,013981238	0,251796882	0	0,257928183
ADDNHEX3		9,18693E-06	0	0	0
H2O		0	0	0	0

CO		0	0	0	0

Stream Name	Units	20	21	22	23
Temperature	C	228,8992771	116,5265739	116,5036593	70
Pressure	bar	1	1	0,11	0,11
Molar Enthalpy	cal/mol	-92201,37458	-105713,6546	-105715,4193	-94798,13008
Mass Flows	kg/hr	36583,16349	17639,93171	17639,93171	22714,5262
DECANOL		0,973680798	0,14320574	0,14320574	0,111944879
NET3		2,25084E-14	0,103257379	0,103257379	0,093214695
NHEX3		0,00736717	4,23255E-13	4,23255E-13	0,000100092
H2		0	0	0	0
CO2		0	0	0	0
FOR-ACID		0	0	0	0,204692407
ADDNET3		0,018952032	0,753536881	0,753536881	0,589660714
ADDNHEX3		0	0	0	0,000387213
H2O		0	0	0	0
CO		0	0	0	0

Stream Name	Units	64	25	26	27
Temperature	C	29,00375856	31,0429745	59	39,9001319
Pressure	bar	0,11	0,11	0,11	0,11
Molar Enthalpy	cal/mol	-31041,92887	-34083,84599	-99002,40902	-93661,86432
Mass Flows	kg/hr	10932,70034	11199,77864	677180,772	5341,672787
DECANOL		3,00862E-08	7,82032E-05	0,002603319	0,003278176
NET3		0,998911297	0,976480897	0	0,058305054
NHEX3		2,0927E-05	3,11119E-05	0,994986904	0,000448025
H2		0	0	0	0
CO2		0	0	0	0
FOR-ACID		8,95213E-09	0,021849093	0,002409776	0,916229081
ADDNET3		0,001067385	0,00151902	0	0,020006452
ADDNHEX3		3,52394E-07	4,16755E-05	2,63428E-10	0,001733213
H2O		0	0	0	0
CO		0	0	0	0

Stream Name	Units	29	30	31	32
Temperature	C	39,9001319	213,9317388	130	40,88464364
Pressure	bar	0,11	0,11	0,11	0,11
Molar Enthalpy	cal/mol	-93661,86432	-75592,80119	-89115,13893	-98384,02016
Mass Flows	kg/hr	5074,594489	1495504,124	1495504,124	8869,794244
DECANOL		0,003278176	0,004020713	0,004020713	0,301323713
NET3		0,058305054	1,93013E-11	1,93013E-11	3,25432E-09
NHEX3		0,000448025	0,991188964	0,991188964	0,235626853
H2		0	0	0	0
CO2		0	0	0	0
FOR-ACID		0,916229081	0,0047902	0,0047902	0,463028631
ADDNET3		0,020006452	6,69164E-17	6,69164E-17	0
ADDNHEX3		0,001733213	1,23513E-07	1,23513E-07	2,07987E-05
H2O		0	0	0	0
CO		0	0	0	0

Stream Name	Units	34	35	36
Temperature	C	214,8122774	39,31011458	119,480604
Pressure	bar	0,11	0,11	0,11
Molar Enthalpy	cal/mol	-74986,67747	-95125,29805	-99759,43633
Mass Flows	kg/hr	1486632,843	3852,181141	5017,613103
DECANOL		0,002246896	8,75959E-16	0,53265951
NET3		5,19407E-23	3,80229E-09	2,83363E-09
NHEX3		0,995696919	3,29493E-15	0,416525082
H2		0	0	0
CO2		0	0	0
FOR-ACID		0,002056185	0,999999995	0,050778639
ADDNET3		0	0	0
ADDNHEX3		1,56976E-10	1,22879E-09	3,67656E-05
H2O		0	0	0
CO		0	0	0

E.2 Stream table pressure-swing distillation process

Stream	Temperature	Pressure	Molar Enthalpy	Mass Flows	H2	CO2	FA	N-BIM
	C	(bar)	(cal/mol)	(kg/hr)				
1	20	1	-94044,10955	4363,684754	0	1	0	0
2	20	30	-25,27173534	199,8795478	1	0	0	0
3			-20723,03867	0	0	0	0	0
4	70,37269109	1	-52222,78319	33266,26284	0,034801813	0,965198187	0	0
11	75	40	-52294,16942	33266,26284	0,034801813	0,965198187	0	0
13	55,54603969	40	224,6607091	199,8795478	1	0	0	0
14	73,19082726	40	-48582,65669	33466,14238	0,040566546	0,959433454	0	0
16	75	0,133322368	-16050,09403	517595,3896	0	0	0	1
17	75,50667509	40	-15909,16018	517595,3896	0	0	0	1
18	76,72413565	40	-24137,91622	551061,5321	0,002463619	0,058266699	0	0,939269681
19	75	40	-24441,2576	551061,5321	0,002100902	0,050348011	0,008281406	0,939269681
20	75	1	-48780,76683	28902,57808	0,040056158	0,959943842	0	0
21	75	1	-17274,99917	522158,9541	0	0	0,008739799	0,991260201
22	74,99335692	0,159986842	-17277,61677	522158,9541	0	0	0,008739799	0,991260201
50	131,2480357	0,159986842	-21604,74501	1272328,521	0	0	0,069651867	0,930348133
23	176	0,159986842	-17481,42591	1272328,521	0	0	0,069651867	0,930348133
24	167,261	0,159986842	-8385,283653	517595,3896	0	0	0	1
31	75	0,133322368	-16050,09403	517595,3896	0	0	0	1
25	201,617	0,15998	-	754733,	0	0	0,11741	0,88258

	02	6842	23291,25223	1313			9062	0938
26	180	0,159986842	-25130,26799	754733,1313	0	0	0,117419062	0,882580938
27	179,9996738	0,133322368	-25130,33895	754733,1313	0	0	0,117419062	0,882580938
30	180,75	0,133322368	-24186,04117	750236,7851	0	0	0,112129546	0,887870454
28	43,763	0,133322368	-101533,6062	4496,346136	0	0	1	0
29	20	0,133322368	-101797,3664	4496,346136	0	0	1	0
30	20,02578817	1	-101796,5455	4496,346136	0	0	1	0
31	180,75	0,159986842	-24185,96164	750236,7851	0	0	0,112129546	0,887870454

E.3 Economic analysis

The fixed OPEX costs are dependent on the labor requirement of the plant. This was calculated based on the number of operators required on site and the average yearly salary. The country of choice is The Netherlands where the average yearly salary is 60.000 euro/year, based on 8 hour shifts [1]. The labor requirement can be calculated according to:

$$N_{OL} = (6.29 + 31.7\,P^2 + 0.23N)^{0.5} \qquad E.1$$

where N is the number of non-particulate processing steps such as compression, heating/cooling, mixing and reaction. Based on the assumptions stated in Table 6.4, we should consider 15 operators for the amine-exchange process and 14 operators for the pressure-swing distillation process.

The annualized CAPEX (ACAPEX) is determined under the assumption of constant yearly OPEX costs by multiplying the total CAPEX (based on the Lang factor methodology) with an annualization factor:

$$ACAPEX = CAPEX \cdot \frac{r(1+r)^{L_t}}{(1+r)^{L_t} - 1} \qquad E.2$$

where r is the fractional interest rate, also called the weighted average cost of capital (WACC) and L_t is the lifetime of the plant, assumed to be 20 years. The WACC is calculated by:

$$WACC = D_R \cdot i_d + (1 - D_R) \cdot i_e \qquad E.3$$

where D_R is the debt ratio, i_d is the interest rate and $i_e$is the cost of equity, an overview of these values is given in Table 6.4. To determine the minimum formic acid selling price (MFSP), an discounted cash flow (DCF) analysis was performed. The annual cash flow ACF is defined as the profit of each year i.e. the difference between yearly production sales and the TAC (total annual cost). To account for the cost of capital, the net present value (NPV) is defined the sum of the cash flow of each year n, depending on the fractional interest rate i which is equal to the WACC.

$$NPV = \sum_{n=1}^{L_t} \frac{A_{CF,n}}{(1 + i)^n} \qquad E.4$$

where the $A_{CF,n}$ is dependent on the gross profit P_n, tax rate t, depreciation D_n, construction costs CC and construction period CP:

$$A_{CF,n} = P_n(1 - t) + D_n t - \frac{CC}{CP} \qquad E.5$$

To determine the MFSP, the NPV was set to 0, and the interest rate equal to the discount rate.

E.4 Reactor modelling amine-exchange case

Within industrial scale reactors, mass and/or heat transfer limitations can often occur, resulting in lower conversions than predicted by kinetic systems. In a regular fixed bed reactor, these mass and/or heat transfer limitations can occur at several length scales: within the catalyst particle (intra-particle mass/heat transfer limitations) and between the catalyst particle and the build fluid (external mass/heat transfer limitations). Within this work, these different length scales were studied for the packed bed reactor.

At all length scales, the following assumptions were taken:

1. Steady state conditions
2. 1D ideal plug flow: axial and radial heat and mass dispersion are neglected
3. No pressure drop is considered, which entails a constant interstitial velocity in the axial direction both gas and liquid.
4. The CO_2 and H_2 concentration at the start of the column in the liquid phase is equal to saturation conditions
5. No phase separation between reactants and products at any length scale
6. The catalyst particle can be a flat plate, cylindrical or spherical
7. Film theory is assumed to be valid
8. The catalyst remains stationary during operation
9. The liquid enters the column at saturation conditions
10. The catalyst is fully wetted

Particle scale

First, the governing equations and boundary conditions of the rigorous particle model are discussed. The particle model is used to evaluate the extent to which internal mass and/or heat transfer limitations play a role, allowing to design appropriate catalyst particles.

The particle model consists out of mass and energy balances. Convection was considered to be negligible at this scale. The steady state balance for any component *I* for any catalyst geometry is known to be:

$$0 = \frac{1}{r^v}\frac{\partial}{\partial r}\left(r^v\, D_{i,eff}\frac{\partial c_i}{\partial r}\right) - R_i \qquad E.6$$

Here, *r* is the characteristic length of the catalyst particle, *v* the geometry factor (0 =

flat plate, 1 = cylindrical, 2 = spherical), $D_{i,eff}$ the effective diffusivity of component i, c_i the molar concentration of component i and R_i the reaction rate of component I in terms of catalyst volume.

The coordinate system was chosen such that the particle center is the origin. At the center a finite concentration is enforced, also known as the symmetry boundary condition, in the form of a Neumann boundary condition:

$$\left.\frac{\partial c}{\partial r}\right|_{r=0} = 0 \qquad E.7$$

At the outer edge of the particle, where r = $R_{particle,}$, the concentration is equal to the fluid bulk concentration (Dirichlet boundary condition):

$$\left.\frac{\partial c}{\partial r}\right|_{r=R} = c_B \qquad E.8$$

As the formation of formic acid from CO_2 is known to be exothermic, heat is generated by the reaction within the catalyst particle. The heat within the catalyst particle was assumed to only be governed by thermal conductivity, resulting in the following balance:

$$0 = \frac{1}{r^v}\frac{\partial}{\partial r}\left(r^v\,\lambda_{eff}\,\frac{\partial T}{\partial r}\right) + \sum \Delta H\,\cdot R_i \qquad E.9$$

Here, the same definition are used as presented previously, with λ_{eff} the effective thermal conductivity and ΔH the reaction enthalpy. The reaction rate is a function of temperature following the Arrhenius approach. The boundary conditions employed are equal to those used within the mass balances. The particle model was subject to extensive verification based on irreversible first order reactions using a derived analytical expression, assuming a constant diffusivity. Two separate cases were studied, isothermal (flat plate geometry and spherical geometry) and non-isothermal.

The results of the isothermal case can be found in Figure E.1.

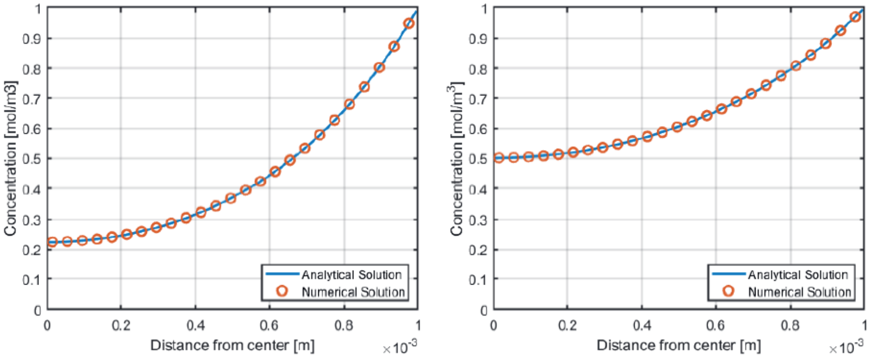

(a) Flat plate geometry.

(b) Spherical geometry.

Figure E.1: a) The concentration profile of verification compound A as a function of particle radius [m] obtained numerically and analytically for a flat plate geometry using an irreversible first order reaction under isothermal conditions, using 100 equidistant grid cells. b) The concentration profile as a function of particle radius obtained numerically and analytically for a spherical geometry using an irreversible first order reaction under isothermal conditions, using 100 equidistant grid cells.

The error between the analytical and numerical profiles was defined as follows:

$$\in = \max\left(\left|\frac{c_{numerical} - c_{analytical}}{c_{analytical}}\right|\right) \qquad E.10$$

The maximum error was found to be < 1e^{-3} for both geometries when using 100 grid cells, indicating a high model accuracy and correct equation implementation for the isothermal case. To evaluate the non-isothermal case, representing the coupling of the mass and concentration balance using an Arrhenius law, the Weizs-Hicks solution is used. Within this approach, the coupled ODEs were transformed to a single ODE, which is solved using MATLAB's ode15s solver. The result is depicted in Figure E.2. In order to solve the Weisz-Hicks case two parameters are required: the Arrhenius number (β) and the Prater number (γ):

$$\beta = \frac{c_B\,\Delta H\,D_{eff}}{\lambda_{eff}\,T_B} \qquad E.11$$

$$\gamma = \frac{E_{act}}{R\,T_B} \qquad E.12$$

The latter represents the dimensionless heat of the reaction and the Arrhenius number expresses the sensitivity of the rate to temperature. These two dimensionless parameters are central to the Weisz and Hicks solution, allowing to describe the multiple steady states often found in mass and heat balances with Arrhenius coupling.

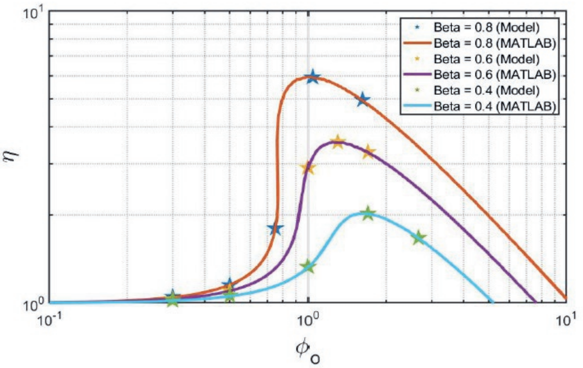

Figure E.2: Comparison between Weisz & Hicks curves and numerically obtained model results for a model of 10, based on a spherical particle geometry.

In Figure E.2, the multiple steady state curves of Weisz and Hicks (1995) and the numerical model results are shown for an Arrhenius number of 10, again using 100 grid cells. The error was again observed to be below 1e^{-3}, therefore confirming model accuracy and implementation.

The kinetic parameters of the CO_2 hydrogenation towards formic acid are described using a power law, with the temperature dependency implemented using an Arrhenius law. The rate constants are based on the work of Hensen *et al*. for a commonly employed gold catalyst (Au/Al_2O_3), within this work triethylamine (NEt_3) is used as the trialkylamine extraction base. The produced formic acid is assumed to immediately bind to the available triethylamine, forming an adduct. Because of this very fast step, the total process is described using a single rate expression. In short the reaction can be summarized by:

$$CO_2 + H_2 + NEt_3 \rightleftarrows (\mathrm{FA} \cdot NEt_3) \qquad E.13$$

Here, the forward rate is given by:

$$R_F = k_F\,[CO_2]\,[H_2]^{0.5}\,[NEt_3] \qquad E.14$$

While the reverse reaction is given by:

$$R_R = k_R\,[y \cdot FA \cdot NEt_3] \qquad E.15$$

The kinetic constants are described using an Arrhenius law, with the following kinetic parameters:

Parameter	Forward reaction	Reverse reaction
E_{act} [J/mol]	5000	74000
A_0 [1/s]	0.0052	4.74e8
ΔH [kJ/mol]	-60.0	-167.0

Table 2 : Kinetic parameters of the catalytic hydrogenation of CO_2 to FA, based on the work of Filonenko et al. [2]

The reaction enthalpy of the forward reaction was experimentally determined, while the reaction enthalpy of the backward reaction was estimated based on formation enthalpies taken from NIST.

Particle-fluid interphase scale

Within the previous section Dirichlet boundary condition were used, meaning the concentration of any reagent and product at the edge of the catalytical concentration is equal to the bulk conditions. However, this assumption is often subject to the type of reactor used, as well as of the reaction conditions. For this reason, at the particle-fluid interphase, this assumption is often not valid. For this reason, the mass and heat transfer from the bulk fluid to the catalyst particle is modelled, allowing us to study the extent of external mass/heat transport resistance present allowing for an additional comparison between different reactor types.

According to film theory, the following relations can be used to describe the flux transport (J_i) of mass and heat between the bulk and particle phase, respectively:

$$J_i = k_{ext}\left(c_{i,b} - c_i|_{r=R}\right) \qquad E.16$$

$$J_i = h_{ext}\left(T_{bulk} - T|_{r=R}\right) \qquad E.17$$

Here, k_{ext} and h_{ext} are the external mass and heat transfer coefficients, both were obtained using appropriate correlations of previous works. When applying the above equations to a particle model, the above equation can be enforced using the boundary conditions of the particle model. Here, the aforementioned Dirichlet boundary condition, in which the bulk concentration is imposed, is replaced by a Robin boundary condition, in which a flux is imposed. The flux boundary conditions for mass and heat are given by:

$$D_{eff,i} \left.\frac{\partial c_i}{\partial r}\right|_{r=R} = k_{ext} \left(c_{i,b} - c_i|_{r=R}\right) \qquad E.18$$

$$\lambda_{eff} \left.\frac{\partial T}{\partial r}\right|_{r=R} = h_{ext} \left(T_B - T|_{r=R}\right) \qquad E.19$$

The analytical expression used in the previous section was adapted to the boundary condition discussed above, resulting in the following analytical expression for isothermal irreversible reaction for a spherical and flat plate geometry respectively:

$$\frac{c}{c_b} = \frac{\sinh(\lambda_c\, \varphi)}{\sinh(\varphi)} \cdot \frac{1}{\lambda_c} \cdot C_w \qquad E.20$$

$$\frac{c}{c_b} = \frac{\cosh(\lambda_c\, \varphi)}{\cosh(\varphi)} \cdot C_w \qquad E.21$$

Here, λ_c is the dimensionless particle coordinate, φ the Thiele modulus and C_w the drag coefficient given by:

$$\frac{1}{C_w} = \frac{\varphi \cdot \tanh(\varphi)}{Bi} + 1 \qquad E.22$$

$$Bi = \frac{k_{LS} \cdot L_c}{D_{eff}} \qquad E.23$$

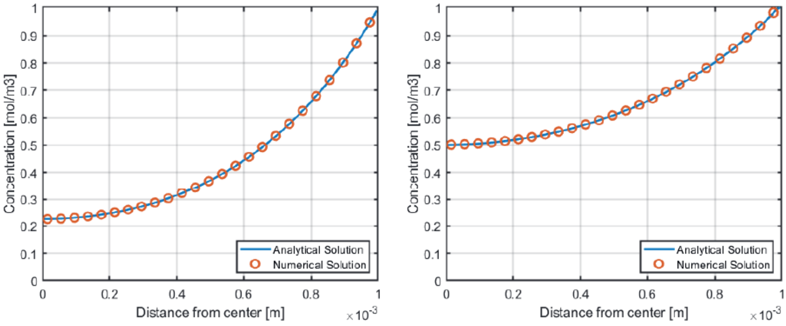

(a) Flat plate geometry.

(b) Spherical geometry.

Figure E3 : a) The concentration profile as a function of particle radius obtained numerically and analytically for a flat plate geometry subject to Robin boundary conditions using an irreversible first order reaction under isothermal conditions, using 100 equidistant grid cells. b) The concentration profile as a function of particle radius obtained numerically and analytically for a spherical geometry subject to Robin boundary conditions using an irreversible first order reaction under isothermal conditions, using 100 equidistant grid cells.

Within the above equations, k_{LS} is the external liquid-solid mass transfer coefficient and L_C the characteristic length of the corresponding geometry. The comparison of the obtained analytical and numerical results can be found in Figure E.3, for a flat plate and spherical geometry using 100 grid cells. The error was again observed to be below $1e^{-3}$, therefore confirming model accuracy and implementation.

Fixed bed reactor scale

Within the previous section the particle was connected to a bulk fluid while accounting for external transfer resistances. However, within the bulk fluid there is convective flow and in some cases axial dispersion. However, as stated before, axial dispersion is neglected by using L/dp ≥ 50 and a D/dp ≥ 25, respectively. The following governing equation was used to design the fixed bed reactor:

$$\frac{\partial}{\partial z}(v\, c_i) = R_i \qquad E.24$$

Here, *v* is the velocity of the phase (gas or liquid) for which the balance is used. It was opted to study a upflow co-current model as these flow configurations are known to have higher liquid-solid mass transfer rates and often higher liquid hold-ups compared to a downflow configuration. The definition of the reactive term is dependent on the rigorous particle model in order to take external mass transfer into account, for a spherical particle the rate expression is given by:

$$R_i = D_{cat}(1 - \varepsilon_{bed}) \frac{6}{d_{part}} \left(D_{eff,i} \left. \frac{\partial c_i}{\partial r} \right|_{r=R} \right) \qquad E.25$$

The governing equation for heat is analogous to the governing equation previously shown for mass. As is the case for the mass axial dispersion, heat axial dispersion is also neglected:

$$\frac{\partial}{\partial z}\left(v \sum_i \left(c_i \cdot C_{p,i}\right) T \right) - \sum \Delta H_i R_i \qquad E.26$$

Here, *Cp,i* is the heat capacity of component *i*. At the reactor inlet (x = 0), it was opted to enforce the concentration and temperature (Dirichlet boundary condition).

$$c_i|_{x=0} = c_{i,in} \qquad E.27$$

$$T|_{x=0} = T_{i,in} \qquad E.28$$

At the reactor outlet (x = L), the gradient in terms of mass and temperature should be equal to zero (Neumann boundary condition):

$$\left. \frac{\partial c_i}{\partial z} \right|_{z=L} = 0 \qquad E.29$$

$$\left. \frac{\partial T}{\partial z} \right|_{z=L} = 0 \qquad E.30$$

To allow for the derivation of analytical expressions, enabling the verification of the packed bed reactor model, two limiting verification cases were studied. Within the first case, the gas concentration was assumed to remain constant, while in the second case the liquid concentration was assumed constant. Additionally, as was done in the previous cases, an isothermal first order irreversible reaction was used, allowing for the usage of a Thiele modulus efficiency factor, leading to the following governing equation for the catalyst phase:

$$0 = -\eta \cdot k \cdot c_s + k_{ls} \cdot a_{LS} \cdot (c_L - c_s) \qquad E.31$$

Using the above governing equation to obtain an expression for the solid concentration results in:

$$c_s = c_L \left(\frac{k_{ls} \cdot a_{LS}}{\eta \cdot k \cdot c_s + k_{ls} \cdot a_{LS}} \right) \qquad E.32$$

Upon substituting the obtained expression for the catalyst phase concentration profile in the liquid phase balance:

$$\frac{\partial c_L}{\partial z} = A - c_L \cdot B \qquad E.33$$

With:

$$\mathrm{A} = \left[\frac{\varepsilon_G \, k_{GL} \, a_{GL}}{v_L} \, c_G \right] \qquad E.34$$

$$\mathrm{B} = \left[\frac{\varepsilon_G \, k_{GL} \, a_{GL}}{v_L} + \frac{\varepsilon_{void} \, k_{LS} \, a_{LS}}{v_L} - \frac{\varepsilon_{void} \, \varepsilon_{bed} \, k_{LS} \, a_{LS}}{v_L} \cdot \left(\frac{k_{ls} \cdot a_{LS}}{\eta \cdot k \cdot c_S + k_{ls} \cdot a_{LS}} \right) \right] \qquad E.35$$

Integration leads to the final verification expression for the limiting gas of constant gas concentration:

$$c_L = c_{L,0} \cdot \exp(-B \cdot z) - \frac{A}{B} \cdot \exp(-B \cdot z) + \frac{A}{B} \qquad E.36$$

Within Figure E.4, the analytical expression was compared to the numerical model results using 100 grid cells in the axial direction and 100 grid cells within the particle model. The maximal error obtained was 4.6e^{-6}, similar results were obtained for the case of constant liquid concentration.

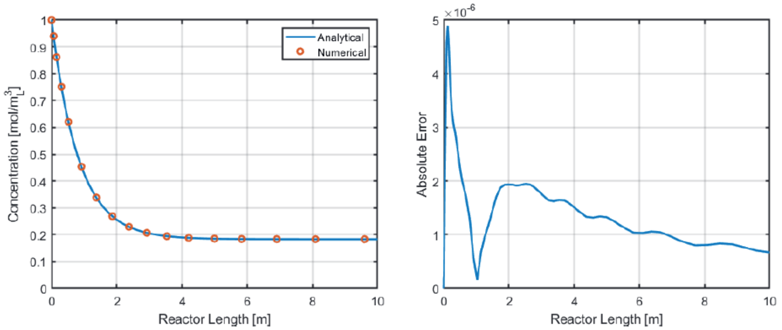

(a) Concentration profiles.

(b) Difference.

Figure E.4: a) The concentration profile in the axial direction obtained analytically and numerically for an isothermal irreversible first order reaction, using 100 grid cells in the axial direction using spherical particles. b) The maximum error between the analytical expression and the numerical simulation

E.5 C_p value n-butylimidazole

The theoretical work of Turner *et al.* revealed a linear trend between the Cp value and the chain length of n-alkylimidazoles [3]. However, no data was available for n-butylimidazoles. For this reason, we employed linear regression, resulting in a R^2 of 0.9984.

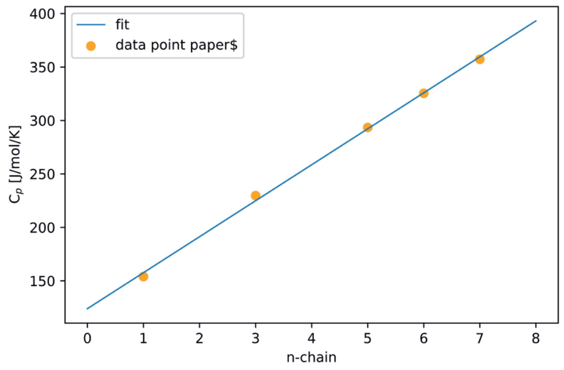

Figure E5 : Plotting and fitting of experimental C_p values of n-alkylimidazoles against the number of carbon atoms in the alkyl chain based on the work of Turner et al. [3]

E.6 n-butylimidazole - formic acid VLE

A_{ij}	A_{ji}	B_{ij}	B_{ji}	C_{ij}	T_{lower} (K)	T_{upper} (K)
-21,9458533	1,145775	6257,026	4778,741	0,101537	0	723

Table E.3 : Regressed FA-nBIM binary interaction parameters based on the NRTL-HOC thermodynamic model. Obtained from Aspen Plus V12 based on the work of Park et al. [4]

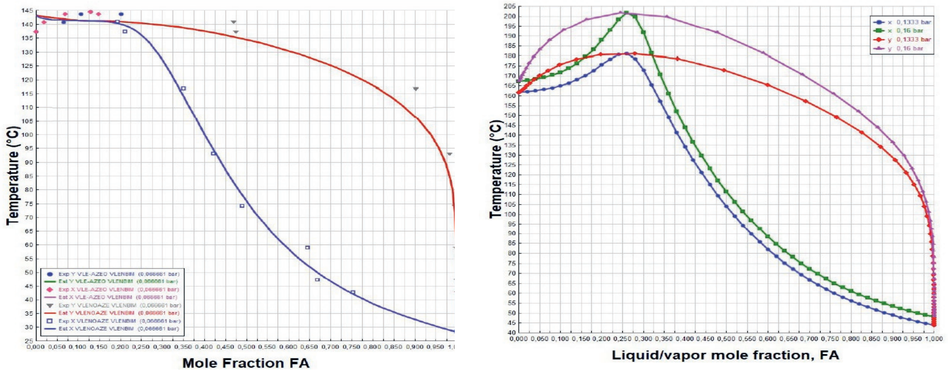

Figure E.6: left) Fitting of experimental VLE data of the nBIM-FA binary system at 50 mmHg. Data obtained from Park et al. [4]. Fitting performed in Aspen Plus V14. Right) nBIM-FA VLE curves at 100 and 120 Torr based on the binary interaction parameters shown in Table 2.

E.7 Methods for the Purchase Equipment Cost (PEC) determination

Within this section the correlations and cost factors used to determine the PEC are summarized. All correlations were taken from [5], and shown in Section 6.2.4. In case the cost basis is material mass, the wall thickness needs to be calculated. The wall thickness is calculated by [6]:

$$wall\ thickness = \frac{PD}{2S_{max}E_w - 1.2P} \qquad E.37$$

with, P the pressure, D the vessel diameter, S_{max} the maximum allowable stress taken from [6], and E_w the welded joint efficiency. The welded joint efficiency is taken to be 1. According to the ASME Boiler and Pressure Vessel Code [6], a minimum wall thickness of 5 mm is required for corrosive materials. Thus, if a wall thickness < 5 mm was obtained, the wall thickness was set to 5 mm. With exception of the reactor, a height/diameter ratio of 3 was assumed.

Pressure vessels

Unit	Cb ($)	Qb(ton)	Q (ton)	M	F_m	F_p	F_T
R1	98400	6	101,2	0,82	3,2	1,5	1
F1	98400	6	5,1	0,82	3,2	1	1

Table E.4 : Factors used for determination of the PEC of the pressure vessels used within the amine-exchange process

Unit	Cb ($)	Qb(ton)	Q (ton)	M	F_m	F_p	F_T
R1	98400	6	270,36	0,82	3,2	1,5	1
F1	98400	6	0,1	0,82	3,2	1	1

Table E.5 : Factors used for determination of the PEC of the pressure vessels used within the pressure swing distillation process

Distillation towers

Unit	Cb ($)	Qb(ton)	Q (ton)	M	F_m	F_p	F_T
T1	65600	8	101,7	0,89	3,2	1	1
T2	65600	8	38,8	0,89	3,2	1,3	1
T3	65600	8	35,3	0,89	3,2	1,3	1
T4	65600	8	30,1	0,89	3,9	1,3	1
T5	65600	8	4,2	0,89	3,9	1,3	1

Table E.6 : Factors used for determination of the PEC of the distillation column (empty shell) used within the amine-exchange process

Unit	Cb ($)	Qb(m)	Q (m)	M	F_m	F_p	F_T
T1	18000	0,5	4	0,97	3,2	1	1
T2	18000	0,5	4	0,97	3,2	1,3	1
T3	18000	0,5	4	0,97	3,2	1,3	1
T4	18000	0,5	4	0,97	3,9	1,3	1
T5	18000	0,5	1,5	0,97	3,9	1,3	1

Table E.7 : Factors used for determination of the PEC of the distillation column stages (valve trays) used within the amine-exchange process

Unit	Cb ($)	Qb(ton)	Q (ton)	M	F_m	F_p	F_T
T1	65600	8	5,7	0,89	3,2	1,3	1
T2	65600	8	1,1	0,89	3,9	1,3	1

Table E.8 : Factors used for determination of the PEC of the distillation column (empty shell) used within the pressure-swing process

Unit	Cb ($)	Qb(m)	Q (m)	M	F_m	F_p	F_T
T1	18000	0,5	11,3	0,97	3,2	1	1
T2	18000	0,5	3,63	0,97	3,2	1,3	1

Table E.9 : Factors used for determination of the PEC of the distillation column stages (sieve trays) used within the pressure-swing process

Compressors and pumps

Unit	Cb ($)	Qb(kW)	Q (kW)	M	F_m	F_p	F_T
C1	98400	250	177,64	0,46	1	1,5	1
C2	98400	250	188,47	0,46	1	1,5	1
C3	98400	250	188,47	0,46	1	1,5	1
C4	98400	250	48,92	0,46	1	1,5	1
P1	11000	10	147,9	0,44	3,2	1,3	1
P2	11000	10	147,9	0,44	3,2	1,3	1
P3	9840	4	56,3	0,55	3,2	1,3	1
P4	11000	10	0,3	0,44	3,2	1,3	1
P5	11000	10	0,8	0,44	3,9	1,3	1

Table E.10 : Factors used for determination of the PEC of the compressors and pumps used within the amine-exchange process

Unit	Cb ($)	Qb(kW)	Q (kW)	M	F_m	F_p	F_T
C1	98400	250	1477,79	0,46	1	1,5	1
C2	98400	250	1385,43	0,46	1	1,5	1
C3	98400	250	1383,49	0,46	1	1,5	1
C4	98400	250	1349,12	0,46	1	1,5	1
P1	11000	10	683,15	0,44	3,2	1,5	1
P2	11000	10	12,99	0,44	3,2	1,3	1
P3	11000	10	0,6	0,44	3,2	1,3	1
P4	11000	10	0,09	0,44	3,9	1,3	1
P5	11000	10	0,67	0,44	3,2	1,3	1

Table E.11 : Factors used for determination of the PEC of the compressors and pumps used within the pressure-swing process

Heat exchangers

Unit	Cb ($)	Qb(m2)	Q (m2)	M	F_m	F_p	F_T
E1	32800	80	90	0,68	1	1,5	1
E2	32800	80	97	0,68	1	1,5	1
E3	32800	80	162	0,68	3,2	1,5	1
E4	32800	80	162	0,68	3,2	1,5	1
E5	32800	80	50	0,68	3,2	1	1
E6	32800	80	246	0,68	3,2	1	1
E7	32800	80	2974	0,68	3,2	1	1
E8	32800	80	675	0,68	3,2	1,3	1
E9	32800	80	3502	0,68	3,2	1,3	1
E10	32800	80	3080	0,68	3,2	1,3	1

E11	32800	80	129	0,68	3,2	1,3	1
E12	32800	80	5296	0,68	3,2	1,3	1
E13	32800	80	1174	0,68	3,2	1,3	1
E14	32800	80	396	0,68	3,9	1,3	1
E15	32800	80	6415	0,68	3,9	1,3	1
E16	32800	80	121	0,68	3,9	1,3	1
E17	32800	80	48	0,68	3,9	1,3	1
E18	32800	80	71,8	0,68	3,9	1,3	1
E19	32800	80	10	0,68	3,2	1,3	1
E20	32800	80	97	0,68	1	1,5	1
E21	32800	80	49	0,68	1	1,5	1

Table E.12 : Factors used for determination of the PEC of the heat exchangers used within the amine-exchange process

Unit	Cb ($)	Qb(m2)	Q (m2)	M	F_m	F_p	F_T
E1	32800	80		0,68	1	1,5	1
E2	32800	80		0,68	1	1,5	1
E3	32800	80		0,68	1	1,5	1
E4	32800	80		0,68	1	1,5	1
E5	32800	80		0,68	3,2	1,3	1
E6	32800	80		0,68	3,2	1,3	1
E7	32800	80		0,68	3,2	1,3	1
E8	32800	80		0,68	3,2	1,3	1
E9	32800	80		0,68	3,9	1,3	1
E10	32800	80		0,68	3,9	1,3	1
E11	32800	80		0,68	3,9	1,3	1

Table E.13 : Factors used for determination of the PEC of the heat exchangers used within the pressure-swing process

Refences Appendix E

[1] Payscale, “Average Chemical Operator Salary in Netherlands.” https://www.payscale.com/research/NL/Job=Chemical_Operator/Salary (accessed Jun. 30, 2024).

[2] G. A. Filonenko, W. L. Vrijburg, E. J. M. Hensen, and E. A. Pidko, “On the activity of supported Au catalysts in the liquid phase hydrogenation of CO2 to formates,” *J. Catal.*, vol. 343, pp. 97–105, 2016, doi: 10.1016/j.jcat.2015.10.002.

[3] C. H. Turner, A. Cooper, Z. Zhang, M. S. Shannon, and J. E. Bara, “Molecular simulation of the thermophysical properties of N-functionalized alkylimidazoles,” *J. Phys. Chem. B*, vol. 116, no. 22, pp. 6529–6535, 2012, doi: 10.1021/jp3029787.

[4] K. Park *et al.*, “CO2 hydrogenation to formic acid over heterogenized ruthenium catalysts using a fixed bed reactor with separation units,” *Green Chem.*, vol. 22, no. 5, pp. 1639–1649, 2020, doi: 10.1039/c9gc03685g.

[5] R. Smith, *Chemical Process Design and Integration*, John Wiley. 2016.

[6] The American Society of Mechanical Engineers, *ASME Boiler and Pressure Vessel Code. An International Code*. 2019.

References

[1] U. S. Global Change Research Program, “Fourth National Climate Assessment.”

[2] P. M. Modisha, C. N. M. Ouma, R. Garidzirai, P. Wasserscheid, and D. Bessarabov, “The Prospect of Hydrogen Storage Using Liquid Organic Hydrogen Carriers,” *Energy and Fuels*, vol. 33, no. 4, pp. 2778–2796, 2019, doi: 10.1021/acs.energyfuels.9b00296.

[3] A. Y. Faid and S. Sunde, “Anion Exchange Membrane Water Electrolysis from Catalyst Design to the Membrane Electrode Assembly,” vol. 2200506, 2022, doi: 10.1002/ente.202200506.

[4] N. Du, C. Roy, R. Peach, M. Turnbull, S. Thiele, and C. Bock, “Anion-Exchange Membrane Water Electrolyzers,” 2022, doi: 10.1021/acs.chemrev.1c00854.

[5] N. Frischauf *et al.*, “The hydrogen value chain: Applying the automotive role model of the hydrogen economy in the aerospace sector to increase performance and reduce costs,” *Acta Astronaut.*, vol. 88, pp. 8–24, 2013, doi: 10.1016/j.actaastro.2013.01.002.

[6] E. Tzimas, C. Filiou, S. D. Peteves, and J. Veyret, *Hydrogen Storage : State-of-the-Art and Future Perspective*. 2003.

[7] M. Felderhoff, C. Weidenthaler, R. Von Helmolt, and U. Eberle, “Hydrogen storage: The remaining scientific and technological challenges,” *Phys. Chem. Chem. Phys.*, vol. 9, no. 21, pp. 2643–2653, 2007, doi: 10.1039/b701563c.

[8] K. Mazloomi and C. Gomes, “Hydrogen as an energy carrier: Prospects and challenges,” *Renew. Sustain. Energy Rev.*, vol. 16, no. 5, pp. 3024–3033, 2012, doi: 10.1016/j.rser.2012.02.028.

[9] T. H. Ulucan *et al.*, "Hydrogen storage in liquid hydrogen carriers: recent activities and new trends," *Prog. Energy*, vol. 5, no. 1, 2023, doi: 10.1088/2516-1083/acac5c.

[10] P. Preuster, C. Papp, and P. Wasserscheid, "Liquid organic hydrogen carriers (LOHCs): Toward a hydrogen-free hydrogen economy," *Acc. Chem. Res.*, vol. 50, no. 1, pp. 74–85, 2017, doi: 10.1021/acs.accounts.6b00474.

[11] H. Herzog, C. Schmidt, and E. Drake, *CO2 sequestration*. Dijon: Springer Berlin Heidelberg, 1999.

[12] J. Eppinger and K. W. Huang, "Formic Acid as a Hydrogen Energy Carrier," *ACS Energy Lett.*, vol. 2, no. 1, pp. 188–195, 2017, doi: 10.1021/acsenergylett.6b00574.

[13] R. van Putten, T. Wissink, T. Swinkels, and E. A. Pidko, "Fuelling the hydrogen economy: Scale-up of an integrated formic acid-to-power system," *Int. J. Hydrogen Energy*, vol. 44, no. 53, pp. 28533–28541, 2019, doi: 10.1016/j.ijhydene.2019.01.153.

[14] M. Pérez-Fortes, J. C. Schöneberger, A. Boulamanti, G. Harrison, and E. Tzimas, "Formic acid synthesis using CO2 as raw material: Techno-economic and environmental evaluation and market potential," *Int. J. Hydrogen Energy*, vol. 41, no. 37, pp. 16444–16462, 2016, doi: 10.1016/j.ijhydene.2016.05.199.

[15] C. Kim, Y. Lee, K. Kim, and U. Lee, "Implementation of Formic Acid as a Liquid Organic Hydrogen Carrier (LOHC): Techno-Economic Analysis and Life Cycle Assessment of Formic Acid Produced via CO2 Utilization," *Catalysts*, vol. 12, no. 10, 2022, doi: 10.3390/catal12101113.

[16] D. Kim and J. Han, "Comprehensive analysis of two catalytic processes to

produce formic acid from carbon dioxide," *Appl. Energy*, vol. 264, no. December 2019, p. 114711, 2020, doi: 10.1016/j.apenergy.2020.114711.

[17] S. E. Sanni *et al.*, "Strategic examination of the classical catalysis of formic acid decomposition for intermittent hydrogen production, storage and supply: A review," *Sustain. Energy Technol. Assessments*, vol. 45, no. December 2020, p. 101078, 2021, doi: 10.1016/j.seta.2021.101078.

[18] S. Schlussel and S. Kwon, "A review of formic acid decomposition routes on transition metals for its potential use as a liquid H2 carrier," *Korean J. Chem. Eng.*, vol. 39, no. 11, pp. 2883–2895, 2022, doi: 10.1007/s11814-022-1276-z.

[19] Riquelme-García, P.; Navlani-García, M.; Cazorla-Amorós, D, "Hydrogen Storage System Attained by HCOOH-CO 2 Couple : Recent Developments in Pd-Based Carbon-Supported Heterogeneous catalysts," Energies 2024, 17, 260. https://doi.org/10.3390/en17010260.

[20] M. Iguchi, Y. Himeda, Y. Manaka, K. Matsuoka, and H. Kawanami, "Simple Continuous High-Pressure Hydrogen Production and Separation System from Formic Acid under Mild Temperatures," *ChemCatChem*, vol. 8, no. 5, pp. 886–890, 2016, doi: 10.1002/cctc.201501296.

[21] C. Fellay, P. J. Dyson, and G. Laurenczy, "A viable hydrogen-storage system based on selective formic acid decomposition with a ruthenium catalyst," *Angew. Chemie - Int. Ed.*, vol. 47, no. 21, pp. 3966–3968, 2008, doi: 10.1002/anie.200800320.

[22] A. Banu, N. Mir, D. Ewis, M. H. El-Naas, A. I. Amhamed, and Y. Bicer, "Formic acid production through electrochemical reduction of CO2: A life cycle assessment," *Energy Convers. Manag. X*, vol. 20, no. June, p. 100441, 2023, doi: 10.1016/j.ecmx.2023.100441.

[23] K. Müller, K. Brooks, and T. Autrey, “Hydrogen Storage in Formic Acid: A Comparison of Process Options,” *Energy and Fuels*, vol. 31, no. 11, pp. 12603–12611, 2017, doi: 10.1021/acs.energyfuels.7b02997.

[24] J. Hietala, A. Vuori, P. Johnsson, P. Ilkka, W. Reutemann, and H. Kieczka, “Formic acid,” *Ullmann’s Encycl. Ind. Chem.*, vol. A12, no. 29, pp. 1–12, 2016, doi: 10.1002/14356007.a12.

[25] G. H. Gunasekar, J. Shin, K. D. Jung, K. Park, and S. Yoon, “Design Strategy toward Recyclable and Highly Efficient Heterogeneous Catalysts for the Hydrogenation of CO2 to Formate,” *ACS Catal.*, vol. 8, no. 5, pp. 4346–4353, 2018, doi: 10.1021/acscatal.8b00392.

[26] X. Chen, Y. Liu, and J. Wu, “Sustainable production of formic acid from biomass and carbon dioxide,” *Mol. Catal.*, vol. 483, no. November 2019, p. 110716, 2020, doi: 10.1016/j.mcat.2019.110716.

[27] D. A. Bulushev and J. R. H. Ross, “Towards Sustainable Production of Formic Acid,” *ChemSusChem*, vol. 11, no. 5, pp. 821–836, 2018, doi: 10.1002/cssc.201702075.

[28] M. Achour *et al.*, “Formic acid as renewable reagent and product in biomass upgrading,” *Tetrahedron Green Chem*, vol. 2, no. March, 2023, doi: 10.1016/j.tgchem.2023.100020.

[29] Y. Chen *et al.*, “Sustainable production of formic acid and acetic acid from biomass,” *Mol. Catal.*, vol. 545, no. May, p. 113199, 2023, doi: 10.1016/j.mcat.2023.113199.

[30] Ö. Tezer, N. Karabağ, A. Öngen, C. Ö. Çolpan, and A. Ayol, “Biomass gasification for sustainable energy production: A review,” *Int. J. Hydrogen Energy*, vol. 47, no. 34, pp. 15419–15433, 2022, doi:

10.1016/j.ijhydene.2022.02.158.

[31] R. Segurado, S. Pereira, D. Correia, and M. Costa, “Techno-economic analysis of a trigeneration system based on biomass gasification,” *Renew. Sustain. Energy Rev.*, vol. 103, no. January, pp. 501–514, 2019, doi: 10.1016/j.rser.2019.01.008.

[32] C. Kim *et al.*, “Accelerating the net-zero economy with CO2-hydrogenated formic acid production: Process development and pilot plant demonstration,” *Joule*, vol. 8, no. 3, pp. 693–713, 2024, doi: 10.1016/j.joule.2024.01.003.

[33] K. Fernández-Caso, G. Díaz-Sainz, M. Alvarez-Guerra, and A. Irabien, “Electroreduction of CO2: Advances in the Continuous Production of Formic Acid and Formate,” *ACS Energy Lett.*, vol. 8, no. 4, pp. 1992–2024, 2023, doi: 10.1021/acsenergylett.3c00489.

[34] T. M. Suzuki, T. Takayama, S. Sato, A. Iwase, A. Kudo, and T. Morikawa, “Enhancement of CO2 reduction activity under visible light irradiation over Zn-based metal sulfides by combination with Ru-complex catalysts,” *Appl. Catal. B Environ.*, vol. 224, no. November 2017, pp. 572–578, 2018, doi: 10.1016/j.apcatb.2017.10.053.

[35] I. Schmidt, K. Müller, and W. Arlt, “Evaluation of formic-acid-based hydrogen storage technologies,” *Energy and Fuels*, vol. 28, no. 10, pp. 6540–6544, 2014, doi: 10.1021/ef501802r.

[36] A. Álvarez *et al.*, “Challenges in the Greener Production of Formates/Formic Acid, Methanol, and DME by Heterogeneously Catalyzed CO2 Hydrogenation Processes,” *Chem. Rev.*, vol. 117, no. 14, pp. 9804–9838, 2017, doi: 10.1021/acs.chemrev.6b00816.

[37] T. Schaub and R. A. Paciello, “A process for the synthesis of formic acid by

CO2 hydrogenation: Thermodynamic aspects and the role of CO," *Angew. Chemie - Int. Ed.*, vol. 50, no. 32, pp. 7278–7282, 2011, doi: 10.1002/anie.201101292.

[38] G. Fachinetti and D. Preti, "PROCESS FOR PREPARING FORMIC ACID," WO 2012/168396 Al, 2012.

[39] D. Preti, C. Resta, S. Squarcialupi, and G. Fachinetti, "Carbon dioxide hydrogenation to formic acid by using a heterogeneous gold catalyst," *Angew. Chemie - Int. Ed.*, vol. 50, no. 52, pp. 12551–12554, 2011, doi: 10.1002/anie.201105481.

[40] M. Narita, K. , Sekiya, "Vapor-Liquid Equilibrium for Formic Acid - Triethylamine System Examined by the Use of a Modified Still. Formic Acid - Trialkylamine azeotropes," *Chem. Pharm. Bull.*, vol. 17, no. 11, pp. 1460–1462, 1994.

[41] K. Park *et al.*, "CO2 hydrogenation to formic acid over heterogenized ruthenium catalysts using a fixed bed reactor with separation units," *Green Chem.*, vol. 22, no. 5, pp. 1639–1649, 2020, doi: 10.1039/c9gc03685g.

[42] A.W.N. de Leeuw den Bouter, L.M.P. Meijer, L.Brito , A. Miquelot, P.Olivier,J. van der Schaaf, "Effect of tertiary amine selection on CO2 to formic acid hydrogenation with Au-np catalyst," *Submitted to to Industrial & Engineering Chemistry Research*

[43] Chemanalyst, "Formic acid price trend and forcast." https://www.chemanalyst.com/Pricing-data/formic-acid-1242 (accessed Jun. 30, 2024).

[44] R. Xiong, S. I. Sandler, and R. I. Burnett, "Reply to "comment on 'an improvement to COSMO-SAC for predicting thermodynamic properties,'" *Ind.*

Eng. Chem. Res., vol. 53, no. 21, p. 8936, 2014, doi: 10.1021/ie501775s.

[45] C. C. Pye, T. Ziegler, E. Van Lenthe, and J. N. Louwen, “An implementation of the conductor-like screening model of solvation within the amsterdam density functional package - Part II. COSMO for real solvents,” *Can. J. Chem.*, vol. 87, no. 7, pp. 790–797, 2009, doi: 10.1139/V09-008.

[46] G. Manzolini, A. Giuffrida, P. D. Cobden, H. A. J. van Dijk, F. Ruggeri, and F. Consonni, “Techno-economic assessment of SEWGS technology when applied to integrated steel-plant for CO2 emission mitigation,” *Int. J. Greenh. Gas Control*, vol. 94, no. December 2019, p. 102935, 2020, doi: 10.1016/j.ijggc.2019.102935.

[47] Gago Da Camara Simoes S, Nijs W, Ruiz Castello P, Sgobbi A, Radu D, Bolat P, Thiel C, Peteves E., “The JRC-EU-TIMES model - Assessing the long-term role of the SET Plan Energy technologies,” Publications Office of the European Union, Luxembourg (Luxembourg), 2013. doi: 10.2790/97799 (print), 10.2790/97596 (online).

[48] Chemanalyst, “Formic Acid Market Analysis: Industry Market Size, Plant Capacity, Production, Operating Efficiency, Demand & Supply, End-User Industries, Sales Channel, Company Share, Regional Demand, Foreign Trade, 2015-2035 Decode the Future of Formic Acid,” 2023. https://www.chemanalyst.com/industry-report/formic-acid-market-688 (accessed Jun. 30, 2024).

[49] M. Pérez-Fortes, J. C. Schöneberger, A. Boulamanti, and E. Tzimas, “Methanol synthesis using captured CO2 as raw material: Techno-economic and environmental assessment,” *Appl. Energy*, vol. 161, pp. 718–732, 2016, doi: 10.1016/j.apenergy.2015.07.067.

[50] G. A. Filonenko, W. L. Vrijburg, E. J. M. Hensen, and E. A. Pidko, “On the

activity of supported Au catalysts in the liquid phase hydrogenation of CO2 to formates," *J. Catal.*, vol. 343, pp. 97–105, 2016, doi: 10.1016/j.jcat.2015.10.002.

[51] N. B. J. H. Balbi, L. Elegant, and Y. Girault, "THERMAL AND DYNAMIC ANALYSIS OF THE REACTIONS BETWEEN FORMIC ACID AND TRIETHYLAMINE," vol. 37, pp. 2347–2352, 1991.

[52] D. Usosky, V. Aharkov, K. Rok Lee, K. D. Jung, and U. Lee, "Vapor-liquid equilibria in the 1-methylpyrrolidine + 1-butylimidazole binary system: Experimental measurements and theoretical modelling," *J. Ind. Eng. Chem.*, vol. 126, pp. 418–431, 2023, doi: 10.1016/j.jiec.2023.06.030.

[53] S. Poto, T. Vink, P. Oliver, F. Gallucci, and M. F. Neira D'angelo, "Techno-economic assessment of the one-step CO2conversion to dimethyl ether in a membrane-assisted process," *J. CO2 Util.*, vol. 69, no. December 2022, p. 102419, 2023, doi: 10.1016/j.jcou.2023.102419.

[54] K. M. N. Warren D. Seider, Daniel R. Lewin, J. D. Seader, Soemantri Widagdo, Rafiqul Gani, *Product and Process Design Principles: Synthesis, Analysis and Evaluation, 4th Edition*. Wiley, 2016.

[55] Nordic Steel, "The difference between 304, 304L, 316 and 316L: The main chemical and mechanical differences." https://en.nordicsteel.no/fagartikler/forskjellen-pa-304-304l-316-og-316l (accessed Jun. 30, 2024).

[56] Bal Seal Engineering, "Metallic Materials Used in Bal Seal Products," pp. 4–28, 1999.

[57] R. Smith, *Chemical Process Design and Integration*, John Wiley. 2016.

[58] C.Maxwell, “Cost Indices.” https://toweringskills.com/financial-analysis/cost-indices/#cepci-2001-to-present (accessed Jun. 30, 2024).

[59] Payscale, “Average Chemical Operator Salary in Netherlands.” https://www.payscale.com/research/NL/Job=Chemical_Operator/Salary (accessed Jun. 30, 2024).

[60] R. J. Detz, J. N. H. Reek, and B. C. C. Van Der Zwaan, “The future of solar fuels: When could they become competitive?,” *Energy Environ. Sci.*, vol. 11, no. 7, pp. 1653–1669, 2018, doi: 10.1039/c8ee00111a.

[61] M. Hachhach, D. A. Sladkovskiy, T. Salmi, and D. Y. Murzin, “Selective Oxidation of Arabinose on Gold Catalysts: Process Design and Techno-economic Assessment,” *Chem. Eng. Technol.*, vol. 44, no. 10, pp. 1775–1782, 2021, doi: 10.1002/ceat.202100211.

[62] APMEX, “Gold Spot Price.” https://www.apmex.com/gold-price (accessed Jun. 30, 2024).

[63] Intratec, “Aluminum Oxide Prices | Current and Forecast.” https://www.intratec.us/chemical-markets/aluminum-oxide-price (accessed Jun. 30, 2024).

[64] Merck, “1-Decanol.” https://www.sigmaaldrich.com/NL/en/product/aldrich/150584 (accessed Jun. 30, 2024).

[65] Chemanalyst, “Triethylamine price trend and forecast.” https://www.chemanalyst.com/Pricing-data/triethylamine-1198#market-overview.

[66] S. Poto, T. Vink, P. Oliver, F. Gallucci, and M. F. Neira D’angelo, “Techno-

economic assessment of the one-step CO2conversion to dimethyl ether in a membrane-assisted process,” *J. CO2 Util.*, vol. 69, no. February, p. 102419, 2023, doi: 10.1016/j.jcou.2023.102419.

[67] V. Spallina, D. Pandolfo, A. Battistella, M. C. Romano, M. Van Sint Annaland, and F. Gallucci, “Techno-economic assessment of membrane assisted fluidized bed reactors for pure H2 production with CO2 capture,” *Energy Convers. Manag.*, vol. 120, pp. 257–273, 2016, doi: 10.1016/j.enconman.2016.04.073.

[68] D. Weisser, “A guide to life-cycle greenhouse gas (GHG) emissions from electric supply technologies,” *Energy*, vol. 32, no. 9, pp. 1543–1559, 2007, doi: 10.1016/j.energy.2007.01.008.

[69] Y. Yang, J. Liu, W. Shen, J. Li, and I. L. Chien, “High-efficiency utilization of CO2 in the methanol production by a novel parallel-series system combining steam and dry methane reforming,” *Energy*, vol. 158, pp. 820–829, 2018, doi: 10.1016/j.energy.2018.06.061.

[70] L. C. Assessment, “Life Cycle Greenhouse Gas Emissions from Electricity Generation : Update,” pp. 1–4, 2013.

[71] V. J. Inglezakis and S. G. Poulopoulos, “Heterogeneous Processes and Reactor Analysis,” *Adsorpt. Ion Exch. Catal.*, pp. 57–242, 2006, doi: 10.1016/b978-044452783-7/50003-3.

[72] A. D. Becke, “Thermochemistry. III. The role of exact exchange,” *J. Chem. Phys*, vol. 98, no. 7, pp. 5648–5652, 1993, doi: https://doi.org/10.1063/1.464913.

[73] R. Rüger, M. Franchini, T. Trnka, Y. Yakovlev, E. van Lenthe and and T. S. T. Van vuren, B. Klumpers, “Theoretical chemistry.” .

[74] P. Berton, S. P. Kelley, H. Wang, and R. D. Rogers, “Elucidating the triethylammonium acetate system: Is it molecular or is it ionic?,” *J. Mol. Liq.*, vol. 269, pp. 126–131, Nov. 2018, doi: 10.1016/j.molliq.2018.08.006.

[75] A.W.N. de Leeuw den Bouter, E.J.M. Vogels, L.Brito , A. Miquelot, P.Olivier, J. van der Schaaf, “Chemical and phase equilibrium of formic acid – trialkylamine complexes,” Under review in ACS Omega.

[76] M. Sekiya, “ギ酸による還元反応．,” *有機合成化学協会誌（Journal Synth. Org. Chem. Japan）*, vol. 34, no. 2, pp. 67–81, 1976.

[77] D. Usosky, K. Kim, J. H. Moon, K. D. Jung, and U. Lee, “Isobaric Vapor-Liquid Equilibria for the Formic Acid- N-methyl-2-pyrrolidone Binary System at 50, 20, and 10 kPa and Modeling Using the NRTL-HOC and PC-SAFT Models,” *J. Chem. Eng. Data*, vol. 66, no. 12, pp. 4516–4525, 2021, doi: 10.1021/acs.jced.1c00573.

[78] G. Park, “Introduction to Pinch Technology,” 1998.

[79] P. Moriarty and D. Honnery, “Hydrogen’s role in an uncertain energy future,” *Int. J. Hydrogen Energy*, vol. 34, no. 1, pp. 31–39, 2009, doi: 10.1016/j.ijhydene.2008.10.060.

[80] A. Qazi *et al.*, “Towards Sustainable Energy: A Systematic Review of Renewable Energy Sources, Technologies, and Public Opinions,” *IEEE Access*, vol. 7, pp. 63837–63851, 2019, doi: 10.1109/ACCESS.2019.2906402.

7

Conclusion and outlook

7.1 Conclusion

In this thesis, the potential of the production of formic acid based on the direct hydrogenation of CO_2 was investigated, addressing various aspects from the exploration of the influence of the aliphatic chain length of the tertiary amine on formic acid binding capacity, the influence of the reactive amine on key aspects such as activity and selectivity, the development of catalytic materials and lastly a demonstration of the technology at reactor and process scale, based on a combination of numerical and experimental tools.

The primary objective of **Chapter 2** was to gain a deeper understanding into the nature of different formic acid – aliphatic tertiary amine adducts. Here, a combination of ^{1}H-NMR and IR spectroscopy was used to shed light into the type of chemical bonds occurring within the formic acid – trialkylamine adducts and the degree of proton transfer between formic acid and several trialkylamines. The phase equilibrium was established to be independent of the alkyl chain length with the critical point determined to be at a molar ratio of 1.5 acid to amine.

IR spectroscopy was employed to probe the chemical interactions present within these systems and revealed the existence of a complex mixture of hydrogen bonding and ionic interactions. The red-shift observed for the asymmetrical COO^- band gave an indication for a decrease in proton transfer as a function of chain length. For smaller alkyl chains (up to C_4) this effect was found to be pronounced, while longer chains (C_6 and C_8) resulted in less pronounced shifts. Due to significant overlap between the characteristic bands of COO^- and NH^+ combined with a significant red shift of the symmetrical COO^- stretch frequency, it was not possible to determine the ionicity of the PILs using FTIR. Thus, to allow for quantitative analysis of the degree of proton transfer, NMR spectroscopy was employed.

The behavior observed within the IR study qualitatively aligns with the behavior observed within the ^{1}H-NMR study, with the degree of proton transfer decreasing as a function of alkyl chain length. The asymmetrical amines, DMBA and DMOA, both reveal a high degree of proton transfer comparable to triethylamine. Remarkably, it is observed that the decrease in ionicity is exactly compensated by in the increase in hydrogen bonding, resulting in a constant acid to amine ratio irrespective of the nature of the amine.

For trioctylamine-based adducts a significant color change from colorless to magenta to blue was observed over a time span of several months. UV-VIS revealed the highly dynamic nature of these complexes, while DLS revealed an average aggregate size of 1.78 nm independent of the acid:base ratio.

Based on this study, several promising tertiary amines were identified and further studied in **Chapter 3** and **4**.

Specifically, **Chapter 3** focused on an attempt to intensify the reaction through removal of the additional alcohol based solvents in a batch reactor. Solventless batch experiments at elevated pressures were performed to gain insights into the performance of using triethylamine as an extraction base during the direct hydrogenation of CO_2 to formic acid.

After several hours of reaction, no formic acid was observed within the bulk liquid of the batch experiments. Due to the biphasic nature of formic acid – triethylamine systems, the formic acid concentration within the catalyst pores after reaction was evaluated by placing the spent catalyst in water. Here, the total molar amount of formic acid in the pores being orders of magnitude larger than those in the reactor fluid.

In order to investigate this at pore level, a 2D fundamental, continuum based model describing Cahn-Hilliard spinodal decomposition model describing spinodal decomposition was created and verified in C++. Here, the Cahn – Hilliard equation was used to describe the temporal evolution of spinodal decomposition through describing the Helmholtz free energy as a function of composition and the spatial derivative of the composition at the grid point.

The biphasic nature of the tertiary alkylamine – formic acid system was found to have significant implications for the reaction performance of the proposed system. The inability of the adduct to dissolve in the available non-binding amine results in the catalyst pores readily reaching the equilibrium condition, therefore reducing the average reaction rate to zero.

In **Chapter 4**, the influence of the tertiary amine on CO_2 conversion and product selectivity was experimentally studied in batch and packed bed reactors using a Au/TiO_2 catalyst. A wide range of tertiary amines were selected, based on their boiling point, kinetic diameter, pKa and solubility with alcohol-based solvents and formic acid. Following these criteria, 15 amines were selected having a wide range of pKa values and molecule sizes. Due to the slow kinetic nature of the CO_2 hydrogenation to formic acid, the formic acid decomposition reaction was used to screen a wide variety of tertiary amines based on the principle of microscopic reversibility. Steric hindrance and the pKa of the tertiary amine were identified as a key parameters influencing both the observed kinetic rates as well as the FA conversion. The usage of polar tertiary amine allowed for the removal of additional solvents, allowing for significantly higher kinetic rates due to higher amine concentrations. Here, the amount of OH-groups showed a strong influence on the observed kinetic rates, most likely due to viscosity effects.

The assumption of microscopic reversibility was verified in a high pressure packed bed reactor. Here, the usage of solventless polar amines such as diethylethanolamine allowed for FA productivity up to 5x that of the benchmark triethylamine system. Catalyst deactivation of the Au/TiO_2 catalyst was observed for all amines studied within this work, and the deactivation mechanism was shown to be sintering of the Au nanoparticles with no significant leaching, morphological changes or oxidation of the Au species observed. The catalyst deactivation was found to be very rapid, with the catalyst allowing for stable FA production up to 50 hours after the initial gold nanoparticle growth.

Chapter 5 concerned the development of mono-metallic (Au/Al_2O_3, Pd/Al_2O_3 and

Ru/Al_2O_3) and bimetallic catalysts (Au-Pd, Au-Ni, and Au-Cu/Al_2O_3). The synthesized catalysts were characterized through XPS, XRD, TEM, ICP and CO pulse chemisorption to identify possible deactivation mechanisms.

As was the case in **Chapter 4,** it was opted to perform an initial screening of the bimetallic catalysts based on the formic acid decomposition reaction, comparing the conversion, selectivity and catalyst stability to Au/TiO_2 due to the slow kinetic nature of the hydrogenation reaction. Here, it was found that Au-Cu based catalysts result in complete FA conversion for all Au:Cu molar ratios, therefore producing significant amounts of undesired CO. Au-Ni catalysts supported on alumina generally demonstrated poorer catalytic activity compared to mono-metallic gold on titania, with the catalysts showing significant deactivation, therefore suggesting the synergetic effects between gold and nickel or copper to be detrimental. Lastly, promising behavior in terms of catalysts activity and selectivity was observed for Au-Pd based catalysts with low Pd concentrations.

Performing CO_2 hydrogenation experiments at elevated pressures revealed significant catalyst deactivation for the mono-metallic Au/TiO_2 and Pd/Al_2O_3 catalysts. The influence of the triethylamine:1-decanol ratio on the catalyst deactivation was studied, identifying different deactivation mechanisms for the Au and Pd based catalysts. In case of Au supported on titania, the deactivation is caused by Au nanoparticle agglomeration. For Pd, the amount of CO produced was found to be inversely proportional to the amount of amine present within the reactive mixture. Stable FA productivity was observed for low amine:solvent ratios, making that the deactivation cannot solely be attributed to CO poisoning.

Testing under constant triethylamine:1-decanol ratio revealed comparable initial FA productivity for the Au, Pd and Au-Pd catalysts supported on alumina, while the Ru/Al_2O_3 catalyst has low (<10%) selectivity towards FA. Furthermore, all alumina supported catalysts result in the unwanted production of CO, with the Ru-based catalyst yielding CO as the major product. The replacement of triethylamine:1-decanol with diethylethanolamine was observed to result in an increase in FA productivity and selectivity for gold based catalysts, while Pd and Ru-based materials have comparable or lower FA productivity compared to when triethylamine is used.

Chapter 6 proposed a comparison on techno-economic level of two routes for the direct hydrogenation of CO_2 towards formic acid in the context of DFAFC applications: 1) the conventional route based on the patents of BP and BASF; 2) a direct route based on the utilization of a high-boiling amine such as n-butylimidazole. The objective of this study was to identify, if any, the plant operating conditions that would make the high boiling reactive amine case more economically competitive compared to the conventional amine-exchange process, analysing both the technical and economic performance of both processes. The formic acid productivity was set to 35 kton/year, with the formic acid produced at fuel cell purity (<1 ppm impurities).

The first route represents the conventional CO_2 hydrogenation route based on the state-of-the-art literature to perform the azeotropic separation between formic acid and the low boiling tertiary amine used to shift the equilibrium towards formic acid in the reactor. Here, the low boiling amine (triethylamine) is replaced by a higher boiling amine using reactive distillation, followed by thermal splitting. The second route presents a methodology to circumvent the amine-exchange through the usage of a higher boiling amine (n-butylimidazole) within the reactor, followed by vacuum pressure-swing distillation. The overall energy efficiency, defined as the ratio between the energy stored and the energy required to obtain high purity formic acid,0 significantly increased (i.e. 2.08% to 3.47%) when n-butylimidazole was used as the reactive amine due to a decrease in heating requirement in the distillation train (i.e. 347 MW vs 240 MW).

The environmental analysis revealed no net carbon emission reduction if fossil-based or renewable sources are used for steam and electricity production. From an economic perspective, the determined minimum selling price of formic acid was found to be heavily dominated by the OPEX, i.e. 90.4 and 96.2% of the total annual expenses (TAC) for the amine-exchange and pressure-swing process, respectively.

The majority of these costs arises from the large energy consumption of both processes, as well as the very significant amounts of catalysts required (i.e. 2.7 and 8.5 kton). The minimum formic acid selling price was calculated to be €10821.47 and €18913.15 per ton of formic acid for the amine-exchange and pressure-swing process, respectively. A sensitivity and forecasting analysis was conducted. Here, it was observed that an increase in the catalyst activity of at least a factor 100 is required for the catalyst to no longer be the dominant contribution to the minimum formic acid selling price, with the energy consumed by the distillation processes becoming the major price factor.

7.2 Outlook and recommendations for future research

In this work, the potential of the direct hydrogenation of CO_2 towards formic acid was evaluated, while addressing various aspects from the exploration of the influence of the aliphatic chain length of the tertiary amine on formic acid binding capacity, the influence of the reactive amine on key aspects such as activity and selectivity, the development of catalytic materials and lastly a demonstration of the technology at reactor and process scale.

Despite promising developments made in terms of reactive amine optimization and the development of catalytic materials in Chapter 4 and 5, the techno-economic evaluation in Chapter 6 revealed the overall energy efficiency of the proposed processes to be only ~3.5% in the most favorable scenario (i.e. pressure-swing distillation using n-butylimidazole as reactive amine), and formic acid selling prices up to 22 times the current market value. The low overall energy efficiency was shown to be caused by the large amounts of energy required to break the formic acid – amine bond combined with the low FA concentrations, while the high prices were the consequence of low catalyst activity and the aforementioned energy consumption. In order to circumvent this, it could be considered to release hydrogen while the formic acid is still bound to the amine. However, due to the energy density of the LOHC significantly decreasing, a techno-economic evaluation and life cycle assessment would be required to determine the viability of such an operational strategy.

Even if substantial improvements in terms of catalyst activity and stability are achieved, resulting in significantly smaller reactors, the low energy efficiency caused by the complex and costly separation of the low FA concentrations makes it unlikely that the proposed production routes become competitive with the conventional fossil-based production route under the studied conditions. Such low energy efficiencies are also highly undesirable when using formic acid for energy storage applications, as it would result in major energy losses.

To decrease the energy consumption of the proposed processes, further optimization of the reactive amine is required, as well as an increase in FA productivity. Previous work has shown FA productivities up to 2.5x the ones observed in this work on gold-based catalysts when using supercritical CO_2 combined with high H_2 pressures [1]. The higher H_2 and CO_2 pressures lead to higher FA concentrations and thus higher FA percentages in the outgoing reactor stream. If is it assumed that the OPEX is linearly proportional to the FA concentration, the increase in pressure results in a lower OPEX per kg of formic acid, while also the CAPEX is significantly decreased due to requiring 2.5x less catalyst. Such CAPEX and OPEX reductions would possibly be sufficient to result in a process which is competitive with the current formic acid market price for the proposed pressure-swing process using n-butylimidazole as reactive amine.

As the process is driven by the enthalpy obtained from tertiary amine protonation to circumvent the thermodynamic limitations of the reaction, the overall energy consumption is largely determined by the protonation enthalpy. Thus, to decrease the energy requirement, an amine with a low protonation enthalpy would have to be utilized, which in turn would significantly limit the formic acid concentrations at thermodynamic equilibrium. Currently, the optimum of this trade-off remains unknown. Preferably, the selected amine allows for direct thermal splitting of the adducts to circumvent the necessity of complex separation strategies such as pressure-swing distillation or amine-exchange strategies, and should thus have a large boiling point difference between the amine and formic acid. To identify such a tertiary amine, a combination of reactive testing at elevated pressures, calorimetric measurements to determine the protonation enthalpy, vapor-liquid equilibrium measurements to determine the existence and position of the azeotrope, and techno-economic evaluation at process scale would be required. However, within this work, it was shown that bulky amines, often having high boiling points, do not allow for the production of formic acid. In order to asses the viability of utilizing polar amines, vapor-liquid equilibrium measurements were performed. Here, it was observed that the vacuum distillation of mixtures of such amines with formic acid do not result in observable split between formic acid and the polar amine, but rather decompose the formic acid into carbon monoxide. It is thus highly unlikely that a plausible solution to the aforementioned trade-off can be found.

While FA productivities could be enhanced through the utilization of increased pressures and the optimization of the reactive amine, the direct formic acid synthesis remains hampered by the thermodynamic nature of the reaction. Alternatively, inspiration could be taken from the current FA synthesis method, in which methyl formates or alkali formates are used as an intermediate compound to aid the thermodynamic behaviour of the reaction.

A possible method could be the two-step hydrogenation of CO_2, as recently demonstrated by Reymond *et al.* [2]. Here, three consequential packed bed reactors are placed in series, to produce formic acid and methanol exploiting the formation of methyl formate as intermediary. Methanol is produced from CO_2 over a Cu-based catalyst in the first packed bed, followed by the production of methyl formate (through the reaction of methanol, CO and H_2) in a second reactor employing a Ag-based catalyst and the subsequential hydrolysis to result in methanol and formic acid over an acid resin [2].

Alternatively, the current industrial methyl formate pathway could be continued with syngas obtained from sustainable sources. Examples include the utilization of CO_2 for the production of syngas through the reverse water gas shift reaction [3], or the gasification of biomass [4].

While such integrated processes are less developed than the process proposed within this work and thus still require significant research efforts, the rationale behind the processes is building on the current FA synthesis methods. This could significantly shorten the time required to develop such methods, and thus allow for faster implementation of such methods at industrial scale, possibly even using existing equipment/infrastructure.

References

[1] D. Preti, C. Resta, S. Squarcialupi, and G. Fachinetti, “Carbon dioxide hydrogenation to formic acid by using a heterogeneous gold catalyst,” *Angew. Chemie - Int. Ed.*, vol. 50, no. 52, pp. 12551–12554, 2011, doi: 10.1002/anie.201105481.

[2] H. Reymond, J. J. Corral-Pérez, A. Urakawa, and P. Rudolf Von Rohr, “Towards a continuous formic acid synthesis: A two-step carbon dioxide hydrogenation in flow,” *React. Chem. Eng.*, vol. 3, no. 6, pp. 912–919, 2018, doi: 10.1039/c8re00142a.

[3] N. Kalmoukidis, A. Barus, S. Staikos, M. Taube, F. Mousazadeh, and A. A. Kiss, “Novel process design for eco-efficient production of green formic acid from CO2,” *Chem. Eng. Res. Des.*, vol. 210, no. September, pp. 425–436, 2024, doi: 10.1016/j.cherd.2024.09.001.

[4] Y. Gao *et al.*, “Syngas Production from Biomass Gasification: Influences of Feedstock Properties, Reactor Type, and Reaction Parameters,” *ACS Omega*, vol. 8, no. 35, pp. 31620–31631, 2023, doi: 10.1021/acsomega.3c03050.

Journal articles

- **A.W.N. de Leeuw den Bouter**, E.J.M. Vogels, L.Brito , A. Miquelot, P.Olivier, J. van der Schaaf, "Chemical and phase equilibrium of formic acid – trialkylamine complexes," *Under review in ACS Omega*

- **A.W.N. de Leeuw den Bouter**, L.Brito , A. Miquelot, P.Olivier,J. van der Schaaf, "Modelling of formic acid production using solventless trialkylamine reduction strategies," *Under review in Chemcial Engineering Science*

- **A.W.N. de Leeuw den Bouter**, L.M.P. Meijer, L.Brito, A. Miquelot, P.Olivier,J. van der Schaaf, "Effect of tertiary amine selection on CO_2 to formic acid hydrogenation with Au-np catalyst" *Under review in Industrial & Engineering Chemistry Research*

- **A.W.N. de Leeuw den Bouter**, P.Naik, Z.Adnin, L.Brito , A. Miquelot, P.Olivier,J. van der Schaaf, "Development of bimetallic catalysts for the direct hydrogenation of CO_2 to formic acid" *Under review in Applied Catalysis O*

- **A.W.N. de Leeuw den Bouter**, A.Chila, D.Castillo Guerra, L.Brito, A. Miquelot, P.Olivier, J. van der Schaaf, "Techno-economic comparison of low-pressure FA production via the direct hydrogenation of CO_2 towards formic acid using triethylamine and n-butylimidazole" *To be submitted to the Journal of CO_2 Utilization*

- **A.W.N. de Leeuw den Bouter**, A.Chila, L.Brito , A. Miquelot, P.Oliver,J. van der Schaaf, "Accelerated formic acid decomposition under the influence of tertiary OH-substituted trialkylamines " *In preparation*

- **A.W.N. de Leeuw den Bouter**, A.Chila, L.Brito , A. Miquelot, P.Olivier,J. van der Schaaf, "Integrated capture and conversion of CO_2 to methanol using dipropylamine: an optimization of process conditions " *In preparation*

- **A.W.N. de Leeuw den Bouter**, A.Chila, L.Brito, A. Miquelot, P.Olivier,J. van der Schaaf, "Combined carbon capture and hydrogenation towards methanol: a two-step N-formamide assisted process " *In preparation*

Journal articles outside the scope of this thesis

- C. Brencio, R. Gough, **A.W.N. de Leeuw den Bouter**, A. Arratibel, L. Di Felice, and F. Gallucci, "Kinetic model for Pd-based membranes coking/deactivation in propane dehydrogenation processes," *Chem. Eng. J.*, vol. 452, no. P1, p. 139125, 2023, doi: 10.1016/j.cej.2022.139125.

- V. Cechetto, C. L. Struijk, L. Di Felice, **A W.N. de Leeuw den Bouter**, and F. Gallucci, "Adsorbents development for hydrogen cleanup from ammonia decomposition in a catalytic membrane reactor," *Chem. Eng. J.*, vol. 455, no. 2023, p. 140762, 2023, doi: 10.1016/j.cej.2022.140762.

- A. Delparish, **A.W.N. de Leeuw den Bouter**, A. Yercan, J. van der Schaaf, and M. Fernanda Neira d'Angelo, "Bringing the promises of microreactors and gold catalysis to lignocellulosic biomass valorization: A study on oxidative transformation of furfural," *Chem. Eng. J.*, vol. 452, no. P1, p. 138903, 2023, doi: 10.1016/j.cej.2022.138903.

- M. Demnitz, Y. M. Lamas, R. L. Garcia Barros, **A.W.N. de Leeuw den Bouter**, J. van der Schaaf, and M. Theodorus de Groot, "Effect of iron addition to the electrolyte on alkaline water electrolysis performance," *iScience*, vol. 27, no. 1, p. 108695, 2024, doi: 10.1016/j.isci.2023.108695.

Oral presentations

- **A.W.N. de Leeuw den Bouter**, L.M.P. Meijer, L. Vogels, E.Vogels, L.Brito, A. Miquelot, P.Olivier,J. van der Schaaf, "On the influence of trialkylamine reduction strategies in the direct hydrogenation of CO_2 ", (AIChE), Phoenix (United States of America), November 2022

Poster presentations

- **A.W.N. de Leeuw den Bouter**, A. Miquelot, P.Olivier, C.Makhloufi, J. van der Schaaf, "Catalytic performance study of supported Au catalysts for the direct hydrogenation of CO_2 to formic acid: monitoring reaction progress using in-line ^{1}H-NMR", Netherlands Process Technology Symposium (NPS17), Delft (Netherlands), April 2022

- **A.W.N. de Leeuw den Bouter**, T. Wissink, Z. Aminuddin, C. Makhloufi, A. Miquelot, P.Olivier, J. van der Schaaf, "Performance study of supported Au catalysts for the direct hydrogenation of CO_2 towards formic acid ", Netherlands Catalysis and Chemistry Conference (N3C), Noordwijkerhout (Netherlands), May 2022

- **A.W.N. de Leeuw den Bouter**, L.M.P. Meijer, D. Castillo Guerra, L.Brito, A. Miquelot, P.Olivier, J. van der Schaaf, "On the influence of trialkylamine reduction strategies in the direct hydrogenation of CO_2", Netherlands Process Technology Symposium (NPS18), Enschede (Netherlands), July 2023

Acknowledgements

Some people compare pursuing a doctoral degree with taking a ride on a roller coaster, and while the PhD journey definitely has some ups that are very high, and downs that are very low, the journey is made possible by the many people who are around you, support and help you along the way. Now that I am writing the final section of my PhD thesis, I would very much like to thank my colleagues, former colleagues and friends who have followed or are following with me this path, and who can relate to these feelings.

First, I would like to thank my supervisors during my PhD years who helped me grow into the independent researcher I am at the end of this journey.

Dear John, thank you for granting me one of the most formative experiences I ever could have imagined, on a professional and personal level. Despite your busy schedule, you somehow always found the time to talk to me about the challenges of the project or to just have an informal talk about education or the current hydrogen strategy. Thank you for your enthusiasm for science, pushing me to become more critical and always strive for high quality, coming up with endless suggestions to try, always pushing me to do better, and the total freedom you have given me to pursue research I found interesting. Our discussions were always a source of new ideas to advance the project. Thank you for complaining about the formic acid reaction together, and for reminding me on a regular basis that the disappointing results we obtained say nothing about me as a researcher.

Then, my ENGIE supervisors. Adeline and Larissa, thank you very much for helping me with whatever I needed during my PhD, thank you for the guidance. Both of you provided endless discussion on the data obtained and problems faced, and some very valuable feedback on this thesis, giving invaluable input into this work. Also, thank you for checking up every so often on how I was doing and how I was feeling about the research. I always looked forward to our constructive meetings. Pierre, even though we did not have many meetings, thank you for always being available

if I needed anything and for providing feedback on the techno-economic work. Your suggestions helped a lot in improving the quality of that work. To all three of you, thank you very much for supporting my crazy idea to start combining carbon capture and hydrogenation to produce methanol at the end of my PhD, and helping in securing the funding to keep working on it together with Andreas. I am sure it will results in some very nice publications.

Furthermore, I would like to thank the rest of my committee: prof.dr.eng. F. Gallucci, prof.dr.ir. W. de Jong, prof.dr.ir. D. Brilman, prof.dr.ir. E. Hensen, prof.dr.ir. M. van Sint Annaland, and dr. L. Brito Sousa for the time spent evaluating this manuscript and for taking the time to attend my defence. Prof.dr.ir. K. Nijmeijer, thank you for chairing my PhD defence.

Also a heartfelt thank you to the SPE supporting staff: Saskia, Carlo, Marlies, Joris, Roberto, Erik and Peter, thank you for making PhD life a lot easier and more pleasant by your endless patience and willingness to help and support in the challenging tasks of the project. Saskia, thank you for your help with the administrative and organizational tasks of my PhD, and always pushing for meetings or tasks on my behalf when deadlines were approaching. Also, thank you for all the talks and advise given at the coffee machine or your office. Carlo, thank you for you never ending commitment to keep our labs safe and clean. Often I would ask you if you had a minute to answer my questions, which of course would always take much longer. I enjoyed our talks and I wish you all the best travelling Europe with your camper. Marlies, thank you for all the help with analytical techniques, making GC methods and patiently explain me everything, from data interpretation to method development. I learned a lot from you about GC and GC-MS. Thank you for all the pleasant conversation at the morning coffee break. Joris, I always enjoy your dark humour and thank you for always being quick to help out when needed. Roberto, while you joined towards the last 2 years of my PhD, we did get to work together on AntFARM2. While we both agree that the selection of a control box over a PLC was a terrible choice, your improvising work enabled me to not only obtain most results in this thesis, but also my later methanol side project. Thank you for your unwavering commitment to help everyone, and for all the pleasant conversations in your office. Thank you for always picking me up when the PhD seemed very dark. Erik, thank you for designing and building AntFARM1 and helping me get AntFARM2 operational (and to keep it running). I walked into your office so many times with a vague description of what I needed, but you always managed to understand me in the end. I greatly liked learning the basics of set-up building and Swagelok from you, thank you for showing me how to do it, and teaching me how to design and build great set-ups with what we have at hand. Peter, you were invaluable to my PhD. From ICP to BET, I learned almost everything I know about analytical techniques from you. Thanks to you, I don’t only understand the underlying technique, but also the inner workings of the machines, which greatly helped in my PhD. Thank you for the commitment in maintaining the equipment, and teaching me how to do so. Also, thank you for all the wonderful social conversations.

During my PhD I was fortunate enough to work with many great students, a special thanks goes to them. Without your collaboration, I would not have been able to obtain so much data, and this thesis would have been a lot shorter. I hope I managed to show you some of the beauty of science and research. Your work was essential in allowing me to study so many different subjects, and in completing this thesis. Ahmad, you were my very first student when I had only started my PhD for a couple months. Thank you for building the very first set-up with me, and thank you for never loosing enthusiasm every though we did not get to actually study the VLE behaviour of formic acid – trialkylamine complexes. Lars, thank you for debugging AntFARM1 with me, allowing us to take the first steps towards formic acid formation. Even though we never got above ppm levels, your work did provide me valuable input on how to get the reaction working. Ezgi, thank you for the detailed literature study on all the possible catalysts and their activity in formic acid production. Danny, even though your project was a very last minute one, you did great on creating the heterogeneous packed bed and spinning disc models. They were very helpful to me and several other students in Chapter 6. Esther, thank you for not only doing your bachelor thesis with me, but coming back for your Capita Selecta. It resulted in a very nice publication together, and a chapter within this thesis, thank you for all the effort you put into this! Daniel, you performed the initial techno-economic evaluation of the CO_2 to formic acid process. Getting this process into Aspen Plus was a steep learning curve for both of us as the adducts were not present in the database, but thanks to your endless perseverance we managed. Thank you for sharing the Aspen frustrations with me, and all the pleasant conversations we had during the debug stages. Zafina, your project ended up forming the basis for most of the work done in this thesis, from the development of the formic acid decomposition protocol, to the synthesis and testing of over 50 different catalyst formulations. Thank you for all the discussion on catalysis, characterization and whatever was going on in the world. I always admired your curiosity, it will get you very far in your career! Luca, I am still amazed at the amount of reactions you managed to perform during your thesis, thank you for always agreeing to testing yet another unconventional amine I would come up with. Thank you for all the social conversation during the long lab days, and all the time spend debugging AntFARM2 together. Every though we did not really get to use the set-up in the end, your work formed the basis for Chapter 4 and 5. Hopefully, we can publish our paper soon. Param, you had the difficult task of continuing on the great work of Zafina, but you did so amazingly. Thank you for finishing the bimetallic catalyst work with me, and we will publish it soon in a nice journal! While I never finished the flow UV-VIS synthesis work we started together, I did very much enjoy developing this novel synthesis approach with you. Also to you, thank you for all the nice conversations on the lab, over coffee and in the fort. Maurice, you took on the hugely challenging task of making the Cahn-Hilliard model with me. It truly was a learning curve for the both of us, but thank you for sharing it with me. Seeing you get better and better at programming in Python and C++ was a pleasure. I am still impressed by how quickly you managed the complex derivations. Alex, as you did not work on formic acid, your project was completely new to me as it was on coatings and photochemistry! While your work is not part of this thesis for that reason, I always liked the long lab days with you, and learned a lot from you on various topics. It was nice to discuss working life and life in general with you, and I still very much respect you obtaining your master degree after so many years of working in industry. Thank you for sharing some ‘exciting’ experiments with piranha acid with me! Bas, thank you for the many experiments you did to extent the

knowledge on formic acid – trialkylamine adducts to longer carboxylic acids such as acetic acid and propionic acid. Your work on characterization has greatly aided in this thesis, thank you for the enthusiasm in showing me all the wonderful colours the adduct formed over time. Rixt, you did not only your bachelor thesis with me, but decided to come back for your master thesis. Thank you for discovering the basics of combined carbon capture and hydrogenation with me, and thank you for all the conversation over a nice cup of coffee or tea! I wish you all the best in your future career. Wan Rong, you extended the work of Rixt into a techno-economic evaluation of such a novel process. Thank you for designing the intricate separation trains in such detail! Andreas, thank you for working with me these last one and a half years on your master thesis, your Capita Selecta, and finally getting to work together as colleagues on the novel methanol process! When you started your thesis, I had promised you no lab work. It quickly went from no lab work, to a week… and ended up being several months. Thank you for accepting this struggle, you never gave up. Your master thesis was hugely challenging, as Aspen decided it had its own will instead of obeying standard thermodynamics. You solved this beautifully by performing some good old fashioned McCabe-Thiele design, resulting in a nice publication and Chapter 6. I promise I will finish the second paper of your master thesis, and the 2 papers we will have together on methanol. It has been an honour to get to know you on a personal level, and an ever bigger honour to call you a friend. Thank you very much from the bottom of my heart for accepting to be my paranymph. Robbert, also you did not work on formic acid or methanol, but we got to work together on modelling electrochemistry! Thank you for all the hours of hanging out in my office trying to debug the model, and all the pleasant conversation shared while doing so. Thank you for reminding me to also relax sometimes, which often turned into sharing a couple of beers. It turned out to be the start of a valuable friendship, for which I am very grateful. I will come visit you in Zeeland soon. And lastly, Sterre. While I only joined your project at the very end due to your supervisor leaving, I still enjoyed working on photochemistry again with you! The drive you had to continue the project despite all the set backs was impressive!

To all my colleagues and friends at SPE, thank you for the endless support and all

the relaxing coffee breaks, lunches, PhD outings etc. You made these four years unforgettable. I have been very fortunate to share the PhD journey with you guys, making the long days in the lab lighter and more enjoyable. Every time I needed a break, I know I could meet one of you at the coffee machine to share some conversation with. Thank you for all the support, but above all, all the good time shared!

First of all, my co-inhabitants of STW 1.22: Merin, Camilla, Orlando, Domenico, Akmal, Andreas and Pranav. Looking back, I can say I was lucky to be placed in that office. Thank you all for the useful discussions, providing a pleasant atmosphere and all our non-working conversations. Camilla, you joined the group when I had just started my PhD. Thank you for taking so much time to teach me all the valuable lessons you had learned during your PhD! Orlando, I always enjoyed our endless social conversations, and conversations about the struggle of set-ups breaking and Aspen. I will never forget your cough. It is a pleasure to still be in touch with you, your 10 minute voice messages always bring a smile to my face. I will come to Rome soon! Akmal, thank you for your interest in others. You might not have been in the office much, it was always a pleasure to share a coffee with you. Pranav, thank you very much for all the pleasant and relaxing times we have shared in the office, and all our discussions on science. It has been wonderful to see you grow this much since starting your PhD. I wish you all the best in your PhD, but I am sure you will do fantastic! Don’t forget to enjoy as well! Alessia and Negar, while you are not officially inhabitants of STW 1.22, both of you have spent plenty of time there the last year. I always enjoy these social times. Thank you for helping me take a break from writing every so often. I am very sure both of you will do great in your PhDs!

Carola, the beating heart of the social part of SPE. Thank you for all the events organized, reminding me to take a break every so often, helping me so much in the beginning of my PhD on the lab, and the pleasant hikes in Deventer and the Veluwe. Let’s do it again soon! I very much enjoyed our collaborations on ammonia soap detection using NMR and the VLE set-up, and of course the results were never as we expected. Serena 1, thank you for being such a wonderful friend to me and all the collaborations we had. I always very much enjoyed traveling with you, and admired your knowledge on any topic. Serena 2, the enthusiasm you have for research is infectious, as is your very enthusiastic good morning to everyone. Alessia, our conversations on reactor engineering, photochemistry, coatings and analytics are often multiple hours long. Thank you for teaching this engineer some chemistry and I hope I managed to help you a bit with set-ups and modelling. Thank you for all the conversations about the struggles of PhD life, and life in general. You are doing a great job! Amin, Camilla and Valentina, thank you for the wonderful collaborations on catalysis characterization, resulting in my first publications. Max, thank you for the XPS collaborations resulting in nice papers, but even more for the morning coffee breaks. I always enjoyed our conversations about any topic. Thank you for all the reminders that there is more to life than the PhD. Rodrigo, thank you for always being available for a quick social talk over coffee or in the lab. You often had as many students as I did, and I learned a lot from you on how to manage the chaos. I am not surprised your life at VDL is as chaotic as your time at TUe. Adarsh, thank you for always being available for some quick advise, a discussion on anything scientific and all the times you borrowed me reactor parts. I could always trust on you and Naveen being in the office if I wanted to work late or weekends. Thank you for your endless interest in the research of others, and willingness to provide valuable insights to everyone. Thijs, thank you for always being available to discuss the struggles of PhD life, understanding all the effort and struggles it takes. Thank you for making me feel like I was not the only person struggling. I also enjoyed our discussions on analytical techniques. Giulia, thank you for all the social and sporting events organized, and the enthusiastic good mornings. I wish you all the best in your postdoc! Gaetano, I always enjoyed our social conversations in the hall way, and discussions on set-up and characterization struggles. Thank you very much for always being there to break the low moments with your humour, and making everyone smile. Daniel, thank you for all the help you provided with the cluster, and the programming advice given to my students. Your willingness to help everyone is inspiring. Jelle, I always enjoy our social conversations and jokes in STW 1.09, and your concern for safety. I hope you enjoy your backpacking trip! Roberto, I admire the work ethic you already showed as an Erasmus intern and now as a PhD. Your enthusiasm for science while striving for high quality work is inspiring. It was always very pleasant to share some social conversation with you, and also to share/complain about our Autochem struggles. Don’t forget to take a break every so often. I wish you and Alberto all the best in your PhDs. Huub, thank you for always being kind and cheerful. I always looked forward to hearing what random fact you would come up with over coffee. Clara, thank you for all the conversations shared in the lab, all the times you made me laugh in times of stress and the endless XPS measurements performed for me. I am sure you will do fantastic finishing your PhD! Rouzbeh, whenever I would run into you, you would tell me: ‘leave the lab, no more students and write your thesis!’. I have to admit, I very much needed this push, thank you. Thank you for all the pleasant evenings spent hanging out in the backyard of Arash and Niki. Shilpa, even though you only joined SPE towards the end of my project, thank you very much for asking every day how my writing as going, and sharing so much good advice. Zançat, we started our journey together all the way back in 2015, when we started our bachelor degrees. We even did our master internships together at ExxonMobil, being office mates there and working on the same topic. Thank you for all the support through the years, be it scientific or social. Our conversations on microkinetics were always very enriching, great to hear it finally works! Jasper and Stefan, thank you for all the conversations on science and the differences between Amsterdam and Eindhoven shared whenever you guys would visit! Stefan, great to hear you are coming back to TUe and all the best with your postdoc! And all the others, thank you very much for all the great times at conferences, borrels, lunch and coffee breaks, PhD outings etc.!

To my paranymphs, Arash and Andreas, I want to express my deepest gratitude for the friendship we share, and the support and encouragement received. Arash, thank you for showing me all the tricks in the lab when I just started my PhD. But above all, thank you for all the wonderful evenings spent at your place relaxing with Niki, and just always being there for me. I am always very grateful for the good conversations shared, endless discussions on crazy projects, and our shared hobby of watching mindless stuff on YouTube on the couch, of course with a beer or good glass of whiskey. You are one of those persons who you can always call for

whatever, no matter how busy you are, which is something I value very much. I wish you and Niki all the best in the future. Andreas, when you started your thesis I never imagined the friendship that started from it. It has truly been a pleasure and honour to work with you these 1.5 years. I have loved getting to work together as colleagues trying to develop a new process to produce methanol, and loved our trip to Boston and New York even more. Your creativity and kindness never cease to amaze me. But above all, thank you for always being there for me. Your endless kindness, patience, and wisdom have been instrumental to me navigating the challenges of life and this PhD. I am beyond grateful for the coffee breaks, dinners etc. we have shared, discussing our projects and lives. Your advice and unwavering support have been nothing short of amazing, and I cannot thank you enough for it. It has been a pleasure to see you start your life outside of university with Lauren, and I wish the both of you a beautiful, blessed future together.

Being part of a European project came with the opportunity to travel. Several consortium related activities would not have been as much fun without Tim and Serena. I always enjoyed the travel to all the meetings with you, and of course the free time spend enjoying several places in Europe together!

To my family and friends outside of university, thank you for always providing a place to go to whenever I needed to relax or needed a conversation to stay sane. Thank you for always believing in me, thank you for understanding when I was too busy to come by and listening to my complaints about the crazy life that is a PhD. Femke, we know each other for a very long time already and your support has been instrumental. I promise I will have more time available now that this thesis is over.

Now that I am approaching the end of this journey, I look back with a big smile thinking about the last 4 years. Thank you to everyone that took this journey with me and touched my heart doing so. With that, here is to new beginnings!

Yours sincerely,
Anouk

Anouk de Leeuw den Bouter was born on November 9, 1995 in Breda, the Netherlands. She completed most of her secondary (high school) education in 2014 at the Willem van Orange College in Waalwijk, and the remainder in 2015 at Luzac College Eindhoven in Eindhoven. She received her Bachelor's degree in Chemical Engineering and Chemistry with honours in July 2018, from the Eindhoven University of Technology, the Netherlands, for her thesis entitled: "Study of permeation fluxes with porous membranes for OCM reactor applications", under the supervision of prof.dr.ir. M. van Sint Annaland and Prof.Dr.Eng. F. Gallucci.

Anouk then enrolled in the Chemical Engineering Master's (Chemical Process Technology Track) program at the same university, where she focused on innovative processes and reactor modelling. She received her Master's degree cum laude, for her thesis titled "Multiscale modelling of the Fischer-Tropsch reaction: The effect of intraparticle diffusion on catalyst activity & selectivity" under the supervision of prof.dr.ir. E. Hensen, dr.ir. I.A.W. Filot and ir. B.Klumpers in 2020.

Anouk began her PhD program on December 1st, 2020, as part of the European program C2Fuel, in the Sustainable Process Engineering group at Eindhoven University of Technology under the supervision of prof.dr.ir. J. van der Schaaf. This resulted in her PhD thesis titled "On the direct hydrogenation of CO_2 towards formic acid".